

Technische Universität München
Institut für Energietechnik

Lehrstuhl für Thermodynamik

Design Method for Flow Reactors Producing Ammonia from Urea-Water Solution

Katrin Häcker

Vollständiger Abdruck der von der Fakultät für Maschinenwesen der Technischen Universität München zur Erlangung des akademischen Grades eines

DOKTOR – INGENIEURS

genehmigten Dissertation.

Vorsitzender:

Prof. Dr.-Ing. Markus Lienkamp

Prüfer der Dissertation:

1. Prof. Dr.-Ing. Thomas Sattelmayer
2. Prof. Dr.-Ing. Bert Buchholz

Die Dissertation wurde am 02.07.2018 bei der Technischen Universität München eingereicht und durch die Fakultät für Maschinenwesen am 27.11.2018 angenommen.

Früher war mehr Lametta!

LORIOT

Vorwort

Die vorliegende Arbeit entstand während meiner Zeit als wissenschaftliche Mitarbeiterin am Lehrstuhl für Thermodynamik der Technischen Universität München. Sie wurde durch MAN Diesel und Turbo SE gefördert.

Besonders danken möchte ich meinem Doktorvater, Prof. Dr.-Ing. Thomas Sattelmayer, für die Betreuung der Arbeit und die Übernahme des Hauptreferats. Herzlich danke ich Prof. Dr.-Ing. Buchholz für die freundliche Übernahme des Koreferats, sowie Prof. Dr.-Ing. Lienkamp für die Übernahme des Vorsitzes.

Für die freundschaftliche Zusammenarbeit möchte ich mich bei allen aktuellen und ehemaligen Mitarbeitern sowie insbesondere dem Sekretariat des Lehrstuhls bedanken.

Der Brotzeit-Gruppe danke ich für die wunderbaren Streichwurst-Diskussionen und stellvertretend Mathieu Zellhuber, Eva Loew, Frederic Collonval, Gary Jasor, Balbina Hampel, Jens Hümmer, Gerhard Giel und Johannes Weinzierl für ihre Freundschaft.

Mein Dank gilt auch meinen ehemaligen Studenten, die durch ihre Unterstützung beim Aufbau des Prüfstandes, bei Messkampagnen sowie bei der Auswertung einen wertvollen Beitrag zum Gelingen des Projektes geliefert haben. Stellvertretend für alle möchte ich mich bei Henrik Bär, Matthias Gigl, Tobias Böttcher und Zita Baumann bedanken.

Weiterhin bedanke ich mich bei Plamen Toshev, Michael Kolb und Lorenz Böck für ihre Unterstützung. Mein besonderer Dank gilt Udo Glückert, Johannes Weinzierl, Martin Schmid und dem Werkstatt-Team. Durch ihre freundschaftliche und fachliche Unterstützung trugen sie wesentlich zum Erfolg dieser Arbeit bei.

Meinen Eltern danke ich für ihre langjährige Unterstützung und den Rückhalt während meiner gesamten Ausbildung. Ohne meine Familie und engste Freunde wäre diese Arbeit nicht möglich gewesen. Meinen innigsten Dank richte ich an Christian. Er hat mich seit Beginn des Studiums immer wieder motiviert niemals aufzugeben, das Ziel nicht aus den Augen zu verlieren, und dennoch das Leben zu genießen.

München, im Februar 2019

Katrin Häcker

Abstract

The catalytic generation of ammonia from a liquid urea solution is a critical process determining the performance of SCR systems in maritime applications. Solid deposits on the catalyst surface from the decomposition of urea have to be avoided, as this leads to reduced system performance or even failure. At present, reactor design is often empirical, which constitutes a risk for costly iterations due to insufficient system performance. In this context, the research project aimed at proposing a new modelling approach for hydrolysis reactors generating ammonia from urea for the SCR. As a base for model development, different configurations of a hydrolysis reactor were investigated experimentally. Ammonia concentration measurements provided information about reaction steps and the influence of each reaction step on system performance. Parameter configurations revealed main influencing factors on the reaction steps. It is demonstrated that the thermolysis is the critical process step in the ammonia generation. Thereby, the evaporation of urea which means the water content of the urea solution as well as the velocity of the droplets is representative for the influencing factors. The spray of urea solution was characterised in terms of velocity distribution by means of particle-image velocimetry. Results were compared with theoretical predictions and an analytical distribution and mixing model was derived. Numerical simulations are used as validation opportunity of the proposed model and provide an additional design tool. The analytical and numerical calculation steps are summarised in a process flow model in form of a step-by-step method. Design constraints and operating conditions for hydrolysis reactors are taken into account and a prediction of hydrolysis reactor performance is provided.

Kurzfassung

Die vorliegende Arbeit beschreibt eine Auslegungsmethode für Hydrolyse-Reactoren zur Herstellung von Ammoniak aus einer wässrigen Harnstofflösung. Ein kritischer Prozess in Anlagen zur SCR-Abgasnachbehandlung ist die Bildung von Ablagerungen bei der Ammoniakherzeugung aus Harnstofflösung. Diese Ablagerungen führen zur Minderung der Systemleistung und zu einem möglichen Systemausfall. Die Auslegung von Hydrolyse-Reactoren zur Ammoniakherzeugung beruht derzeit auf Literaturdaten und Erfahrungswerten. Die inhärente Unsicherheit führt zu einem hohen Risiko für kostenintensive Iterationen im Entwicklungsprozess.

Um dieses Risiko zu reduzieren, zielt das hier beschriebene Forschungsprojekt auf die Entwicklung einer effizienten Methode zur Erstausslegung von Hydrolyse-Reactoren ab. Auf Basis experimenteller Untersuchungen wurden kritische Einflussgrößen für die Bildung von Ablagerungen bestimmt. Hierfür wurden zunächst Ammoniak-Konzentrationsmessungen durchgeführt, die die Reaktionsschritte und ihren Einfluss auf die Reaktorleistung spezifizieren. Der Thermolyse Prozess und dabei die Verdampfung und Verteilung der Harnstofflösung durch Spray-Injektion erwies sich als besonders kritisch. Insbesondere der Wassergehalt der Harnstofflösung und die Geschwindigkeit beziehungsweise Größe der Tropfen wurden als maßgebliche Einflussfaktoren identifiziert. Kenngrößen des Harnstoff-Sprays wurden durch PIV- und LDS-Messungen ermittelt. Auf Basis der turbulenten Freistrah-Theorie wurden analytische Geschwindigkeits- und Verteilungsprofile des Sprays berechnet und mit numerischen Modellen verglichen. Die analytischen und numerischen Berechnungsschritte sind in einem Flussdiagramm zusammengefasst, welches die Methode zur Auslegung schrittweise darstellt. Das entwickelte Modell bietet eine analytische Beschreibung des gesamten Reaktors und reduziert die Unsicherheit bei der Auslegung.

Contents

1	Introduction	1
1.1	Motivation	1
1.2	Current Situation of Exhaust Gas After-Treatments	3
1.3	Research Context and Objectives	7
1.4	Structure of the Thesis	10
2	Theoretical Background	12
2.1	Overview of SCR Chemistry	12
2.1.1	Selective Catalytic Reduction	14
2.1.2	Catalyst Deactivation	14
2.1.3	Marine Diesel Fuels	17
2.2	Decomposition of Urea and Hydrolysis Reactors	18
2.2.1	Energetic Considerations	22
2.2.2	Diffusion and Catalytic Reaction Kinetics	23
2.2.3	Basic Evaluation and Efficiencies	26
2.2.4	Components of Hydrolysis Reactors	28
2.3	Atomisation	34
2.3.1	Classification of Sprays	35
2.3.2	Correlations	36
2.4	Evaporation	39
2.4.1	Droplet Evaporation	39
2.4.2	Urea Evaporation	42
2.5	Theory of Turbulent Jets	43
2.5.1	Jets in Coflow	44
2.5.2	Two-Phase Jets	47
2.5.3	Jets in Finite Space	49

2.5.4	Two-Phase Jets in Coflow and Finite Space	49
3	Experimental Setups and Diagnostics	52
3.1	Hydrolysis Reactor Experiment	53
3.1.1	Hydrolysis Reactor Dimensions and Components	56
3.1.2	Design of Swirl Generators	58
3.1.3	Operating Conditions of Concentration Measurements	61
3.1.4	Velocity Measurement Operating Conditions	63
3.2	Injector Test Rig	66
3.3	Fourier Transform Infrared Spectroscopy	66
3.4	Velocity Measurement Methods	68
3.5	Spray Measurement Methods	69
3.5.1	Laser Diffraction Spectrometry (LDS)	69
3.5.2	Shadowgraphy and Patternator Measurements	69
4	Numerical Modelling	71
4.1	Numerical Domains	71
4.1.1	Hydrolysis Reactor Domain	72
4.1.2	Swirl Generator Domain	73
4.2	General Settings and Boundary Conditions	74
4.3	Droplet Injection Boundary Conditions	74
5	Baseline Reactor Performance	78
5.1	Experiments	78
5.1.1	Concentration Measurements	78
5.1.2	Velocity Measurements	86
5.1.3	Atomisation and Spray Measurements	91
5.2	Analytical Models	96
5.2.1	Droplet Evaporation Model	96
5.2.2	Diffusion Model and Kinetics	96
5.3	Comparison of the Turbulent Jet Model to the PIV Measurements	99
5.4	Radial Concentration and Temperature Profiles	102
5.5	RANS Simulation of the Hydrolysis Reactor	106
6	Optimised Reactor Performance	115
6.1	Experiments	115

6.1.1	Concentration Measurements	115
6.1.2	Velocity Measurements	119
6.2	RANS Simulation of the Optimised Hydrolysis Reactor	121
7	Hydrolysis Reactor Design Method	130
7.1	Steps of the Design Method	130
7.2	Application of the Design Method (Case Study)	141
8	Summary and Conclusion	146
A	Appendix	149
A.1	Droplet Breakup	149
A.2	Droplet Evaporation	151
A.2.1	Droplet Evaporation on a Surface	156
A.3	Turbulent Jets	158
A.3.1	Jets in Coflow	158
A.4	MATLAB Code for Droplet Distribution	167
A.5	Summary Test Conditions and Additional Results	170
A.5.1	Summary Test Conditions	170
A.5.2	Additional Results	173
	Supervised Theses	174
	Bibliography	185

List of Figures

1.1	Annual emissions (base year 2000) of CO ₂ , NO _x , SO ₂ and PM caused by the transportation sector as well as the fuel consumption (FC) for selected transport systems in million metric tons per year [28].	2
1.2	SCR process with the standard system of urea decomposition unit (here: hydrolysis reactor) and SCR catalyst [37].	6
1.3	SCR process with a bypass system for the urea decomposition unit and following SCR catalyst [37].	6
1.4	Flow chart of the step-by-step method for hydrolysis reactor designs.	9
2.1	Products of the intermediate reactions during the heating process of urea according to <i>Schaber et. al.</i> [82].	20
2.2	Limitation of the chemical reaction rate by mass transfer (molecular diffusion), Knudsen diffusion or kinetic limitation [64].	25
2.3	Injector types: (a) one-phase (plain-orifice) nozzle, (b) two-phase nozzle with internal mixing and (c) two-phase nozzle with external mixing.	30
2.4	General structure of a two-phase nozzle with external mixing of the Düsen-Schlick GmbH (model 970).	30
2.5	Geometric parameters for a square cell (a) and for a triangular cell (b) [24].	32
2.6	Metal substrate (a) and ceramic honeycomb monolith (b).	33
2.7	Vapour pressure curves for water (solid line), 32.5 % urea (dashed line) and 67.5 % urea (dashed dotted line) in an aqueous solution.	42
2.8	Schematic illustration of a turbulent jet in coflow [1].	45

LIST OF FIGURES

2.9	Two phase jet out of a nozzle.	48
2.10	Jet in coflow in finite space.	50
3.1	Test rig for hydrolysis reactors: cold air (blue arrow) from the Roots blower is heated (red arrow) by the two heaters, passes the hydrolysis reactor and the ammonia slip catalyst, before exiting the setup (green arrow).	54
3.2	Hydrolysis reactor with its components.	54
3.3	Hydrolysis reactor setup for concentration measurements with swirl generator (optional), nozzle, evaporation section (highlighted in blue), catalyst and diagnostics.	55
3.4	Used nozzles: (a) Schlick model 940 and (b) MAN nozzle.	57
3.5	Used catalysts: (a) Emitec ST structure (200 cpsi) and (b) Emitec MX structure.	57
3.6	Tangential velocity distribution of a Burgers vortex (resembles irrotational vortex) in (a), a solid body vortex in (b) and a wall jet in (c) in a pipe flow [87].	59
3.7	Swirl generator blade with the characteristic diameters d_{SN} and d_h as well as the turning angle Φ	60
3.8	Hydrolysis reactor setup for Pitot tube measurements.	64
3.9	Hydrolysis reactor setup for PIV measurements.	65
3.10	Injector setup with shadowgraphy system (7 and 8), LDS system (9) and patternator (10).	67
3.11	Laser Diffraction Spectrometry [97].	70
4.1	Numerical domains for the swirl generator and the reactor.	72
4.2	Hydrolysis reactor domain.	73
4.3	Swirl generator domain.	73
5.1	Solid by-products created at the catalyst during operating point OP2. Left: at the rear surface of the catalyst; Right: at the front surface of the ST structure.	80
5.2	Comparison of the urea decomposition rate (UDR) for TC1–TC3 and RC.	82
5.3	Comparison of the hydrolysis efficiency level (HEL) TC1–TC3 and RC.	82

5.4	Comparison of the urea decomposition rate (UDR) for TC4–TC6 and RC.	84
5.5	Comparison of the hydrolysis efficiency level (HEL) for TC4–TC6 and RC.	84
5.6	Axial cross sections (CS) with distances to the nozzle.	87
5.7	Axial velocities measured for PT1 (black circles) and PT2 (grey circles), in comparison with numerical simulations.	88
5.8	Axial droplet velocity at CS1: (a) for a liquid mass flow rate of 2.4 kg h^{-1} and (b) for a liquid mass flow rate of 7.3 kg h^{-1} for three temperatures (black: 300°C , grey: 350°C , white: 400°C).	90
5.9	Droplet size distributions for Schlick 940: Variation of liquid mass flow rate (a) and variation of measurement cross sections for OP1 (b). All tests with 100 L min^{-1} pressurised air volume flow.	91
5.10	Droplet size distributions: Comparison of Schlick 940 and MAN for OP4 at CS1 (a) and for OP4 at CS4 (b).	93
5.11	Normalised mass distribution from patternator measurements: 7.3 kg h^{-1} liquid mass flow and 100 L min^{-1} pressurised air flow.	95
5.12	Spray cone angle, between 26° and 32° for Schlick 940 (a) and between 23° and 31° for the MAN nozzle (b).	95
5.13	Mass reduction of different droplet sizes for OP1 (liquid: 7.3 kg h^{-1} and bulk temperature: 460°C), OP2 (liquid: 13.4 kg h^{-1} and bulk temperature: 490°C), OP3 (liquid: 20.3 kg h^{-1} and bulk temperature: 510°C) and OP4 (liquid: 25.3 kg h^{-1} and bulk temperature: 550°C): in (a) $50 \mu\text{m}$ in (b) $70 \mu\text{m}$ and in (c) $100 \mu\text{m}$	97
5.14	Mass transfer coefficient in (a) and diffusion length in (b) for isocyanic acid and water.	99
5.15	Normalised axial droplet velocity decrease along the symmetry axis measured for OT3 (liquid: 2.4 kg h^{-1} , pressurised air: 100 L min^{-1}) and OT6 (liquid: 2.4 kg h^{-1} , pressurised air: 100 L min^{-1}) in comparison with the theoretical progress (see equation 2.42).	100
5.16	Normalised radial distribution of the normalised axial velocity at different axial cross sections (CS1 till CS3) compared with model 1 (equation 2.39) and model 2 (equation 2.40).	101

5.17	Theoretical concentration distributions upstream the catalyst (model 1: equation 2.51 and model 2: equation 2.52) and after passing the catalyst including the dispersion factor f (equation 5.4) (MX Dispersion 1 refers to model 1 and MX Dispersion 2 to model 2), in comparison with the normalised measured ammonia concentrations downstream the catalyst.	103
5.18	Calculated temperature profiles at CS4 for all operation points (OP1 calc till OP4 calc) by model 1 (equation 2.51) in comparison with measured temperatures (points) at CS4 for OP1 and OP2. . .	105
5.19	Calculated diffusion length profiles of HNCO (equation 5.2) at CS4 for OP1 with constant temperature (OP1 HNCO const. Temp) and with temperature profile (OP1 HNCO) (equation 2.51). . .	107
5.20	Calculated diffusion length profiles of HNCO at CS4 for all operation points (OP1 HNCO till OP4 HNCO) with temperature profiles.	108
5.21	Droplet size distribution of OP1 at CS1 and of NT3 at CS0.	109
5.22	Axial velocity decrease along the symmetry axis for NT1 and NT2 in comparison with the jet theory adapted to the optical tests. . .	109
5.23	Axial velocity for NT1 at CS1–CS4 in comparison with the jet model 1 (equation 2.39) and model 2 (equation 2.40).	110
5.24	Axial velocity for NT2 at CS1–CS4 in comparison with the jet model 1 (equation 2.39) and model 2 (equation 2.40).	110
5.25	Water vapour concentration for NT1 at CS1–CS4 in comparison with the jet model 1 (equation 2.51) and model 2 (equation 2.52). . .	111
5.26	Water vapour concentration for NT2 at CS1–CS4 in comparison with the jet model 1 (equation 2.51) and model 2 (equation 2.52). . .	111
5.27	Temperature profiles for NT3 (black line), NT4 (blue line) with remaining liquid mass and NT3 evap (dashed black line), NT4 evap (dashed blue line) incorporating the evaporation of the remaining liquid in comparison with temperature measurement points (all at CS4).	114
6.1	The UDR and HEL for TC7 in comparison to the reference case (RC).	117

6.2	Axial droplet velocity with swirl flow at CS1: three temperature changes for a liquid mass flow rate of 2.4 kg h^{-1} in (a) and for a liquid mass flow rate of 7.3 kg h^{-1} in (b).	120
6.3	Tangential droplet velocity to the normalised channel radius in swirling coflow at CS1 (OT3 swirl and OT6 swirl).	120
6.4	Vector plot of the velocity magnitude for the swirl generator flow field.	122
6.5	Tangential velocity profiles at the outlet of the swirl generator vanes ($x = -170 \text{ mm}$: solid line), at $x = -120 \text{ mm}$ (dashed line) and at CS0 (dashed dotted line).	123
6.6	Nomalised axial droplet velocity decrease along the axis for OT3, OT6, NT1 and NT2 with swirl and for NT2 without swirl.	124
6.7	Axial velocity profiles for NT3 and NT4 (without swirl) and NT3 swirl and NT4 swirl (with swirl) at CS4.	125
6.8	Tangential velocity profiles of NT3 swirl and NT4 swirl at CS4.	125
6.9	Temperatures profiles for NT3 (black line), NT3 swirl (blue line) with remaining liquid mass and NT3 evap (dashed black line), NT3 swirl evap (dashed blue line) incorporating the evaporation of the remaining liquid mass at CS4.	126
6.10	Temperatures profiles for NT4 (black line), NT4 swirl (blue line) with remaining liquid mass and NT4 evap (dashed black line), NT4 swirl evap (dashed blue line) incorporating the evaporation of the remaining liquid mass at CS4.	127
6.11	Mass fraction of water vapour of NT3 and NT4 for the baseline as well as NT3 swirl and NT4 swirl for the optimised reactor design at CS4.	128
6.12	Length of diffusion profiles of NT3 HNCO and NT4 HNCO for the baseline and of NT3 swirl HNCO and NT4 swirl HNCO for the optimised reactor design.	129
7.1	Procedure of the hydrolysis reactor design method.	131

7.2	Temperature profiles calculated for OP3: surface evaporation of all liquid (OP3 calc surface evap: black line), droplet evaporation and bulk temperature decrease until the catalyst (OP3 calc drop evap: blue line) and incorporating droplet evaporation and surface evaporation of the remaining liquid mass (OP3 calc drop + surface evap: light blue line).	142
7.3	Temperature profiles for simulation of OP3 with swirl generator at CS4: with remaining liquid mass (NT5 swirl: blue line) and incorporating the evaporation of the remaining liquid mass (NT5 swirl evap: dashed blue line).	143
7.4	Length of diffusion of HNCO: OP3 HNCO for the baseline reactor setup and NT5 swirl HNCO for the optimised reactor design. . .	144
A.1	Modes of disintegration for the primary breakup by Reitz [64]. . .	150
A.2	Secondary droplet breakup mechanisms [63].	151
A.3	Boiling curve of <i>Nukiyama</i>	157
A.4	Schematic illustration of the boundary layer at the initial region of a jet in coflow [1].	158
A.5	The results for the boundary relation of \bar{r} to \bar{x} for different initial velocity ratios m	164
A.6	Tangential droplet velocity to the normalised channel radius in coflow at CS1 (OT3 and OT6).	173

List of Tables

2.1	Catalyst deactivation mechanisms according to <i>Bartholomew</i> [8].	16
2.2	Geometric and classification properties for uncoated metal substrates [24].	33
3.1	Engine operating points.	62
3.2	Operating conditions for the baseline reactor type.	63
3.3	Operating conditions for the optimised reactor type.	63
3.4	Pitot tube tests for gas velocity measurements.	64
3.5	Operating conditions for droplet velocity measurements.	65
5.1	Results of tests representing engine operating points.	79
5.2	Results of fundamental test cases RC and TC1–TC3.	81
5.3	Results of fundamental test cases RC and TC4–TC6.	85
5.4	Boundary conditions for numerical simulations of the pipe flow with and without gaseous jet.	88
5.5	Characteristic droplet sizes for Schlick 940 and MAN nozzle.	94
5.6	Boundary conditions for simulations.	107
6.1	Test conditions and calculated parameters of test cases for the optimised reactor.	116
6.2	Test conditions and calculated parameters for the engine operating points of the optimised reactor.	119
6.3	Temperatures and evaporated liquid for NT3 and NT4 without and with swirl.	124
7.1	Required or optional input parameters.	132
7.2	Required or optional input parameters.	133

LIST OF TABLES

7.3	Temperatures measured and calculated with turbulent jet theory for all engine operating points.	142
7.4	Evaporated liquid due to droplet evaporation for OP3.	143
A.1	Classification of jet breakup regimes according to Reitz [64] . . .	149
A.2	Summary of concentration measurement conditions.	171
A.3	Summary Pitot, PIV, injector tests and simulation conditions. . .	172

Nomenclature

Latin Symbols

a	Thermal diffusivity	$[\text{m}^2 \text{s}^{-1}]$
a	Variable, constant	$[\]$
a	Specific phase boundary	$[\text{m}^{-1}]$
A	Surface	$[\text{m}^2]$
A_1, A_2	Integral function	$[\]$
b	Boundary layer thickness of jet	$[\text{m}]$
b	Variable, constant	$[\]$
B_1, B_2	Integral function	$[\]$
B_M	Mass transfer	$[\]$
B_T	Thermal transfer	$[\]$
c	Experimental coefficient	$[\]$
C	Concentration	$[\text{mol m}^{-3}]$
C	Contour	$[\]$
C_1, C_2	Integral function	$[\]$
c_p	Specific Heat	$[\text{J kg}^{-1} \text{K}^{-1}]$
c_w	Drag coefficient	$[\]$
d	Diameter	$[\text{m}]$
D	Diameter	$[\text{m}]$
\vec{D}	Angular momentum	$[\text{kg m}^2 \text{s}^{-1}]$
\dot{D}	Axial flux angular momentum	$[\text{kg m}^2 \text{s}^{-2}]$
D_{12}	Mass diffusivity	$[\text{m}^2 \text{s}^{-1}]$
D_1, D_2	Integral function	$[\]$
D_{32}	Sauter Mean Diameter	$[\text{m}]$
D_{V50}	Mass Mean Diameter	$[\text{m}]$

Nomenclature

D_{V90}	Characteristic droplet diameter	[m]
E	Absorbance	[]
E_a	Activation energy	[J mol ⁻¹]
E_t	Total energy	[J]
f_{dis}	Dispersion factor	[]
F	Surface	[m ²]
f_i	Body forces	[N]
f_1, f_2	Integral functions	[]
g	Acceleration of gravity	[m s ⁻²]
G_π	Admixture weight flow rate	[kg m s ⁻³]
G_B	Gas phase weight flow rate	[kg m s ⁻³]
Δh_v	Specific evaporation enthalpy	[J kg ⁻¹]
Δ_v	Diffusion volume	[]
I	Intensity	[W m ⁻²]
\vec{I}	Axial momentum	[kg m s ⁻¹]
\dot{I}	Axial flux axial momentum	[kg m s ⁻²]
J	Diffusion flux	[mol m ⁻² s ⁻¹]
k	Reaction rate constant	[s ⁻¹]
k_0	Pre-exponential factor	[s ⁻¹]
k_{eff}	Effective reaction rate constant	[s ⁻¹]
k_p	Vapour pressure constant	[Pa]
L	Length	[m]
m	Mass	[kg]
m	Velocity ratio	[]
\dot{m}	Mass flow	[kg s ⁻¹]
n	Number	[]
n	Integral function	[]
N	Number	[]
p	Pressure	[Pa]
p	Variable, constant	[]
q	Variable, constant	[]
\dot{q}	Heat flux	[W s ⁻²]
\dot{Q}	Heat flow	[W]
r	Radius	[m]

\bar{r}	Dimensionless radius	[]
R	Radius	[m]
\bar{R}	Gas constant	[J mol ⁻¹ K ⁻¹]
R_{sp}	Specific gas constant	[J kg ⁻¹ K ⁻¹]
s	Contour element	[]
S	Swirl number	[]
t	time	[s]
T	Temperature	[K]
\vec{u}	Velocity	[m s ⁻¹]
u	Axial velocity	[m s ⁻¹]
u_{π}	Admixture velocity	[m s ⁻¹]
u_H	Coflow velocity	[m s ⁻¹]
u_B	Gas phase jet velocity	[m s ⁻¹]
V	Volume	[m ³]
\dot{V}	Volume flow	[m ³ s ⁻¹]
X	Concentration	[ppm]
Y	Mass fraction	[]
x, y, z	Cartesian coordinates	[]
x	Distance	[m]
x_H	Lenght initial region	[m]
x_n	Lenght initial ant transitional region	[m]
y	Distance	[m]

Greek Symbols

α	Heat transfer coefficient	[W m ⁻² K ⁻¹]
β	Mass transfer coefficient	[m s ⁻¹]
χ	Concentration	[]
δ_{ij}	Kronecker delta	[]
ϵ	Attenuation coefficient	[m ³ mol ⁻¹ m ⁻¹]
φ	Swirl angle	[°]
Φ	Angle	[°]
η	Dimensionless abscissa	[]

Nomenclature

η_{mix}	Mixing rate	[]
λ	Air ratio	[]
λ	Thermal conductivity	[W m ⁻¹ K ⁻¹]
μ	Dynamic viscosity	[Pa s]
ν	Kinematic viscosity	[m ² s ⁻¹]
ω	Vorticity	[]
ρ	Density	[kg m ⁻³]
σ	Surface tension	[N m ⁻¹]
τ	Stress tensor	[kg m ⁻¹ s ⁻²]
ξ	Dimensionless ordinate	[]

Chemical Symbols

C ₃ H ₄ N ₄ O ₂	Ammelide	[]
C ₃ H ₅ N ₅ O	Ammeline	[]
C ₂ H ₅ N ₃ O ₂	Biuret	[]
C ₃ H ₆ N ₆	Melamine	[]
CO	Carbon oxid	[]
CO ₂	Carbon dioxid	[]
CO _x	Carbon oxids	[]
C _n H _{2n+2}	Hydrocarbons	[]
CYA	Cyanuric acid	[]
H ₂ O	Water	[]
HNCO	Isocyanic acid	[]
N ₂	Nitrogen	[]
NH ₃	Ammonia	[]
(NH ₂) ₂ CO	Urea	[]
NO	Nitrogen oxid	[]
NO ₂	Nitrogen dioxid	[]
NO _x	Nitrogen oxides	[]
O ₂	Oxygen	[]
SO ₂	Sulfur dioxides	[]
SO _x	Sulfur oxides	[]

TiO ₂	Titanium dioxid	[]
------------------	-----------------	----

Abbreviations

CFD	Computational Fluid Dynamics	[]
CHF	Critical Heat Flux	[]
ECA	Emission Controlled Area	[]
e. g.	exempli gratia (for example)	[]
FC	Fuel Consumption	[]
FTIR	Fourier Transform Infrared	[]
GHSV	Gas Hourly Space Velocity	[h ⁻¹]
HEL	Hydrolysis Efficiency Level	[]
i. e.	id est (that is)	[]
IMO	International Maritime Organization	[]
LIF	Laser Induced Fluorescence	[]
MARPOL	Marine Pollution	[]
MHF	Minimum Heat Flux	[]
MMD	Mass Mean Diameter	[]
NCR	Non-Selective Catalytic Reduction	[]
PIV	Particle Image Velocimetry	[]
PM	Particulate Matter	[]
ppm	parts per million	[]
SCR	Selective Catalytic Reduction	[]
SMD	Sauter Mean Diameter	[]
SNCR	Selective Non-Catalytic Reduction	[]
UDR	Urea Decomposition Rate	[]
UWS	Urea-Water Solution	[]

Subscripts

0	Initial, standard, or boundary value	[]
∞	Ambient value	[]
<i>A</i>	Air	[]
<i>c</i>	Specific location	[]
<i>cat</i>	Catalyst	[]
<i>diff</i>	Diffusion	[]
<i>dr</i>	Droplet	[]
<i>evap</i>	Evaporated	[]
<i>g</i>	Gas	[]
<i>h</i>	Hub	[]
<i>hyd</i>	Hydraulic	[]
<i>i</i>	Index	[]
<i>in</i>	In	[]
<i>i, j</i>	Cartesian coordinates	[]
<i>m</i>	Maximum	[]
<i>loss</i>	Loss	[]
<i>L</i>	Liquid	[]
<i>out</i>	Out	[]
<i>ref</i>	Reference	[]
<i>R</i>	Relative	[]
<i>S</i>	Substance	[]
<i>SN</i>	Swirl nozzle	[]
<i>st</i>	Static	[]
<i>sur</i>	Surface	[]
<i>t</i>	Total	[]
<i>T</i>	Temperature	[]
<i>tan</i>	Tangential	[]
<i>u</i>	Velocity	[]
<i>vap</i>	Vapour	[]
χ	Concentration	[]

Superscripts

()'	Fluctuating component	[]
(-)	Related value	[]
(-)	(Time-)Averaged value	[]
(·)	Time derivative	[]

Dimensionless Numbers

Le	Lewis Number	[]
Ma	Mach number	[]
Nu	Nusselt Number	[]
Oh	Ohnesorge Number	[]
Pr	Prandtl Number	[]
Re	Reynolds Number	[]
Sc	Schmidt Number	[]
Sh	Sherwood Number	[]
We	Weber Number	[]

1 Introduction

1.1 Motivation

Newspaper headlines from The New York Times (on April 26, 2012) “*Study Indicates a Greater Threat of Extreme Weather*” or The Guardian (on July 10, 2012): “*Scientists attribute extreme weather to man-made climate change*” make discussions about climatic changes omnipresent in media and international politics. Scientists investigating “extreme weather” conditions have proven an increasing frequency of occurrence [25, 40]. They stated that the continuous increase of greenhouse gas emission by human activities and the consequential atmospheric pollution are the cause for these extreme weather conditions and lead to an unusual warming of the climate system [76]. The last G7 summit just ended, once again reasserting that global warming and emissions have to be reduced significantly. One aim of the annual United Nations Climate Change conferences is to define legally binding regulations for developed countries in future emission controls. Currently the regulations are only directives that have to be implemented by the nations themselves. Nevertheless, in the course of such meetings the Kyoto Protocol was adapted, including reduction of greenhouse gas targets. The first commitment period, accepted by 192 parties, ended in 2012 and lasted four years. A possible extension of the protocol is being discussed.

Alongside industry, energy supply and housing emissions, the global transportation sector contributes a significant share to the world’s emissions, thus causing global warming and pollution. The latter includes road traffic, aviation and shipping. Emissions caused by the transportation sector are shown in figure 1.1, including the most important emission compounds and the fuel consumption for each of the three transportation modes. It is visible evident that road traffic has the highest carbon dioxide (CO₂) emission per year com-

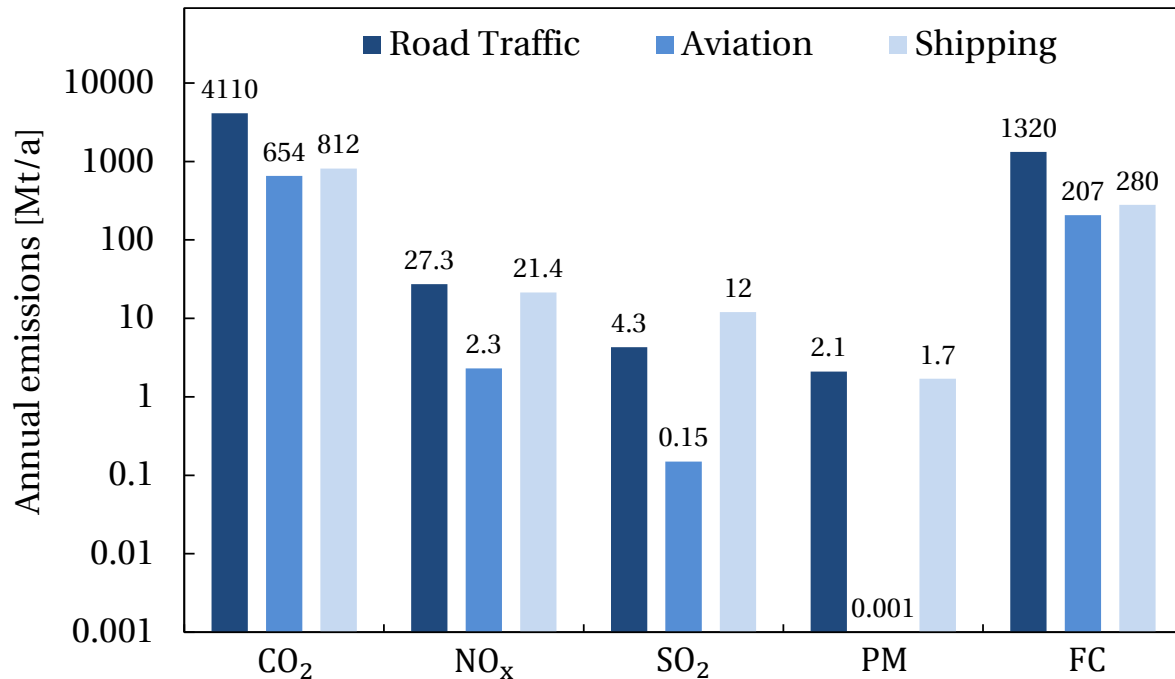


Figure 1.1: Annual emissions (base year 2000) of CO₂, NO_x, SO₂ and PM caused by the transportation sector as well as the fuel consumption (FC) for selected transport systems in million metric tons per year [28].

pared to the others. By contrast the emission of nitrogen oxides (NO_x) as well as particulate matter (PM) is similar between the road traffic sector and the shipping sector. However, the continuing increase in road traffic in the past decades has led to an increased public awareness particularly for this mode of transportation. Hence, the first European restriction for passenger and commercial vehicles was established in 1970 for carbon oxides (CO_x) and hydrocarbons (C_nH_{2n+2}), followed in 1977 by limits for NO_x and PM for diesel engines in 1988. Since their introduction, the restrictions have been tightened regularly.

In the course of extensive investigations about the contribution of each emission compound to climate changes and human health, PM and NO_x are in the centre of attention. Scientists have made them responsible to be harm-

ful for the environment and to the human health. Acidification of the natural ecosystem and freshwater, air pollution, cardiopulmonary disease, lung cancer, respiratory illnesses etc. However, as research is in progress the impact of these emissions cannot be specified conclusively. The shipping transport business causes a significant amount of these emission compounds, and thus has drawn particular attention. Marine diesel engines operate at high temperatures and use heavy oil with a high sulfur content [27]. This leads to high emissions of NO_x , particles and sulfur dioxide. The air pollution caused along coastal lines and major shipping routes is even apparent on satellite observations [28]. With the introduction of the marine pollution (MARPOL) norms by the International Maritime Organization (IMO) restrictions for shipping have been realised. In Emission Controlled Areas (ECAs) for example, most of the coastlines of Europe and North America, these norms are binding. The norm addresses different types of pollution caused by shipping such as water pollution from rubbish or air pollution caused by exhaust gas emissions (annex VI of the IMO-MARPOL protocol records the air pollution) [67]. Besides the reduction of the high concentration of sulfur oxides (SO_x), limits for NO_x are at the focus of the air pollution regulation. For NO_x the TIER norm is mandatory. Three emission stages were negotiated over the course of the last 15 years. The next stage of this norm (TIER III) came into force in January 2016 [47, 67]. This requires a reduction of NO_x by about 70 % [47].

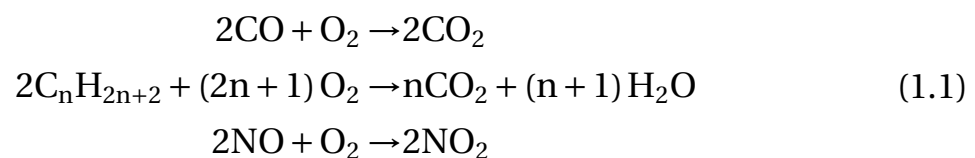
1.2 Current Situation of Exhaust Gas After-Treatments

For vehicle engines in the private and commercial sector exhaust gas treatment has become industry standard, as engine based measures and combustion optimisation alone do not meet the emission targets. For combustion optimisation exhaust gas recirculation, turbocharging, water injection and the air ratio (λ) adjustment are the methods of choice. Exhaust gas treatments are categorised according to the different combustion products, including PM, CO_x , hydrocarbons and NO_x . An unfavourable by-product of all of these treatments is the increase in fuel consumption and installation size. For this reason improvements in efficiency and size are analysed in detail by research and

development teams. In the cargo ship business engine-based measures have been sufficient to achieve the given limits for a long time. The introduction of the new regulations in MARPOL/Annex VI will require exhaust gas treatment methods for the shipping industry. The regulations aim at reducing SO_x and NO_x in particular. Thus, the research and development emphasis is on treatment methods for those substances. As a first step to reduce SO_x a decrease of the sulfur content in marine diesel fuel is being discussed. In addition, when the TIER III norm comes into force, exhaust gas treatments for NO_x will be unavoidable. Selective Catalytic Reduction (SCR) is one of the most effective methods for reducing the NO_x content of the exhaust gas.

Oxidation Catalyst

In contrast to diesel engines, which operate with excess air, the fuel-air ratio is adjusted to near-stoichiometric conditions in gasoline engines by the lambda sensor. The stoichiometric composition allows for using standard three-way-catalytic converters (they operate efficiently only in a small range around the stoichiometric condition) for a combined oxidation and reduction of the combustion products. Diesel engines with their lean combustion system prevent their utilisation. The oxidation and reduction of the combustion products have to be separated. In a first step, the combustion products are oxidised in the oxidation catalyst. Oxidation reactions for the emission compounds write:



SNCR and NCR

Selective Non-Catalytic Reduction reduces NO_x without the aid of a catalyst. This requires significantly higher temperatures to overcome the activation energy for the conversion process. Temperatures range between 900°C and 1100°C which is far beyond the temperature range of a typical diesel engine

exhaust system, between 250 °C and 500 °C [80]. Thus, this reduction method is not applicable. Non-Selective Catalytic Reduction can be found in the standard three-way-catalytic converter as mentioned before.

NO_x Storage Catalyst

The NO_x Storage Catalyst was developed for combustion processes with air excess in specific operating points for temporary storage of NO_x. The reduction of NO_x and a subsequent regeneration of the catalyst are performed during phases of rich combustion [80]. The storage process is based on absorption and desorption. During absorption, NO_x are stored as nitrates on the alkaline storage component of the platinum catalyst. Desorption takes place during a short rich combustion phase where the temperatures are raised and the stored nitrates decompose with carbon monoxide and hydrocarbons to nitrogen (N₂) and CO₂. The benefit of this system is the absence of an additional reducing agent such as a urea-water solution for the SCR, the downside is the higher fuel consumption and the expensive noble metal catalyst.

SCR

Selective Catalytic Reduction is the selective conversion of NO_x, with the aid of catalysts and a reducing agent, into water and N₂. During the whole process, the chemical components involved proceed through different stages of conversion (detailed information about the SCR process is given in section 2.1.1). In general ammonia is used as the reducing agent. The toxicity of this gas requires complex storage restrictions and dedicated safety measures, hence a urea-water solution (commercial name: AdBlue) is used as precursor instead. In a first step the conversion to ammonia is realised. In the following step ammonia reacts catalytically with NO_x to water and N₂. Two designs of SCR systems can be found: a combined system for the decomposition of urea and the SCR process (standard system, see figure 1.2) and a geometrical separation of decomposition and reduction (bypass system, see figure 1.3). The urea decomposition unit is called *hydrolysis reactor*.

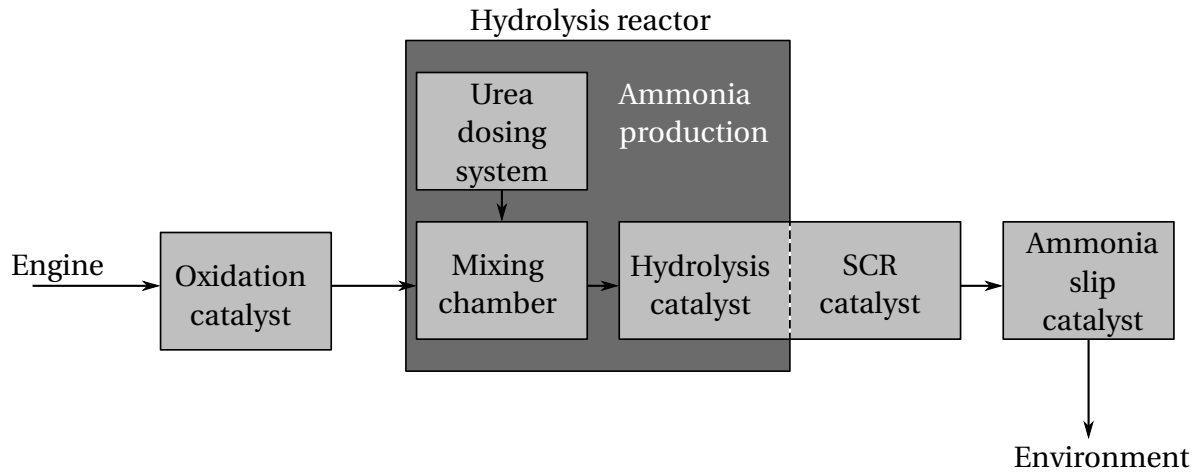


Figure 1.2: SCR process with the standard system of urea decomposition unit (here: hydrolysis reactor) and SCR catalyst [37].

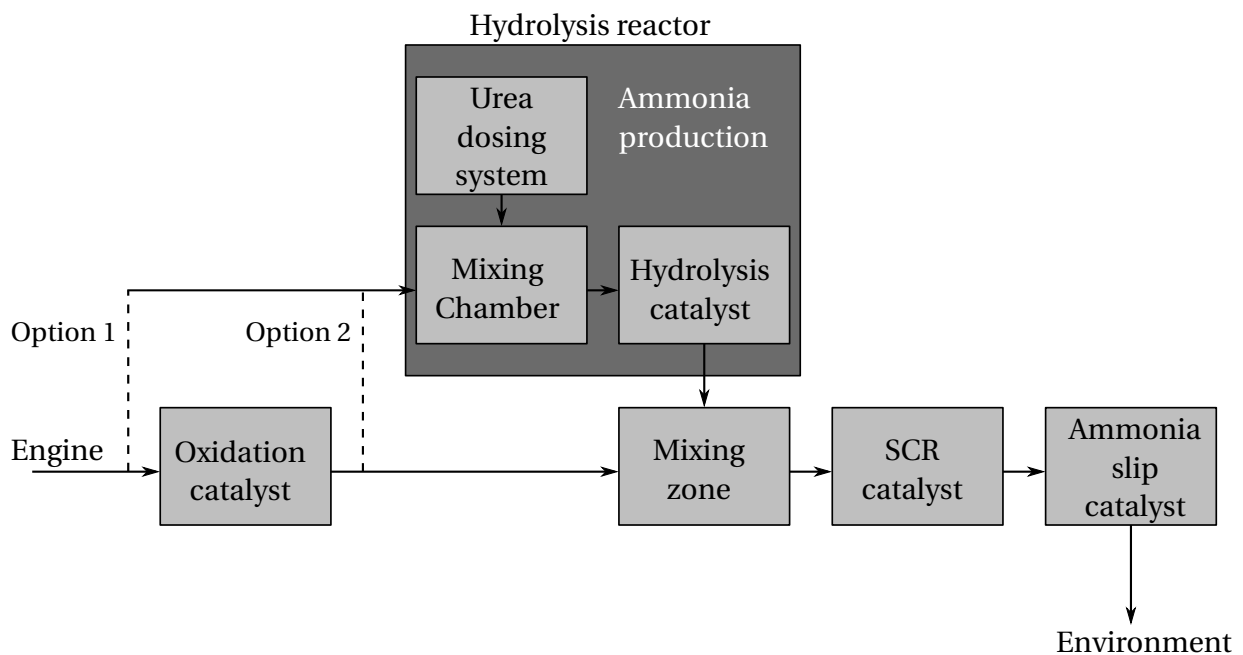


Figure 1.3: SCR process with a bypass system for the urea decomposition unit and following SCR catalyst [37].

The standard system with combined hydrolysis and SCR catalyst has disadvantages in terms of size and flexibility to changing conditions, but provides a lower system complexity compared to the bypass system. The bypass system offers the possibility of separated component optimisation, thus a higher flexibility to accommodate different conditions compared to the standard system. High flexibility is of interest in particular due to the high dependence of the ammonia production on the system temperature. Urea-water solution has to be heated until decomposition of urea into ammonia begins (details are given in [89] and [82]). If the temperature of the hydrolysis catalyst falls below a critical level, urea forms irreversible solid deposits which can block the catalyst. Hence, the temperature must always be kept above the critical temperature. In bypass systems the thermodynamic conditions can be regulated more readily, even during load fluctuations. The basis for this thesis is the bypass system (figure 1.3), as high flexibility is required.

1.3 Research Context and Objectives

The hydrolysis process of urea for SCR of exhaust gases has been investigated extensively since the late 1970's. Chemical reaction steps occurring during the decomposition process of urea are well understood [82]. Likewise, the effect of catalyst coatings on the hydrolysis performance and the kinetics of catalytic reactions have been examined in great detail [9, 18, 21, 36]. However, practical design of hydrolysis reactors still faces challenges. Poor design methods can lead to insufficient performance and costly design iterations.

This thesis originated from a research collaboration with the marine diesel engine producer MAN Diesel & Turbo SE, initiated by the introduction of the new TIER III regulations. The project objective was the development of a hydrolysis reactor for the production of ammonia from urea-water solution for large marine diesel engines exhaust gas systems. In a first step the exhaust gas treatment systems (with SCR systems using ammonia) of the energy industry were adapted. These do not represent adequate on-board solutions due to required installation space. Hence, the focus was placed on the significant reduction of the system size. For years, the commercial vehicle division of MAN

SE (MAN Truck & Bus) has successfully utilised a bypass system for the SCR hydrolysis process. Consequently, it was a natural decision to exploit synergies and develop a bypass system for marine diesel engines. The boundary conditions were given by the engine load cycles, in which about 2 % of the overall exhaust gas stream was made available for the hydrolysis reactor. The system size should be similar to those used in trucks, but with a significant increase of performance. The resulting challenge was the high liquid load of urea-water solution in the gas phase (in the hydrolysis reactor) and the associated evaporative cooling. As a consequence, the main question to be answered in this work is:

- Which design of a hydrolysis reactor leads to a reliable performance, satisfying specific boundary conditions and system constraints?

At present reactor design is often empirical, which poses a risk for costly design iterations. A step-by-step method is developed within this thesis which takes into account design constraints and operating conditions for hydrolysis reactors. This leads to the following related questions:

- What are the parameters influencing the decomposition process of urea?
- What is the effect of each of these parameters on the overall system performance?
- What measurement methods are applicable for model validation?
- How can the model parameters be determined theoretically?

The step-by-step method for hydrolysis reactor design is summarised schematically in figure 1.4. Engine specifications, operating conditions and design constraints of the reactor compose the input information for this method. The first calculation step is named basic evaluation. A fundamental feasibility study is conducted within this step based on the input parameters. The following step combines analytical and numerical methods. These methods were validated by experiments presented in this thesis. Iterative steps are

visualised in the flow chart by the two decision points: a first one after the basic evaluation of the reactor design and a second one after performing the analytical and numerical calculations. If a reliable production of ammonia is not reached for the given input parameters, the iteration step suggests improvements. Eventually, the method provides a hydrolysis reactor design which allows reliable ammonia production.

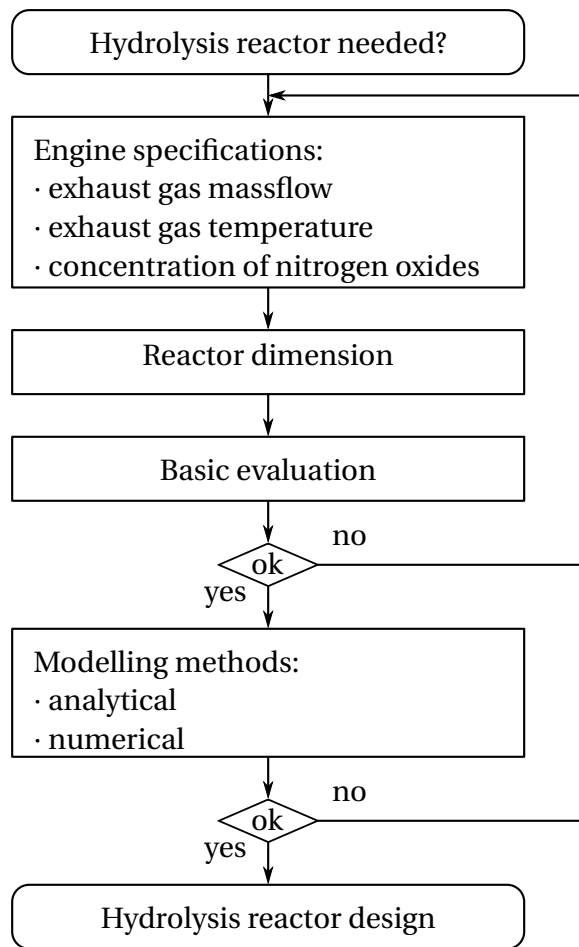


Figure 1.4: Flow chart of the step-by-step method for hydrolysis reactor designs.

1.4 Structure of the Thesis

Beginning with the motivation for exhaust gas treatment in chapter 1, an overview of treatment methods was given. The research context and the main questions to be addressed within this thesis were specified, and an overview of the design method for hydrolysis reactors developed within the present work was given.

In chapter 2 the theoretical background is provided with a detailed consideration of SCR chemistry, atomisation, evaporation and the theory of turbulent jets. A literature review on research related to SCR treatment, chemical reaction steps of the SCR process, catalyst deactivation processes as well as a short introduction to marine diesel fuels and their impact on the different processes are given in section 2.1. The decomposition process of urea, energetic considerations of urea decomposition depending on the phase of urea, kinetics and efficiencies of the process as well as the components needed for a hydrolysis reactor are provided in section 2.2. Components commonly used in a hydrolysis reactor are explained (*baseline hydrolysis reactor setup*). The atomisation process is presented in section 2.3. Droplet evaporation and urea evaporation are discussed in section 2.4. The theory of turbulent jets is reviewed in section 2.5, a core part of the analytical model.

The experimental setups and measurement methods are explained in chapter 3. A short overview of common experimental methodologies and experimental setups is provided at the beginning of this chapter, followed by the setup of the hydrolysis reactor used in this thesis (section 3.1). The swirl generator as an additional component of the hydrolysis reactor is introduced (*optimised reactor setup*). Fundamentals regarding the influence of swirl generators on the flow field are presented in this context. Different configurations of the measurement setup are explained and operating conditions are specified. The second experimental setup used for spray characterisation is presented in section 3.2. The measurement methods applied in this thesis are explained in sections 3.3, 3.4 and 3.5.

Chapter 4 introduces the numerical modelling approaches with relevant fun-

damentals. The employed CFD software is presented and the numerical domains and specific operating conditions are explained.

The experimental and numerical results as well as applied calculation steps are presented subsequently. Results for the baseline hydrolysis reactor setup are described in chapter 5. The experimental results of concentration, velocity as well as spray measurements are given in section 5.1. In section 5.2 the analytical models (turbulent jet model, evaporation model and diffusion model with kinetics) with the adjusted parameters for the test conditions are explained. The turbulent jet modelling approach is validated by experimental results (section 5.3) and compared to the corresponding numerical results (section 5.5). In chapter 6 the results of investigations considering the optimised reactor setup, including swirl generator, are provided. Experimental results of the urea decomposition process as well as the velocity measurement results are presented in section 6.1. The numerical results are given for the optimised case and compared to the results of the baseline reactor type (section 6.2).

The transfer of analytical and numerical modelling methods into a design method, as well as its application, are presented in chapter 7. Each step of the process displayed in figure 1.4 is defined. A prediction of the reactor performance is provided. The application of the design method is explained using an example based on the hydrolysis reactor constructed during this research project. Finally, a summary is provided and open research questions are discussed in chapter 8.

2 Theoretical Background

Relevant theory for this work is presented in the following. First, a brief overview of the chemistry including a summary of relevant literature for the entire SCR process involving the decomposition of urea, chemical reaction steps of the SCR process itself and catalyst deactivation in conjunction with relevant fuels is provided. Ammonia generation from urea with its chemical reaction steps is explained in more detail, including energetic considerations, diffusion and kinetics. Values to characterise the conversion efficiency of the reaction steps are explained. Afterwards, the injection system with atomisation and evaporation process fundamentals are discussed. Finally, the turbulent jet theory, resulting in an analytical calculation method for the injection of the urea solution, is explained.

2.1 Overview of SCR Chemistry

One of the most powerful conversion techniques for NO_x is selective catalytic reduction (SCR), commonly using ammonia as reducing agent [29]. Urea represents a nontoxic precursor for ammonia which allows a safe process.

Selective reduction of NO_x supported by catalysts has been investigated in detail for decades. Early publications considering the catalytic reduction on vanadium pentoxide (V_2O_5) coated catalysts were released by *Bauerle et. al.* [9] in 1978. *Bjorklund et. al.* [18] examined the activity of $\text{V}_2\text{O}_5/\text{SiO}_2$ coated catalysts for SCR with different promoters, whereas *Grossale et. al.* [36] discussed the reduction on FeZSM₅ catalysts. *Casapu et. al.* [21] investigated niobium-ceria as a coating substance for the SCR treatment as well as for the urea hydrolysis and soot oxidation. Besides the niobium-ceria coating, all studies showed a similar catalytic activity of the coatings for the conversion of NO_x .

The niobium-ceria coating revealed a lower activity.

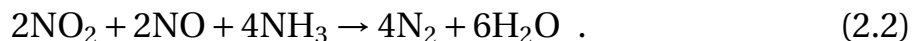
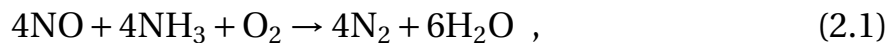
Research focusing on the ammonia precursor urea is divided into two groups: investigations of the decomposition and hydrolysis process of urea in general and examinations related to urea conditioning for the SCR technology in particular. *Lynn* [66] focused on the hydrolysis and the reaction kinetics of urea and suggested that urea hydrolysis does not proceed as a simple bimolecular process of first order. Extensive research on the urea decomposition process in an open reaction vessel was conducted by *Schaber et. al.* [82]. Temperature-dependent urea pyrolysis reaction steps and intermediate species of the decomposition process were found. *Koebel and Elsener* [53] and *Kleemann et. al.* [52] investigated the hydrolysis of urea for application to SCR catalysts. Common SCR catalyst coatings such as V_2O_5 as well as a special coating for the hydrolysis of urea, TiO_2 , were examined. TiO_2 showed higher decomposition rates than V_2O_5 coated SCR catalysts, but TiO_2 is completely inactive for NO_x reduction. *Casapu et. al.* [21], as mentioned above, also investigated the activity of niobium-ceria as a coating for the hydrolysis of urea. They showed that this coating reached decomposition rates as high as TiO_2 catalysts. More application-oriented research considering the overall SCR process was performed by *Peitz et. al.* [77] in a laboratory test reactor. They showed that the most critical process requirement is the homogeneous atomisation and distribution of the liquid reducing agent. *Grünwald* [37] and *Steinbach* [89] examined a hydrolysis reactor in a bypass system for the application in trucks at full scale. *Grünwald* focused on the liquid reducing agent homogenisation and effects of the urea evaporation and *Steinbach* investigated the interaction of droplets with a solid surface and the overall decomposition of urea at TiO_2 coated catalysts. The recently published review by *Nova and Tronconi* [71] provides a broad overview of the Urea-SCR technology for diesel exhaust gas treatments. They discussed, SCR and related technologies for mobile and off-highway applications as well as common catalyst types, reaction kinetics and ammonia supply.

Catalyst deactivation is an inevitable process occurring after a certain operating time [8]. The time scale of activity loss and its cause can vary significantly. *Bartholomew* [8], *Moulijn et. al.* [68] and *Forzatti and Lietti* [31] inves-

tigated different catalyst deactivation mechanisms. It was found that there are basically three causes of deactivation, namely chemical, mechanical and thermal [8].

2.1.1 Selective Catalytic Reduction

In the following the catalytic reduction of NO_x using ammonia is discussed. Main reaction paths occurring at the catalyst are shown. For further information please refer to [54]. Catalysts for SCR treatments are usually composed of a monolithic substrate with metal oxide coating, where vanadium pentoxide is the most frequently used coating. The chemical reactions considered depend on thermodynamic conditions. The reaction paths of the *Standard-SCR* (see equation 2.1) and the *Fast-SCR* (see equation 2.2) are presented in the following equations:



The first reaction applies in the case of exhaust gases without oxidation treatment at which the NO/NO_2 ratio is about 90 to 95 %. However, for the *Fast-SCR* oxidation of the exhaust gas up to 50 % for the NO/NO_2 ratio is required. This reaction proceeds faster; hence, it is preferred and represents the standard in technical applications. A further decrease of the NO/NO_2 ratio should be avoided because this leads to the so-called *NO_2 -SCR* reaction which proceeds even slower than the *Standard-SCR*. SCR reactions are exothermic [54, 55].

2.1.2 Catalyst Deactivation

In general, catalyst deactivation describes the loss of catalytic activity or selectivity over time. Mechanisms mainly responsible for the deactivation process

within the catalyst are poisoning, fouling, thermal degradation, vapour compound formation, vapour-solid and/or solid-solid reactions as well as attrition/crushing. The reasons for deactivation can be categorised into chemical, mechanical and thermal causes, listed in table 2.1 [8]. Deactivation mechanisms affecting catalysts depend on their application, since the catalyst material and coating as well as the temperature and composition of feed stream and catalyst surface are determined by the application. For SCR catalysts the main deactivation causes are poisoning, fouling and, with respect to a TiO_2 based hydrolysis catalyst, especially thermal degradation [22]. These three mechanisms are presented in more detail in the following.

Poisoning refers to a strong chemisorption of reactants or chemical substances present in the feed stream on the active catalyst surface. NO_x are reduced by ammonia only if both reactants are absorbed simultaneously on vanadium sites of the V_2O_5 -coated catalysts. Hence, an absorption of poisoning species on active vanadium sites reduces the surface available for the reaction. Depending on the applied quality of fuel and the combustion process, alkali and alkaline earth metals, phosphorus, zinc and arsenic are the main poisons during the SCR process [22].

Fouling decreases the catalysts activity by physical deposition. Salts and ash in particular cause loss of active sites. Salts and ash are in general a product of the combustion process with a specific fuel. In particular ammonia in combination with H_2O and SO_2 may react to ammonia bisulphate or ammonium sulphate. They may agglomerate at the catalyst surface at temperatures typical for the SCR process and grow with exposure time. Deposition occurs although both forms of ammonium salt are reversible, as their melting points are below typical SCR process temperatures [22]. The physical deposition of these substances induces plugging of the catalyst channels. The two combined indicators to determine the fouling phenomenon are an increase of pressure loss across the catalyst and an efficiency decrease of the reaction.

As already mentioned, the *thermal degradation* is of special interest for TiO_2 -based catalysts and arises from a thermally induced loss of catalytic surface area. TiO_2 -coated catalysts have a higher surface area in the crystalline form anatase. Unfortunately this form is unstable and tends to convert to the crys-

Mechanism	Type	Description	Relevance for SCR
Poisoning	Chemical	Strong chemisorption of species on catalytic sites, reduction of active catalytic surface → less space left necessary for process	Yes
Fouling	Mechanical	Physical deposition of species from fluid phase onto the catalytic surface and in catalyst pores → physical blocking	Yes
Thermal degradation	Thermal	Thermally induced loss of catalytic surface area, support area and active phase-support reactions → less space left necessary for process, irreversible defect of catalyst coating	Yes
Vapour formation	Chemical	Reaction of gas with catalyst phase to produce volatile compound	No
Vapour-solid and/or solid-solid reactions	Chemical	Reaction of fluid, support, or promoter with catalytic phase to produce inactive phase → oxidation or sulfation of metals, closely related to poisoning	No
Attrition/crushing	Mechanical	Loss of catalytic material due to abrasion Loss of internal surface area due to mechanical-induced crushing of the catalyst particle → erosion of catalysts	Yes

Table 2.1: Catalyst deactivation mechanisms according to *Bartholomew* [8].

talline form rutile which leads to a lower catalytic surface area. The conversion of anatase to rutile is comparable to a sintering process and occurs at catalyst temperatures above 500 °C. Changes in the crystalline form are irreversible.

Catalyst erosion occurs due to a mechanical abrasion of the coating material of the catalyst. This deactivation mechanism has to be considered if a liquid reducing agent is injected to a gaseous feed stream. In general, liquid urea is injected by a nozzle in front of the SCR or hydrolysis catalyst. The droplet impingement on the coated surface leads to an abrasion of the coating, which increases with exposure time. The mechanical erosion is an irreversible process and reduces the active surface area. In addition, uncoated surfaces are disadvantageous for the evaporation process (see section A.2.1).

Favorable exhaust gas composition and the temperature can lead to reduced catalyst deactivation effects. Poisoning is mainly effected by the exhaust gas composition, while in case of fouling the temperature has an additional impact. Sintering processes, thus thermal degradation, are only dependent on the temperature. A catalyst surface temperature between 350 to 500 °C as well as an adjusted selection of the channel sizes will extend a catalysts life-time considering fouling and thermal degradation. In turn, the effects caused by the exhaust gas compounds differ between fuel used and the combustion process. The application (e. g. automotive or industrial application) determines the applied fuel, thus a hardly changeable parameter. To summarise, temperature is the only parameter that can be influenced to a certain extend which leads to a narrow operation range to reduce deactivation effects for each application.

2.1.3 Marine Diesel Fuels

Distillation of crude oil generates four product fractions, which are classified by their boiling temperature. Refinery gas, like ethane or hydrogen, is the first fraction at the lowest temperature. Thereafter liquefied petroleum gas (primarily propane or butane) is separated; followed by gasoline and distillate fuels. Residual oil is the share of crude oil, which is not boiling even at the highest temperatures during the distillation process [27].

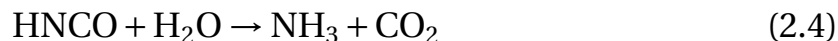
The distillate fuels are subdivided into multiple groups, again classified by their boiling temperature, including fuels for automotive, aviation or industrial applications. The different groups can be categorised into land-use fuels and marine fuels. Land-use fuels imply on-highway, diesel, off-highway and heating oil. Marine fuels include distillate, intermediate as well as residual oil [27]. These groups not only differ in their boiling temperature, but also in their flash point and the amount of sulfur and other undesired compounds. HFO (heavy fuel oil) which MAN uses in their marine diesel engines is part of the residual oil. Residual oil is again subdivided into different groups which include HFO, MFO (medium fuel oil) and LFO (light fuel oil). In marine applications the fuels contain at least thirty times more sulfur than normal diesel and the amount of ash is up to twenty times higher.

With respect to the loss of catalytic activity, poisoning but also fouling of the SCR catalysts will occur more readily for marine application than for automotive or truck application. The most efficient prevention of these deactivation mechanisms is the selection of appropriate fuel types. For example, a reduction of the sulfur content will decrease the loss of catalytic activity due to fouling, as sulfur is oxidised during the combustion to SO_2 and a further oxidation to SO_3 is the main reason for salts [22].

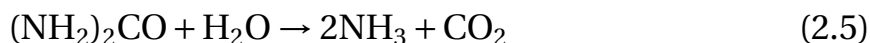
2.2 Decomposition of Urea and Hydrolysis Reactors

In general the conversion of urea to ammonia is determined by two chemical reactions, the thermolysis (see equation 2.3) and the hydrolysis (see equation 2.4) reaction. The thermolysis reaction describes the thermal decomposition of urea which starts at the melting temperature of urea followed by the evaporation of urea. In this reaction isocyanic acid (HNCO) and ammonia is formed. The hydrolysis reaction forms ammonia and CO_2 from HNCO and water.





The global reaction (equation 2.5) shows that the full decomposition of one mole urea leads to two mole of ammonia.



As already described, the thermal decomposition temperature correlates with the melting point (about 133 °C) and starting decomposition of urea (about 140 °C). For slow heating of solid or liquid urea several intermediate reactions proceed and undesirable solid by-products can be observed. During the heating process of urea, HNCO is formed. It is the desired substance for the following hydrolysis reaction. HNCO is highly reactive and decomposes in a wide temperature range starting at 160 °C, in the presence of water, into several reaction intermediates and ammonia [82]. *Schaber et. al.* investigated the thermal decomposition (pyrolysis) of urea in an open vessel without catalytic support [82]. They categorised the pyrolysis process into four reaction regions, which represent different temperature ranges. The first reaction region, from room temperature up to 190 °C, shows a negligible mass loss of urea until the melting point. Thereafter, but still in the first reaction region, the mass loss increases significantly due to vaporisation and decomposition of urea. HNCO is formed starting at 160 °C, but reacts with remaining urea to liquid biuret ($\text{C}_2\text{H}_5\text{N}_3\text{O}_2$). Further heating induces reaction of HNCO with biuret or itself to cyanuric acid (CYA) and ammeline ($\text{C}_3\text{H}_4\text{N}_4\text{O}_2$), which are both solid products [82]. The second reaction region, between 190 and 250 °C, is dominated by further evaporation of urea and the decomposition of the liquid biuret. Whereas cyanuric acid and ammeline are formed mainly from the pyrolysis of biuret, ammeline ($\text{C}_3\text{H}_5\text{N}_5\text{O}$) and melamine ($\text{C}_3\text{H}_6\text{N}_6$) appear in small amounts at the higher temperatures (225 to 250 °C) of this second reaction region. Ammeline and melamine are solid products, too. Within the third reaction region (250 to 360 °C) the mass loss is significantly reduced, in general the beginning of the pyrolysis of the composed solid products is observed, and HNCO and ammonia are formed. CO_2 is detected for the first time,

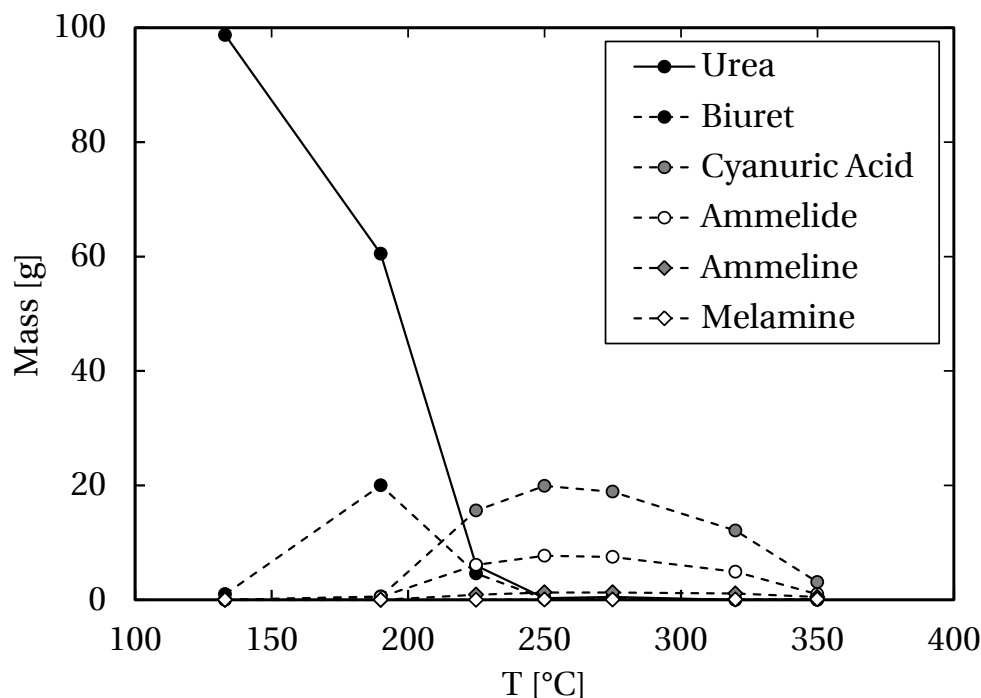


Figure 2.1: Products of the intermediate reactions during the heating process of urea according to *Schaber et. al.* [82].

which results from the hydrolysis of HNCO without catalytic support. *Schaber et. al.* found the complete elimination of the remaining solid products in the last reaction region, above 360 °C. Ammelide decomposes completely at temperatures above 600 °C [82]. In contrast to *Schaber et. al.* [82], *Fang and Da-Costa* [29] observed that melamine was not decomposed even at temperatures above 600 °C, and remained as a polymeric deposit. The four reaction regions of the urea pyrolysis are displayed in figure 2.1. More detailed information regarding intermediate reactions of urea and possible by-products are given in the literature [29, 82, 89].

The hydrolysis process of HNCO was observed in small amounts within the third reaction region. As already mentioned, HNCO is highly reactive and possibly polymerises. This circumstance leads again to undesired intermediate products, if the reaction process (especially thermolysis) is incomplete. Polymerisation of HNCO occurs either from liquid HNCO or if gaseous HNCO

is condensed [30]. HNCO is gaseous at room temperature and condensation is impossible for temperatures expected in an exhaust system. *Fischer et. al.* found that decomposition products of HNCO above 80 °C are only CO₂ and NH₃ [30]. In both cases, for the pyrolysis of urea and the hydrolysis of HNCO, the application of special catalysts is advantageous. The catalyst allows quick heating for the decomposition/evaporation [56] and the hydrolysis is supported efficiently due to the reactive surface.

The ammonia precursor urea is often used in a urea-water solution. In technical applications two main decomposition methods for liquid urea exist. First option is the direct injection in the main exhaust gas mass flow prior the SCR catalyst and the second option is the conversion by a separate catalyst (see figures 1.2 and 1.3). As mentioned in section 2.1.2, catalysts for the decomposition of urea are usually coated with titanium dioxide (crystalline form: anatase). In general a metal substrate is used as catalyst basis. The benefit of a separate catalyst for the urea decomposition is the smaller activation energy needed for the reactions. In this thesis a urea-SCR-system with a bypass system for the hydrolysis reactor (see figure 1.3) is investigated.

Summarising, there are some critical aspects of the pyrolysis for a hydrolysis reactor. First, it was shown that urea decomposes to ammonia in two steps: the thermal decomposition and the hydrolysis. As mentioned, depending on temperature and heating rate solid by-products can be formed during the decomposition of urea. These by-products can be either reversible or irreversible. Once by-products have been formed, their amount will keep increasing, if the thermodynamic conditions are kept constant and, in a worst-case, can lead to a system breakdown due to blockage of the catalyst. Hence, the formation of any by-products must be avoided under all circumstances.

Second, as previously mentioned a quick heating process is advantageous for the entire process. The temperature of the reactor has a major impact, especially the temperature of the catalyst surface. For further discussion a distinction needs to be made between the gas temperature, the catalyst surface temperature and the temperature of the urea-water solution, present in droplets. Initially the assumption that the temperature of the catalyst is equal to the gas temperature is justified. The composition of by-products mainly appears due

to the crystallisation of liquid urea or its intermediates on cold surfaces. The probability of establishing cold surfaces increases if the concentration of liquid is too high or the surface is not coated. The latter scenario is negligible in this thesis, as only coated catalysts are used. Here, the cooling due to evaporation and liquid impingement are the key factors. This effect starts with the injection of the liquid solution which reduces the gas temperature of the system through evaporation. In the second step the remaining amount of liquid droplets impinge on the catalyst which leads to a direct cooling of the surface. Finally, the temperature of the catalyst is a combination of the residual heat transferred by the gas to the catalyst and the cooling due to droplet evaporation at the surface. The temperature of the catalyst should not drop below 200–250 °C to avoid by-products. The catalyst front surface is most critical for the formation of solid deposits because of the highest withdrawal of energy due to liquid impingement.

And finally, using the SCR technology in marine applications has further critical points to be considered. A main difference to automotive application is the usage of lower-quality fuels. Fuel characteristics such as sulfur content and ash content are important to the SCR process [71]. Depending on catalyst types fast deactivation can occur. Another aspect is the oxidation of SO_2 to SO_3 or the formation of salts [71]. Metal oxide catalysts have a high tolerance against deactivation due to sulfur, but the oxidation of SO_2 to SO_3 is observed especially at higher temperatures [23, 71]. The hydrolysis process itself is affected only slightly, as only small changes of activation energies for the reaction are observed [23].

2.2.1 Energetic Considerations

At standard conditions, 1 bar and 25 °C, the thermolysis reaction 2.3 is endothermic and the hydrolysis reaction 2.4 is exothermic. The combined thermo-hydrolysis reaction 2.5 is endothermic. With respect to general application temperatures and the phase of urea (solid or as solution) the energetic calculations of the reactions have to consider these boundary conditions. *Koebel and Strutz* [56] calculated the energy consumption for the com-

bined thermo-hydrolysis reaction for a spectrum of conditions. Due to the fact that the water content of the solution needs to be heated as well, it can be stated that the higher the water content is, the higher is the energy consumption. This circumstance affects the decomposition process in two ways which is discussed implicitly in section 2.2.2. Firstly, despite the higher energy consumption of water, it evaporates at lower temperatures than urea. Hence, the water content influences the evaporation time of the droplet (see section 2.4.2). Secondly, the diffusion process of water is different to the diffusion of HNCO (effects on the decomposition process are described in chapter 5). Summarising these aspects it can be stated that solid urea has the lowest energy consumption for the combined thermo-hydrolysis reaction, but needs high concentrations of water in the exhaust gas for the hydrolysis. Urea in an aqueous solution needs more energy for the decomposition process, but water is beneficial for the hydrolysis. *Koebel and Strutz* found an optimum at a 1:1 urea-water solution.

2.2.2 Diffusion and Catalytic Reaction Kinetics

Diffusion is a molecular transport process which occurs in every system with species concentration gradients, pressure gradients and temperature gradients. It describes the motion of atoms or molecules from regions with higher concentration to regions with lower ones; a mixing process is induced. Generally, diffusion is considered for gases or liquids, rarely for solid substances due to the limited mobility of molecules. In closed systems, diffusion occurs until complete mixing is reached. With a concentration gradient in a binary mixture at rest (in y -direction), the diffusion flux is given by Fick's law:

$$J = -\frac{D_{12}}{\bar{R}T} \frac{dp_1}{dy}, \quad (2.6)$$

for the assumption of an ideal gas. D_{12} is the binary diffusion coefficient of substance one diffusing in substance two [7], where dp_1 is the partial pressure of species one. The binary diffusion coefficient for gases is dependent on the temperature and the pressure and in good assumption independent of con-

centrations. Hence these are neglected [93]. For molecular gaseous diffusion at low ambient pressure Fuller's method [33] provides an estimate of the binary diffusion coefficient [93]:

$$D_{12} = \frac{0.00143 \cdot T^{1.75} (M_1^{-1} + M_2^{-1})^{0.5}}{p \cdot \sqrt{2} (\sqrt[3]{\sum \Delta v_1} + \sqrt[3]{\sum \Delta v_2})^2} . \quad (2.7)$$

Δ_v is the diffusion volume. The mass transfer coefficient is defined as [2]:

$$\beta = \frac{D_{12} \cdot \text{Sh}}{d_h} , \quad (2.8)$$

with

$$\begin{aligned} \text{Sh} &= 0.664 \cdot \sqrt[3]{\text{Sc}} \cdot \sqrt{\text{Re}} \\ \text{Re} &= \frac{d_h \cdot u}{\nu} \\ \text{Sc} &= \frac{\nu}{D_{12}} . \end{aligned} \quad (2.9)$$

Diffusion processes in porous media are a major topic in technical chemistry. Especially, the heterogeneous catalysis or in general reaction of gases on solid surfaces are often dependent on the diffusion rate of the reacting media. Here a differentiation between the already considered molecular diffusion and the so-called Knudsen diffusion needs to be made. Knudsen diffusion occurs, if the mean free path of a molecule is larger than the specific length scale of the porous medium. Hence, for small pressures or pores the molecules get in contact with the walls of the pores more often than with each other.

For reactive species the reaction rate is given by the Arrhenius law. It relates reaction rate constant k , once the reactive components are in contact, with a pre-exponential factor k_0 , temperature and activation energy E_a :

$$k = k_0 \cdot \exp\left(-\frac{E_a}{RT}\right) . \quad (2.10)$$

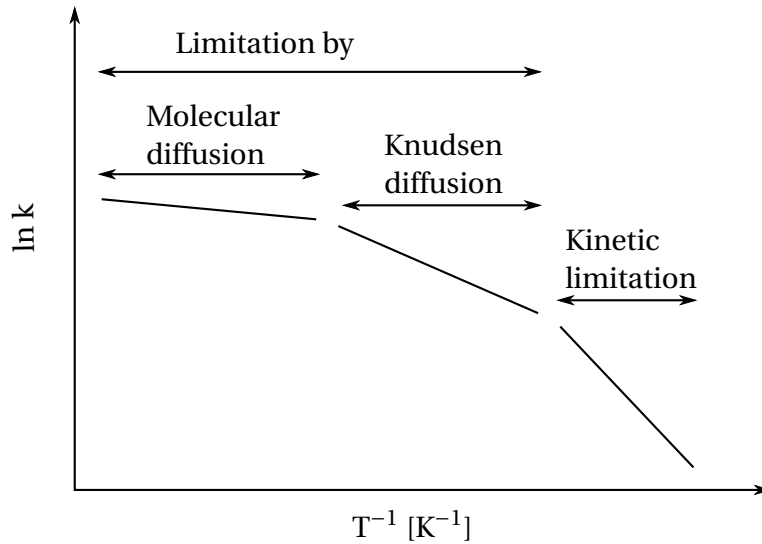


Figure 2.2: Limitation of the chemical reaction rate by mass transfer (molecular diffusion), Knudsen diffusion or kinetic limitation [64].

The so-called effective reaction rate constant k_{eff} (in equation 2.11) combines the chemical reaction rate constant k (in equation 2.10) with the mass transfer (diffusion process) [89].

$$k_{eff} = \frac{1}{\frac{1}{k} + \frac{1}{\beta \cdot a}} , \quad (2.11)$$

where β is the mass transfer coefficient and a the specific phase boundary.

Depending on temperature the reaction progress is either limited by Knudsen diffusion or the mass transfer of the components to the catalyst surface (molecular diffusion) or a kinetic limitation exists. In figure 2.2 the dependence of the effective reaction rate constant on temperature for the heterogeneous catalysis is illustrated. A kinetic limitation exists in low temperature regions [7].

Equation 2.10 shows an exponential dependency of reaction rate constant k on temperature. By contrast, the mass transfer coefficient β is proportional to temperature ($\propto T^{1.75}$). Hence, increasing temperature leads to significant faster increase of k compared to β . Considering common temperature levels

in SCR applications, a limitation by mass transfer is typical [42,52]. In this case $\beta \cdot a \ll k$ and the effective reaction rate is simplified to

$$k_{eff} = \beta \cdot a , \quad (2.12)$$

which reflects the mass transfer limitation. According to *Baerns et. al.* [7] mass transfer limitation exists for any chemical reaction with activation energies of about 5 kJ mol^{-1} . *Hauck* [42] and *Kleemann et. al.* [52] find activation energies in the range of 7 to 12.7 kJ mol^{-1} for the hydrolysis of HNCO at TiO_2 -coated catalysts.

2.2.3 Basic Evaluation and Efficiencies

For the basic evaluation two parameters are used to characterise the expected decomposition process.

The overall system temperature is the first parameter. The heat flow of the exhaust gas and the urea solution are considered. The thermal energy sink due to evaporation of the urea solution results in a temperature decrease of the gas phase. The energy balance for the evaporation section (see chapter 3.1) of the reactor is as follows:

$$\dot{Q}_{in} = \dot{Q}_{out} + \dot{Q}_{loss} + \dot{Q}_{evap} . \quad (2.13)$$

\dot{Q}_{in} is the heat flow of the exhaust gas, \dot{Q}_{out} the heat flow leaving the domain, \dot{Q}_{loss} the heat losses across the system boundary and \dot{Q}_{evap} the energy needed to evaporate the urea solution. The latter can be identified by considering the specific evaporation enthalpy:

$$\dot{Q}_{evap} = \dot{m}_l \cdot \Delta h_v . \quad (2.14)$$

It is assumed that all liquid mass is evaporated until the catalyst front surface is reached. Hence, the gas bulk temperature at the front surface of the catalyst

can be found from the energy balance.

The second parameter is the gas hourly space velocity (GHSV) (equation 2.15). This value refers to the entering reactants' volume flow (in this case the exhaust gas volume flow and the evaporated urea solution flow) divided by the catalytic reactor volume. It indicates how many catalyst volumes of feed flow (reactants) can be treated in one unit of time. *Steinbach* [89] reveals that the reaction rate decreases significantly for GHSV values higher than $100 \cdot 10^3 \text{ h}^{-1}$, at $250 \text{ }^\circ\text{C}$ for AdBlue. *Yim et. al.* [98] measured a decrease in decomposition efficiency, too. In general, the higher the space velocity, the lower the hydrolysis efficiency. Same is found for the NO_x reduction in the SCR process itself [71].

$$\text{GHSV} = \frac{\dot{V}_{\text{gevap}}}{V_{\text{cat}}} \quad (2.15)$$

Both parameters are commonly used to characterise hydrolysis reactors and are often applied for reactor design [88].

Referring to the decomposition of urea to ammonia, efficiency values quantify the ratio of the species present after catalytic conversion. These can be applied to the results of concentration measurements. The urea decomposition rate (UDR) is calculated as follows:

$$\text{UDR} = \frac{X(\text{CO}_2) + X(\text{HNCO}) + X(\text{NH}_3)}{3 \cdot X((\text{NH}_2)_2\text{CO})} \quad (2.16)$$

Concentrations of each substance result from the thermolysis and hydrolysis process (equation 2.3 and 2.4). The UDR provides a relation between the measured concentrations (numerator) and the calculated concentration of urea prior to the catalyst (denominator). The numerator indicates that this efficiency value describes the amount of liquid urea transferred to its gaseous reaction products.

The hydrolysis efficiency level (HEL) refers to the hydrolysis process (equation 2.4):

$$\text{HEL} = \frac{X(\text{CO}_2)}{X(\text{CO}_2) + X(\text{HNCO})} . \quad (2.17)$$

It quantifies the hydrolysis efficiency by considering the amount of HNCO remaining after the catalyst. A complete hydrolysis is achieved if no remaining HNCO is detected. Both efficiency coefficients are especially important in application tests where the general functionality of the hydrolysis reactor has priority.

2.2.4 Components of Hydrolysis Reactors

In general hydrolysis reactors consist of an injector for urea and the hydrolysis catalyst. In the following different types of both components are briefly explained. Components used in this work are described in chapter 3.

Injectors

Injectors can be categorised into several groups; pressure (one-phase) and two-phase nozzles are the most common ones for fuel or urea atomisation. Ultrasonic, rotary or electrostatic atomisers are used e. g. for coatings, painting or spray drying. In the following only pressure and two-phase nozzles are described in more detail.

Pressure nozzles operate with a liquid under high pressure for the atomisation (injection pressures for common rail systems usually 80 to 300 MPa [92]), while two-phase nozzles imply additional gas for atomisation [64]. The gas of choice is usually compressed air, thus they are often called air-assisted nozzles. Compared to pressure nozzles, two-phase systems have a more homogeneous droplet distribution and smaller droplet sizes. The most significant disadvantage of air-assisted nozzles is the additionally needed carrier gas, as in many automotive applications no compressed air is available on-board. Designs of one-phase (a) and two-phase (b and c) nozzles are shown schematically in figure 2.3. Both groups again can be subdivided in different sub groups. Sub-groups of one-phase nozzles are for example plain-orifice,

simplex, duplex or dual-orifice injectors. The design of the one phase nozzle shown in figure 2.3 (a) is a rather simple plain-orifice injector [64]. Droplet diameters from this nozzle-type depends only on the orifice diameter and length and the velocity of the liquid (which is mainly dependent on pre-pressure and liquid properties) [97]. An example for a plain-orifice nozzle is a diesel injector. Sub-groups of two-phase nozzles are mainly two-phase nozzles with either internal or external mixing and airblast atomisers. A two-phase nozzle with internal mixing is shown in figure 2.3 (b), with external mixing in figure 2.3 (c). As the names imply, an air-assisted injector with internal mixing brings the air and liquid into contact inside the body of the nozzle, whereas air and liquid come into contact outside the nozzle body in case of external mixing. Depending on air flow rate the spray cone angle of internal mixing nozzles varies and fine sprays are obtained even for very low liquid flow rates. In contrast, the spray cone angle is constant for changing air flow rates for external mixing nozzles. This type is less efficient regarding the utilisation of air compared to the internal mixing injectors, but there is no danger of liquid blocking the air channels [64]. An airblast atomiser has the same working principle as the other two air-assisted nozzle types, with the main difference that the air velocity has not to exceed a certain maximum value and therefore higher air flow rates are necessary. Further information about injector types and their applications is provided by *Lefebvre* [64], *Nasr et al.* [70] or *Wozniak* [97].

In first SCR applications, diesel injectors have often been adopted for urea spray generation by the OEMs. Meanwhile there are specialised producers of urea atomisers. One of the worldwide leading manufactures is the Düsen-Schlick GmbH. They produce a broad spectrum of atomisers for various specialised sectors of application. Injectors for SCR applications require special features, besides small droplet sizes for quick evaporation of urea, crystallisation at the nozzle orifice or inside the nozzle has to be avoided. Nozzles are available for a wide range of liquid flow rates. The structure of the nozzles is nearly identical for different types and sizes. In figure 2.4 an example of a two-phase nozzle with external mixing of Düsen-Schlick GmbH is shown. Main parts of the nozzle are the nozzle body with air and liquid connection, the liquid insert with swirl generator and the nozzle cap. The liquid insert is

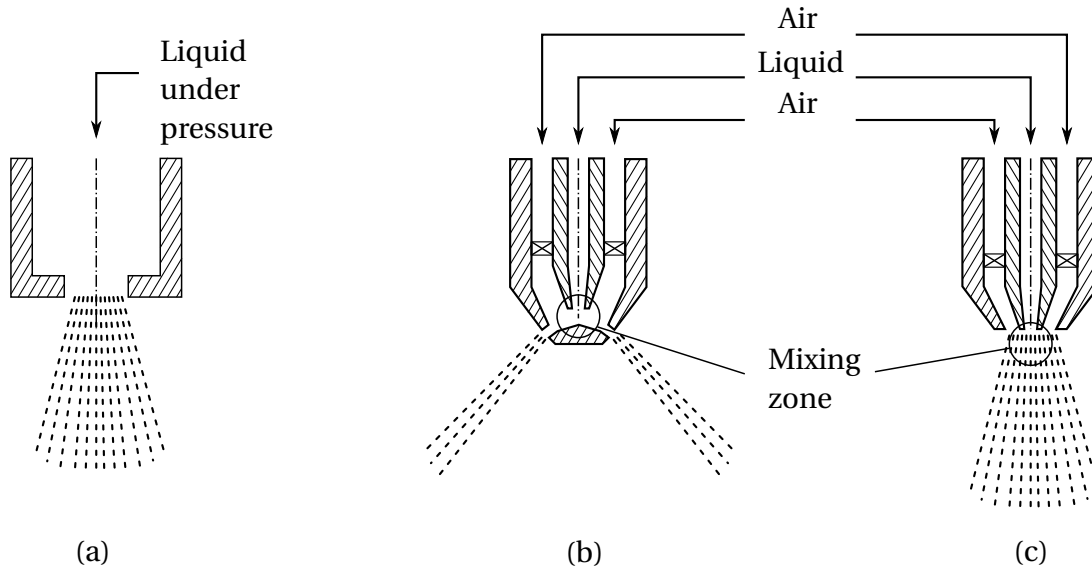


Figure 2.3: Injector types: (a) one-phase (plain-orifice) nozzle, (b) two-phase nozzle with internal mixing and (c) two-phase nozzle with external mixing.

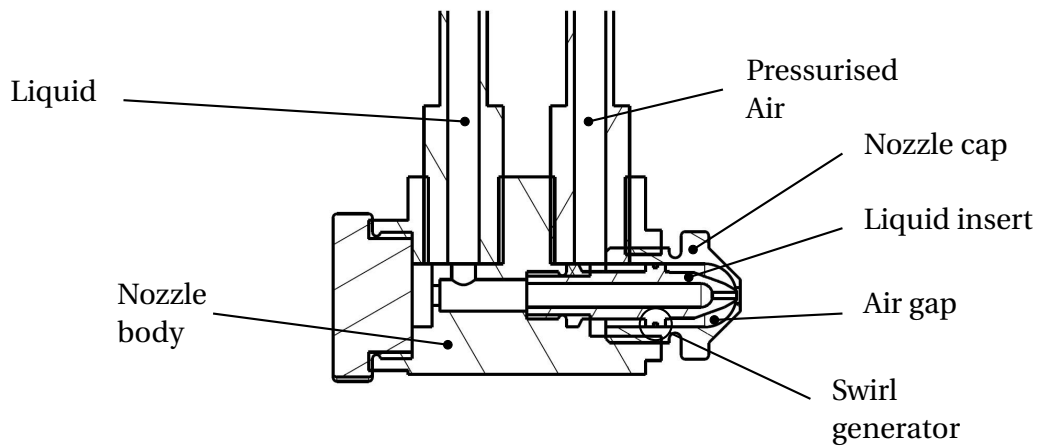


Figure 2.4: General structure of a two-phase nozzle with external mixing of the Düsen-Schlick GmbH (model 970).

exchangeable and is produced with different orifice diameters. The swirl generator connected to the outer surface of the liquid insert extends into the air gap, hence the air is provided with swirl. The nozzle cap is adjustable by the thread to regulate the air flow rate.

Catalysts

Various catalyst types exist in the chemical and process engineering industry. Perhaps the most important ones are packed-bed (fixed-bed) catalytic reactors, honeycomb monoliths or metal substrates. Examples of honeycomb monolith and metal substrate are shown in figure 2.6. Packed bed catalytic reactors have originally been offered as SCR catalysts, but are not state of the art anymore [24]. The pressure drop is several times higher than for honeycomb monoliths or metal substrates and the resilience against plugging and poisoning is smaller. Hence, these catalytic reactors are not considered further. To classify different catalyst types properties such as cell density, geometric surface area (GSA), open frontal area (OFA) and hydraulic diameter are necessary [96]. Cell densities are usually given in number of cells per square inch of catalyst surface (unit: cpsi) [96]. The GSA represents the active surface area per volume. Depending on the shape of the catalyst (cell spacing) it can be calculated by number of cells and thickness of walls [24] (see equations 2.18 and 2.20). The OFA is a function of wall thickness and cell density and spacing and the hydraulic diameter of wall thickness and cell spacing [24, 96] (see equations 2.19 and 2.21).

In the following equations L is the cell spacing, t the wall thickness and R the fillet radius as shown in figure 2.5. The cell density n is defined differently for square cells or triangular cells.

GSA and OFA for catalysts with square cell geometry, where $n = \frac{1}{L^2}$:

$$GSA_{sq} = 4n \left[(L - t) - (4 - \Pi) \frac{R}{2} \right] , \quad (2.18)$$

$$OFA_{sq} = n \left[(L - t)^2 - (4 - \Pi) R^2 \right] . \quad (2.19)$$

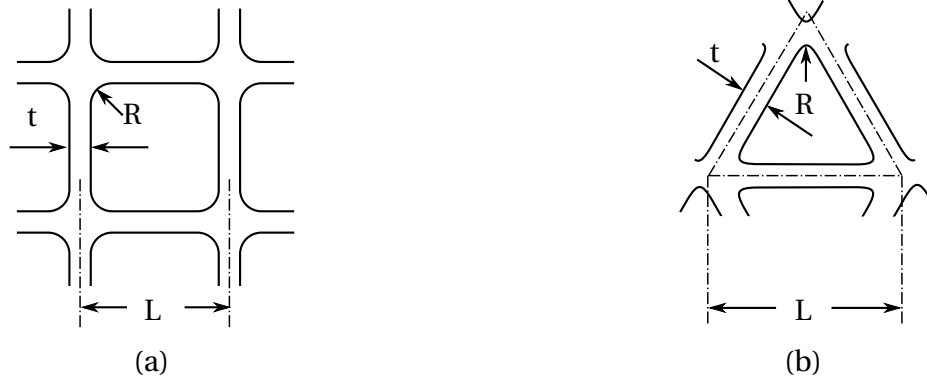


Figure 2.5: Geometric parameters for a square cell (a) and for a triangular cell (b) [24].

GSA and OFA for catalysts with triangular cell geometry, where $n = \frac{4}{\sqrt{3}L^2}$:

$$GSA_{tri} = 4 \frac{\sqrt{3}}{L^2} \left[(L - \sqrt{3}t) - \left(\frac{2\Pi}{3} - 2\sqrt{3} \right) R \right] , \quad (2.20)$$

$$OFA_{tri} = \frac{1}{L^2} \left[(L - \sqrt{3}t)^2 - 4 \left(3 - \frac{\Pi}{\sqrt{3}} \right) R^2 \right] . \quad (2.21)$$

Applied washcoats containing different amounts of V_2O_5 , TiO_2 , SiO_2 , WO_3 or Al_2O_3 are investigated. Another option are monolith catalysts extruded from ceramic or catalytic active materials [20]. Monolithic honeycomb reactors are common especially as diesel particulate filters or in power plant NO_x control applications [20, 96]. Both catalyst types have a significantly lower pressure drop and higher geometric surface areas compared to packed-bed catalytic reactors [24, 96]. An advantage of honeycomb monoliths is their high thermal durability (melting point exceeds $1450^\circ C$), but they are fragile and prone to shock fracture [78, 96]. By contrast, metal substrates have less thermal durability due to coatings, but have a high shock resistance. And metal substrates have a lower pressure drop (10 to 15 %) than for honeycomb monoliths, which is due to higher OFAs (about 10 to 20 % higher) and smaller wall thicknesses of

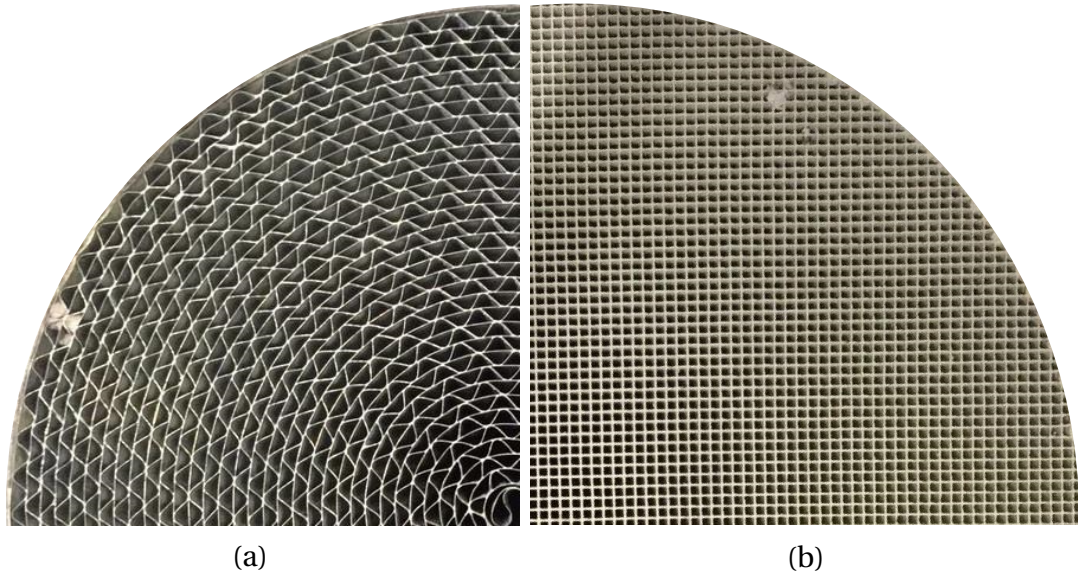


Figure 2.6: Metal substrate (a) and ceramic honeycomb monolith (b).

Uncoated metal substrate properties	Example 1	Example 2	Example 3
Cell density [cps]	400	500	600
Wall/foil thickness [mm]	0.05	0.05	0.05
Substrate Diameter [mm]	105.7	105.7	105.7
GSA [$\text{m}^2 \text{L}^{-1}$]	3.65	4.00	4.15
OFA	0.89	0.88	0.87
Hydraulic diameter [mm]	0.98	0.88	0.84

Table 2.2: Geometric and classification properties for uncoated metal substrates [24].

the metal substrates [24, 78]. *Pratt and Cairns* and *Cybulski and Moulijn* give common values for classification properties for different honeycomb monoliths and metal substrates [24, 78] (see table 2.2).

As this thesis focuses on hydrolysis reactors, special catalysts are now considered. TiO_2 -coated (crystalline form: anatase) metal substrates showed the highest efficiency for this application [14, 52]. The metal substrate consists of thin layers of a coated metal foil with different shapes. Cells are usually trian-

gular. The foil shapes (catalyst structure) can be divided into unstructured and structured. The structured foils increase the mass transfer by generating turbulence in discrete channels or even provide an interaction between several channels, while the unstructured foils consist of plain channels where a laminar flow develops [24]. The catalysts applied in the present work are metal substrates from Continental Emitec GmbH. A short overview of the catalyst structures produced by Emitec is presented in the following. Their plain standard structure (thus the unstructured form) is found with the ST structure. The structured foil types are categorised by their ability to produce turbulence. The TS/ST structure represents the structured foil with the lowest turbulence creation and the PE/LS structure is the foil with highest turbulence creation. Furthermore, there is a mixer structure (MX) which provides an additional dispersion of the gas phase. A detailed overview of the structured catalysts of Emitec is also given in *Cybulski and Moulijn* [24]. *Steinbach* investigated the mixing performance of the different Emitec structure types [89]. The catalyst type Emicat (Emitec GmbH) as a special type is briefly described since it was considered as an alternative in the beginning of the research project. Emicat comprises an ST structure catalyst and a decoupled electrically heated catalyst part (also ST structure) to avoid cooling at the front surface of the catalyst. The advantage of this catalyst form is the reduced exhaust gas temperature required due to an increase of the liquid evaporation at the heated front surface. However, electrical power must be provided. Investigations using this catalyst type for automotive applications, with AdBlue and GuFo as ammonia precursor, were conducted by *Toshev* [91].

2.3 Atomisation

Atomisation of a liquid is the generation of a disperse phase (liquid) in a continuous phase (gas). Disperse phases are often found in technical applications. An increase of mass transfer between liquid and gaseous phases due to the large liquid surface area is often desired and advantageous. One of the best known fields of application for disperse phases are fuel injection sprays. For technical atomisers various models to characterise the distribution of the

generated spray exist. A broad spectrum is shown in *Lefebvre* [64] with information about assembly, operating mode and application.

This section provides a brief introduction of atomisation theory and practice. More detailed explanations, especially droplet breakup mechanisms, can be found in the literature [5, 10, 64, 70].

2.3.1 Classification of Sprays

Each atomiser type generates different sprays depending on inlet and geometric boundary conditions. In order to characterise the distribution of sprays and the quality of atomisation, several parameters exist. In most applications an important parameter is the droplet size which is usually a representative value of a droplet size spectrum.

Several representative droplet sizes (mean diameters) have been defined (general equation for mean diameters calculation: see *Babinsky and Sojka* [6]). The so-called Sauter mean diameter (SMD) is one of the most important ones. It is defined as the average droplet volume of the droplet spectrum (represented by N droplet size classes) divided by the average droplet surface area [64, 97]:

$$SMD = D_{32} = \frac{\sum_{i=1}^N n_i d_i^3}{\sum_{i=1}^N n_i d_i^2} . \quad (2.22)$$

The $D_{V50} = \text{MMD}$ (Mass Median Diameter) and D_{V90} are further characteristic droplet size parameters. Each of these represents the droplet diameter at which a certain percentage (50 % or 90 %) of the total liquid volume of the collective has a smaller diameter [64]. These characteristic droplet diameters can be calculated from [6]:

$$D_{ab} = \left[\frac{\int_0^{\infty} D^a f(d) dD}{\int_0^{\infty} D^b f(d) dD} \right]^{1/(a-b)} . \quad (2.23)$$

The droplet size distribution generated by atomisers is an additional characterisation opportunity for sprays. Droplet size distributions are usually given in histograms which correlate the droplet size to the volumetric frequency of occurrence. For each defined droplet size class the amount or the liquid volume of the droplet class is identified [6].

Further characterisation parameters for the spray generated by atomisers are the spray cone geometry and cone angle and the mass distribution [6]. Atomisers can provide a solid cone or a hollow cone spray, the spray cone angle is especially of interest if a certain wetting area is required. Symmetry of the pattern, for example in terms of mass distribution, is often desired.

2.3.2 Correlations

Atomisers are characterised regarding their performance by the quality of spray and the droplet sizes generated. The effort needed in order to reach a certain quality of spray specifies the efficiency of the atomiser. In general the droplet sizes generated by air-assisted atomisers are smaller than those from pressure based one-phase nozzles. Several methods exist to calculate the expected characteristic droplet sizes [64]. These methods have been verified by droplet size distributions obtained from measurements. Hence, the application spectrum of each method is limited by operating conditions used in these measurements [6, 69, 99].

Rosin-Rammler (equation 2.26 and 2.27), Nukiyama-Tanasawa (equation 2.28), upper-limit, root-normal, log-normal, log-hyperbolic and normal distribution (Gaussian distribution) represent classical modeling opportunities for droplet size distributions [6, 64]. The normal distribution gives the number of particles of one specific diameter [64]:

$$f(D) = \frac{dn}{dD} = \frac{1}{\sqrt{2\pi}\sigma_n} \exp \left[-\frac{1}{2\sigma_n^2} (D - \bar{D})^2 \right] , \quad (2.24)$$

where σ_n is the deviation of diameters from a mean diameter (\bar{D}), usually it refers to the standard deviation. The log-normal distribution represents the Gaussian distribution with the logarithm of particle diameters and deviation [6]:

$$f(D) = \frac{1}{D\sqrt{2\pi}\ln(\sigma_n)} \exp \left[-\frac{1}{2} \left(\frac{\ln(D/\bar{D})}{\ln(\sigma_n)} \right)^2 \right] . \quad (2.25)$$

One of the most widely used modeling approach for droplet size distributions and often found in models for numerical simulation [64] is the Rosin-Rammler distribution. It is given with [6]:

$$f(D) = q\bar{D}^{-q} D^{q-1} \exp \left[-\left(\frac{D}{\bar{D}} \right)^q \right] , \quad (2.26)$$

or

$$f_V(D) = 1 - \exp \left[-\left(\frac{D}{\bar{D}} \right)^q \right] , \quad (2.27)$$

where index q indicates the width of the distribution and $f_V(D)$ represents the cumulative volume distribution [6].

The Nukiyama-Tanasawa distribution is a relatively simple equation with adequate results (a, b, p, q are independent variables) [64]:

$$f(D) = \frac{dn}{dD} = aD^p \exp - (bD)^q . \quad (2.28)$$

From the distribution it is possible to calculate characteristic droplet sizes (e. g. SMD, MMD or D_{V90} see section 2.3.1). For Rosin-Rammler it is particularly

easy, as characteristic droplet sizes are uniquely related to each other via q [64].

Empirical correlations were improved and adapted in several studies to different atomiser types. This leads to specific correlations for pressure nozzles or air-assisted nozzles.

For air-assisted atomisers the operational parameters are the mass flows of air and liquid, the air-liquid ratio and the pressure of the air used for the atomisation. *Ashgriz* stated, that the *Nukiyama-Tanasawa* and the log-hyperbolic provide good results for an air-assisted atomiser, while log-normal is inferior and *Rosin-Rammler* provides poor results [5]. *Lefebvre* provides a summary of further studies [64].

Kim and Marshall stated that the method published by *Nukiyama and Tanasawa* is one of the most often quoted correlations for air-assisted nozzles [51]:

$$\text{SMD} = \frac{585}{u_R} \sqrt{\frac{\sigma_L}{\rho_L}} + 597 \left(\frac{\mu_L}{\sqrt{\sigma_L \rho_L}} \right)^{0.45} \left(\frac{\dot{V}_A}{\dot{V}_L} \right)^{1.5}, \quad (2.29)$$

but it neglects geometric parameters of the nozzle and is dominated by relative velocity, surface tension and viscosity. For low viscosity fluids the SMD is inversely proportional to the relative velocity and for larger air-to-liquid ratios the influence of viscosity is negligible [64].

Waim [94] found that the calculation method of *Kim and Marshall* [51] has shown the best agreement for the nozzle types used in the present work:

$$\text{MMD} = \left[\frac{249 \sigma_L^{0.41} \mu_L^{0.32}}{(u_R^2 \rho_A)^{0.57} A_A^{0.36} \rho_L^{0.16}} \right] + 1260 \left[\left(\frac{\mu_L}{\sigma_L \rho_L} \right) \left(\frac{L}{u_R^{0.54}} \right) \left(\frac{\dot{m}_A}{\dot{m}_L} \right) \right], \quad (2.30)$$

and the SMD is found with:

$$\text{SMD} = 0.83 \cdot \text{MMD} . \quad (2.31)$$

Hence to calculate the MMD or SMD the liquid viscosity, density and surface

tension, the air to liquid mass flow ratio and geometric nozzle parameters are needed.

2.4 Evaporation

In this chapter the evaporation processes are discussed considering the general evaporation mechanism of single component droplets (e. g. water) and the urea evaporation itself. Fundamentals of the droplet evaporation on surfaces are given in the appendix A.2.

2.4.1 Droplet Evaporation

Droplet evaporation can be characterised regarding heat and mass transfer, influence of convection and vapour concentration and regarding classification of the evaporation procedure. In the following these aspects and their interdependency are discussed.

A first theory for the evaporation of droplets was given by *Maxwell* in 1877 [32]. *Maxwell's* equations show simple relations for spherical droplets in an infinite, uniform medium without motion [32,81]. Nowadays there is a broad spectrum of correlations and literature about droplet evaporation. *Sazhin* provides a review on correlations and literature [81]. The analogy of heat and mass transfer leads to correlations for mass transfer.

Heating Phase and Isothermal Evaporation

The combined heating and evaporation process of one droplet containing one species is explained, assuming constant ambient temperature and Nusselt number. In this case the process can be divided into the non-isothermal heating phase and the isothermal evaporation of the droplet [64].

During the heating phase the temperature of the droplet increases due to the heat flow from the gas, while during the isothermal evaporation heat feeds

into the evaporation of the droplet and its temperature remains constant. *Lefebvre* [64] suggests a method to consider these steps independently from each other. The mass transfer number (B_M) and the thermal transfer number (B_T) are the indicators for the process progress. The thermal transfer number is given by

$$B_T = \frac{c_{p_{vap}} (T_\infty - T_{sur})}{\Delta h_v} \quad (2.32)$$

and the mass transfer number by

$$B_M = \frac{Y_{S_{sur}}}{1 - Y_{S_{sur}}} = \frac{m_S}{m_g} , \quad (2.33)$$

where $Y_{S_{sur}}$ is the mass fraction of the substance S at the surface of the droplet in ambient gas.

As soon as B_M equals B_T the heating phase is completed and the isothermal process begins. The differentiation of the two phases is beneficial, as the isothermal process phase can be calculated analytically while the heating phase needs to be solved numerically. Two solution methods are given by *Lefebvre* [64] to calculate the heating phase in iterative steps or approximately. For this thesis the reduction in droplet size or mass over time is small for the heating period, thus it is not explained further. The implemented equations are given in appendix A.2.

For the isothermal evaporation phase the so-called d^2 -law is a good approximation for the droplet diameter decrease [64, 81]. The d^2 -law defines a linear change of the droplet surface over time:

$$\frac{d(d^2_{dr})}{dt} = const . \quad (2.34)$$

A reference temperature is needed to incorporate the temperature of the gas flow. The empirical one-third rule [64] is usually taken to calculate the reference temperature. Subsequently, the material properties at the droplet surface

have to be referred to this temperature:

$$T_{ref} = T_{sur} + \frac{T_{\infty} - T_{sur}}{3} . \quad (2.35)$$

Water vapour in the exhaust gas flow is not negligible since it affects the concentration gradient influencing mass diffusion. However, this has not been considered so far in the mass transfer number B_M . The vapour concentration is now included in the mass transfer number by the elaboration of a total mass, consisting of the vapour and the gas mass:

$$m_t = m_s + m_g . \quad (2.36)$$

The combination of these equations, with some intermediate steps (shown in appendix A.2), leads to the differential droplet diameter change. The equation for the differential droplet diameter change is found with:

$$\frac{d(d_{dr})}{dt} = \frac{4 \cdot \lambda_{vap} \ln(1 + B_M)}{\rho_{dr} \cdot c_{p_{vap}} \cdot d_{dr}} \cdot \frac{Nu}{Nu_0} . \quad (2.37)$$

These equations allow the calculation of either the whole evaporation time of one specific droplet size or the diameter decrease within a certain time. In this work the approximate time of spray droplets of different sizes to evaporate, or droplet sizes after a certain path length, are calculated for given test conditions.

Application in MATLAB

A MATLAB script calculates the temporal decrease of droplet diameter and the evaporation time. The script is based especially on the equations 2.33 to 2.37. The droplet evaporation is based on the liquid properties of water (explanation see section 2.4.2). It has to be distinguished between the heating phase and the evaporation phase. During the evaporation phase the diameter is calculated with the d^2 -law. First the initial temperature of the ambient gas

flow and the initial droplet diameter are required, thereafter the program accesses the actual fluid properties in iterative steps based on the new reference temperature (equation 2.35) for the gas flow. The heating time and evaporation time are calculated. Additionally the distance theoretically traveled until complete evaporation is computed, resulting from the average initial droplet velocity.

2.4.2 Urea Evaporation

Urea influences the evaporation process as the vapour concentration of water at the droplet surface changes as a function of the urea concentration. *Birkhold* [15] investigates the change in vapour pressure for two different initial urea concentrations in an aqueous solution. The evaluated vapour pressure curves are illustrated in comparison with water in figure 2.7.

The urea concentration in an aqueous solution causes a vapour pressure drop

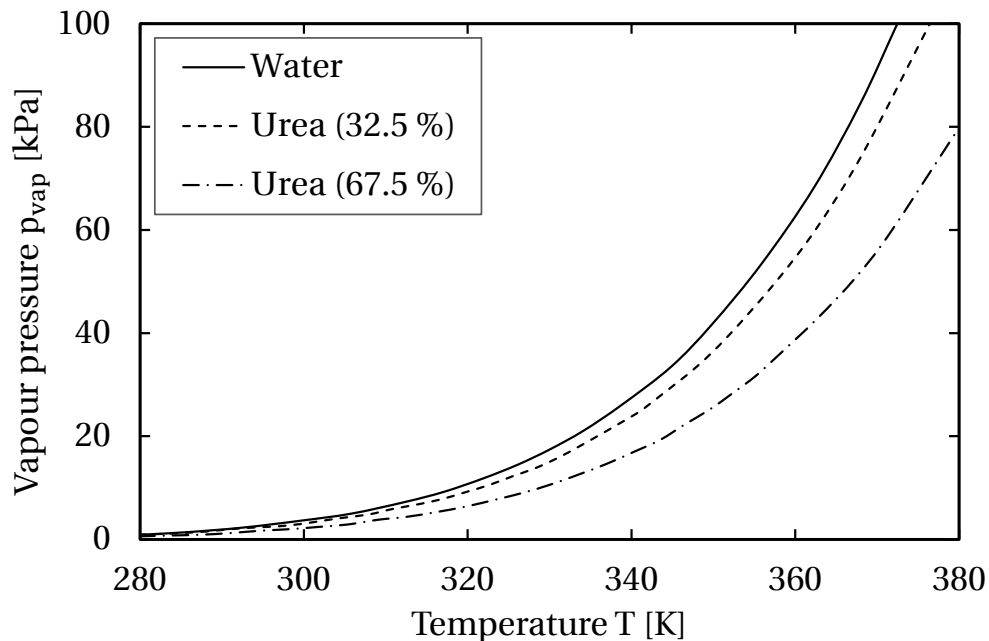


Figure 2.7: Vapour pressure curves for water (solid line), 32.5 % urea (dashed line) and 67.5 % urea (dashed dotted line) in an aqueous solution.

which leads to a slower evaporation of the urea-water solution in comparison with water. This effect increases further as the water evaporates first and the urea concentration increases in the droplet. Beneficial for the urea evaporation process is a high GHSV which is assumed to be unfavourable for the decomposition process of urea [11]. In general, it is expected that the water evaporates completely before the evaporation process of the remaining liquid urea starts [15, 89]. *Grünwald* describes another possibility of urea evaporation using a modelling approach assuming higher concentration of urea at the surface of the water droplet which leads to precipitation and crystallisation of urea [37]. Thereby, a significant limitation in mass transfer of urea and the enclosed water would occur. He states that the described effect occurs once oversaturation arises in the droplet.

The numerical analyses of both explained modelling approaches (performed by *Birkhold* [17] and *Grünwald* [37]) results in the understanding that the evaporation model for water is sufficient to describe the important process steps.

2.5 Theory of Turbulent Jets

Turbulent jets occur in many technical applications, particularly in flows from a nozzle. The theory of turbulent jets allows a general description of the mixing process. The flow characteristics are described by the parameters velocity, temperature and substance concentration. The heat and mass transfer on the tangential separation surface is characterised by instabilities on the surface which arise in randomly moving eddies. In consequence, parameter profiles are formed over the jet region. Depending on the initial jet conditions these profiles can be described mathematically.

In general the simplest case of turbulent jets is found when an initial uniform velocity field is moving into a medium at constant velocity (submerged and coflow jet). In most studies a so-called submerged jet is treated, where a jet is injected into a medium at rest. Considerations of this jet are the basis for the following descriptions of a jet in coflow, as the approach is valid for

coflowing jets as well. In the present case, the turbulent jet is generated from a two phase jet in conjunction with a coflow jet. In addition, the turbulent jet is injected into a mixing chamber, thus into a finite space. Hence, relevant equations to calculate velocity, temperature and concentration profiles need to be described for the two phase jet in coflow in finite space. In the following these approaches are discussed separately, a combination is obtained in chapter 5.2. All given equations refer to axially symmetric jets, as these are relevant for this thesis. Following mathematical formulas and their derivation are obtained from *Abramovic* [1]. Additional explanations and derivations of formulas are given in the appendix A.3.

2.5.1 Jets in Coflow

Turbulent jets injected into a medium moving in the same direction are called jets in coflow. The influence of the surrounding medium (coflow) on the boundary layer is highly dependent on the ratio between the velocity of the surrounding medium u_H and the initial velocity of the jet u_0 . The velocity ratio m is given in equation 2.38. For this thesis only the results for velocity ratios $m < 1$ are of interest, as the coflow velocity does not exceed the jet velocity.

$$m = \frac{u_H}{u_0} \quad (2.38)$$

In figure 2.8 a turbulent jet in coflow is illustrated schematically. At the initial plane ($x = 0$) there is no interaction with the surrounding material, the boundary layer thickness is equal to zero. While propagating downstream the boundary layer is thickening. The cross section increases between the surrounding material and the jet particles until the non-viscous core is mixed completely. In the non-viscous core the static pressure remains constant as result of the constant initial velocity. At some distance from the initial region a widening as well as a variation of velocity can be observed, forming the main region. The length of the transitional region between initial and main region is often assumed to be zero for simplicity.

Derivations of formulas for the initial region as basis for the derivations of the

main region are given in appendix A.3.1.

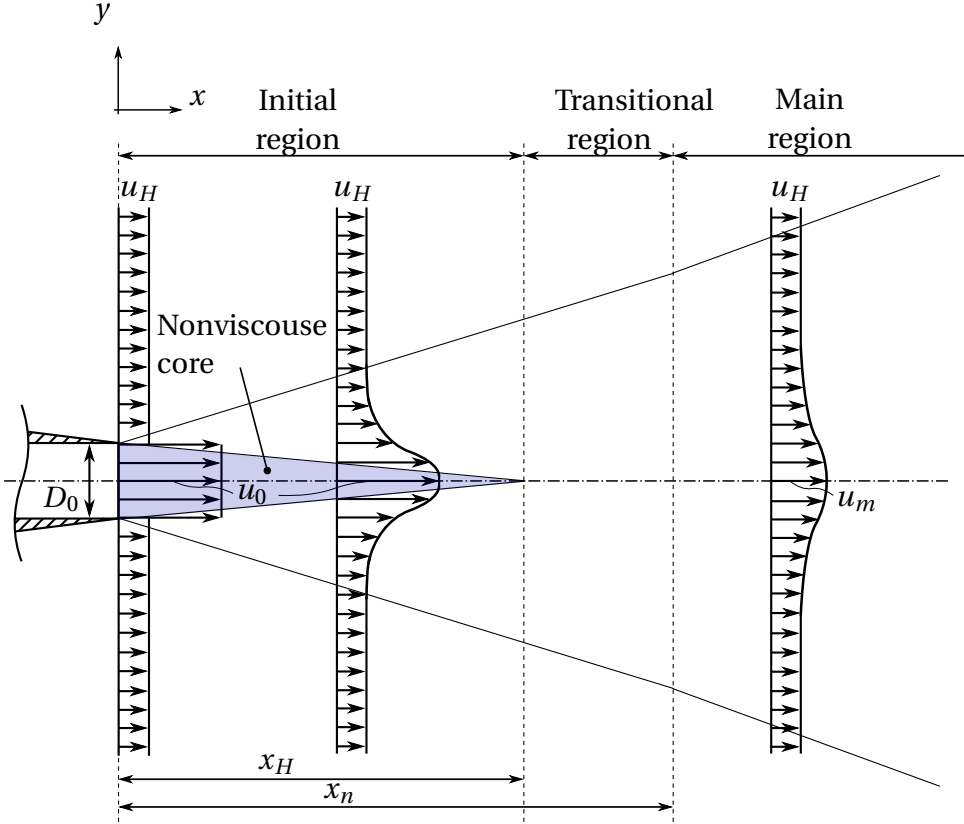


Figure 2.8: Schematic illustration of a turbulent jet in coflow [1].

One characteristic of the main region of a jet in coflow is that the non-viscous core is already mixed completely and only a velocity maximum which differs from the initial jet velocity, remains at the jet symmetry axis. The radial dimensionless velocity profiles for the main region are calculated like the ones for the initial region (see equations A.24 and A.26). Two different formulas are provided by [1]. Equation 2.39 is a direct application of A.24 and equation 2.40 corresponds to A.26:

$$\frac{\Delta u}{\Delta u_m} = \left[1 - \left(\frac{y}{b} \right)^{1.5} \right]^2 = (1 - \xi_1^{1.5})^2 \quad (2.39)$$

$$\frac{\Delta u}{\Delta u_m} = 1 - \left[1 - \left(1 - \left(\frac{y}{b} \right)^{1.5} \right) \right]^2 = 1 - (1 - \eta^{1.5})^2 = 1 - (1 - (1 - \xi_2)^{1.5})^2 \quad (2.40)$$

with $\Delta u = u - u_H$, $\Delta u_m = u_m - u_H$, where u_m is the velocity on the symmetry axis. In order to compare values of different cross sections it is useful to correlate the dimensionless velocity ratio at a defined point y_c . In this case, y_c is the distance from the axis to the location where $\Delta u_c = 0.5 \cdot \Delta u_m$. The dimensionless ordinate $\xi_c = \frac{y_c}{b}$ equals constant values for each formula (2.39 and 2.40):

$$\begin{aligned}\xi_{1c} &= 0.44 \\ \xi_{2c} &= 0.56 .\end{aligned}$$

The temperature and concentration profiles are related to the square root of the velocity profile:

$$\frac{\Delta T}{\Delta T_m} = \frac{\Delta \chi}{\Delta \chi_m} = \sqrt{\frac{\Delta u}{\Delta u_m}} , \quad (2.41)$$

where χ is the concentration. In the following the velocity distribution along the symmetry axis $\Delta u_m(x)$ for the main region is discussed. It is derived from the conservation of momentum along the x-axis. Equation 2.42 shows the dimensionless velocity profile along the axis:

$$\begin{aligned}\Delta \bar{u}_m &= \frac{\Delta u_m}{\Delta u_{0m}} = \frac{mA_1}{2A_2(1-m)} \left(\sqrt{1 + p^2 \frac{r_0^2}{r^2}} - 1 \right) \\ &= \frac{0.258 \cdot m}{0.268 \cdot (1-m)} \left(\sqrt{1 + \frac{8.1(1-m)r_0^2}{m^2 r^2}} - 1 \right) .\end{aligned} \quad (2.42)$$

Formulas to calculate the variables (A_1 , A_2 , p^2 , n_{1u} and n_{1u}) are given in appendix A.3.1.

To obtain the dimensionless velocity distribution, in reference to a dimensionless ordinate in direction of propagation, a relation of the radius in the transverse cross section to an axial control variable has to be identified:

$$c(\bar{x} - \bar{x}_0) = \bar{r} + \frac{0.69}{p^2} \left[(\bar{r}^2 + p^2)^{1.5} + \bar{r}^3 - p^3 \right] , \quad (2.43)$$

where is $\bar{x}_0 = \frac{x_0}{r_0}$. The coefficient c is an experimentally determined constant and defined for axially symmetric jets within a range of $c \approx 0.2 - 0.3$. Derivation and results of this relation between \bar{x} and \bar{r} (out of equation 2.43) can be found in the appendix. Different velocity ratios m can be extracted from diagram A.5.

The corresponding temperature and concentration profiles and their relation to the velocity distribution are given in appendix A.3.1.

Based on the described equations for the initial and main region of an axially symmetric jet in coflow, it is possible to calculate the velocity, temperature and concentration at specific locations in the jet.

2.5.2 Two-Phase Jets

A two-phase jet incorporates a second phase, e. g. particles or liquid droplets which generates a mixture with the gaseous phase of the jet. Hence, mass and density differences have to be considered. In figure 2.9 a two-phase jet is illustrated schematically, where u_π is the initial velocity of the admixture (particles or liquid droplets) and u_B is the initial velocity of the gas phase.

Basis for the adaptations is the conservation of momentum (equation 2.44) leading to the initial momentum of the two-phase jet (equation 2.45), dependent on the concentrations of admixture (second phase) and of the gas phase:

$$\int_0^F \rho_B \cdot u^2 (1 + \chi) dF = \dot{I}_0 , \quad (2.44)$$

$$\dot{I}_0 = \frac{G_B}{g} u_B + \frac{G_\pi}{g} u_\pi . \quad (2.45)$$

The initial weight flow rates for the admixture G_π and the gas G_B divided by

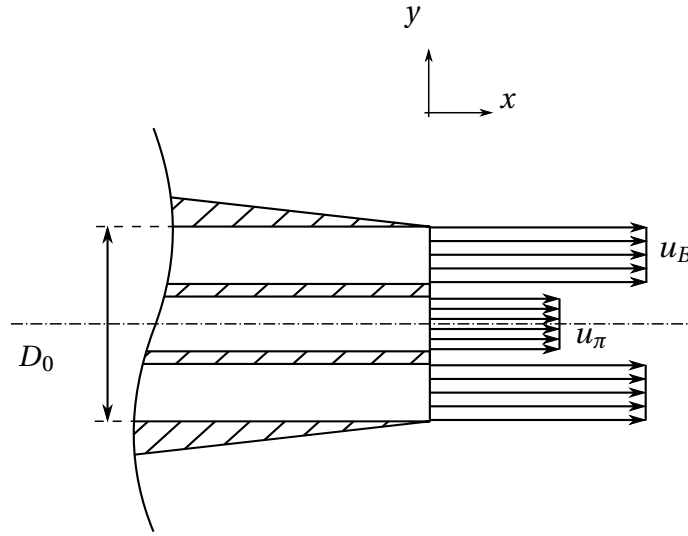


Figure 2.9: Two phase jet out of a nozzle.

the acceleration of gravity g result in the mass flow for each phase.

The velocity decrease on the jet axis can be calculated by (for intermediate steps see equations in appendix A.49 and A.50):

$$\bar{u}_m^2 = \left(\frac{u_m}{u_0} \right)^2 = \frac{\dot{I}_0}{\rho_B u_0^2 F_0} \cdot \frac{F_0}{F} \frac{1}{A_2 + \chi_m C_2} . \quad (2.46)$$

Substituting F and χ , the dimensionless velocity decrease takes the form:

$$\bar{u}_m = 2.25 \cdot \frac{j s}{\bar{r}^2} \left(\sqrt{1 + 1.5 \frac{\bar{r}^2}{j s^2}} - 1 \right) \quad (2.47)$$

with

$$s = \frac{G_\pi u_0}{\dot{I}_0 g} \quad (2.48)$$

and

$$j = \frac{\dot{I}_0}{\rho_B u_0^2 F_0} . \quad (2.49)$$

2.5.3 Jets in Finite Space

Now the adaption of turbulent jet theory in free space, described above, to finite space is provided. Jets in finite space can be found in several technical applications, for example in mixing chambers for combustion. The system boundary leads to a pressure increase along the jet propagation directions (axial, radial), while for the free jet the assumption of constant pressure is valid. This situation and the differences in velocity distribution is represented schematically in figure 2.10. The mixing chamber with the jet propagation (shaded area) and its nonviscous core is illustrated in the upper section of the picture. The velocity profiles with the increase of the global average velocity due to the additional mass flow injected by the jet is illustrated below. In contrast to jets in finite space, the momentum of a jet embedded in an infinite space can be regarded as a perturbation, hence the velocity amplitude will decrease until the undisturbed flow field is reached again.

2.5.4 Two-Phase Jets in Coflow and Finite Space

The equation adaptations refer to experimental investigations of jets in finite space. An influence is primarily observed for the axial velocity component. The radial velocity profiles consider the velocity elevation with respect to the coflow, hence the influence is negligible. The axial velocity distribution is adapted by the experimental coefficient c . For jets in coflow it is given by $c \approx 0.2 - 0.3$, for jets in coflow in finite space it is given with $c \approx 0.18 - 0.28$ [1]. Equations for two phase jets in coflow are adapted to represent jets in finite space. The axial velocity decrease writes:

$$\frac{\Delta u_m}{\Delta u_0} = \frac{u_m - u_H}{u_0 - u_H} = \bar{u}_m \cdot \frac{u_0 - \frac{u_H}{\bar{u}_m}}{u_0 - u_H} \quad (2.50)$$

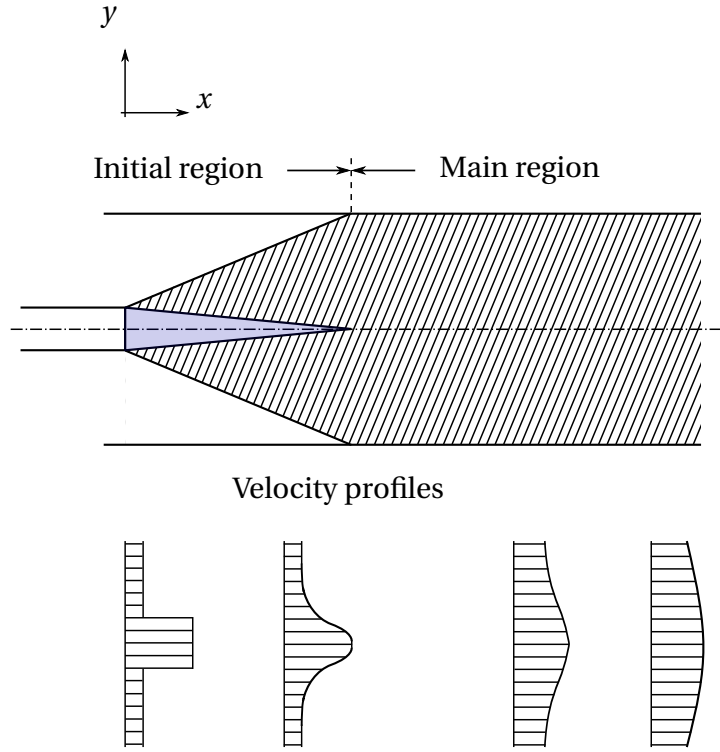


Figure 2.10: Jet in coflow in finite space.

where u_m is the velocity at the jet axis, u_H the velocity of the coflow and \bar{u}_m is the velocity decrease at the jet axis for two phase jets (see equation 2.47). The initial jet velocity u_0 is given by the initial momentum (equation 2.45), divided by the sum of the mass flows (gas and liquid) of the two phase nozzle. The radial distribution of the axial velocity is obtained from equations 2.39 and 2.40. The distance y_c for the dimensionless abscissa is calculated for each experiment and simulation as $u_c = \Delta u_c + u_H$.

Abramovic showed in his studies that radial temperature (T/T_m) and concentration (χ/χ_m) profiles are represented well by the square root of the equation for velocity profiles (equation 2.41) [1]:

$$\frac{\Delta T}{\Delta T_m} = \frac{\Delta \chi}{\Delta \chi_m} = 1 - \left(\frac{y}{b}\right)^{1.5} = 1 - \xi_1^{1.5}, \quad (2.51)$$

$$\frac{\Delta T}{\Delta T_m} = \frac{\Delta \chi}{\Delta \chi_m} = \sqrt{1 - \left[1 - \left(1 - \left(\frac{y}{b} \right)^{1.5} \right) \right]^2} = \sqrt{1 - (1 - (1 - \xi_2)^{1.5})^2} . \quad (2.52)$$

Initial Values

For computations, the initial velocities of the two separate phases are needed. The initial velocity of the liquid mass flow is estimated to be zero at the outlet of the nozzle. The initial velocity of the pressurised air is derived from the air mass flow rate injected through the nozzle (the explicit calculation method is explained by [94]). The axial velocity decrease along the jet's symmetry axis for the desired parameters is gained by including the axial velocity decrease for two-phase flows (equation 2.47) in equation 2.50 to consider the impact of the coflow. The temperature is not included in this treatment. Accordingly, the profile does not change for the three different temperatures. Another parameter to be quantified is the experimental coefficient c which is given in literature in a range between $c \approx 0.2 - 0.3$ (section 2.5.1) for jets in coflow and for jets in finite space it reduces to $c \approx 0.18 - 0.28$ (section 2.5.3).

3 Experimental Setups and Diagnostics

This chapter describes the experimental setups and the applied measurement techniques. Two setups in different configurations have been used for the investigations. The setups and their configurations as well as test conditions are given in sections 3.1 and 3.2. The FTIR spectroscopy, a concentration measurement technique, is explained in section 3.3. Subsequently, velocity measurement methods (section 3.4) are described, followed by the introduction of spray characterisation methods (section 3.5).

Application-oriented investigations of the performance of SCR systems are usually conducted in combination with the engine type which it is designed for. In this approach, the SCR system is combined with the hydrolysis unit and implemented in the main exhaust gas line (see chapter 1.2, figure 1.2). For the majority of SCR system measurements it is sufficient to extract gas samples downstream of the SCR catalyst and analyse the exhaust gas composition [43,44,55,59]. These measurements focus typically on the identification of carbon oxides and nitrogen oxides. Separate studies on hydrolysis reactors have been conducted for truck and automotive applications [15, 37, 89, 91]. Similar to the SCR system measurements, gas samples are extracted downstream of the hydrolysis catalyst to analyse the typical reaction products such as ammonia, carbon dioxide and further products.

Many studies concern the material properties of SCR catalysts. They consider the performance of different coatings and suitable materials of SCR catalysts [18, 19]. Characterisation of urea decomposition are typically performed in small-scale flow reactors. In literature various experiments can be found which examine in detail the chemical composition of the products under various thermodynamic conditions [12–14].

Investigations performed in the present study can be separated into two

groups: The application-oriented experiments at engine operating points specified by the project partner MAN Diesel & Turbo SE, and conditions targeting additional academic questions. Data obtained at engine operating point is used for the validation of the hydrolysis reactor design principles. Test conditions and hardware configurations are presented within this chapter. Experiments were conducted at two different setups: The hydrolysis reactor and the injector experiment. Besides ammonia concentration measurements, velocity measurements were performed at the hydrolysis reactor experiment. Atomisation measurements were conducted at the injector experiment.

3.1 Hydrolysis Reactor Experiment

The hydrolysis reactor experiment is composed of a Roots blower for the main air supply, two air heaters, the hydrolysis reactor itself and an ammonia slip catalyst. A similar setup was used by *Grünwald* and *Steinbach* [37,89], whereas the core part, the hydrolysis reactor, differs from their previous setup. The setup is schematically shown in figure 3.1.

The roots blower delivers air volume flow rates up to $1000 \text{ m}^3\text{h}^{-1}$ to the air heaters which heat the air to temperature up to $600 \text{ }^\circ\text{C}$. After a section homogenising the flow, the heated air enters the reactor, optionally through a swirl generator which optimises the spray distribution. A two-phase nozzle serves as the urea injector and directs the spray coaxially to the main air flow towards the catalyst. The catalyst is installed downstream of the injector in a separate segment followed by a section which accommodates the extraction tube for gas concentration measurements, which can be traversed. The ammonia slip catalyst prevents the emission of toxic ammonia into the environment by oxidising ammonia to nitrogen oxide and water. A three-dimensional view of the hydrolysis reactor is given in figure 3.2.

The measurement section is displayed schematically in 3.3. The evaporation zone is made of glass to have optical access. This section is highlighted in blue (lighter blue for the evaporation section and darker blue for the part with optical access). The overall decomposition process can be analysed through con-

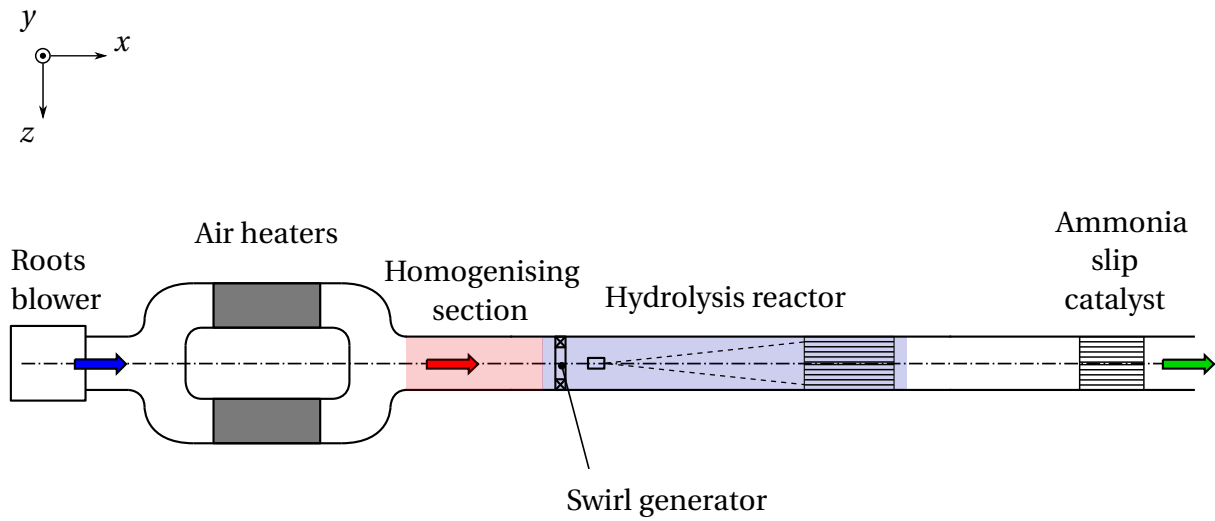


Figure 3.1: Test rig for hydrolysis reactors: cold air (blue arrow) from the Roots blower is heated (red arrow) by the two heaters, passes the hydrolysis reactor and the ammonia slip catalyst, before exiting the setup (green arrow).

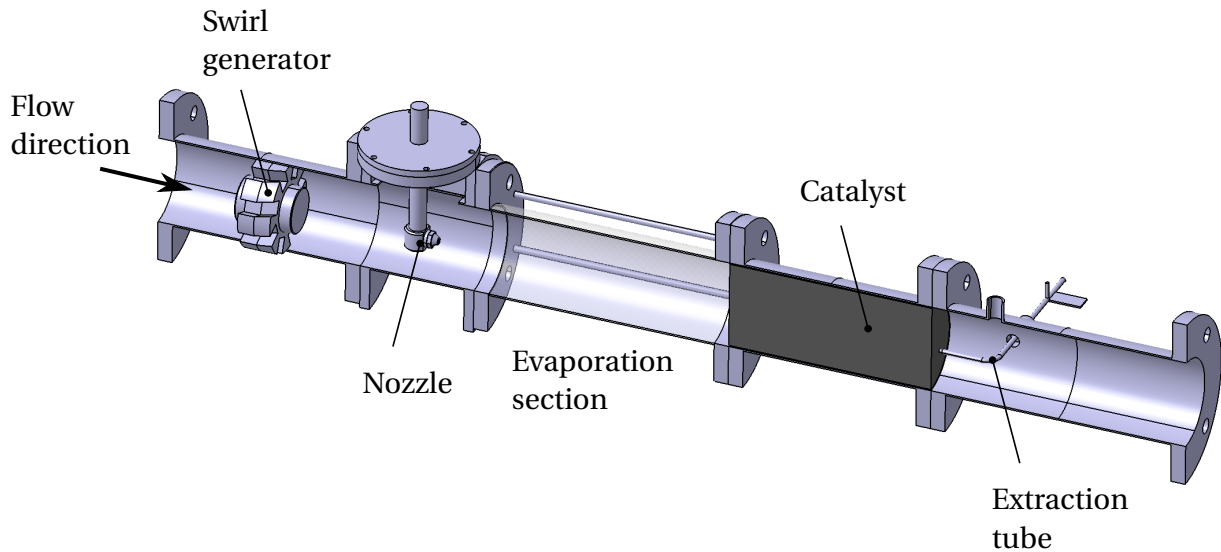


Figure 3.2: Hydrolysis reactor with its components.

centration measurements of the final products ammonia and carbon dioxide. These species and others are measured downstream of the hydrolysis catalyst by FTIR-Spectroscopy. The extraction tube has horizontal and vertical mount-

3.1 Hydrolysis Reactor Experiment

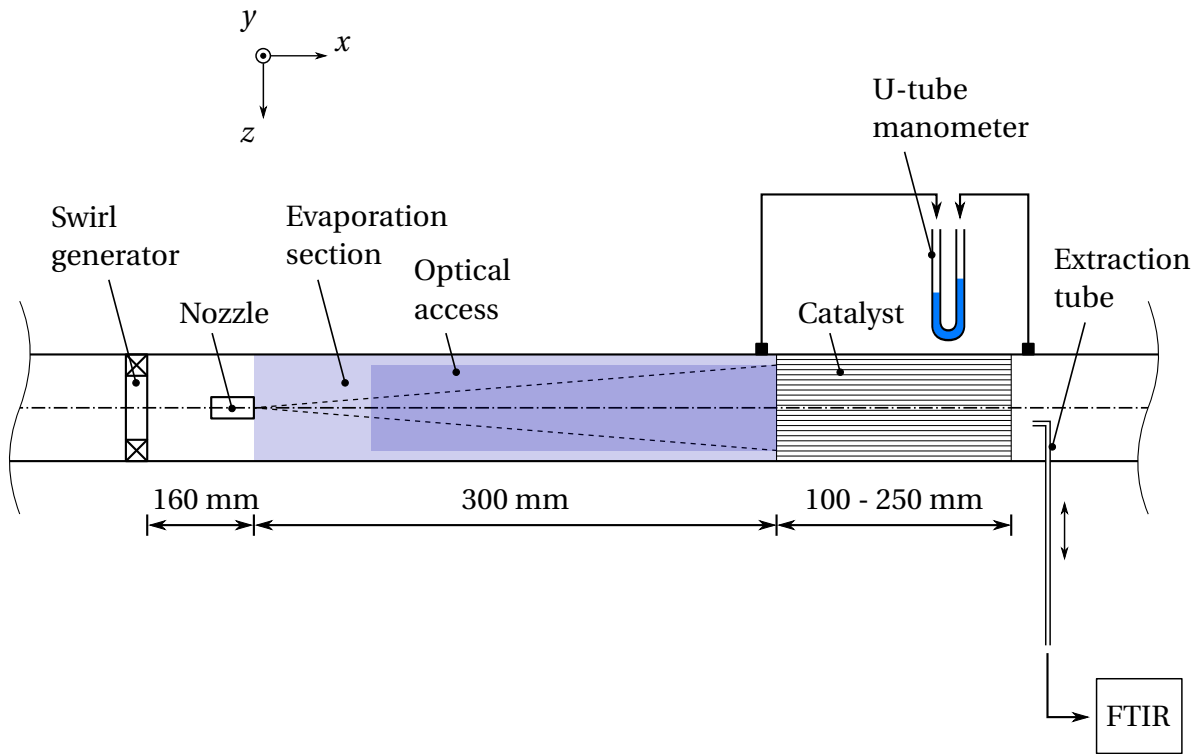


Figure 3.3: Hydrolysis reactor setup for concentration measurements with swirl generator (optional), nozzle, evaporation section (highlighted in blue), catalyst and diagnostics.

ing options and can be traversed by a stepper motor.

The gas for concentration measurements can either be extracted directly from the channel or guided through a dilution unit. A higher measurement error occurs in concentration measurements using the dilution unit.

Six thermocouples (Type K) are integrated in the experimental setup; four of them are located within the catalyst. The positions of the thermocouples in the catalyst change for different catalyst structures. A static pressure measurement was applied to indicate solid deposit formation within the catalyst. The pressure difference across the catalyst is measured by a U-tube manometer.

3.1.1 Hydrolysis Reactor Dimensions and Components

The dimensions of the hydrolysis reactor are restricted by the installation space available. The inner diameter of the reactor is 110 mm in all sections, the reactor varies in length depending on the catalyst length and the optional swirl generator. The evaporation section has a fixed length of 300 mm (see figure 3.3). The size of the evaporation section is of high importance since within this area heating and partial evaporation of the urea-water droplets take place. For heating and evaporation of droplets a long evaporation section is beneficial. As urea tends to crystallise on uncoated surfaces, droplet-wall interaction in front of the catalyst needs to be avoided. This leads to an optimum evaporation section length for a given spray cone angle.

In the present work small droplet sizes are used at high liquid flow rates. An air-assisted nozzle is chosen, as compressed air is usually available on ships in contrast to automotive applications. The two-phase injector used for the research is a proprietary development of MAN Diesel & Turbo SE. The construction and calculation of the nozzle is discussed by *Waim* [94]. The MAN nozzle is designed similar to the two-phase nozzle of Düsen-Schlick GmbH Model 940. In figure 3.4 a sectional drawing of the two nozzles is shown. Main differences are the size of the body and the geometry of the swirl generator. Diameters of the liquid and air orifices are identical. Construction drawings of the two nozzles and their components can be found in [94]. The measurements characterising the spray quality are conducted for the MAN nozzle in comparison with its equivalent of Düsen-Schlick GmbH (model 940: data-sheet [84]) at the injector setup (see section 3.2). The results of these measurements are summarised in chapter 5.1.3.

The applied hydrolysis catalyst from Continental Emitec GmbH is a TiO₂-coated (crystalline form: anatase) metal substrate combination of the MX and the ST structure. The MX structure has a fixed length of 50 mm and a cell-density of 75 cpsi. The ST structure has a variable length between 50-200 mm and a cell-density of 200 or 400 cpsi. Emitec provides GSA values for coated ST structures with $GSA = 3.132 \text{ [m}^2 \text{ L}^{-1}\text{]}$ for 200 cpsi and $GSA = 3.65 \text{ [m}^2 \text{ L}^{-1}\text{]}$ for 400 cpsi. The two structure types are shown in figure 3.5. A combined MX and

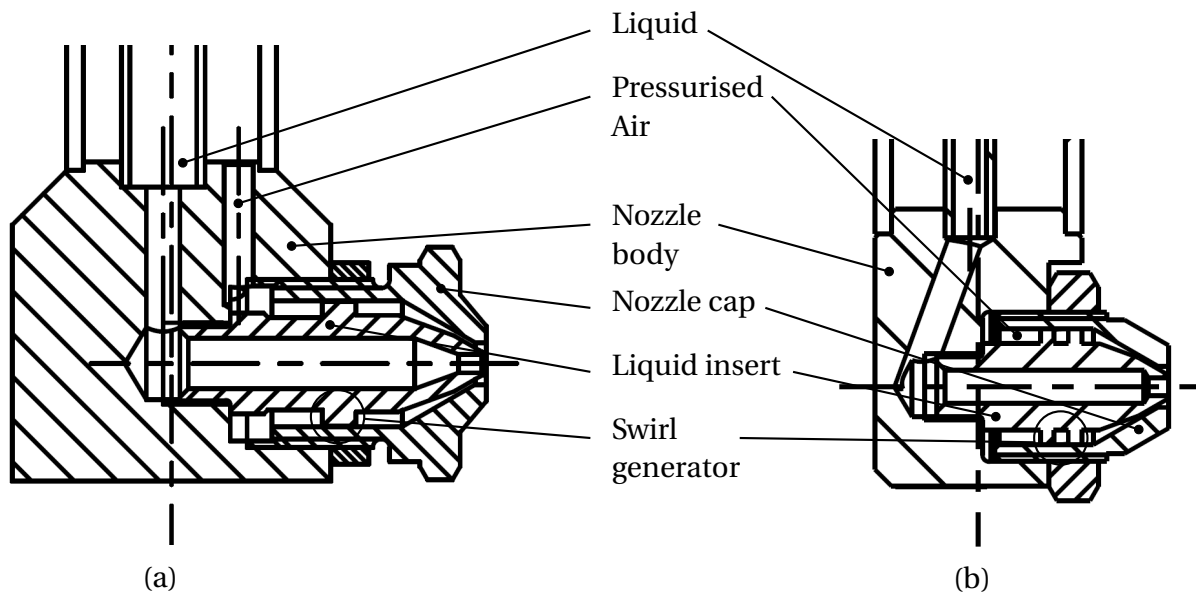


Figure 3.4: Used nozzles: (a) Schlick model 940 and (b) MAN nozzle.

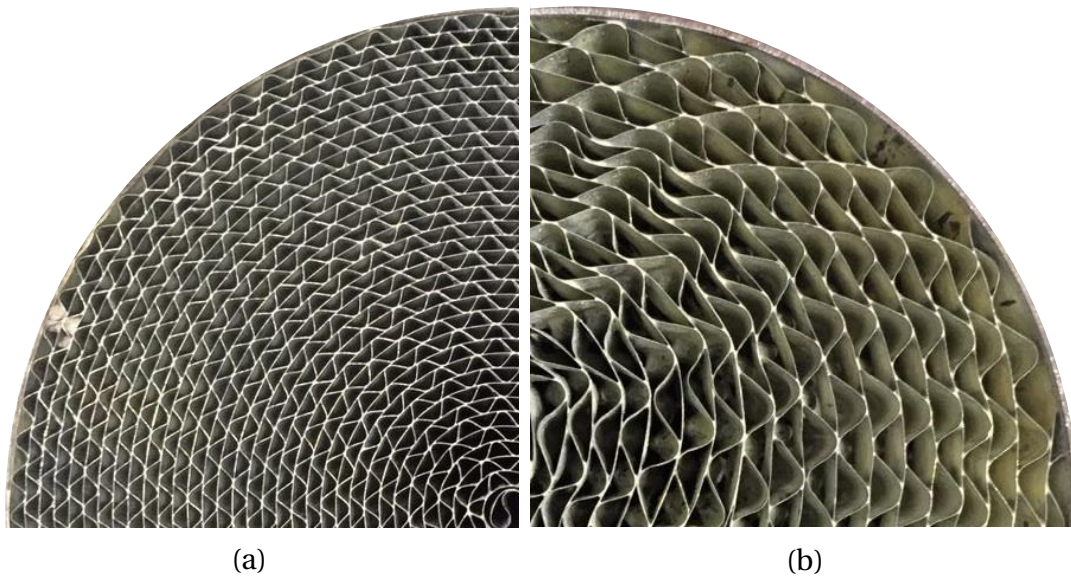


Figure 3.5: Used catalysts: (a) Emitec ST structure (200 cpsi) and (b) Emitec MX structure.

ST catalyst does not allow thermocouple mounting within the MX structure, thermocouples are only mounted at the front surface of the ST structure.

3.1.2 Design of Swirl Generators

An additional component tested is a swirl generator mounted upstream of the injector to optimise the spray distribution and the reactor performance. It is mounted at a 160 mm distance from the nozzle (see figure 3.3), so the total length of the hydrolysis reactor varies between 400 to 660 mm. This component deflects the flow and provides it with a tangential velocity component.

The following simple models for vortices in two dimensions help to define swirling flow: First, the irrotational (potential or free) vortex, derived from potential theory of flows, satisfies the condition of irrotational flow $\vec{\omega} = \nabla \times \vec{u}$ [58, 60]. The tangential velocity is proportional to $1/r$ and therefore tends towards infinity for $r \rightarrow 0$ which can only exist in inviscid flow. Second, the rotational (solid-body or forced) vortex characterised by a tangential velocity proportional to r . Both forms of vortices do not appear in nature. The Rankine vortex is a combination of both models leading to a more realistic vortex representation in viscous flow with rotational vortex in centre, surrounded by an irrotational vortex [86]. In technical applications the swirl number S and the swirl angle φ are often used as indication of the swirl intensity [87]. The swirl number S represent the ratio of axial flux of tangential momentum to the product of axial flux of axial momentum times the equivalent nozzle radius [38] and φ expresses the angle between the main flow direction (axial) to the redirected flow (tangential) [87]:

$$S = \frac{\dot{D}}{R \cdot \dot{I}} , \quad (3.1)$$

$$\varphi = \arctan \frac{u_{tan}}{u} . \quad (3.2)$$

The swirl generator geometry defines the vortex type which is created. The tangential velocity distributions of relevant vortex types in a pipe flow are shown in figure 3.6. An axially guided flow (e. g. twisted tape) as well as direct rotation create vortices with nearly constant increase of tangential velocity over the radius r , thus a solid body vortex. A radially guided flow provides

a Rankine vortex [87]. A third tangential velocity distribution of interest in this context is a wall jet. *Schlichting and Gersten* [83], *Glauert* [35] or *Lauder and Rodi* [62] specify a jet flowing along a wall as a wall jet. A three-dimensional wall-jet occurs when “a fluid issues from a nozzle of finite width along a plane wall” [62]. It occurs generally for swirling flow, which enters the pipe by an annulus. This velocity distribution does not refer directly to one vortex type, but is also a combined vortex. The axial velocity distribution is dependent on the swirl generator type and the intensity of swirl. With increasing swirl intensity the axial velocity decreases at the axis until a stagnation point is observed. A further increase of the swirl intensity leads to vortex breakdown [39] and a flow recirculation zone in the centre.

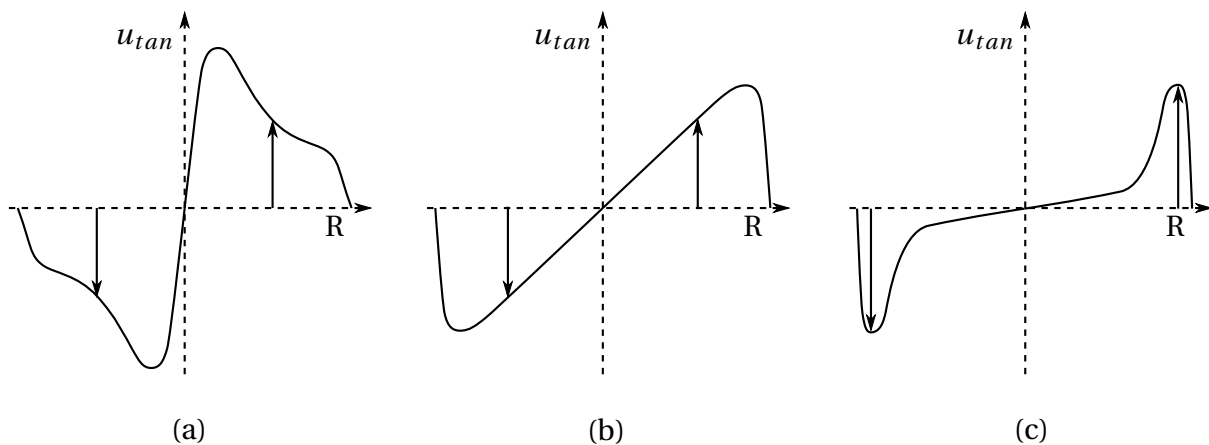


Figure 3.6: Tangential velocity distribution of a Burgers vortex (resembles irrotational vortex) in (a), a solid body vortex in (b) and a wall jet in (c) in a pipe flow [87].

In this thesis an optimisation of the spray distribution by a change of the coflowing gas (section 2.5.1) is obtained. The vortex flow leads to an intensified interaction of the jet with the gas flow. An axial swirl generator (axial flow through annulus) is selected because of favorable mounting and low manufacturing complexity. Thus, a solid body vortex in combination with a wall jet is expected. An axial swirl generator design is presented schematically in figure 3.7.

Gupta provides a possibility to use geometrical data of the axial swirl genera-

tor to calculate the swirl number S . The geometrical design can be calculated directly from the desired swirl number [38]:

$$S = \frac{2}{3} \left[\frac{1 - \frac{d_h^3}{d_{SN}^3}}{1 - \frac{d_h^2}{d_{SN}^2}} \right] \tan \Phi . \quad (3.3)$$

The angle Φ represents the turning angle of the swirl generator vane, d_{SN} and d_h the diameters of the swirl generator nozzle and the vane tip, respectively. The design of the swirl generator for the application in the hydrolysis reactor is restricted by its geometrical boundary conditions. The diameter of the vane tip d_h is defined by the inner diameter of the hydrolysis reactor pipe and the nozzle diameter d_{SN} of the swirl generator implicitly by installation in combination with injector size. Two swirl numbers were selected. For each swirl

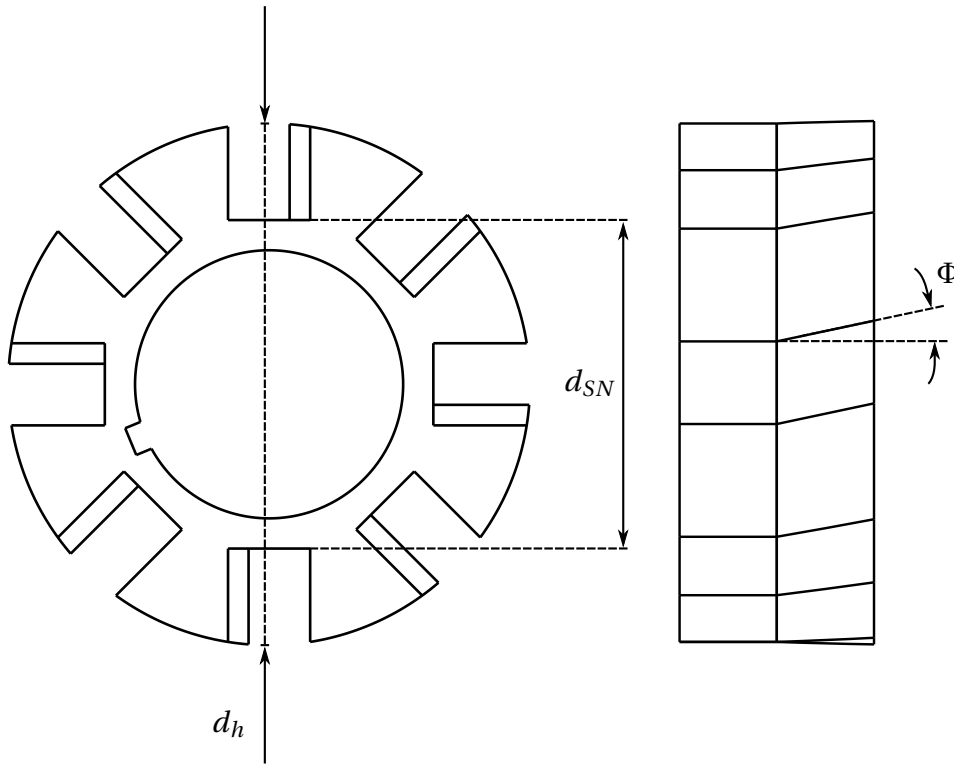


Figure 3.7: Swirl generator blade with the characteristic diameters d_{SN} and d_h as well as the turning angle Φ .

number the turning angle of the vane was calculated.

In the hydrolysis reactor setup the swirl generator is mounted in a separate pipe segment upstream of the injector. The swirl generator consists of two disks, one with straight vanes and one with a turning angle of the vanes. The diameter of the vane pack hub d_h is 110 mm (inner diameter of the hydrolysis reactor pipe), the diameter of the swirl generator nozzle d_{SN} is 70 mm. The first tested swirl number was selected based on swirl numbers used for flame stabilisation at $S_1 = 0.7$. In these studies this swirl number leads to a vortex breakdown where the flame is stabilised. A turning angle of $\Phi = 28^\circ$ is calculated for S_1 . An undesired strong influence to the spray was observed with this first swirl generator, as most of the liquid impinges on the pipe wall. Hence, a second swirl generator with less than the half of the first swirl number ($S_2 = 0.28$ and $\Phi = 12^\circ$) was built. Droplets of the spray were still influenced by the swirl flow, but without impinging on the pipe wall. The results shown in chapter 6 refer to the second swirl generator.

3.1.3 Operating Conditions of Concentration Measurements

Engine Operating Points

Operating points of the engine determine the thermal and the mass flow conditions as well as the amount of the reducing agent for the application-oriented tests. For these tests high urea mass flow rates are necessary. Hence, the concentration measurements are conducted via the dilution unit due to the high ammonia concentrations expected.

Concentration measurements are conducted for a baseline reactor design and for an optimised design extending the operating limits of the system. The swirl generator as illustrated in figure 3.2 as well as the MX-structure is applied only for the optimised reactor design. The test conditions for the baseline and the optimised reactor type and are given in table 3.1. A UWS with 40 % urea is used and a constant pressurised air volume flow of 120 L min^{-1} . The initial aim was to minimise the catalyst structure complexity in order to reduce costs (in general the catalyst is the most expensive part of hydrolysis reactors). Hence,

the baseline hydrolysis reactor tests are performed with a ST structure catalyst of 250 mm length without MX structure. To optimise the catalyst performance a 50 mm MX structure was combined with the ST-structure. The mass flow rate of UWS depends on the desired reduction rate of the nitrogen oxides. The values given would be needed to provide the required ammonia concentration for a 100 % reduction (assuming a 100 % decomposition rate of urea in terms of UDR).

Test		OP1	OP2	OP3	OP4
Swirl generator	baseline	no	no	no	no
	optimised	yes	yes	yes	yes
Length ST [mm]	baseline	250	250	250	250
	optimised	200	200	200	200
Length MX [mm]	baseline	0	0	0	0
	optimised	50	50	50	50
Cell density [cpsi]		200	200	200	200
Main air mass flow [kg h^{-1}]		235	195	255	315
Main air temperature [$^{\circ}\text{C}$]		460	490	510	550
UWS mass flow [kg h^{-1}]	100 %	7.3	13.4	20.3	25.3

Table 3.1: Engine operating points.

Fundamental Test Conditions

For the baseline reactor design the components are the MAN nozzle, the evaporation section with 300 mm length and the catalyst with a cell density of 200 cpsi. The temperature of the main air flow is constant at 400°C and the pressurised air flow for atomisation is 100 L min^{-1} . In table 3.2 the conditions are listed. A reference case (RC) is specified to compare the results. Only small mass flow rates of the UWS are used to have the possibility of a direct measurement by the FTIR-spectroscope.

Measurements conducted for the optimised reactor design are listed in table 3.3. The temperature of the main air flow is 400°C for TC7 and 500°C for the other three cases. The UWS mixture with 40 % urea in water and the pres-

3.1 Hydrolysis Reactor Experiment

Test	RC	TC1	TC2	TC3	TC4	TC5	TC6
Length ST [mm]	100	100	100	100	100	200	150
Length MX [mm]	50	50	50	50	50	50	0
Cell density [cpsi]	200	200	200	200	200	200	200
Main air mass flow [kg h ⁻¹]	290	290	290	290	385	290	290
Temperature [°C]	400	400	400	400	400	400	400
Water vapour [%]	0	3	0	0	0	0	0
UWS [%]	40	40	37	30	40	40	40
UWS mass flow [kg h ⁻¹]	2.4	2.4	2.6	3.2	2.4	2.4	2.4

Table 3.2: Operating conditions for the baseline reactor type.

surised air flow of 100 L min⁻¹ are constant. Tests TC8–TC10 had to be measured via the dilution unit due to the high UWS to air mass flow ratios.

Test	TC7	TC8	TC9	TC10
Length ST [mm]	100	100	100	100
Length MX [mm]	50	50	50	50
Cell density [cpsi]	200	200	200	400
Mass flow ratio (UWS/Air) · 10 ⁻³	8.28	56.0	56.0	56.0
Temperature [°C]	400	500	500	500
Re	695	546	386	386
UWS mass flow [kg h ⁻¹]	2.4	14	9.9	14

Table 3.3: Operating conditions for the optimised reactor type.

3.1.4 Velocity Measurement Operating Conditions

The hydrolysis reactor setup is used for the velocity measurements. Adaptations of the setup used for velocity measurements compared to the setup used for concentration measurements are described in the following.

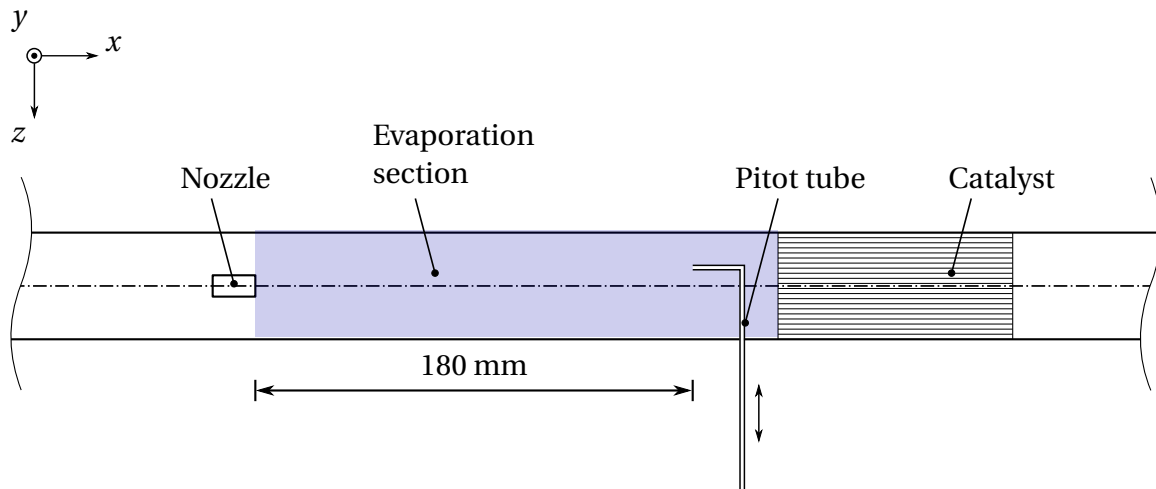


Figure 3.8: Hydrolysis reactor setup for Pitot tube measurements.

Pitot Tube (Gas Velocity)

Gas velocity measurements are conducted with a Pitot tube. The tube is mounted upstream of the catalyst to measure the gas velocity at different radial positions at a 180 mm distance from the injector. The assembly is shown schematically in the figure 3.8. The hydrolysis reactor setup is used for this setup and component dimensions are equal to the setup for the concentration measurements. Measurements are performed only for the baseline reactor design. During the measurements, the injector is supplied only with pressurised air (no liquid is added). Only two test conditions are listed in table 3.4, as they are relevant for the analysis and comparison with numerical results in chapter 5.

Test	PT1	PT2
Main air mass flow [kg h^{-1}]	290	290
Temperature [$^{\circ}\text{C}$]	400	400
Pessurised air volume flow [L min^{-1}]	0	100

Table 3.4: Pitot tube tests for gas velocity measurements.

PIV (Droplet Velocity)

The darker bluish coloured area in figure 3.3 marks the optically accessible region of the hydrolysis reactor setup with a length of 200 mm. In figure 3.9 the measurement sections are visualised. The laser beam is expanded via lenses, the camera detects a square section of 89×89 mm. The laser and the camera can be moved along the x-axis. Overlaps of the particular detection sections decreases measurements errors at the section. The measurement conditions are listed in table 3.5, tests are conducted with pure water instead of UWS.

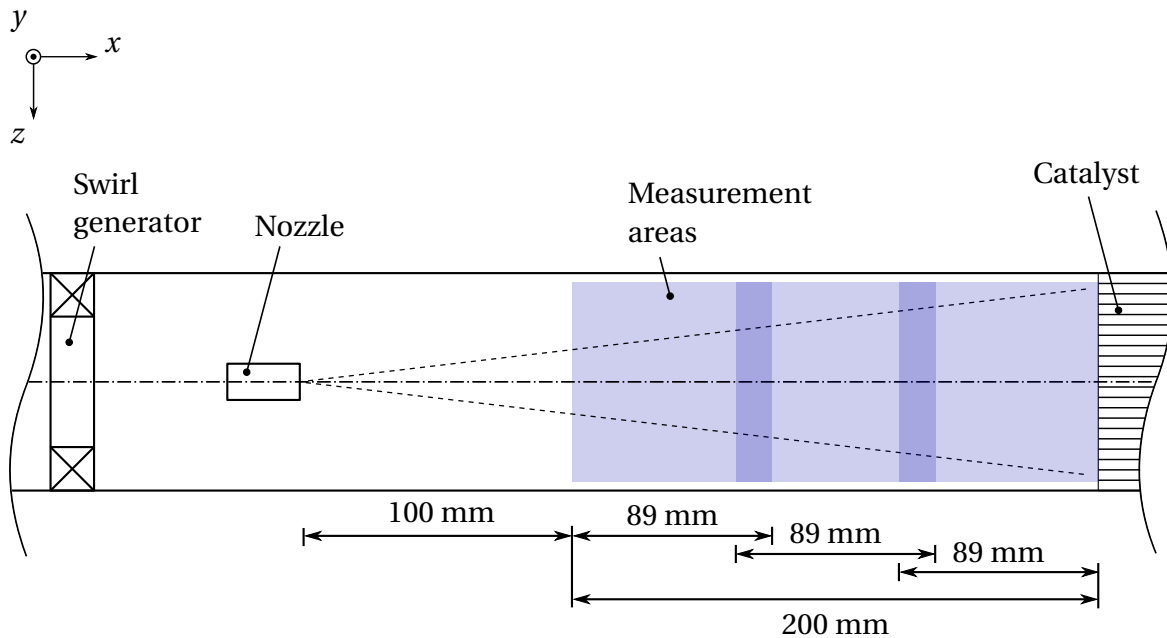


Figure 3.9: Hydrolysis reactor setup for PIV measurements.

Test	OT1	OT2	OT3	OT4	OT5	OT6
Main air massflow [kg h^{-1}]	290	290	290	290	290	290
Pessurised air volume flow [L min^{-1}]	100	100	100	100	100	100
Temperature [$^{\circ}\text{C}$]	300	350	400	300	350	400
Water mass flow [kg h^{-1}]	2.4	2.4	2.4	7.3	7.3	7.3

Table 3.5: Operating conditions for droplet velocity measurements.

3.2 Injector Test Rig

Atomisation performance of the injectors are studied at a separate setup. Three measurement methods are applied to characterise the spray quality. Spray cone angles are measured via shadowgraphy, droplet sizes with a LDS system and liquid mass distributions by a patternator. The injector setup is illustrated schematically in figure 3.10.

A pump (2) supplies water from an external tank (1) to the nozzle (6), the pressurised air (3) for the nozzle is controlled by a mass flow meter (4) and a pressure manometer (5). The shadowgraphy system is composed of a camera (7) and a LED screen (8), which illuminates the spray in a 70×70 mm section directly at the nozzle outlet. The LDS system (Malvern Insitec) detects the particle sizes at different distances from the nozzle. The patternator is positioned at a 300 mm distance from the nozzle. The liquid mass flow rates tested with the MAN and the Schlick nozzle are determined by the engine operating points (see table 3.1: values for 100 % reduction).

3.3 Fourier Transform Infrared Spectroscopy

Fourier Transform Infrared Spectroscopy (FTIR-Spectroscopy) is a measurement method to quantify species concentration within a sample. The principle relies on wavelength-dependent absorption of light passing through a medium composed of various molecules. The method is based on the Lambert-Beer law which describes the attenuation of light by molecules [61]. IR-Spectroscopy allows the simultaneous measurement of various gaseous species of one sample, due to the interaction of molecules with electromagnetic radiation. Energy is transferred from the radiation to the molecules, resulting in characteristic oscillations of the atoms. Molecules consisting of one element are not affected by electromagnetic radiation. Oscillations inducing changes in the dipole moment are IR-active. Accordingly, those atoms not connected to a dipole moment change are IR-inactive. Hence, species like nitrogen or hydrogen are not detected. Molecules consisting of different el-

3.3 Fourier Transform Infrared Spectroscopy

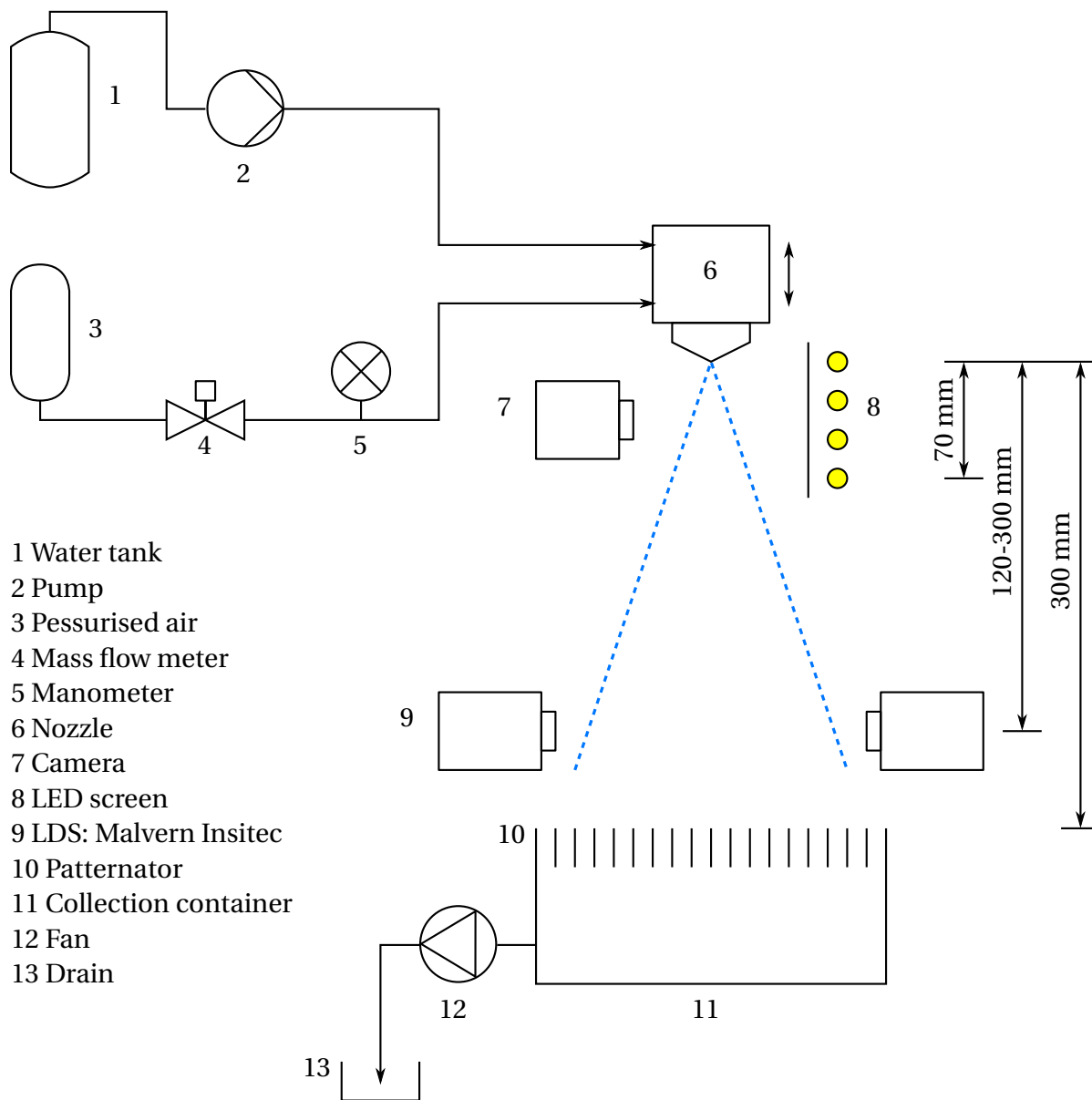


Figure 3.10: Injector setup with shadowgraphy system (7 and 8), LDS system (9) and patternator (10).

elements are identifiable by the spectroscope. Each molecule absorbs only specific spectral wavelengths. This is determined by the inner energy state of the molecule which depends on the atomic mass, the bond strength and the structure of the molecule. A sample mitigates a signal, depending on the containing gaseous species. A detector records the signal in form of intensities. The mea-

sured intensities are given as a function of the wavelength in the so called interferogram. Detailed information about IR-Spectroscopy is given in *Latscha et. al.* [61] or *Otto* [75].

The FTIR-spectroscope has to be calibrated to each desired species by the measurement of each pure element at different concentration levels (i. e. calibration process). The calibration process has to consider primarily relevant species expected from the decomposition process of urea. These are ammonia, carbon-dioxide, isocyanic acid and water as well as possible by-products such as nitrous oxide.

In general, the calibration range of all elements is based on the estimated occurrence. Nevertheless, these ranges have limits due to undesired side reactions. Ammonia in combination with water seeks to be aggressive to the mirrors of the spectrometer cell. A damage of the cell can be avoided by limiting the ammonia concentrations to 3000 ppm. Here, the theoretical concentrations occurring for the engine operating points are 4-6 times higher than 3000 ppm. Hence the whole concentration spectrum cannot be measured directly and a dilution is necessary. The dilution unit applied is an evacuated and heated gas bottle with a manometer. The gas extracted from the channel is fed into the evacuated gas bottle and subsequently mixed with nitrogen in a mass ratio of 1 to 10. Validation tests with the dilution unit have shown a slight decrease in isocyanic acid concentrations due to the further decomposition while resting in the heated gas bottle. The total error concerning the dilution process is in a range of 5 %.

3.4 Velocity Measurement Methods

Velocities arising from the two-phase flow in the hydrolysis reactor are measured by two methods. Gas flow measurements are conducted via a Pitot tube and PIV is used to identify the droplet velocities. A velocity measurement of the gas flow by adding tracers to the gas flow is not performed.

Particle Image Velocimetry (PIV) is an optical measurement method to visu-

alise planar or three dimensional velocity fields. A laser is used to illuminate particles twice in a defined time interval which are recorded by a high-speed camera. The instantaneous velocity is calculated by the time interval between two laser pulses and the path of the particles traveled during the time interval [79].

3.5 Spray Measurement Methods

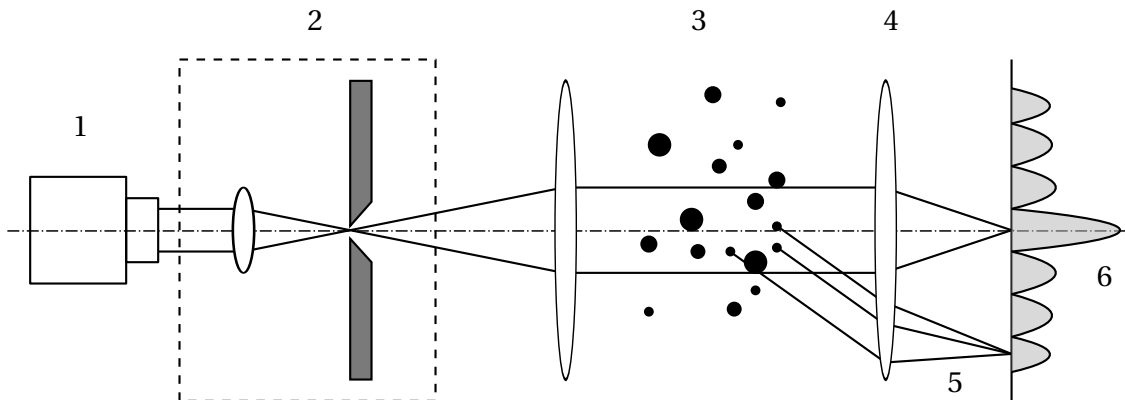
Laser Diffraction Spectrometry (LDS) is used for the quantification of droplet sizes, the spray cone angle is detected by shadowgraphy and the liquid mass distribution by a patternator.

3.5.1 Laser Diffraction Spectrometry (LDS)

Laser Diffraction Spectrometry allows the quantification of droplet sizes and droplet size distributions of the entire spray. Information about the spatial position of droplets within the spray are not available since the measurement is line-of-sight integrated. A statement about the quality of the atomisation is possible. Hence, a comparison with the droplet size calculated from the correlations (see chapter 2.3.2) is possible. The measurement technique is illustrated schematically in figure 3.11 (for further information about the technique please refer to [97]). Results are plotted as volume density functions in a logarithmic histogram and characteristic droplet diameters (e. g. SMD or D_{V50}) are calculated.

3.5.2 Shadowgraphy and Patternator Measurements

The shadowgraphy and patternator measurement methods provide information on spray angle and mass distribution. For the shadowgraphy the spray is illuminated homogeneously, the light is scattered by the droplets and spray regions appear darker. The spray cone angle is measured graphically from the shadowgraphy images.



- 1 Laser
- 2 Expansion optic
- 3 Droplet collective
- 4 Fourier lens
- 5 Stray light
- 6 Diffraction pattern

Figure 3.11: Laser Diffraction Spectrometry [97].

The so-called patternator is a simple quantitative method to analyse the mass flux distribution of the atomiser. Droplets are collected by small containers which are arranged in circles around the atomiser symmetry axis. The samples collected in each container are weighed after each spray test.

4 Numerical Modelling

In this chapter numerical simulations with Ansys Fluent 15.0 are introduced. Necessary information about the grid and boundary conditions are provided. The liquid phase and its implementation is discussed in a separate section.

4.1 Numerical Domains

In this thesis, Ansys Fluent 15.0 is used. The program code uses the Finite Volume Method for discretisation. The RANS method makes use of the Boussinesq hypothesis as a basis for the $k - \epsilon$ or $k - \omega$ models, or the Reynolds-stress model (RSM). Here, the $k - \epsilon$ model is applied.

A pressure-based steady-state RANS simulation with the $k - \epsilon$ model with standard wall function is performed. Several simulations with different inlet boundary conditions representing engine operating points or fundamental research conditions are conducted. Non-reacting flow is assumed.

Two separate 3D domains are considered, the swirl generator domain and the hydrolysis reactor domain. For the reactor domain a 60° wedge of a cylinder with periodic boundary conditions is chosen to balance the calculation effort with cell sizes and potentially poor aspect ratios at the tip of the wedge. The swirl generator domain geometry is a whole cylinder. A 60° wedge could not be set up with periodic boundary conditions as the swirl generator has eight vanes. The swirl generator domain is necessary for calculations of the optimised reactor. Initially, it was attempted to simulate the influence of the swirl generator only with a tangential velocity vector at the main air inlet of the reactor domain. Results obtained had not been plausible since three-dimensional flow structures are neglected. Hence, a simulation of the swirl generator was implemented in a separate domain.

The positioning of the two domains is displayed in figure 4.1. The blue coloured wedge of a cylinder is the hydrolysis reactor domain and the red coloured cylinder is the swirl generator domain. The body of the nozzle is neither included in the swirl generator domain nor in the hydrolysis reactor domain.

4.1.1 Hydrolysis Reactor Domain

The numerical domain of the reactor represents the evaporation section of the hydrolysis reactor. The geometry consists of one fluid domain with the specified surface regions displayed in figure 4.2. The grid is unstructured with refinement at the inlet of pressurised air and liquid. It has a size of about 0.8 million tetrahedral cells. An unstructured grid is chosen as the structured grid leads to singularities at the tip, even if an O-Grid is used for the tip. Additionally, the structured grid leads to poor aspect ratios due to the large difference of scales between the liquid and pressurised air inlets and the entire domain size.

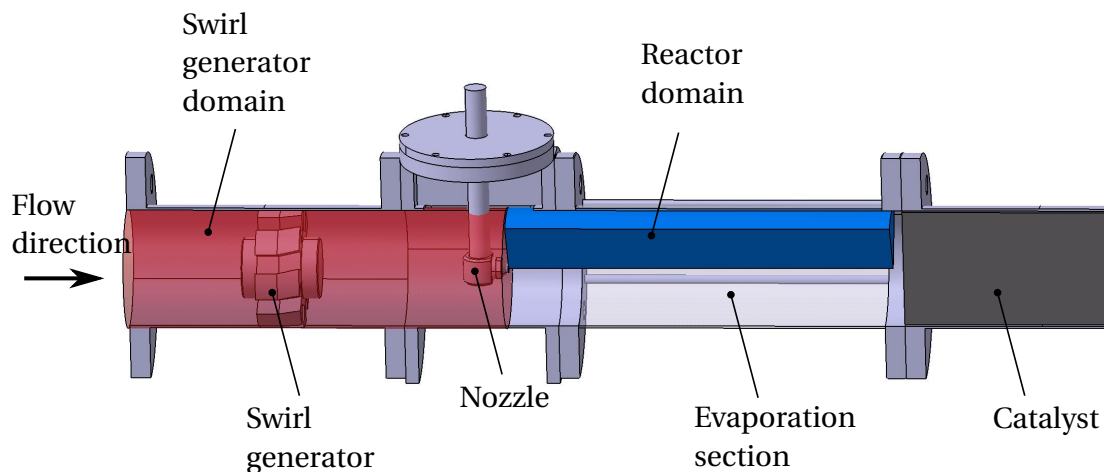


Figure 4.1: Numerical domains for the swirl generator and the reactor.

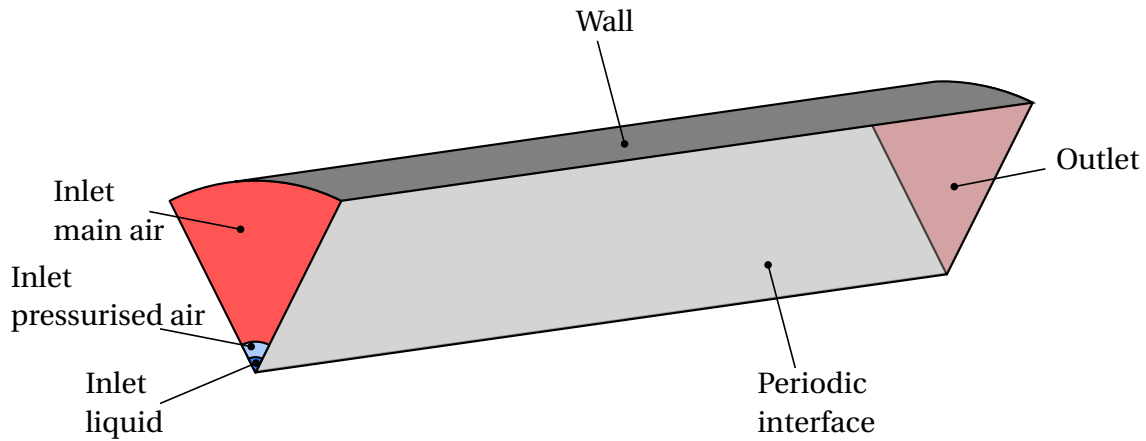


Figure 4.2: Hydrolysis reactor domain.

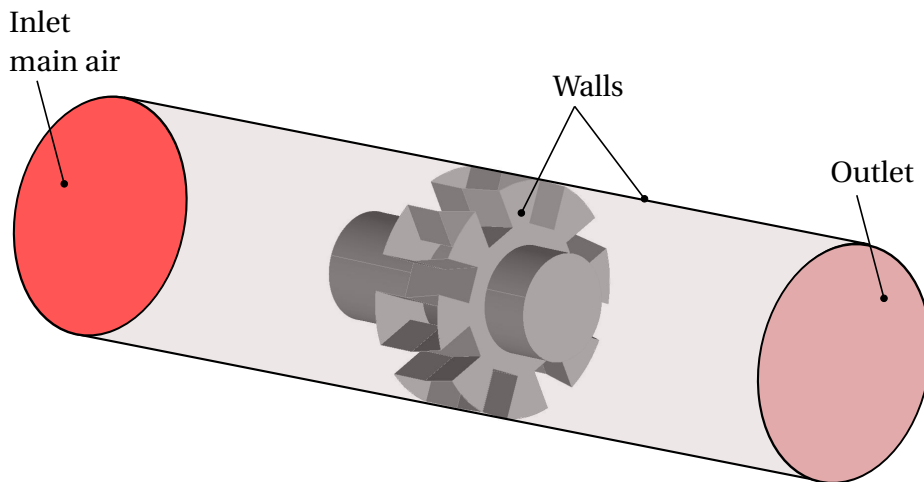


Figure 4.3: Swirl generator domain.

4.1.2 Swirl Generator Domain

An independent second domain is used to simulate the swirl generator. In this numerical domain the geometry of a whole cylinder including the swirl generator is modelled. The grid is unstructured with about 1.8 million tetrahedral cells. Refinements are located at the inlet, outlet and the swirl generator wall. Cell sizes at the outlet are adjusted to the cell sizes of the main air inlet of the reactor domain. Refinements at walls of the swirl generator are added for better resolution of the boundary layer.

4.2 General Settings and Boundary Conditions

Inlet boundary conditions are specified as velocity inlets for both domains. For the main air inlet (both for the reactor domain and the swirl generator domain), the inlet velocity results from the mass flow rate of exhaust gas at each operating point. Chemical reactions are not considered, hence the exhaust gas is simulated as pure air like in the experiments. For the simulation of the optimised cases including the swirl generator the two domains are coupled with each other. Properties from the swirl generator outlet plane (velocity, pressure) are imposed as inlet conditions for the reactor domain. For the liquid and pressurised air inlet conditions an initial velocity equal to the axial velocity of the analytical jet model is used. This jet velocity is calculated with the aid of the momentum equation incorporating liquid and pressurised air mass flow rates in relation to the nozzle geometry (see equation 2.45). Each particular outlet is defined as (in Ansys so-called) outlet-vent and the outer walls have a no slip condition in both cases. To incorporate the pressure drop across the catalyst subsequent to the evaporation section the atmospheric pressure plus the measured pressure drop is used as boundary condition at the outlet of the reactor domain. An uncoupled setting, without discrete phase, of the reactor domain is calculated for each operating condition. It is used as solution initialisation for the coupled setup including the discrete phase.

4.3 Droplet Injection Boundary Conditions

In the following discrete phase modelling is explained in brief (for further information please refer to [3]). Discrete phase modelling covers parts of the numerical modelling of multiphase flows. Discrete phase modelling is used, if the second considered phase (e. g. particles, droplets or bubbles) has a low share with at most 10 % of the total fluid volume [4]. The Lagrange approach is used for the discrete phase. Sprays are covered by discrete phase modelling, as the share of the second phase is normally smaller than the mentioned 10 %. The continuous phase is solved by the Navier-Stokes equations, while for the Lagrangian phase a high number of droplets is traced through the cal-

culated flow field. Momentum, mass and energy between the two phases is exchanged. The interaction between particles or droplets, breakup mechanisms and coalescence effects are specified [3].

Droplets as discrete phase can either be generated numerically with an atomiser option provided by the software or as specific injections. Atomiser setting includes the description of primary breakup phenomena, which rely on empirical atomisation models. These models only use atomiser geometry parameters, such as orifice diameter and the liquid mass flow rate [3]. There is no specific information about droplet sizes or droplet velocities needed. Calculations of the breakup phenomena are highly complex and require the prediction of internal nozzle flow and external atomisation [3]. The internal flow determines e. g. the velocity at the orifice or initial droplet size and spray angle. Boundary conditions to define the internal flow are for example the nozzle diameter and length, radius of the curvature or the internal vapour pressure. For an air-blast atomiser model even more boundary conditions for the internal nozzle flow are required such as the sheet thickness of the liquid film [3]. Droplet size distributions provided by the atomiser models are restricted to the Rosin-Rammler distribution [3]. The second option to describe a discrete phase is the definition of specific injections. In this case information about droplet sizes, velocities and volume fractions are necessary for a realistic description of the discrete phase. Injections can be integrated as single injection or as group injection. An integration as single injection has a higher flexibility in parameter specification, but all spray information mentioned has to be known. Group injections are rather restricted as the distribution of droplet sizes are fixed, e. g. by the Rosin-Rammler distribution option [3]. Settings applied in this thesis are discussed in the following.

In this thesis, initially some simulations were conducted with the air-blast atomiser setting. However, these simulations resulted in an inaccurate droplet size distribution and cone angle compared to measurement results. The measurements results for both injectors (see chapter 5.1.3) show a bimodal droplet size distribution. The air-blast atomiser model only provides monomodal Rosin-Rammler distributions [3]. For this reason in further simulations single injections were used as spray measurements conducted for the injectors

provide all required information. The injections are generated by a separate MATLAB script (see A.4). This script creates a group of injections randomly distributed but restricted by the measured spray characterisation parameters. The specified discrete phase model interacts with the continuous phase and has a two-way turbulence coupling with no further breakup nor stochastic collision. Water is utilised as the droplet substance.

The input parameters for the MATLAB script are the liquid mass flow rate, characteristic droplet size ranges and their volume fraction, the number of droplets to be generated as well as the initial velocity magnitude of the generated droplets. The script calculates the droplet sizes for the desired number of droplets from the defined droplet size ranges and the volume fractions. The volume fraction is based on the droplet size distribution measurements of the Schlick 940 and MAN nozzle. Here, a bimodal droplet size distribution is found for the nozzles (see section 5.1.3). The measured droplet distribution is separated into several segments and each is adapted by a Rosin-Rammler distribution [4]:

$$Y_d = \exp\left(-\left(\frac{d}{\bar{d}}\right)^n\right), \quad (4.1)$$

where Y_d is the mass fraction of droplets, d the droplet diameter, \bar{d} the mean droplet diameter and n the spread parameter. The sum of all Rosin-Rammler distributions result in the final droplet size distribution. The initial velocity magnitude is a constant for all generated droplets, while every droplet has a different initial velocity vector. The velocity magnitude of each droplet is equal to the initial carrier gas flow velocity, as for its calculation the two phases of the jet are already incorporated and represent the initial jet velocity of the mixture (see equation 2.45). The vector components are calculated from the assumed Gaussian mass distribution at the catalyst. The standard deviation σ is an input variable.

$$f(r) = \frac{1}{\sigma\sqrt{2\pi}} \exp\left(-\frac{1}{2}\left(\frac{r}{\sigma}\right)^2\right). \quad (4.2)$$

4.3 Droplet Injection Boundary Conditions

First, from the Gaussian distribution with a specified standard deviation the liquid volume distribution is identified by the script. Second, the number of droplets needed in specific sizes to represent the volume distribution is calculated. Finally, the velocity vector for each droplet to reach the specified point at the catalyst without accounting for the coflow is calculated.

5 Baseline Reactor Performance

This chapter describes the results of the experiments as well as the analytical and the numerical modelling for a baseline hydrolysis reactor. First, measurement results of the hydrolysis reactor test rig and the injector test rig including concentration, velocity and spray characterisation measurements are presented. All test conditions are summarised in appendix A.5.1 (concentration measurements in table A.2 and Pitot, PIV, injector tests and simulations in table A.3) to help maintaining overview of various conditions for the discussion in the following. Thereafter, suitable analytical methods to calculate the reactor performance are introduced. A comparison of analytical models and experimental results follows in a separate section. In the end, results of numerical simulations are compared with experiments as well as with the analytical jet model. This section is the basis for the numerical investigations of the optimised reactor development in chapter 6.

5.1 Experiments

In this section, the results of the ammonia concentration measurements are presented followed by the results for the gas and droplet velocity measurements. Furthermore, droplet size distributions, spray cone angles and liquid mass distributions for the injectors are shown.

5.1.1 Concentration Measurements

Tests Representing Engine Operating Points

The particular test conditions are presented in table 3.1. Some calculated and

measured parameters are shown in the following table 5.1. The ratio of UWS mass flow to main air mass flow is computed in order to specify the liquid loading in the system. The GHSV (see equation 2.15) and the bulk temperature (see equations 2.13 and 2.14) from the basic evaluation are listed. In addition, the temperature measured in the centre of the front surface of the catalyst and the urea decomposition rate is given.

The results shown verify the anticipated effect of cooling due to evaporation (see chapter 2.2). The calculated bulk temperatures for each operating point differ significant from the measured temperatures at the front surface of the catalyst. Operating point OP1 is the only measurable case for ammonia concentrations as urea decomposition is achieved (see urea decomposition rate (UDR) in table 5.1). In all other cases, the temperature falls below the critical level and solid by-products are created (see figure 5.1). During the process of by-product formation the initial formation of solid products is located in the centre of the catalyst and spreads over time in radial direction. At the external radial surface area of the catalyst no formation occurs. Even the measured temperatures show nearly no change compared with the initial main air temperature. This indicates less liquid mass in the outer region of the catalyst. Homogenization of the liquid mass distribution is the obvious solution to this problem.

Fundamental Test Cases

The aim of the fundamental experiments is to specify the influence of several parameters on the system. Therefore, only one inlet condition with re-

Test		OP1	OP2	OP3	OP4
GHSV · 10 ³ [h ⁻¹]		93.7	87.5	116.9	143.9
Temperature front surface [°C]	calculated	386	328	323	361
($r/R = 0$)	measured	250	169	–	–
Mean UDR		0.74	–	–	–

Table 5.1: Results of tests representing engine operating points.



Figure 5.1: Solid by-products created at the catalyst during operating point OP2. Left: at the rear surface of the catalyst; Right: at the front surface of the ST structure.

spect to the reference case (RC) is changed per test case, with the exception of TC2 and TC3 with two simultaneous parameter changes. The aim of test cases TC1 to TC3 is to quantify the influence of water on the decomposition process since the hydrolysis only proceeds efficiently if enough water is available. TC4 to TC6 aim to identify the influence of the GHSV, as this value is a common characterisation parameter for catalytic reactions. Results of tests TC1 to TC3 are listed in table 5.2 and TC4 to TC6 in table 5.3. In both tables RC is the reference case. Efficiency values (see 2.2.3) provide no clear separation between thermolysis and hydrolysis, but they give an indication of the impact of each parameter to the process steps. The urea decomposition rate (UDR) provides an efficiency characterisation of the whole decomposition process and the hydrolysis efficiency level (HEL) of the hydrolysis process itself. Hence, for changes of the UDR with a constant HEL the thermolysis process has to cause the difference.

Additional water can either be injected with the UWS-spray which means a smaller concentration of urea in water, or as water vapour with the main air mass flow. The latter option is analysed with TC1, in which the water vapour

Test	RC	TC1	TC2	TC3
GHSV · 10 ³ [h ⁻¹]	178.6	178.6	178.9	180.1
Mean UDR	0.73	0.76	0.83	0.61
Mean HEL	0.93	0.98	0.94	0.91

Table 5.2: Results of fundamental test cases RC and TC1–TC3.

concentration of the hot air flow is increased. For the cases TC2 and TC3, UWS with lower urea concentrations is injected. Two different urea concentrations are tested, case TC3 with 30 % urea and case TC2 with 37 %. The total mass flow rate of urea is kept constant by reducing the share of urea but increasing the liquid mass flow rate. Hence, equivalent concentrations of ammonia downstream the catalyst are potentially available for RC, TC2 and TC3. The overall water content of TC2 is equal to TC1. Radial profiles of UDR and HEL for test cases TC1–TC3 in comparison with RC are depicted in figure 5.2 and 5.3.

The increase of water due to higher vapour level (TC1) shows an increase of 3 % in the mean UDR and of 5 % in the mean HEL in comparison with RC. The HEL of 98 % for TC1 indicates that the hydrolysis process of the formed HNCO is almost complete. The higher UDR for TC1 compared with RC suggests a more efficient thermolysis process. For the hydrolysis process and its efficiency a higher humidity in the gas flow is beneficial since the reaction of HNCO with water increases which is due to their diffusion velocities (see section 5.2.2). The increase of decomposed urea during the thermolysis has to be interpreted carefully. One aspect is the decreasing concentration gradient between droplet and main air flow followed by a faster saturation of water in air. Another aspect is that vapour pressure increases with higher humidity of air. Both aspects would lead to a slower evaporation of the UWS. Investigations of the influence of vapour content on evaporation processes for hygroscopic substances revealed faster evaporation for higher vapour contents [100]. In its solid form urea is a hygroscopic substance. Assuming that the urea concentration increases at the surface of droplet (see [37]), a higher humidity of air can improve evaporation. Hence, this can provide a potential explanation for the

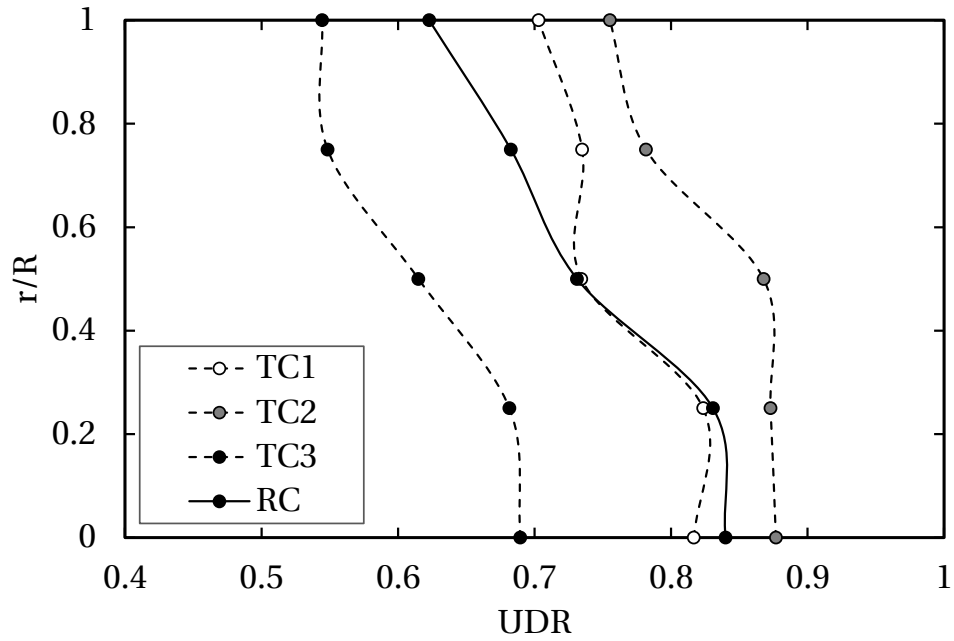


Figure 5.2: Comparison of the urea decomposition rate (UDR) for TC1–TC3 and RC.

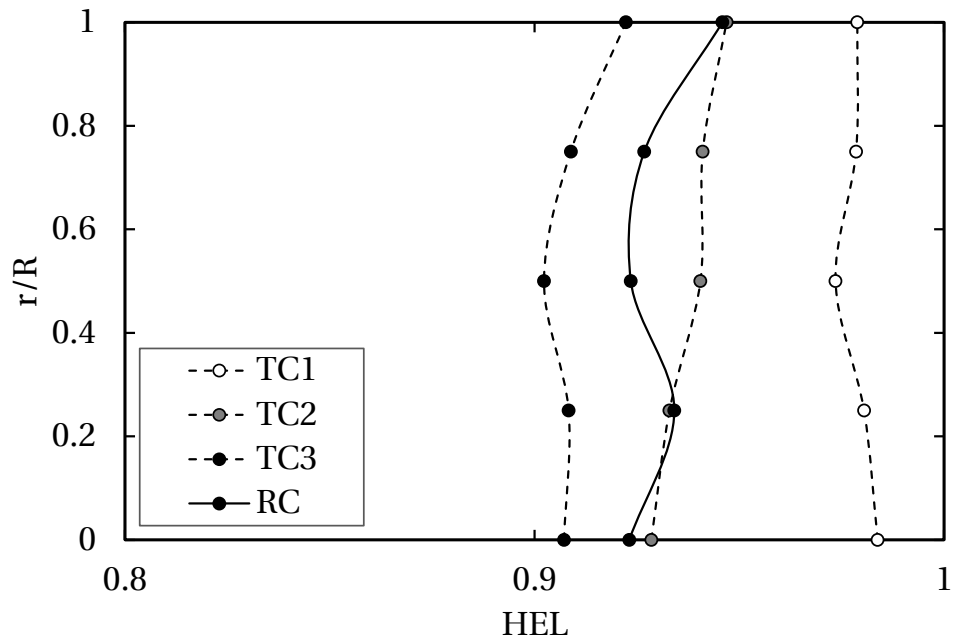


Figure 5.3: Comparison of the hydrolysis efficiency level (HEL) TC1–TC3 and RC.

higher UDR value. Case TC2 shows an increase of the decomposition (UDR) compared with RC, while TC3 with the 30 % UWS results in a decrease of the decomposition rate. The mean HEL remains nearly constant for TC2 and decreases for TC3 compared with RC. The decrease of the UDR and HEL for TC3 can be explained by the energetic considerations of the decomposition process. The consumption of energy for the evaporation is higher for a higher water content in the UWS. So it is obvious that the decomposition process of urea starts later if inlet conditions (mainly bulk temperature of the main air flow) remain constant. Contrary to this explanation the efficiency values for TC2 increase. The vapour pressure decreases with the share of urea in water compared with pure water (see figure 2.7). Hence, the higher the urea concentration, the slower the evaporation proceeds. The reduction of the urea ratio by 3 % for TC2 compared with RC compensates the higher energy consumption and leads to a higher efficiency. With TC2 (37 % urea in water) an optimum between energy consumption and droplet evaporation seems to be found. A further decrease of urea concentration for TC3 does not compensate the higher energy consumption for water evaporation. To summarise, an indication of a lack of water is found, when using a 40 % UWS. A 3 % increase of water content (TC1 and TC2) increases the efficiency values. An increase of water content in the UWS reveals a better performance. A further augmentation of the water share in the UWS is disadvantageous as the energy consumption for the evaporation process increases.

Figures 5.4 and 5.5 show radial profiles of UDR and HEL for tests with different GHSV values. Different GHSV values can be reached by changing the gas volume flow or of the catalyst volume. The change of the GHSV in TC4 is generated by the first method, whereas TC5 involved a variation of the catalyst length by 100 mm. TC6 identifies the influence of the catalyst structure (removing the MX structure and extending the ST structure by 50 mm to maintain the catalyst length of RC) on the decomposition process, while having the same GHSV as RC. This case is of special interest in comparison to the concentration measurements performed for the engine operating points, as these are performed without MX structure for the baseline reactor type.

The GHSV is increased by about 30 % for TC4. The UDR decreases signifi-

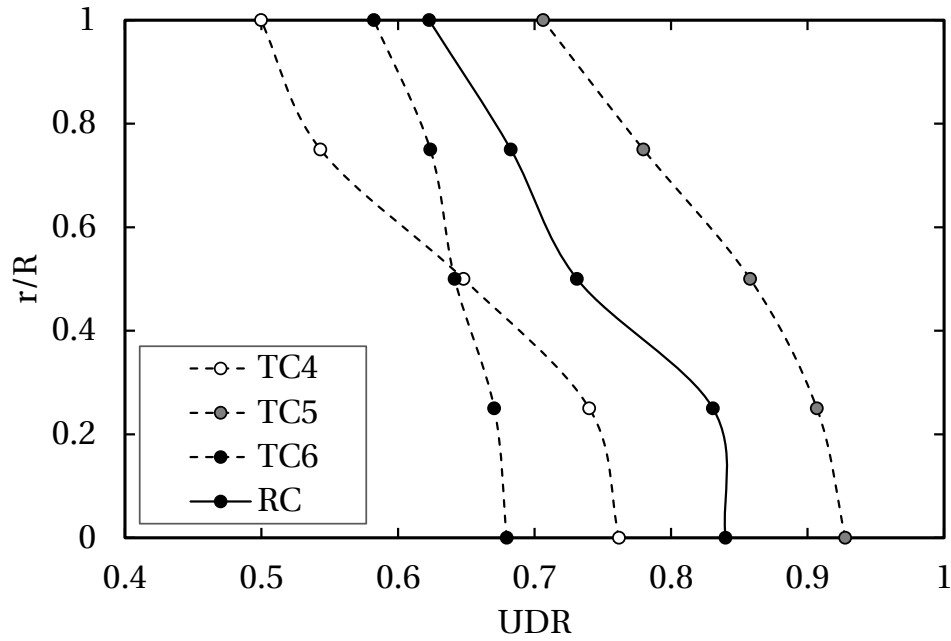


Figure 5.4: Comparison of the urea decomposition rate (UDR) for TC4–TC6 and RC.

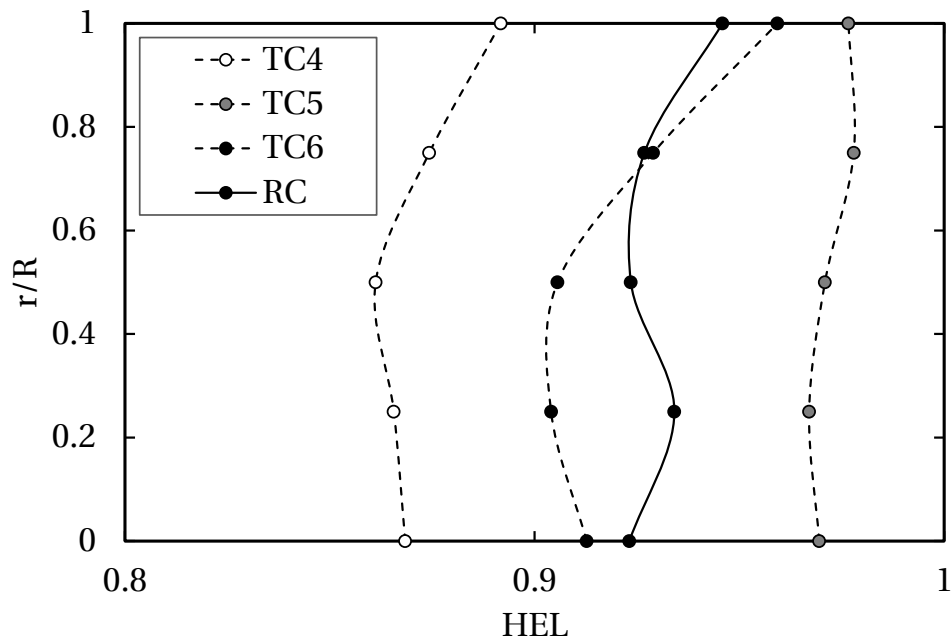


Figure 5.5: Comparison of the hydrolysis efficiency level (HEL) for TC4–TC6 and RC.

Test	RC	TC4	TC5	TC6
GHSV · 10 ³ [h ⁻¹]	178.6	234.1	107.1	178.6
Mean UDR	0.73	0.62	0.83	0.64
Mean HEL	0.93	0.87	0.97	0.92

Table 5.3: Results of fundamental test cases RC and TC4–TC6.

cantly, same as the HEL. The diffusion process of the gaseous substances depends on the gas velocity. The higher the velocity the shorter the residence time of gaseous substances within the catalyst. Hence, the diffusion process has to proceed within a shorter period. This leads to the decrease of the HEL value. Additionally, the hydrolysis process will start later because the penetration depth of the droplets into the catalyst will increase due to higher velocity. This circumstance affects the thermolysis as well. The relative velocity between droplets and gas phase decreases, thus the time available for droplet evaporation increases. Comparing RC and TC5, gas volume flows are equal, only the catalyst length is varied. An increase by about 4 % of the mean HEL and 10 % of the mean UDR for TC5 compared with RC is detected. TC5 itself has the lowest GHSV, the highest UDR and HEL for this series of tests. An increase in catalyst length is beneficial for evaporation and the diffusion processes as it provides more residence time. Finally, comparing TC6 with RC, TC6 has the same GHSV (same catalyst length and same gas volume flow) as RC, but no MX structure. The hydrolysis efficiency is nearly equal to RC and the UDR is about 10 % lower. Beneficial effects of the turbulence generating MX structure in the RC for the evaporation are illustrated by the decrease of UDR. Regarding the measurements of engine operating points, the MX structure would have increased the UDR of OP1, but it would not have avoided the composition of the solid by-products for OP2–OP4.

The presented analysis demonstrates that parameter variations affect the thermolysis to a larger extent than the hydrolysis. In general, HEL results of all tests show higher values and smaller variations compared with the UDR values. It can be stated that, once urea is evaporated, the hydrolysis process proceeds well. This is rather obvious, as solid by-products are mainly produced

from liquid urea or trimers of H₂NCO (e. g. cyanuric acid or melamine) during thermolysis [30]. The UDR profiles in figure 5.2 and 5.4 illustrate the inhomogeneous liquid mass distribution: higher amount of ammonia is always detected in the centre of the catalyst than on the outside. By contrast, the HEL (figure 5.3 and 5.5) increases in most cases with increasing distance from the centre. The penetration distance of the droplets is higher in the centre because of their higher velocities, hence the hydrolysis process has to proceed within a shorter time and the HEL decreases. Influencing parameters revealed in these investigations are the water content of the UWS and the velocity of the main gas. GHSV values have a minor impact. This is confirmed by comparing the fundamental measurements to the ones for the engine operating points. The GHSV level for all operating points is significantly lower than for RC and TC1–TC6 (except TC5). But, considering the results of OP2, it can be seen that the GHSV has no relevance for the functionality of the system. However, the GHSV can be used as an additional indicator for reactor performance incorporating the evaporation process (see TC4 and TC5).

5.1.2 Velocity Measurements

Two types of velocity measurements were conducted at the hydrolysis reactor test rig: the gas velocity measurements (Pitot tube) and the droplet velocity measurements (PIV measurements). These measurements are used for validation of the analytical model and the numerical calculations.

In the following measurement results are shown at different axial cross sections (CS), with defined distances to the nozzle (figure 5.6). Cross section zero (CS0) refers to the nozzle outlet. Further downstream, the first cross section CS1 is located at $x = 120$ mm to the nozzle, CS2 at $x = 180$ mm, CS3 at $x = 240$ mm and CS4 at $x = 300$ mm. One additional cross section is used for the droplet sizes tests, at a distance of $x = 200$ mm to the nozzle (named CS2/3, not shown in figure 5.6).

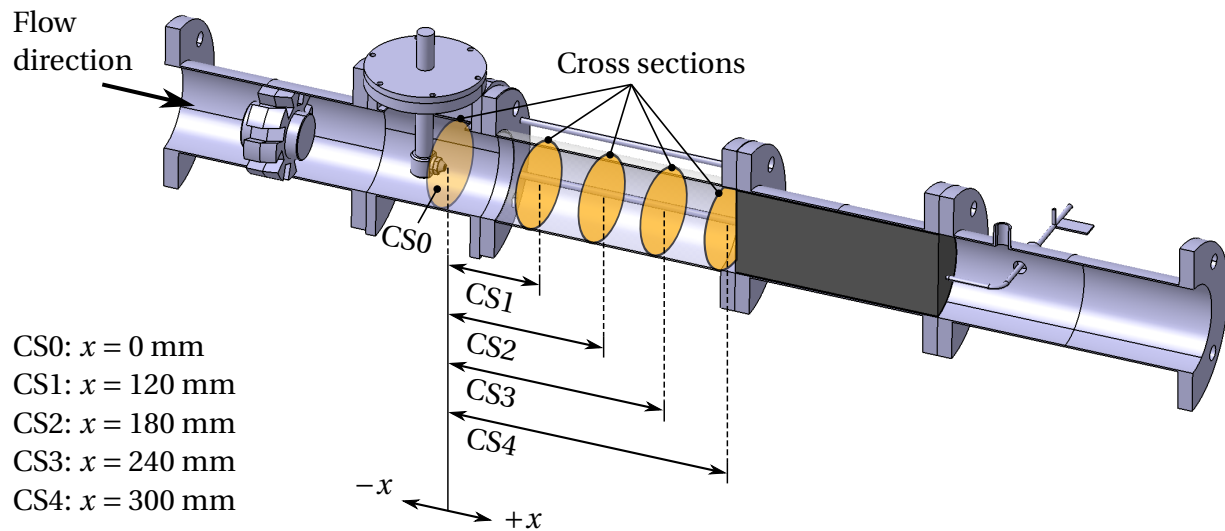


Figure 5.6: Axial cross sections (CS) with distances to the nozzle.

Gas Velocity Measurements and RANS Simulation of the Air Flow

Pitot tube measurements are conducted to determine the gas velocities resulting from the main air flow in combination with the pressurised air through the nozzle. Case PT1 represents the plain pipe flow without compressed air flow from the nozzle. A pressurised air volume flow of 100 L min^{-1} is used for PT2. In figure 5.7 the velocities measured at CS2 are plotted. The values in both cases represent averaged velocities for each radial position. The mean value is obtained from 7 tests. As expected, a fully developed turbulent velocity profile is found for PT1. The velocity near the wall ($r/R \approx 0.95$) is about 22 % smaller than in the centre ($r/R = 0$). For PT2 the injected pressurised air jet leads to a velocity peak on the jet axis. At $r/R \approx 0.95$ the velocity for PT2 is about 22.5 % smaller than the one measured for PT1. Hence, the velocity is smaller at the same position ($r/R \approx 0.95$) if a jet is injected. This effect is the result of the confinement of the jet due to the tube wall. To satisfy the conservation of mass material is entrained into the jet from the outside of the jet. For confined jets, this leads to either a reduction of coflow velocity, or flow reversal, if no coflow is present [46, 74].

In order to verify this velocity decrease and the pressurised air inlet conditions for the numerical model, simulations of the gas flow are conducted. The

Test	Main Air Velocity [m s ⁻¹]	Temperature [°C]	Pessurised Air Velocity [m s ⁻¹]	Wall Slip
PT1 Sim	16.4	400	0	no slip
PT2 Sim	16.4	400	170	no slip

Table 5.4: Boundary conditions for numerical simulations of the pipe flow with and without gaseous jet.

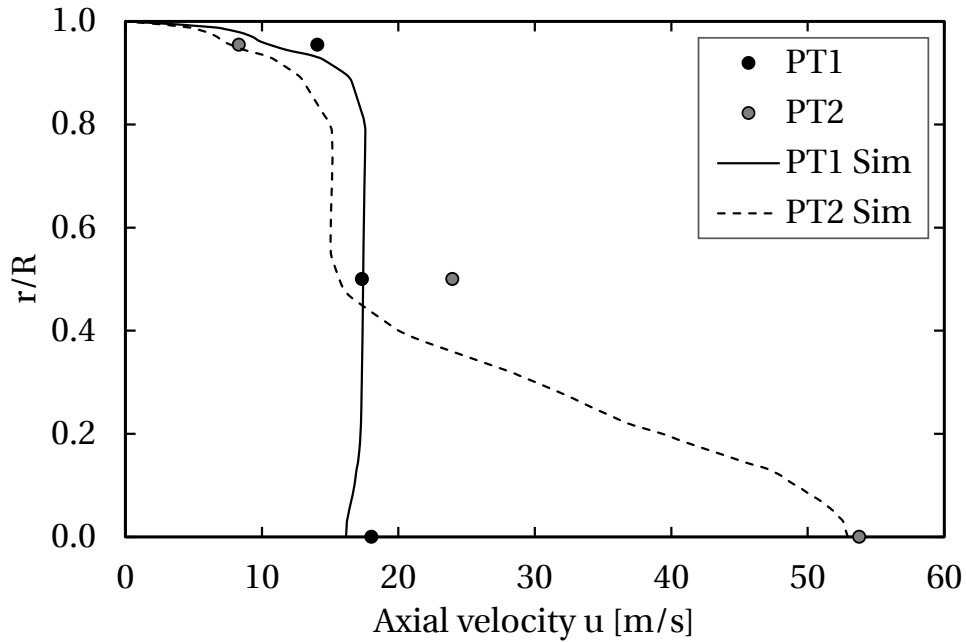


Figure 5.7: Axial velocities measured for PT1 (black circles) and PT2 (grey circles), in comparison with numerical simulations.

boundary conditions are listed in table 5.4. PT1 Sim represents the plain pipe flow and PT2 Sim incorporates the jet, equal to the conditions of PT2. The inlet velocity of the pressurised air is calculated from the volume flow through the nozzle. Results are included in figure 5.7.

In general the measurement results and the simulation show a reasonable agreement. At $r/R = 0.5$ the measurement result of PT2 and the simulation PT2 Sim reveals a difference. Here, the velocity detected by the pitot tube is higher than the velocity calculated by the numerical model. It is suspected that in reality the nozzle geometry induces a three dimensional velocity profile in contrast to the inlet velocity boundary condition for the numerical simulation. Hence, the velocity magnitude is equal, but the interaction of coflow and jet at the shear layer differs and leads to a wider velocity profile in reality. Overall, the calculated velocity for the nozzle is appropriate as an inlet condition for the numerical simulations as well as for the analytical jet model (see section 5.2).

Droplet Velocity Measurements

PIV investigations are used to verify the analytical jet model in the next section (5.2). Camera and laser pulse settings are based on estimated velocities in the detection section. The delay between correlated pulses (Δt) from the PIV laser was set such that droplets travel about 10 px between the pulses, which leads to a PIV interrogation area size on the order of 16 px. The pitot tube measurements with pressurised air injection provide guidance for a velocity estimation. An average velocity of 60 m s^{-1} for the jet in the detection area is assumed incorporating an estimated velocity decrease until the jet reaches the cross section of the pitot tube tip (CS2: 180 mm). Hence, the time delay Δt for the experiments is chosen to be $15 \mu\text{m}$.

The main air mass flow (290 kg h^{-1}) and pressurised air volume flow (100 L min^{-1}) are constant in all tests, the liquid mass flow rate is varied between 2.4 kg h^{-1} and 7.3 kg h^{-1} and the temperature is varied between 300 and 400°C in three steps as listed in table 3.5.

The axial velocity profiles of the six tests (listed in table 3.5) are plotted in fig-

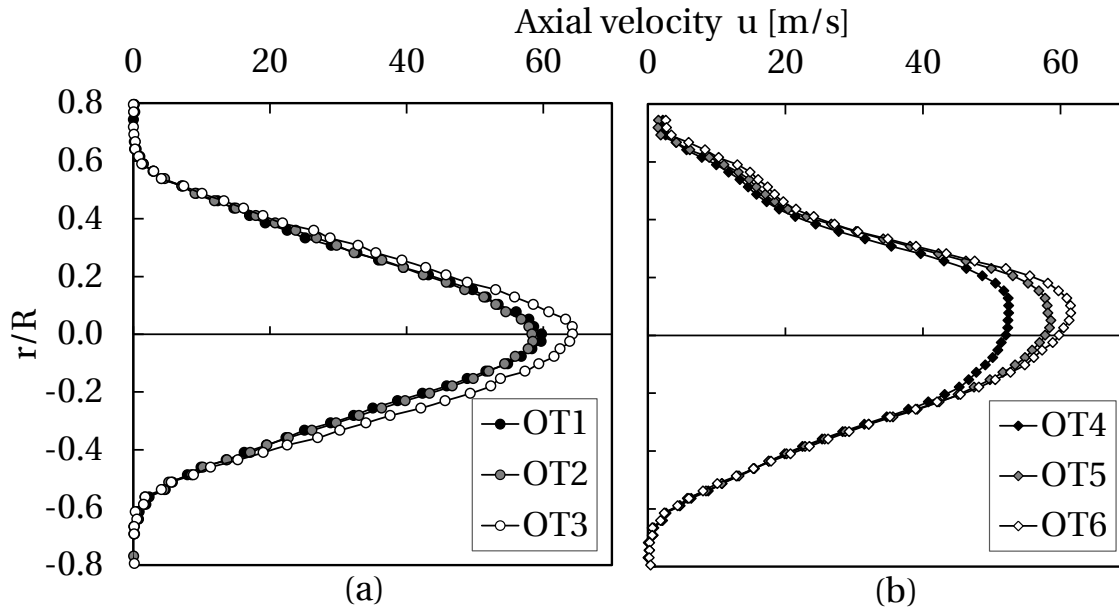


Figure 5.8: Axial droplet velocity at CS1: (a) for a liquid mass flow rate of 2.4 kg h^{-1} and (b) for a liquid mass flow rate of 7.3 kg h^{-1} for three temperatures (black: 300°C , grey: 350°C , white: 400°C).

Figure 5.8 at a 120 mm distance from the nozzle (CS1). Tests with 2.4 kg h^{-1} (figure 5.8 (a)) reveal higher peak velocities than those with 7.3 kg h^{-1} (figure 5.8 (b)) liquid mass flow rate. The available kinetic energy for atomisation is constant for both cases as the volume flow of the pressurised air is not changed. Hence, with increasing mass flow rates of the liquid the peak velocity of the droplets has to decrease. The changes between OT1, OT2 and OT3 are rather small with peak velocity differences of 2.5 m s^{-1} which are within the range of measurement uncertainty. The measurement uncertainty is estimated with $\pm 1\%$ for velocities of Pitot measurements including the pressurised air mass flow. Measurement uncertainty of PIV analysis is also given with $\pm 1\%$ for peak velocities in the centre of the spray, at the borders it is about $\pm 2\%$. A higher difference for the peak velocities of about 10 m s^{-1} is detected for OT4–OT6. The influence of peak velocity differences due to temperature on further analyses based on the analytical jet model (see equations 2.39 – 2.5.1) is considered negligible for radial profiles since these are calculated from normalised values. This assumption is supported by calculated radial profiles for different

cross sections as there is no difference visible (see figure 5.16).

5.1.3 Atomisation and Spray Measurements

Spray measurements consider UWS mass flow rates of the engine operating points. Results of measurements for the Schlick nozzle (model 940) as well as the MAN equivalent are presented and compared with each other in the following. Parameters obtained are particle sizes, mass distribution and spray angle. Inlet boundary conditions of the disperse phase in the simulations are based on these results (see section 5.5).

In figure 5.9 the results for the Schlick nozzle are depicted. For every measurement, the pressurised air flow was kept constant at 100 L min^{-1} . A variation

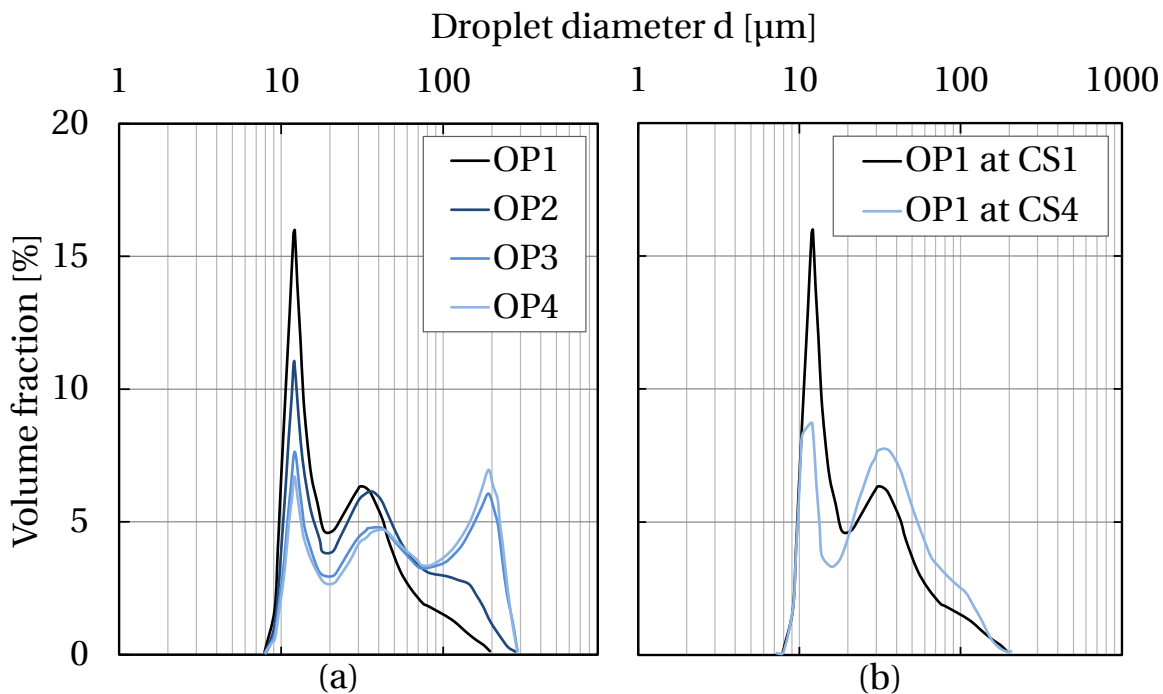


Figure 5.9: Droplet size distributions for Schlick 940: Variation of liquid mass flow rate (a) and variation of measurement cross sections for OP1 (b). All tests with 100 L min^{-1} pressurised air volume flow.

of UWS mass flow rates is depicted in 5.9 (a) at CS1. Characteristic droplet sizes are listed in table 5.5. With increasing mass flow the volume fraction of large particles increases. In 5.9 (b) the particle sizes are recorded at different distances / cross sections from the nozzle to quantify the state of droplet formation. A higher volume fraction of small particles is observed at CS1. For CS4 at 300 mm distance the volume fraction of large particles rises. Increasing particle sizes at a larger distance from the nozzle are often due to coalescence in combination with size separation of droplets [26]. Size separation of droplets refers to a droplet size-related influence of the gas flow surrounding the droplet. Without coflow droplets of small size and with low speed can be transported upstream again due to vortices at the border of sprays [26]. The droplet size distribution in all cases is bimodal with two main peaks. A strongly bimodal distribution was also observed in literature (see e. g. [49,95]). *Juslin et. al.* measured droplet size distributions with a Malvern Spraytec LDS for Schlick 940 for fluids of different viscosity [49]. Their measurement conditions in terms of air-to-liquid ratio and liquid mass flow are comparable to the present conditions. They observed a clearly bimodal droplet distribution for pure water. With increasing liquid viscosity the bimodality decreased and with increasing carrier gas flow rate the bimodality increased. *Wang and Purwanto* investigated the influence of different parameters, such as (carrier) air-to-liquid mass flow ratio or temperature of the liquid as well as different substances / aqueous solutions (changing fluid properties) on the droplet size distribution for an ultrasonic nebuliser [95]. They found that the higher the temperature of the liquid the stronger the bimodal shape. For higher carrier gas flow rates they observed, equal to *Juslin et. al.* [49], a stronger bimodal distribution [95]. In literature mainly two explanations are given for the occurrence of bimodal droplet distributions (see [45, 48, 65, 73, 95]). One explanation is found in the secondary break-up regime of droplets and another one in coagulation (coalescence) effects. Coagulation describes a continuous change in size distribution, number and concentration of droplets, while the volume is constant [95]. *Gel'fand et. al.* [34] explained that the so-called bag break-up regime leads to a bimodal distribution, where the bag breaks up in small droplets and the liquid ring into bigger droplets (see appendix A.1). High speed pictures of this break-up regime show these droplet size differences

(see [73]). *Hsiang and Faeth* [45] found the same effect for shear break-up. *Wang and Purwanto* referred the effect of the bimodal distribution to laminar and turbulent coagulation.

Referring the results of these studies to the measurements conducted in this thesis, the bimodal shape is a result of the high droplet number concentration, the high carrier gas flow velocity and the fluid properties of water. Due to the higher viscosity for UWS as compared with pure water, it can be assumed that the bimodality decreases (for fluid properties of aqueous urea solutions refer to [50]).

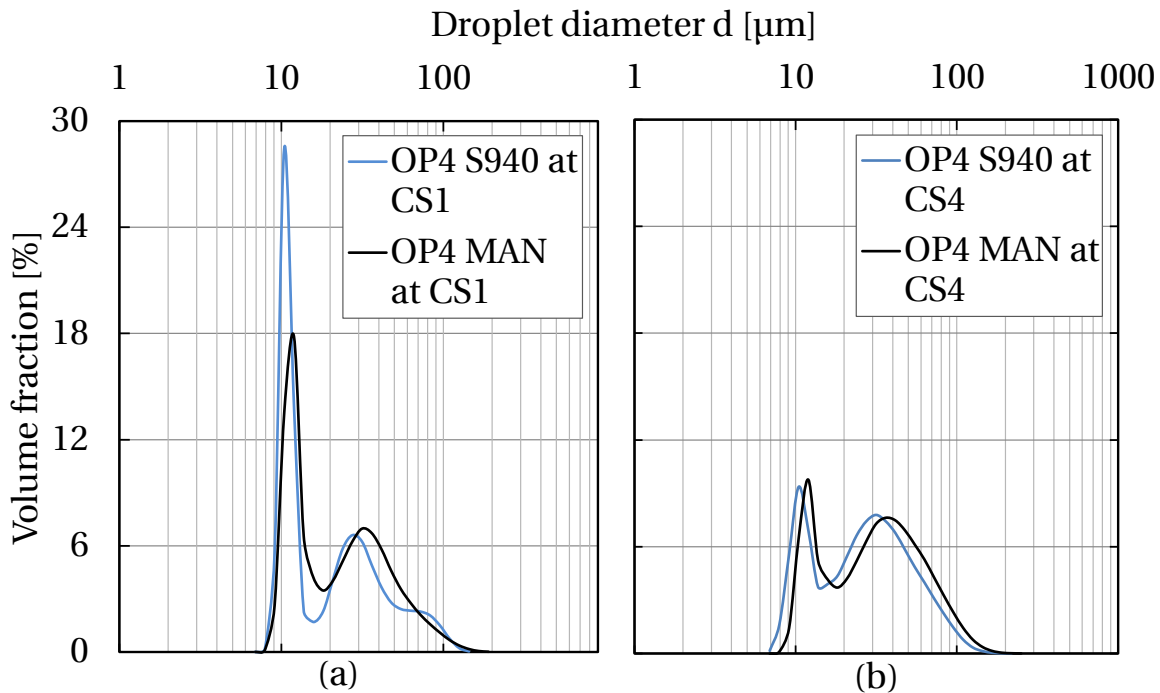


Figure 5.10: Droplet size distributions: Comparison of Schlick 940 and MAN for OP4 at CS1 (a) and for OP4 at CS4 (b).

Figure 5.10 presents the results for the MAN nozzle in comparison with Schlick 940. In figure 5.10 (a) the particle size distribution of the MAN nozzle (OP4 MAN: black line) and Schlick 940 (OP4 S940: blue line) are compared at CS1. The particle size distribution for both nozzles at CS4 are given in 5.10 (b). These experiments are conducted with 190 L min^{-1} of pressurised air volume

		Schlick 940		MAN	
		190 L min ⁻¹	100 L min ⁻¹	190 L min ⁻¹	100 L min ⁻¹
SMD [μm]	CS1	14.97	19.52	17.07	24.91
	CS4	27.25	39.3	22.17	37.43
D_{V90} [μm]	CS1	52.36	78.26	52.39	92.57
	CS4	91.07	139.4	68.81	137.54

Table 5.5: Characteristic droplet sizes for Schlick 940 and MAN nozzle.

flow rate. Thus, the influence of air to liquid ratio to droplet sizes is shown (figure 5.9 compared with figure 5.10). At CS1 the Schlick 940 nozzle has a higher volume fraction of particle sizes of about 10 μm compared with the MAN nozzle (see 5.10 (a)). Consequences from this difference are negligible, since these small droplets contribute little to the total particle volume. This is proven by comparing the characteristic droplet diameters (see table 5.5), e. g. the SMD (D_{32}) or D_{V90} , for both nozzles. The SMD has a difference of 2 μm between both nozzles (Schlick 940: SMD= 14.97 μm and MAN: SMD= 17.07 μm). The D_{V90} is 52.36 μm for the Schlick nozzle and 52.39 μm for MAN. At a 300 mm distance from the nozzle (CS4) the curves of MAN (black line) and Schlick 940 (blue line) are similar. Increasing particle sizes are found for both nozzles with increasing distance from the nozzle (figure 5.10 (b)). A higher fraction of smaller droplet sizes is detected for a higher amount of pressurised air which coincide with theory. A 90 % increase in pressurised air volume flow rate (100 L min⁻¹ to 190 L min⁻¹) leads to a reduction by $\approx 30\%$ for the SMD and $\approx 40\%$ for the D_{V90} at CS1. At CS4 the reduction of the characteristic droplet sizes is even more evident (see table 5.5). The SMD calculated by the correlation of *Kim and Marshall* (equations 2.30 and 2.31) is in line with the measurements. For example the SMD calculated for OP4 with 190 L min⁻¹ is 23.2 μm and the measured values are 27.2 μm for Schlick 940 and 20.3 μm for the MAN nozzle (both at CS4).

In figure 5.11 the mass distributions for the MAN nozzle and the Schlick 940 are given. The mass distribution is normalised by the highest mass collected in one container of the patternator. Tests are performed with 7.3 kg h⁻¹ liquid mass flow rate and 100 L min⁻¹ pressurised air volume flow rate. Mass distri-

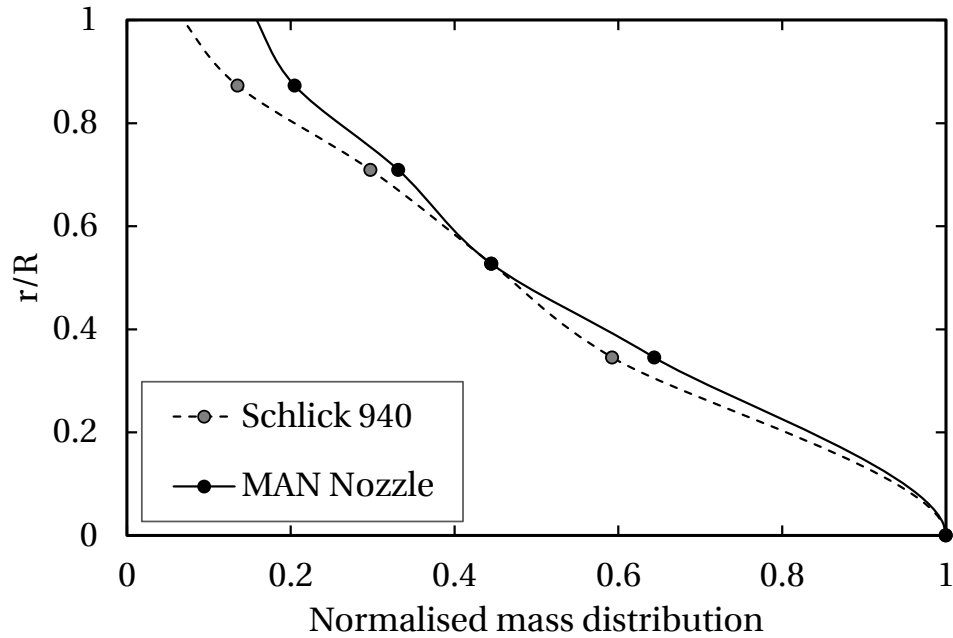


Figure 5.11: Normalised mass distribution from patternator measurements: 7.3 kg h^{-1} liquid mass flow and 100 L min^{-1} pressurised air flow.

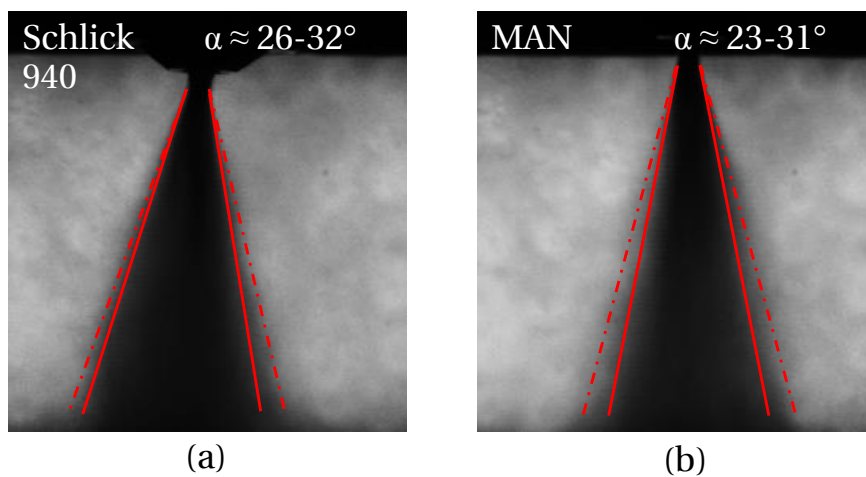


Figure 5.12: Spray cone angle, between 26° and 32° for Schlick 940 (a) and between 23° and 31° for the MAN nozzle (b).

butions do not show major differences. In both cases the injector generates a full cone spray with a high amount of liquid in the centre. This mass distribution is the explanation for the significant reduction in temperature especially in the centre of the catalyst front surface. The spray cone angle of the MAN nozzle is similar Schlick 940 (illustrated in figure 5.12). At the orifice the spray cone angle is larger (dashed dotted line), while with increasing distance the spray is narrowed and the cone angle becomes smaller (solid line).

5.2 Analytical Models

Analytical modelling approaches for processes occurring in the hydrolysis reactor are introduced in this chapter.

5.2.1 Droplet Evaporation Model

Assuming an average velocity of 60 m s^{-1} for the droplets from injection to impingement at the catalyst and a D_{V90} of $70 \text{ }\mu\text{m}$ (see 5.1.3) for droplet collective, the reduction of liquid mass due to evaporation is about 3 - 10 % depending on the gas temperature (OP1 - OP4) before the catalyst front surface is reached (see figure 5.13). The average velocity is calculated from the jet model taking the mean velocity at the axis in combination with the mean velocity in radial direction into account. The average lifetime to complete evaporation of a droplet of this size, in $500 \text{ }^\circ\text{C}$ hot gas flow, is about 34 ms, whereas the average time until impingement is 5 ms. In figure 5.13 the liquid mass reduction due to evaporation of 3 droplet sizes is calculated as an example for the exhaust gas temperatures of OP1 to OP4.

5.2.2 Diffusion Model and Kinetics

Diffusion processes and reaction kinetics are considered for the gaseous species, while passing the channels of the catalyst. In this work diffusion in combination with convective species transport are considered. Isocyanic acid

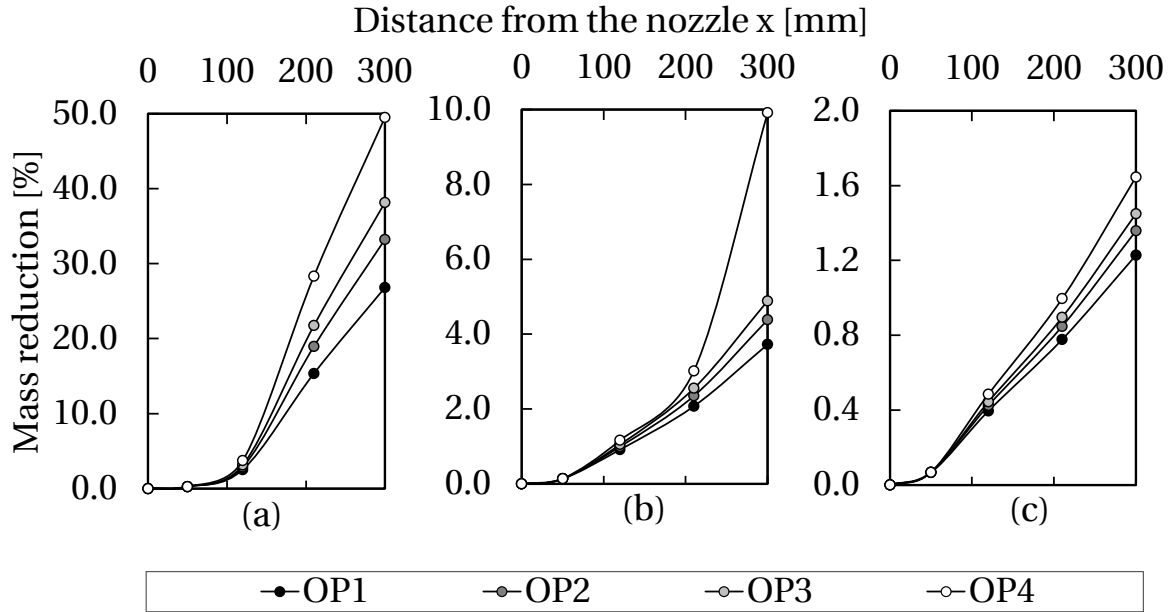


Figure 5.13: Mass reduction of different droplet sizes for OP1 (liquid: 7.3 kg h^{-1} and bulk temperature: $460 \text{ }^\circ\text{C}$), OP2 (liquid: 13.4 kg h^{-1} and bulk temperature: $490 \text{ }^\circ\text{C}$), OP3 (liquid: 20.3 kg h^{-1} and bulk temperature: $510 \text{ }^\circ\text{C}$) and OP4 (liquid: 25.3 kg h^{-1} and bulk temperature: $550 \text{ }^\circ\text{C}$): in (a) $50 \text{ } \mu\text{m}$ in (b) $70 \text{ } \mu\text{m}$ and in (c) $100 \text{ } \mu\text{m}$.

(HNCO) and water are the two species of interest. The conversion of HNCO to ammonia proceeds if HNCO and water react at the coated surface of the catalyst. The effective reaction rate (see equation 2.11) can be simplified to:

$$k_{eff} = \frac{1}{\frac{1}{k} + \frac{1}{\beta \cdot a}} = \beta \cdot a \quad (5.1)$$

if $\beta \cdot a \ll k$ is valid. *Hauck et. al* [41] revealed an activation energy of $E_a = 12.7 \text{ kJ mol}^{-1}$ for a temperature $T = 428 \text{ }^\circ\text{C}$ on TiO_2 based catalysts. A reaction rate $k = 11786 \text{ s}^{-1}$ is found. In the present work the reaction rate will increase further since temperatures are even higher. The mass transfer coefficient β for HNCO is calculated within the range of $0.2 - 0.55 \text{ m s}^{-1}$ depending on Re (see figure 5.14). The active area a is represented by GSA values of the catalyst (see section 3.1.1), thus a is within the range of $3.0 - 3.65 \text{ m}^2 \text{ L}^{-1}$ depending on cell

density. Hence, $\beta \cdot a$ is about 600 – 2000. The velocity constant for chemical reaction k (equation 2.10) is several times larger than the velocity constant of the mass transfer $\beta \cdot a$. Equal to *Hauck et. al* [41] it is found that the global reaction rate is not limited by chemical kinetics according to these estimates based on the Arrhenius equation, but by mass transfer.

This leads to a negligible contribution of reaction kinetics to the effective velocity constant (equation 2.11). Once HNCO and water reach the surface, they react, and this reaction is completed within a fraction of the time needed for the diffusion process. Hence, equation 2.12 is valid. These circumstances are also stated by *Birkhold* [15] and *Steinbach* [89].

For the mass transfer of isocyanic acid and water in the catalyst channels the binary diffusion coefficient is calculated for each substance in air. Due to the low concentrations of isocyanic acid and water compared with air, the assumption of binary diffusion with air can be made. The mass transfer coefficient (equation 2.8) as a function of Reynolds number is given in figure 5.14 (a) for both species. Resulting from this, the length needed for the diffusion of each species is given in figure 5.14 (b). The diffusion length is calculated with:

$$L_{diff} = \frac{0.5 \cdot d_{hyd}}{\beta} \cdot u \quad (5.2)$$

where d_{hyd} is the hydraulic diameter of a catalyst channel, β the mass transfer coefficient and u the axial velocity. It describes the maximal axial traveling length required for a substance to diffuse perpendicular to the flow direction. Due to the higher molar mass of HNCO the mass transfer coefficient is lower than for water. As the consequence, the length needed to diffuse is higher than for water. Isocyanic acid needs water to convert to ammonia, thus both have to get in contact with the surface of the catalyst at the same time. Since water evaporates faster than urea, the diffusion process of water starts earlier than for HNCO. This leads to a deficiency of HNCO at the catalyst walls in addition to the deficiency caused by slow HNCO diffusion. This may explain the lowest HEL of case TC4, see section 5.1.1. TC4 has the highest coflow velocity due to the highest main air mass flow, thus the diffusion length increases.

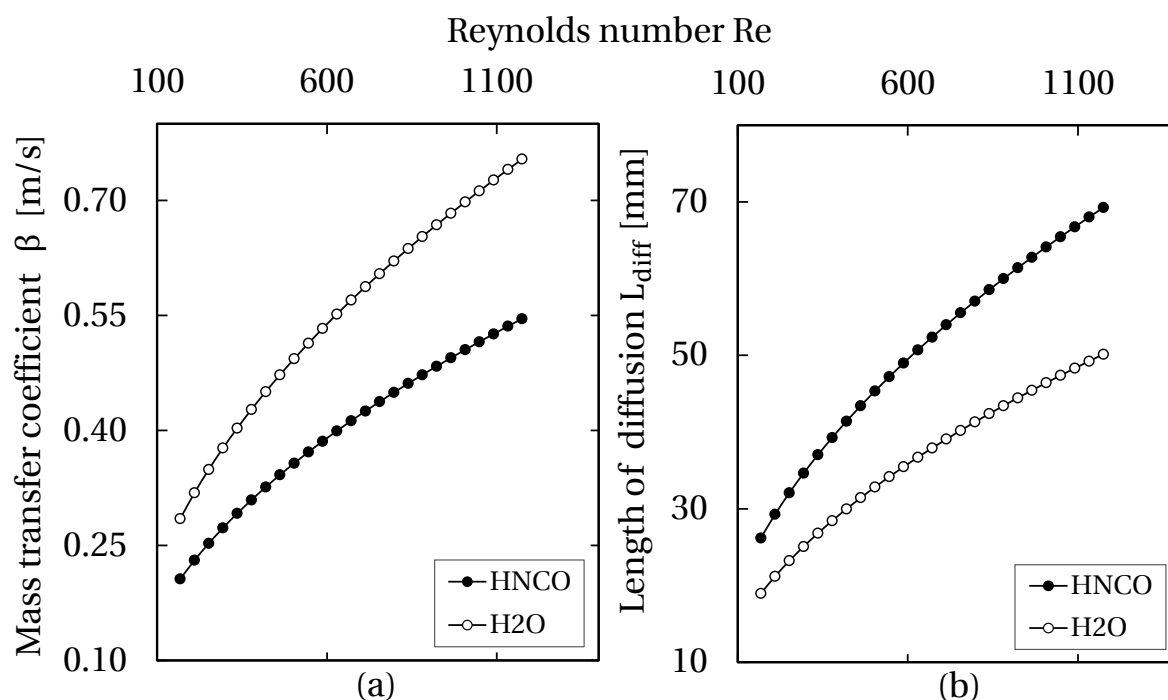


Figure 5.14: Mass transfer coefficient in (a) and diffusion length in (b) for isocyanic acid and water.

5.3 Comparison of the Turbulent Jet Model to the PIV Measurements

In this section PIV measurement results are compared with the analytical jet model. The theoretical velocity profiles and the results from the measurements are analysed for equivalent boundary conditions and initial values. In this context only the results of the experiments conducted at 400 °C are compared with each other, as influences due to temperature are considered to be small (see explanation explained in section 5.1.2 and figure 5.8). The pressure loss across the catalyst influences the flow field in form of a back pressure. Depending on velocity the effect varies radially and influences the jet in form of a decrease of jet penetration and velocity [10]. *Bayvel et. al.* showed the influence of back pressure within the range of 5 to 18.5 bar to jet penetration and jet angle which is far beyond the pressure drop in the present work. The total

pressure loss across the catalyst is about 0.01 bar. Hence, it is assumed that the influence of back pressure is relatively small and is neglected for simplification.

The velocity decrease of the initial axial jet velocity is displayed in figure 5.15 for two different liquid mass flow rates. As a consequence of the limited optical access the first velocity measurement is conducted significantly downstream of the nozzle exit (see figures 5.6 and 3.9) and thus downstream of the initial jet region (see section 2.5.1). The length of the initial jet region can be calculated from equation A.33 and is found for these experiments within a range of $x_H = 20.4 - 21.3$ mm. Consequently high velocities expected near the nozzle are not visible. Nevertheless, the validity range for the theoretical, normalised velocity decrease along the symmetry axis is limited. Clearly visible for x values close to zero, as the normalised velocity exceeds one. The further progress

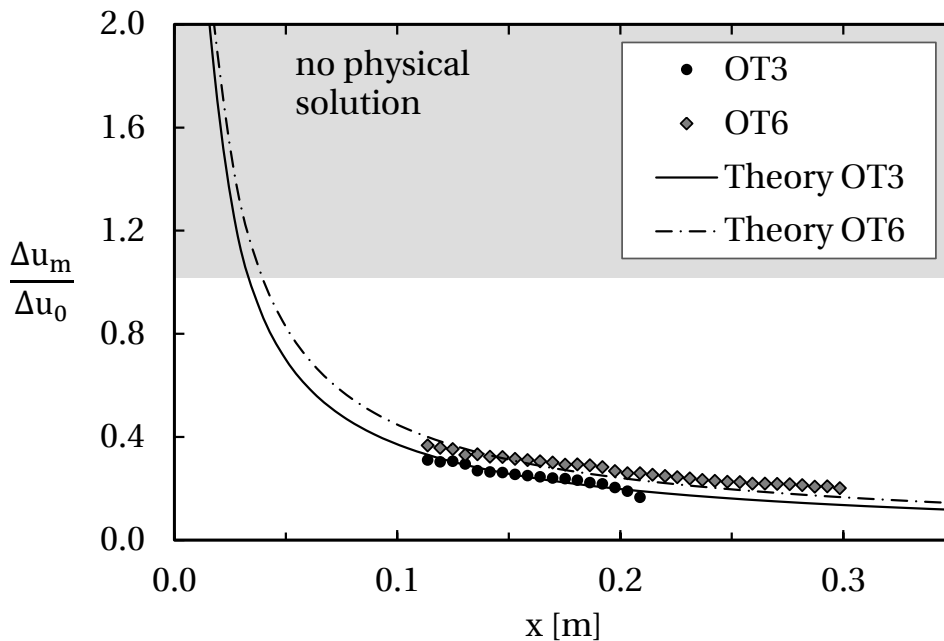


Figure 5.15: Normalised axial droplet velocity decrease along the symmetry axis measured for OT3 (liquid: 2.4 kg h^{-1} , pressurised air: 100 L min^{-1}) and OT6 (liquid: 2.4 kg h^{-1} , pressurised air: 100 L min^{-1}) in comparison with the theoretical progress (see equation 2.42).

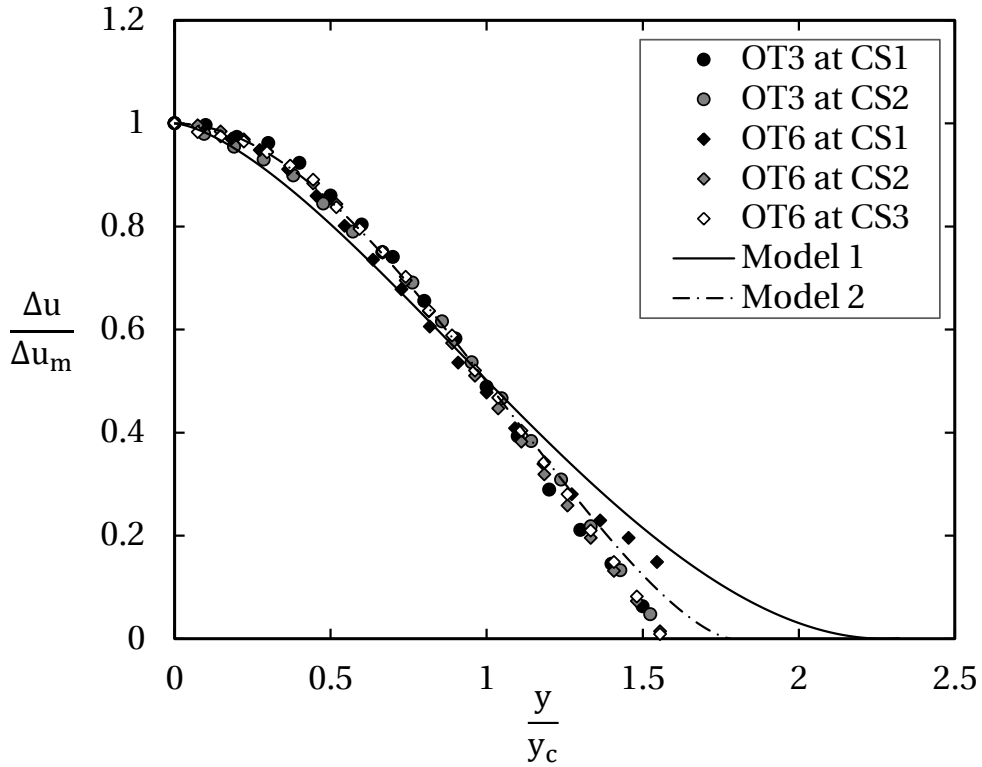


Figure 5.16: Normalised radial distribution of the normalised axial velocity at different axial cross sections (CS1 till CS3) compared with model 1 (equation 2.39) and model 2 (equation 2.40).

is depicted well by both experiments. OT3 allowed less measurement points to be acquired, due to evaporation of droplets.

Radial velocity profiles (figure 5.16) are analysed at different axial cross sections. The first cross section is located at $x = 0.12$ m (OT3 - CS1 and OT6 - CS1), the second at $x = 0.18$ m (OT3 - CS2 and OT6 - CS2) and the last one at $x = 0.24$ m (OT6 - CS3) distance from the nozzle. Model 1 refers to equation 2.39, while model 2 represents equation 2.40, both shown in figure 5.16. The velocity measurement results indicate better agreement with model 2 than with model 1.

5.4 Radial Concentration and Temperature Profiles

As described before, the concentration profile is of high interest, as it correlates directly with the distribution of liquid mass upstream of the catalyst. Hence, it would be beneficial to have a validation option for the theoretical temperature and concentration curves as well. Equations of radial temperature (T/T_m) and concentration (χ/χ_m) profiles are presented in chapter 2.5.4 (see equations 2.51 and 2.52).

In the present work no direct concentration measurement was possible, so that measurements of ammonia concentration downstream the catalyst represent the only way to compare theoretical predictions with the experiments (see figure 5.17). There are two comments to be made regarding the measurements: on the one hand the tip of the probe extracting the gas is mounted with 50 mm distance to the catalyst exit. Its diameter is a multiple of a single catalyst channel which limits the measurement resolution. On the other hand the MX structure of the catalyst produces additional dispersion. Both lead to an underprediction of radial gradients in concentration.

Dispersion due to catalyst structures was experimentally investigated and quantified by *Steinbach* [89]. He calculated the mixing rate for each tested structure with the equation for homogenisation introduced by *Grünwald* [37],

$$\eta_{mix} = 1 - 0.5 \sum_{i=1}^n \left(\left| \frac{X_i - \bar{X}}{\bar{X}} \right| \right) \frac{\dot{V}_i}{\bar{\dot{V}}}, \quad (5.3)$$

where X_i and \dot{V}_i are local values and \bar{X} and $\bar{\dot{V}}$ are the averaged values. The mixing rate is defined equally to an efficiency value, thus η_{mix} attains values between 0 and 1, where 1 would indicate perfect mixing or dispersion of the structure. Equation 5.3 corresponds to the integral of a Gaussian distribution. The dispersion through the catalyst structures is represented by different Gaussian distributions [89]. For the MX structure *Steinbach* found a correlation incorporating the number of turbulence generators and the hydraulic diameter of each catalyst channel. He reveals a correlation for the dispersion factor for the MX structure:

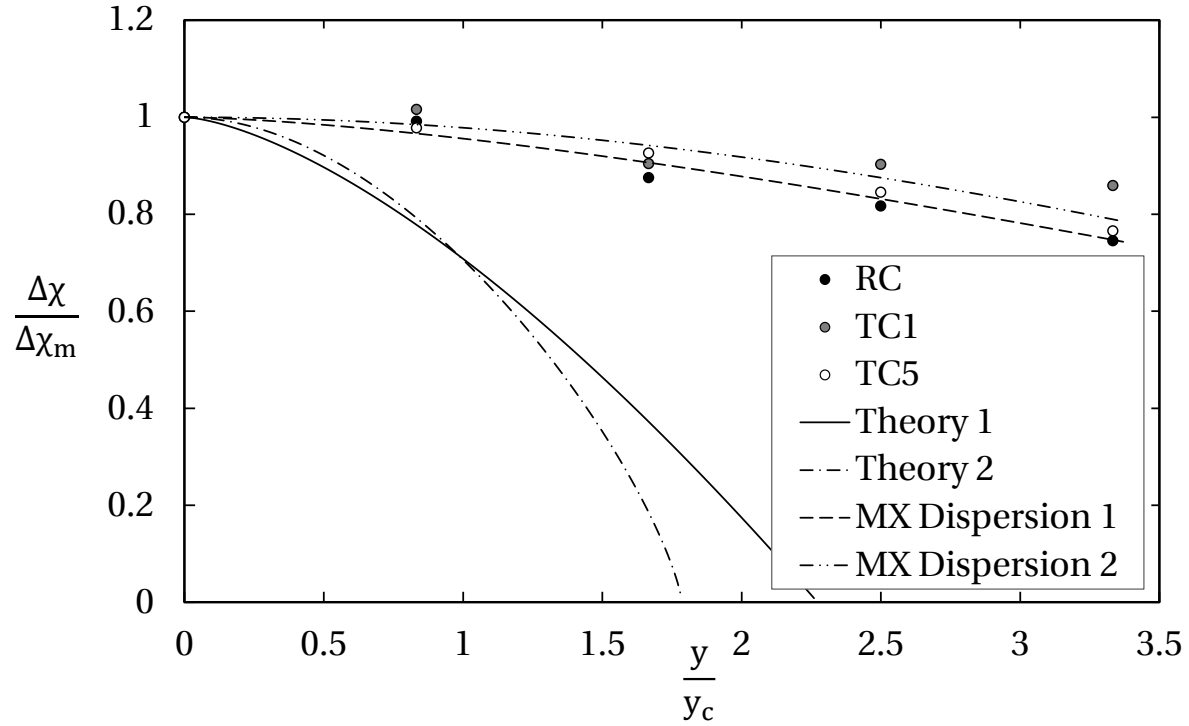


Figure 5.17: Theoretical concentration distributions upstream the catalyst (model 1: equation 2.51 and model 2: equation 2.52) and after passing the catalyst including the dispersion factor f (equation 5.4) (MX Dispersion 1 refers to model 1 and MX Dispersion 2 to model 2), in comparison with the normalised measured ammonia concentrations downstream the catalyst.

$$f_{dis} = \frac{d_{hyd} \cdot n}{R}, \quad (5.4)$$

and finds a dispersion factor of approximately 0.2 for his application [90]. Here, the MX structure has fewer cells and is shorter than the MX structure used by *Steinbach*. The hydraulic diameter $d_{hyd} \approx 3.3$ mm and $n = 3$ turbulence generators are found within the length of 50 mm. This leads to a dispersion factor of $f_{dis} \approx 0.18$ for this thesis.

In figure 5.17 the theoretical concentration distributions from model 1 (solid line) and 2 (dashed dotted line) upstream of the catalyst and with dispersion

factor for model 1 (MX Dispersion 1: dashed line) and for model 2 (MX Dispersion 2: dashed dotted-dotted line) downstream of the catalyst are displayed. For comparison a selection of the ammonia concentration measurements is given. By including the dispersion factor the experiments agree well with both theories. The results reveal that the theoretically calculated concentration and temperature distribution in front of the catalyst can be applied with some confidence. Further work should, however, attempt direct concentration measurements.

The concentration distribution given by model 1 (equation 2.51) is used to calculate the temperature at the catalyst front surface for all operating points (see figure 5.18). The temperature is reduced due to the energy needed to evaporate the liquid mass. This energy is calculated from the evaporation enthalpy for the liquid mass and subsequently weighted by the concentration distribution:

$$T(r) = T_0 - \frac{\dot{Q}_{evap}(r)}{\dot{m}_A \cdot c_p} , \quad (5.5)$$

where

$$\dot{Q}_{evap}(r) = \frac{\dot{m}_L \cdot \Delta h_v}{\int_0^R \chi(r) dr} \cdot \chi(r) . \quad (5.6)$$

Here, $T(r)$ is the radial temperature achieved at the catalyst, T_0 the initial bulk temperature, $\dot{Q}_{evap}(r)$ the needed heat flow, \dot{m}_A the main air mass flow, \dot{m}_L the liquid mass flow, Δh_v the specific evaporation enthalpy and $\chi(r)$ the local concentration obtained from equation 2.51 or 2.52. It is assumed that the whole liquid mass is evaporated at the catalyst front surface. A calculation of temperature decreases or temperature profiles before the catalyst front surface is reached based on droplet evaporation is possible, but results of such calculations are highly dependent on droplet sizes. The more precise the information about droplet size distribution the more precise is the resulting temperature profile. Here, the influence of droplet evaporation upstream of the catalyst front surface is not incorporated. The transient process of evaporation is

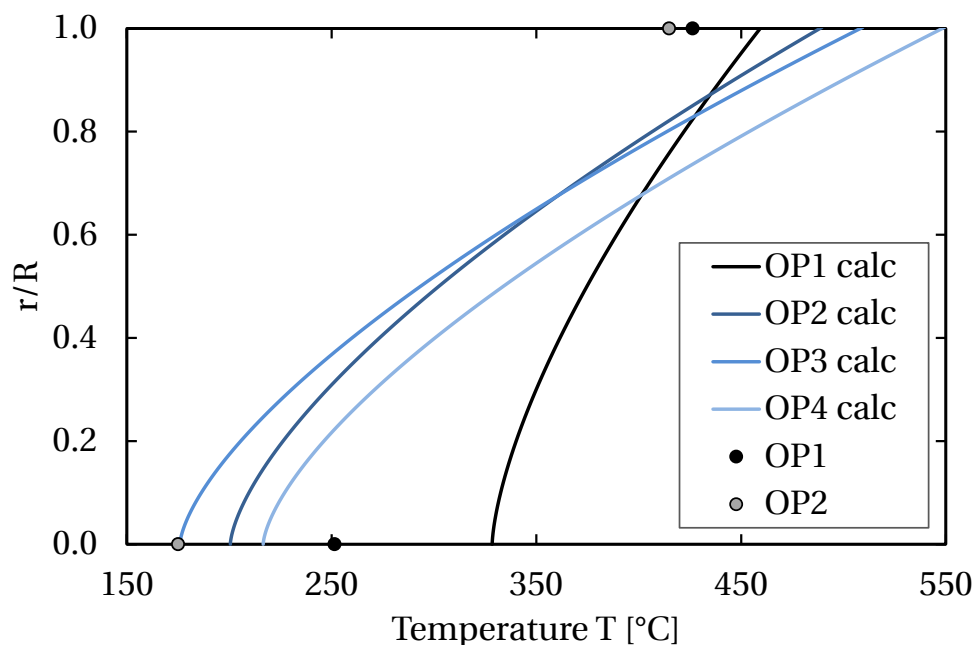


Figure 5.18: Calculated temperature profiles at CS4 for all operation points (OP1 calc till OP4 calc) by model 1 (equation 2.51) in comparison with measured temperatures (points) at CS4 for OP1 and OP2.

neglected, too.

It can be seen that for the calculated temperature profile of OP1 the temperature in the centre is significantly higher (about 80°C) than the measured one. The same is found for OP2, the measured one is about 25°C lower than calculated in the centre. At the wall ($r/R = 1$) the measured temperatures are lower than the calculated ones as well. As there is no feedback between gaseous and liquid phase in this application of theory, all calculated temperature profiles seem to underestimate the temperature decrease due to evaporation. But the tendency is represented well and shows the advantages of this modelling approach for the design of hydrolysis reactors. This aspect is taken up again in chapter 7, where the design method is explained in detail.

Diffusion of gaseous species in the catalyst channels is dependent on the velocity field and temperature field, too. For evaporated liquid the diffusion length L_{diff} needed for HNCO related to the velocity profiles is shown in fig-

ure 5.19 and figure 5.20. The diffusion length is calculated only for HNCO, as it has been shown in section 5.2.2 that HNCO has a longer diffusion length than water. The axial velocity decrease along the x-axis is calculated from equation 2.47 combined with equation 2.50. Thereafter Δu_m at CS4 and the axial velocity distribution at CS4 in radial direction can be calculated with the aid of equation 2.39. From these the theoretically required diffusion lengths are calculated. In figure 5.19 the diffusion length profiles for OP1 are displayed. The diffusion length is calculated with a constant inlet temperature of 460 °C displayed by the dashed dotted black line (figure 5.19: OP1 HNCO const. Temp) and with the calculated temperature profile (equation 2.51) for OP1 shown by the solid black line (figure 5.19: OP1 HNCO). Both clearly indicate the influence of the jet on the diffusion, as the higher velocity leads directly to a longer diffusion length of the species after the thermolysis of urea has proceeded. But the influence of the temperature is not negligible in this context and reveals rather realistic diffusion lengths for all operation points OP1 - OP4 (see figure 5.20: calculated with temperature profiles).

5.5 RANS Simulation of the Hydrolysis Reactor

RANS simulations are used as an optimisation option for reactor design (see chapter 6). Numerical model validation is performed using the baseline reactor. Simulations use the inlet boundary conditions equivalent to PIV measurements in the first step (table 5.6: NT1 and NT2 as equivalent to OT3 and OT6). In the second step flow conditions of the engine operating points are used for simulations (listed in table 5.6, NT3 and NT4) and compared with temperature measurements.

The disperse phase is obtained by single injections generated from a MATLAB script, as described in chapter 4.2. In contrast to *Grünwald* [37], who based the droplet distribution on a Rosin-Rammler distribution, with the MATLAB script in this work a bimodal droplet distribution is achieved. Additionally, the initial droplet velocity vector of each droplet differs. *Grünwald* separated the droplet absolute initial velocity in three groups depending on their droplet size range (small droplets have the velocity of the jet and big droplets the one

Simulation	NT1	NT2	NT3	NT4
Main Air Velocity [m s^{-1}]	16.4	16.4	14.45	12.65
Temperature Main Air [$^{\circ}\text{C}$]	400	400	460	490
Carrier Gas Inlet Velocity [m s^{-1}]	170	170	170	170
Liquid Massflow [kg h^{-1}]	2.4	7.3	7.3	13.4

Table 5.6: Boundary conditions for simulations.

of the coflow). In this thesis the absolute initial velocity of each droplet is equal to the carrier gas inlet velocity (table 5.6: line 3). It is assumed that all droplets have the same velocity (jet velocity) after their formation process and the differences occur due to the interaction with the coflow. In figure 5.21 the droplet size distribution of OP1 at CS1 is compared with obtained droplet sizes from MATLAB for NT3 at CS0. The calculated droplet size distribution agrees rather well with the measurement data, but it must be incorporated that the simu-

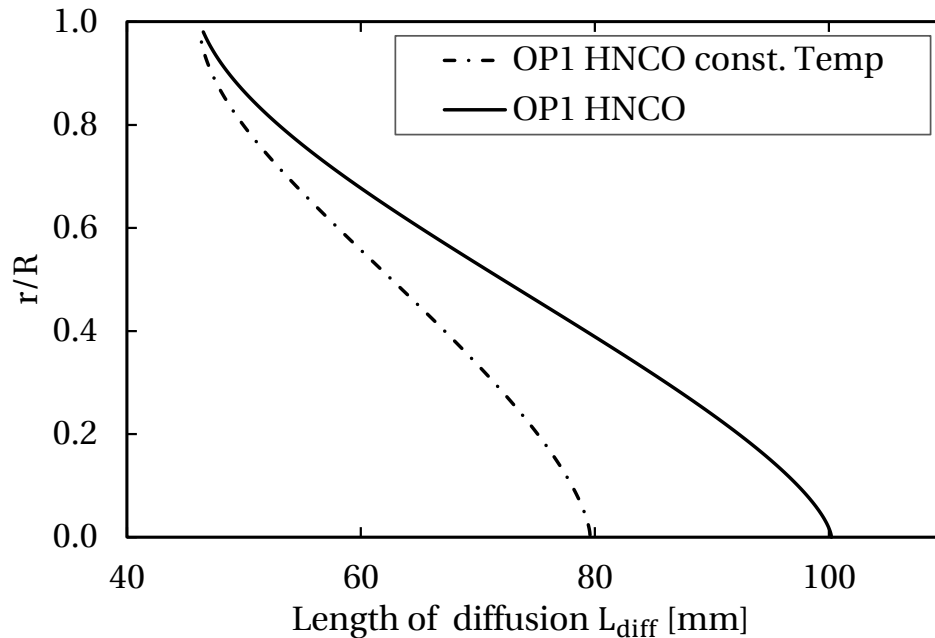


Figure 5.19: Calculated diffusion length profiles of HNCO (equation 5.2) at CS4 for OP1 with constant temperature (OP1 HNCO const. Temp) and with temperature profile (OP1 HNCO) (equation 2.51).

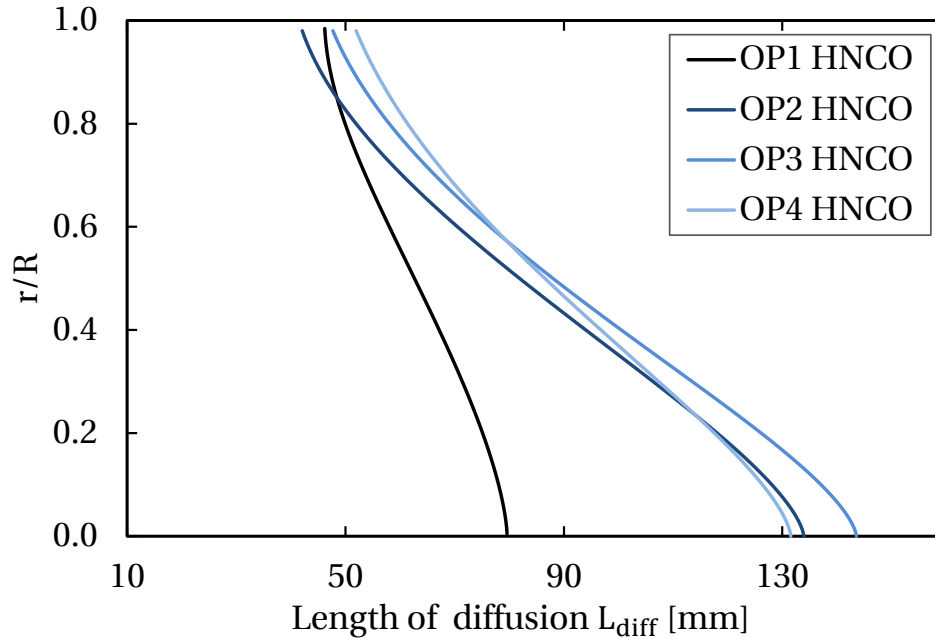


Figure 5.20: Calculated diffusion length profiles of HNCO at CS4 for all operation points (OP1 HNCO till OP4 HNCO) with temperature profiles.

lated droplet size distribution is an initial distribution since atomisation is not calculated.

Figures 5.22 - 5.26 show results of NT1 and NT2 compared with jet theory. The pressurised air in form of the carrier gas flow velocity (see table 5.6) is used for comparison. The initial carrier gas flow velocity is calculated with the equations in chapter 2.5.2 (see equations 2.44 to 2.49) and incorporates density differences between liquid and air.

The axial velocity decrease of NT1 and NT2 at the symmetry axis agrees well with jet theory (figure 5.22). The small deviation of the curves between $x = 0.05$ and $x = 0.15$ results from the non-physical solution of theory exceeding $\Delta u_m / \Delta u_0 = 1$. The simulations produce a realistic velocity decrease in good accordance to the analytical models. The radial distribution of the axial velocity is presented for both simulations (NT1: figure 5.23 and NT2: figure 5.24) at the four different cross sections. Again model 1 refers to equation 2.39

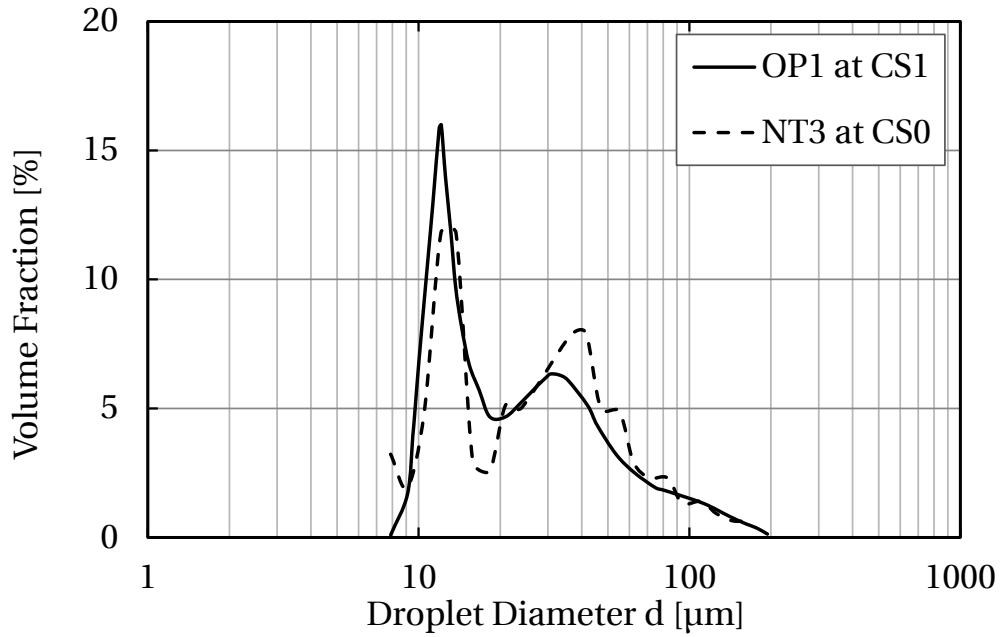


Figure 5.21: Droplet size distribution of OP1 at CS1 and of NT3 at CS0.

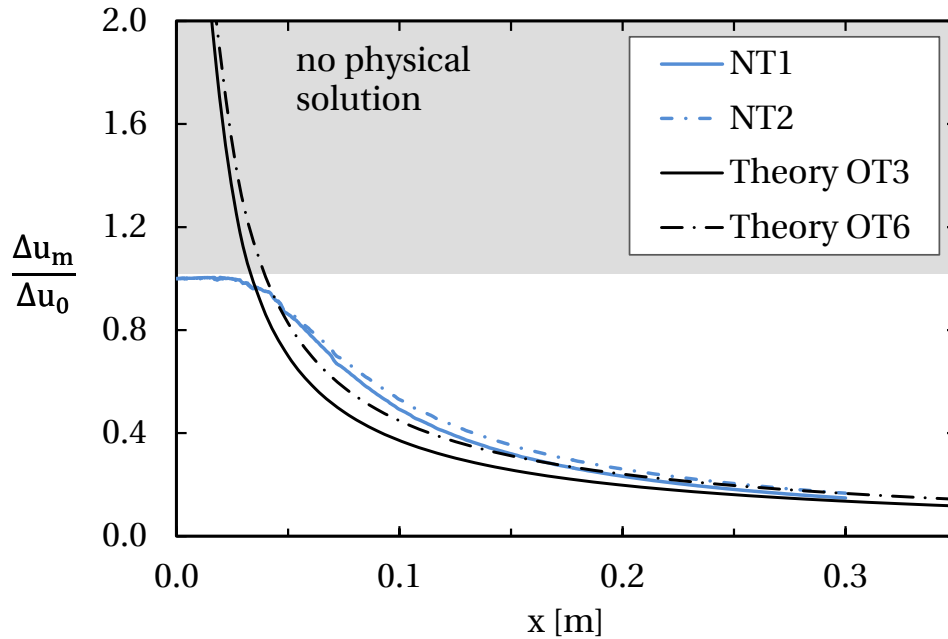


Figure 5.22: Axial velocity decrease along the symmetry axis for NT1 and NT2 in comparison with the jet theory adapted to the optical tests.

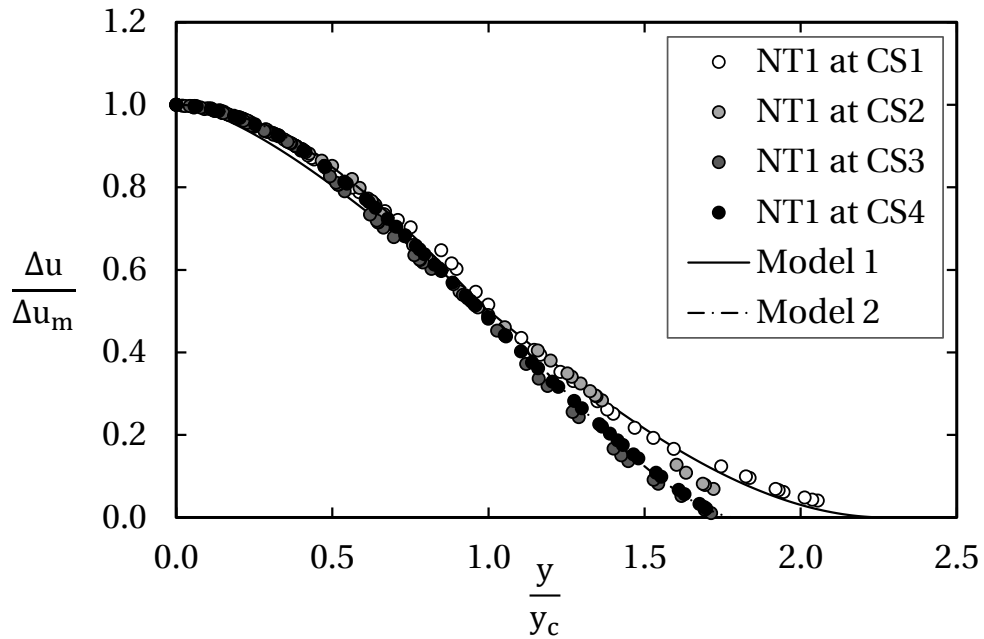


Figure 5.23: Axial velocity for NT1 at CS1–CS4 in comparison with the jet model 1 (equation 2.39) and model 2 (equation 2.40).

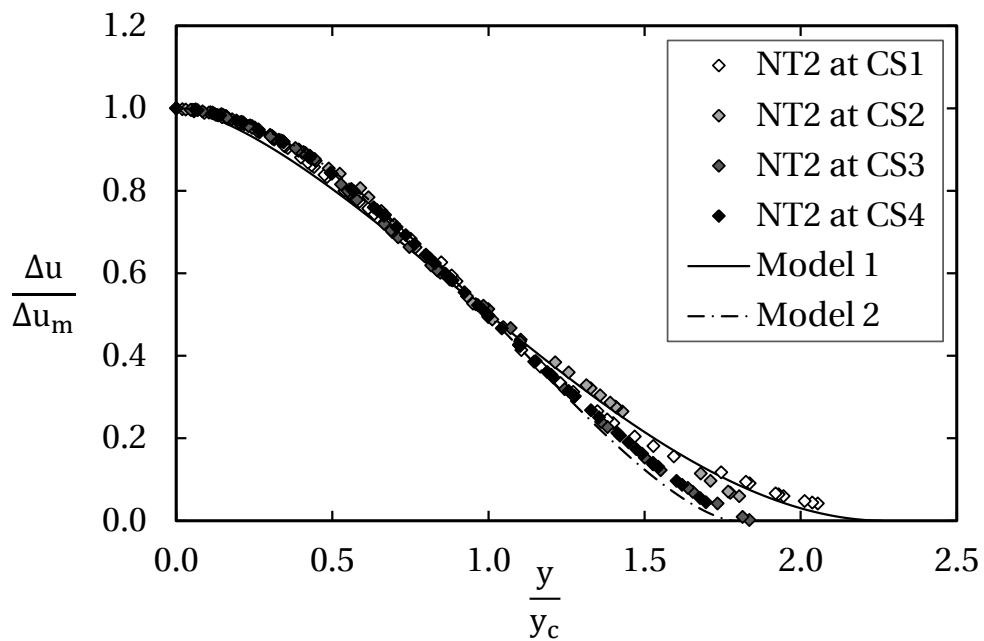


Figure 5.24: Axial velocity for NT2 at CS1–CS4 in comparison with the jet model 1 (equation 2.39) and model 2 (equation 2.40).

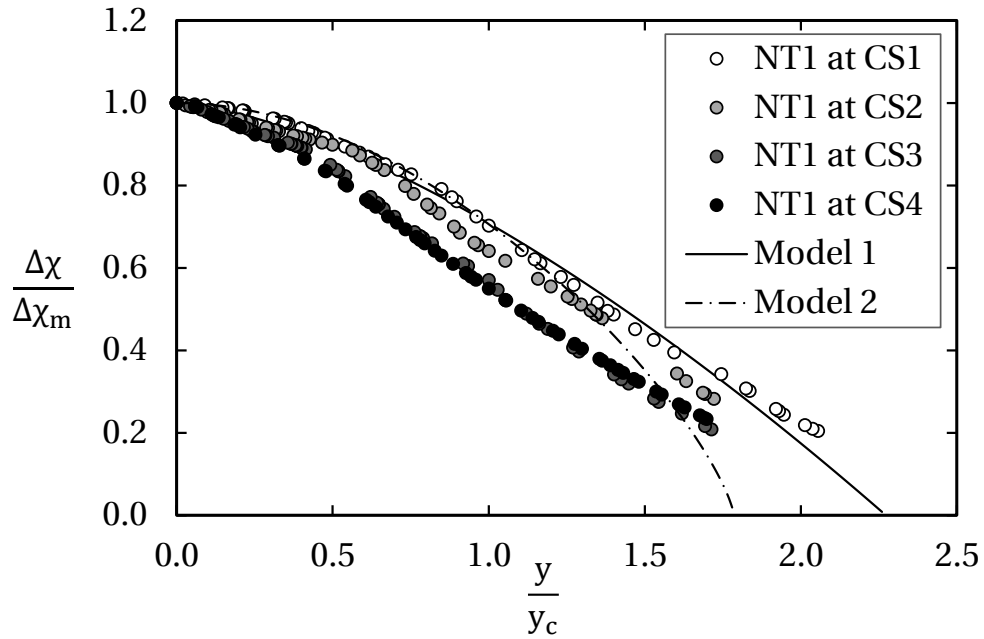


Figure 5.25: Water vapour concentration for NT1 at CS1–CS4 in comparison with the jet model 1 (equation 2.51) and model 2 (equation 2.52).

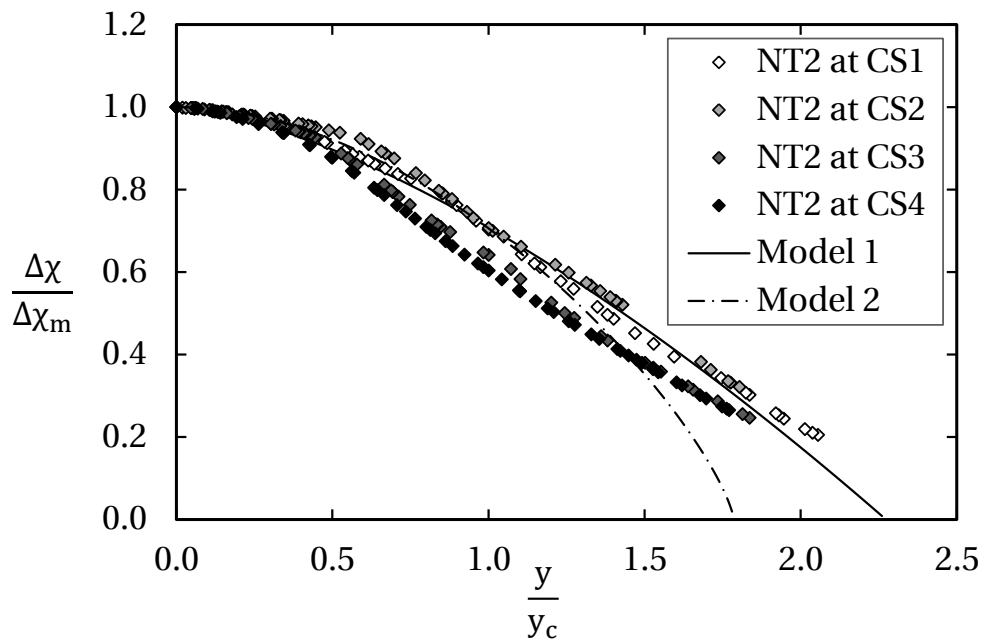


Figure 5.26: Water vapour concentration for NT2 at CS1–CS4 in comparison with the jet model 1 (equation 2.51) and model 2 (equation 2.52).

and model 2 to equation 2.40. For all cross sections and both simulations the velocities are in line with the analytical models. In contrast to results of PIV velocity measurements (chapter 5.3), the velocities of the simulations do not show a clearly better agreement with model 2. In both simulations the velocity profiles at CS1 and CS2 agree better with model 1 and at CS3 and CS4 with model 2. The concentration distributions of vaporised water, plotted in figure 5.25 and 5.26 show a better agreement with model 1 (equation 2.51) than with model 2. However, small deviations remain. The parameters for each droplet injection are distributed randomly and the sum of all injections produces the total mass flow rate, droplet size distribution and mass distribution. This can lead to some deviations caused by the droplet modelling method itself. In addition, the remaining liquid mass which escapes from the domain is not incorporated in this mass distribution. As long as both phases (liquid and gas) for water exist, the concentration distribution at the outlet of the domain is not achieved completely. Summarising these results, it can be stated that analytical theory as well as experiments are reproduced well by the simulations. The boundary conditions and modelling strategy used for the present simulations are regarded appropriate.

In the following, boundary conditions of simulations are adjusted to the engine operating points OP1 and OP2. NT3 refers to OP1 and NT4 to OP2. Only temperatures from experiments and simulations can be compared with each other. Thermocouples are mounted at the symmetry axis and at each side (horizontally) of the catalyst front surface. The temporal mean of measured temperatures from each individual thermocouple is compared with simulations. Temperatures of the simulation represent the gas temperature which occurs as a consequence of the concentration distribution, influenced by droplets already evaporated. In figure 5.27 the results are displayed. The experiments are visualised as single circles for OP1 (black) and OP2 (blue). In both experiments high temperatures (426 °C for OP1 and 414 °C for OP2) are detected at the wall of the catalyst ($r/R = 1$), while in the centre ($r/R = 0$) the temperature for OP1 is 250 °C and for OP2 169 °C. The temperatures of the gaseous phase of NT3 (solid black line) and NT4 (solid blue line) are clearly higher for both cases. For OP1 and NT3 the difference amounts to 7 °C at the wall and 45 °C in the centre. In case of OP2 and NT4 the difference is even

higher with 50 °C at the wall and 95 °C in the centre. Droplets impinging on the catalyst surface evaporate and cool down the surface temperature as well as the gas temperature which is measured by the thermocouples. As mentioned above, only already evaporated liquid mass is taken into account in the simulations. The dashed lines in figure 5.27 represent temperature profiles incorporating the instantaneous and complete evaporation of the remaining liquid mass (in the figures legend abbreviated with evap). These temperatures are calculated from the evaporation enthalpy of the liquid and subsequently weighted by the mass distribution of water vapour similar to the process shown for the analytical model (see section 5.4 and equations 5.5 and 5.6). Comparing the temperatures measured for OP1 with the temperature profile of NT3 (NT3 evap: dashed black line) incorporating the evaporation of the remaining liquid, the temperatures agree well. The same conclusion is found for OP2 compared with the temperature profile of NT4 including total evaporation (NT4 evap: dashed blue line).

Comparing results of figure 5.27 with the analytical calculation (figure 5.18), numerical simulations show a better agreement with temperature measurements than analytical calculations. The exchange of momentum, mass and energy between the gaseous and liquid phase in numerical simulations leads to higher precision and therefore to a higher quality of the results. Nevertheless, the analytical studies and measurements are important for the validation of the numerical simulations.

In a further step the swirl generator as an additional component is incorporated in the numerical model. The results of these simulations are described in chapter 6.

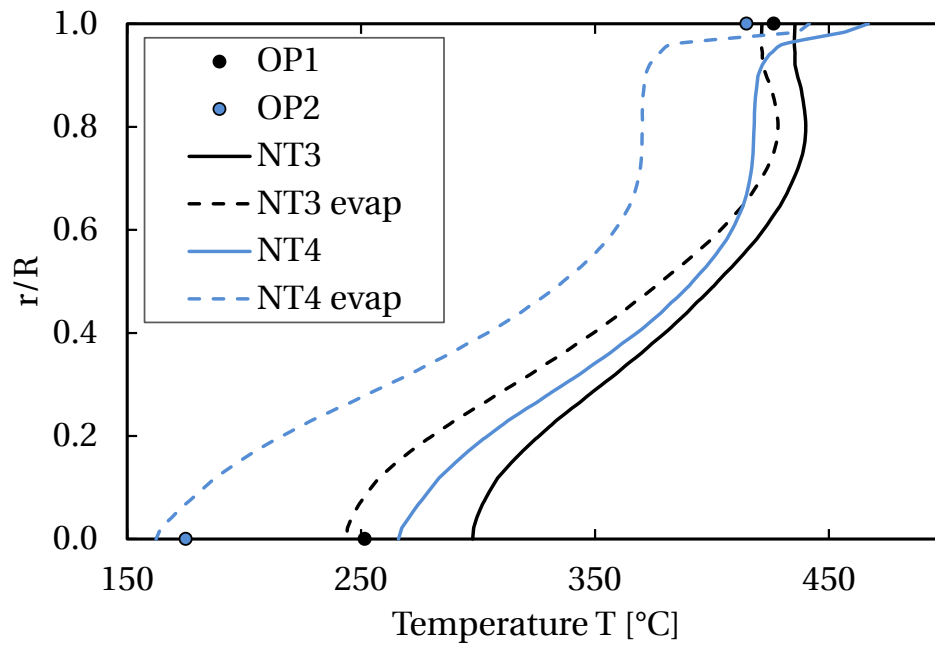


Figure 5.27: Temperature profiles for NT3 (black line), NT4 (blue line) with remaining liquid mass and NT3 evap (dashed black line), NT4 evap (dashed blue line) incorporating the evaporation of the remaining liquid in comparison with temperature measurement points (all at CS4).

6 Optimised Reactor Performance

Concentration measurements for the baseline hydrolysis reactor type resulted in catalyst blocking for the engine operating points OP2–OP4 due to solid by-products created during the process. The temperature in the centre of the front surface falls far below the critical decomposition temperature of urea, 200–250 °C. Even for the first operating point the temperature is near the critical minimum temperature. A link between the non-uniform liquid mass distribution at the catalyst and the high drop in temperature at specific surface areas with a high liquid loading is obvious. In order to extend the operating limits a swirl generator is introduced upstream of the injector to homogenise the liquid mass distribution in the optimised reactor.

6.1 Experiments

In the following results of concentration and droplet velocity measurements are presented.

6.1.1 Concentration Measurements

Similar to the previous chapter, concentration measurement results are presented for the engine operating points and fundamental test cases. First, results for the fundamental test cases are explained, followed by results for the engine operating points.

Fundamental Test Cases

All experiments are conducted with a catalyst length of 150 mm, with 50 mm MX structure and 100 mm ST structure. TC7 has the same boundary conditions as RC (for the baseline reactor), except using the swirl generator. TC8 to TC10 are conducted at 500 °C and constant UWS to main air mass flow ratio, while the cell density of the catalyst and the mass flow rates of UWS and main air are changed. In chapter 5.2.2 the mass transfer coefficient and diffusion length were determined as functions of the Reynolds number. Thus, the influence of the Reynolds number on the decomposition process is investigated in TC8–TC10. TC8 and TC10 have equal mass flow rates of main air (250 kg h^{-1}) and UWS (14 kg h^{-1}). The changed parameter is the cell density of the ST structure of the catalyst which leads to different Reynolds numbers in the catalyst structure. In TC9 and TC10 the Reynolds number is equal, while testing different cell densities of the ST structure. As a consequence, the mass flow rates of main air (177 kg h^{-1}) and UWS (9.9 kg h^{-1}) are selected, maintaining a constant mass flow ratio. Concentration measurements of the decomposition products are performed via the dilution unit, as the mass flow rates are too high for direct measurements.

Figure 6.1 presents the decomposition rate (UDR) and the hydrolysis efficiency level (HEL) for TC7 (white circles) in comparison to RC (black circles). The mean efficiency values are listed in table 6.1. An increase in mean UDR by 18 % is reached due to the swirl generator. The HEL is nearly constant in both cases because the swirl generator predominantly influences the fluid distribution in front of the catalyst. Another effect shown in figure 6.1 is that there are only small variations in radial direction of UDR and HEL for TC7. This is a

Test	TC7	TC8	TC9	TC10
GHSV · 10 ³ [h ⁻¹]	178.6	178.4	127.5	178.4
Mean UDR	0.91	0.80	0.91	0.79
Mean HEL	0.94	1	1	1

Table 6.1: Test conditions and calculated parameters of test cases for the optimised reactor.

curs within the heated dilution unit. The further decomposition of HNCO may occur in form of NH_3 or in form of a rapid polymerisation to CYA [82]. TC8 and TC10 have equal main air and UWS mass flow rates, with the same catalyst volume, so the GHSV is identical. As the difference in the Reynolds numbers refers to the hydrolysis process and the HEL is equal in both cases, a further consideration is not expedient. A higher UDR is found for TC9 which can be attributed to the atomisation and evaporation process of the droplets.

Tests Representing Engine Operating Points

The beneficial effects of the swirl generator on the decomposition process are especially apparent for the engine operating points (table 6.2). Experiments for all operating points are realisable with the optimised reactor without solid by-product formation. For all operating points the UDR achieves more than 80 %. Notable is that OP1 has the lowest UDR for the optimised case in comparison with the other operating points. It is still an increase compared with OP1 for the baseline reactor type, but the swirl seems to have less impact on the turbulent jet flow. For the other three measurement points the homogenisation by the swirl generator leads to a decomposition rate of 87 % for OP2 and OP3 and of 84 % for OP4. Due to the MX-structure of the catalyst the thermocouples could not be positioned directly at the front surface of the catalyst; they are positioned at the front of the ST structure. Hence, there is no information about temperature at the front surface. However, no solid by-products are created at the front surface, thus the assumption that the temperature of the surface is higher than 200–250 °C can be made. Temperatures measured at the walls ($r/R = 0.95$) downstream of the MX structure are nearly equal to those in the centre of the catalyst (within a range of 10 K), which reflects again the homogeneous liquid mass distribution.

In summary, the swirl generator provides the desired improvements for the hydrolysis reactor. An even better homogenisation could potentially be achieved with higher swirl numbers. However, tests with higher swirl numbers lead to impingement of urea droplets at the wall of the evaporation section upstream of the catalyst and result in the formation of solid depositions since the evaporation section walls are neither coated nor heated.

Test	OP1	OP2	OP3	OP4
Mass flow ratio (UWS/air) $\cdot 10^{-3}$	31.1	68.7	79.6	80.3
GHSV $\cdot 10^3$ [h ⁻¹]	93.7	87.5	116.9	143.9
Temperature measured ST structure [°C] ($r/R = 0$)	313	276	289	301
Mean UDR	0.81	0.87	0.87	0.84
Mean HEL	1	1	1	1

Table 6.2: Test conditions and calculated parameters for the engine operating points of the optimised reactor.

6.1.2 Velocity Measurements

Droplet velocity measurements are conducted for the optimised reactor with equal test conditions as for the baseline reactor (see chapter 5.1.2), but with the swirl generator implemented.

In figure 6.2 the axial velocity for the optimised reactor at cross section one (CS1) is presented. A first insight is that the velocity magnitude is higher in all tests compared with the ones for the baseline reactor. Velocity profiles for swirl flows discussed in literature (e. g. *Gupta* [38]) indicate a shift of the velocity component magnitudes. With increasing swirl numbers the axial, radial and tangential velocity in the centre decreases and increases again with increasing radial distance from the centre. This circumstance influences the axial velocity of the jet (see chapter 3.1.1). In the beginning, the jet is less disturbed by the coflow as the velocity in the centre of the vortex flow is smaller. With increasing distance from the nozzle the momentum exchange is higher than for the flow without swirl. This can be identified by comparing the axial velocity decrease along the axis for both reactor types with each other. The gradient for the axial velocity influenced by swirl flow is higher than the one without. A comparison of the normalised axial velocity decrease (OT3 swirl and OT6 swirl) along the symmetry axis to the numerical results for the optimised reactor (NT1 swirl and NT2 swirl) as well as the baseline reactor (NT2) is plotted in figure 6.6.

Figure 6.3 shows the tangential velocity profile with swirl generator for OP6 and OT3. Values of the tangential velocity are averaged over the length of

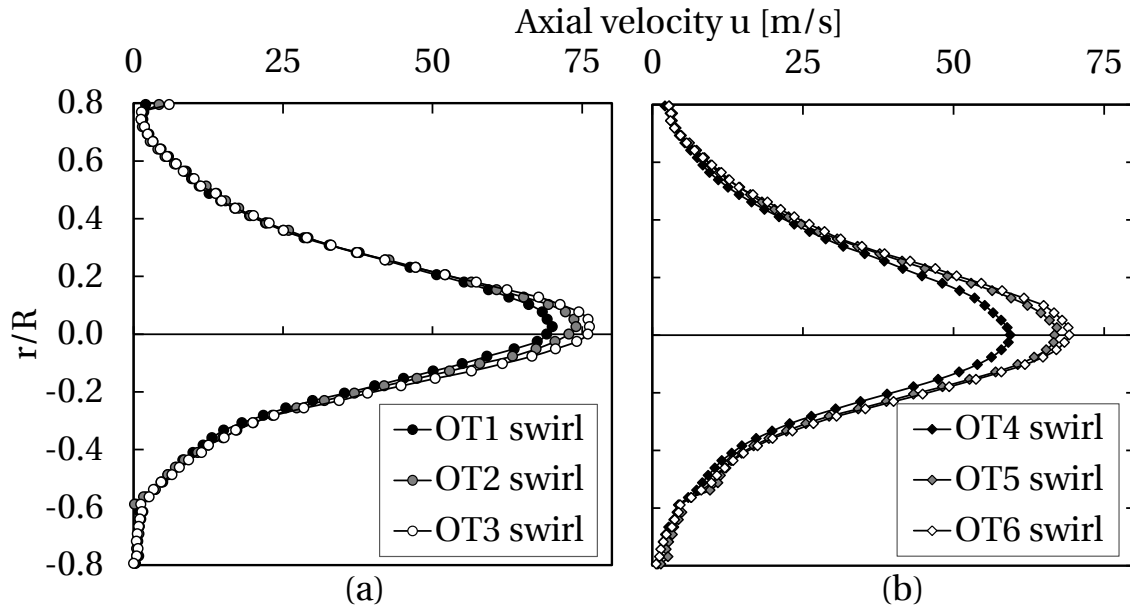


Figure 6.2: Axial droplet velocity with swirl flow at CS1: three temperature changes for a liquid mass flow rate of 2.4 kg h^{-1} in (a) and for a liquid mass flow rate of 7.3 kg h^{-1} in (b).

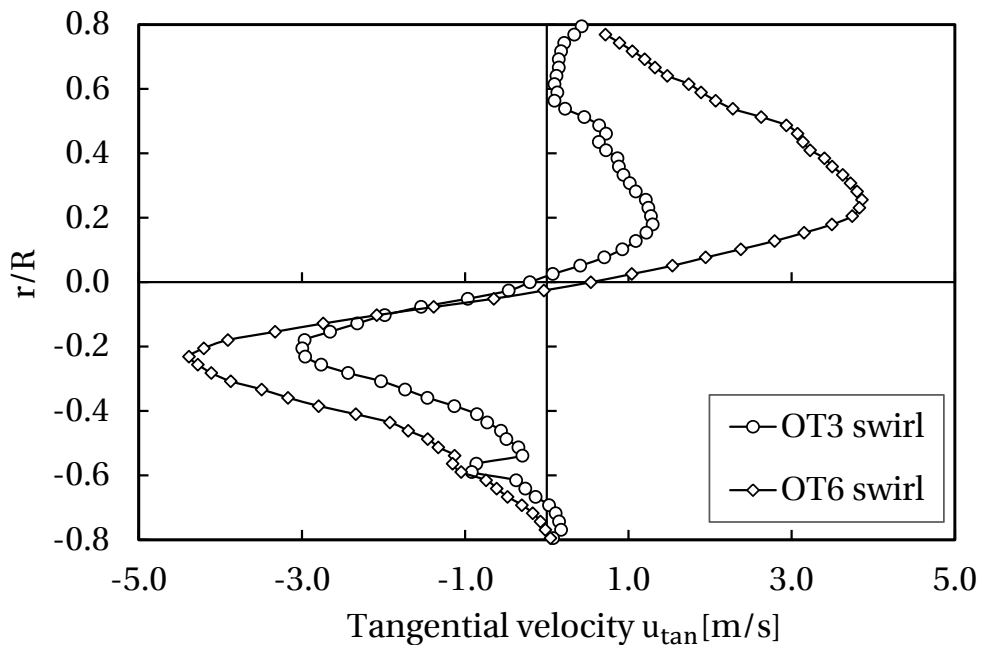


Figure 6.3: Tangential droplet velocity to the normalised channel radius in swirling coflow at CS1 (OT3 swirl and OT6 swirl).

one interrogation area. The swirl generator should provide a wall jet for the tangential velocity distribution at its outlet because of the annular holes which develops into a solid body vortex further downstream (see chapter 3.1.1). However, the tangential velocity profile measured is rather similar to a free vortex. It has to be noted that the PIV measurements are performed for droplets in the jet, not for the coflow gas. The velocities measured are highly influenced by the injector. The injector supplies the carrier gas with additional swirl (see chapter 3.1.1). A similar tangential droplet velocity profile is also found for cases without swirling coflow (see appendix A.6).

6.2 RANS Simulation of the Optimised Hydrolysis Reactor

For the optimised reactor no analytical model exists to describe the swirled turbulent jet. The numerical model comprises the swirl generator and the reactor domain (chapter 4.1). Calculations performed are equal to those conducted for the baseline reactor, listed in table 5.6. For each change of the main air inlet boundary condition a calculation of the gas flow through the swirl generator domain is necessary. Results at the outlet of the swirl generator domain are taken as the inlet boundary conditions for the main air inlet of the reactor domain. Validation options for the simulations are PIV measurements conducted with swirl flow for NT1 and NT2. Temperature results of NT3 and NT4 for the optimised reactor design can be compared with temperature measurements of OP1 and OP2 (see table 6.2).

The flow field established by the swirl generator is shown for NT1 in figure 6.4. The tangential velocity distribution provided by the swirl generator is given in figure 6.5. As expected, the velocity field is similar to a wall jet (see chapter 3.1.2) directly at the outlet of the swirl generator ($x = -170$ mm) and develops to a solid body vortex further downstream. Between the outlet of the swirl generator and CS0 the transition of the tangential velocity distribution occurs with a reduction of the velocity peak at the wall (at $x = -120$ mm).

The swirl number S (equation 3.1) is given for NT1 at the outlet of the swirl generator vanes with $S \approx 0.3$ and at CS0 with $S \approx 0.15$, which will decrease

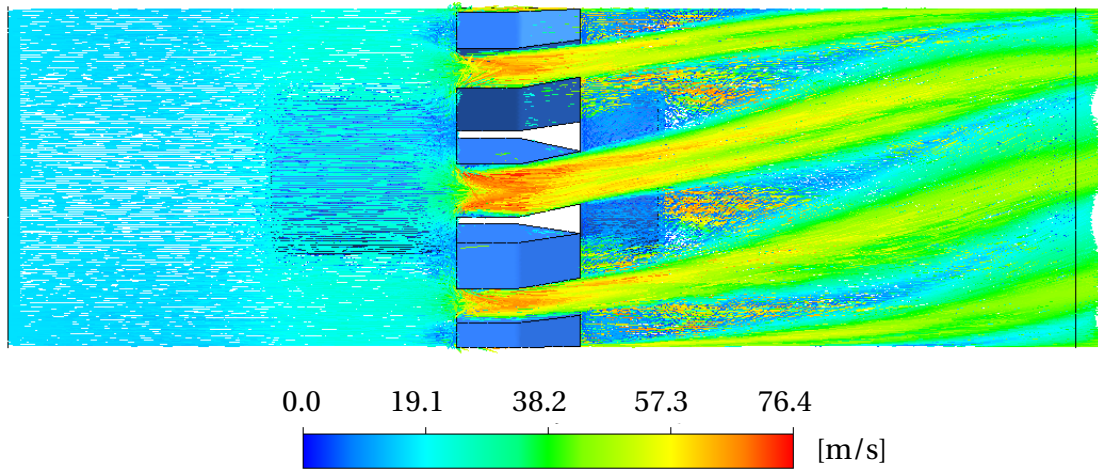


Figure 6.4: Vector plot of the velocity magnitude for the swirl generator flow field.

further in the downstream direction.

The normalised axial velocity decrease of PIV measurements (OT3 swirl: black circles and OT6 swirl: grey rhombi) and simulations (NT1 swirl: solid line and NT2 swirl: dashed line) including swirl are presented in figure 6.6. The simulation result of NT2 for the baseline reactor (dotted line) is displayed for comparison. The simulations with swirl reproduce the velocity evolution measured experimentally well. The higher momentum exchange for the optimised reactor compared with the baseline reactor manifests in the higher velocity gradient for the optimised reactor. In figure 6.7 and 6.8 the radial velocity profiles at CS4 are displayed for NT3 swirl and NT4 swirl (blue lines). For the axial velocity the radial profiles for NT3 and NT4 (black lines) without swirl generator are shown as well. Note that the jet in the cases without swirl seems to completely compensate the coflow momentum at the walls, as no velocity plateau but a continuous decrease towards the walls occurs. The cases with swirl show a velocity plateau for the coflow near the walls. The tangential velocity profiles are displayed only for the optimised setup, as for the baseline reactor the tangential velocities are zero in the simulations. The tangential velocity profiles resemble a solid body vortex.

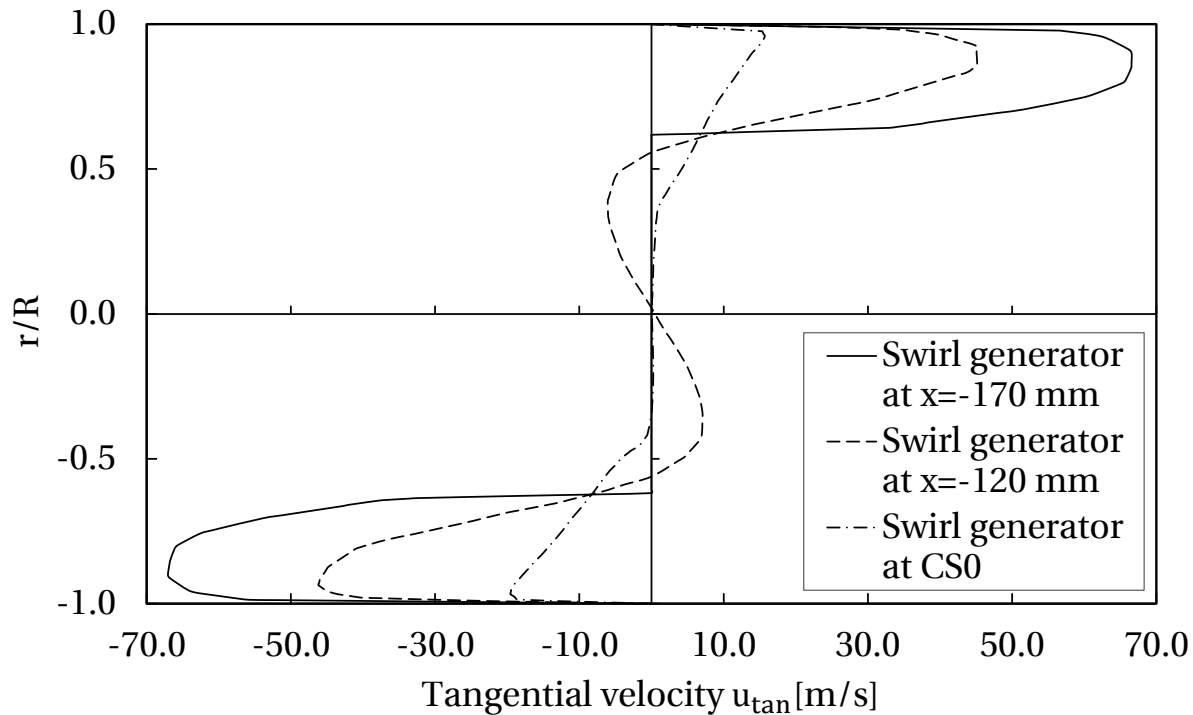


Figure 6.5: Tangential velocity profiles at the outlet of the swirl generator vanes ($x = -170$ mm: solid line), at $x = -120$ mm (dashed line) and at CS0 (dashed dotted line).

In figure 6.9 and 6.10 the temperature profiles at the outlet of the reactor domain (CS4) for the baseline and the optimised reactor are compared. Figure 6.9 gives the results for NT3 (respective to OP1) and figure 6.10 for NT4 (respective to OP2). Again the temperature profiles with remaining droplets are depicted as solid lines and the dashed lines represent the temperature profiles incorporating the evaporation of the remaining liquid mass (NT3 evap, NT3 swirl evap, NT4 evap and NT4 swirl evap). As already explained in chapter 5.5 the energy needed to evaporate the remaining liquid mass is calculated from the evaporation enthalpy for the liquid mass and subsequently weighted by the mass distribution of water vapour (see figure 6.11). Homogenisation effects of velocity and temperature are clearly visible for both simulations with swirl (NT3 swirl and NT4 swirl) compared with the ones without swirl.

Comparing simulations without swirl to the ones with swirl the homogenis-

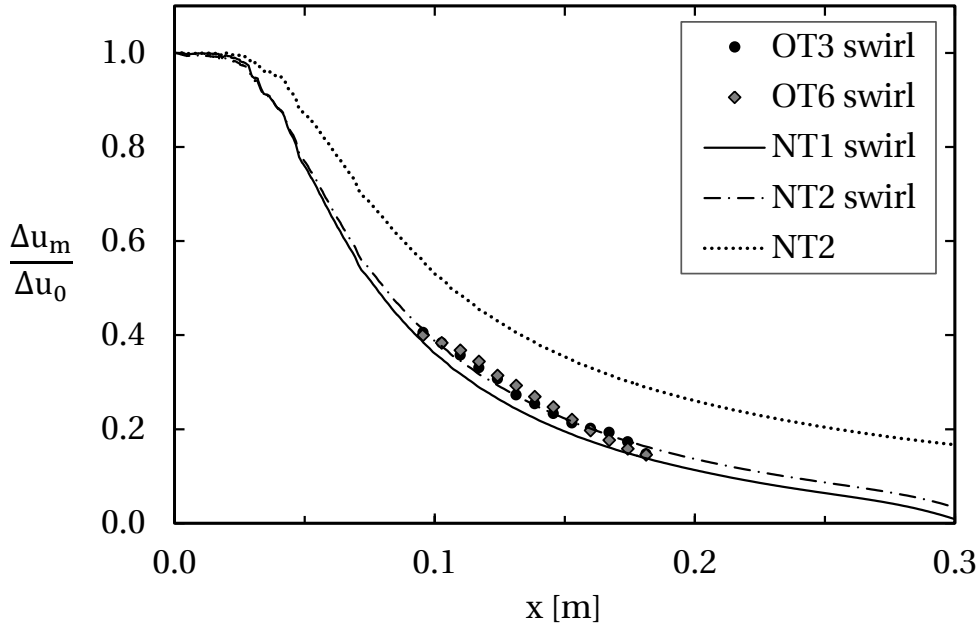


Figure 6.6: Normalised axial droplet velocity decrease along the axis for OT3, OT6, NT1 and NT2 with swirl and for NT2 without swirl.

Test	NT3	NT3 swirl	NT4	NT4 swirl
Temperature centre [°C] ($r/R = 0$)	298	298	267	262
Temperature wall [°C] ($r/R = 0.95$)	435	430	430	369
Evaporated liquid mass flow [kg h^{-1}] (CS4)	4.25	4.9	7.59	8.97
Share total liquid mass flow [%]	58	67	57	67

Table 6.3: Temperatures and evaporated liquid for NT3 and NT4 without and with swirl.

ing effect through the swirl generator is represented well. For both simulations with swirl (see figures 6.9 and 6.10 as well table 6.3) the temperatures in centre are equal to the cases without swirl. However, changes are visible for the temperature gradients between wall and centre. These gradients are smaller for these simulations. Hence, the liquid mass flow has to be more uniform. In addition the amount of evaporated liquid has increased significantly with swirl flow conditions until the catalyst front surface is reached (see ta-

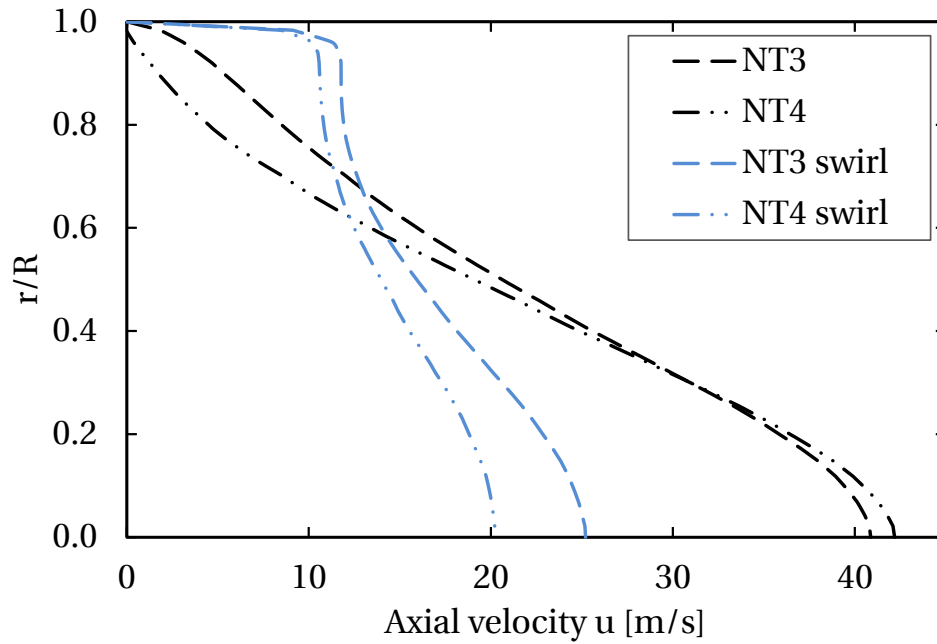


Figure 6.7: Axial velocity profiles for NT3 and NT4 (without swirl) and NT3 swirl and NT4 swirl (with swirl) at CS4.

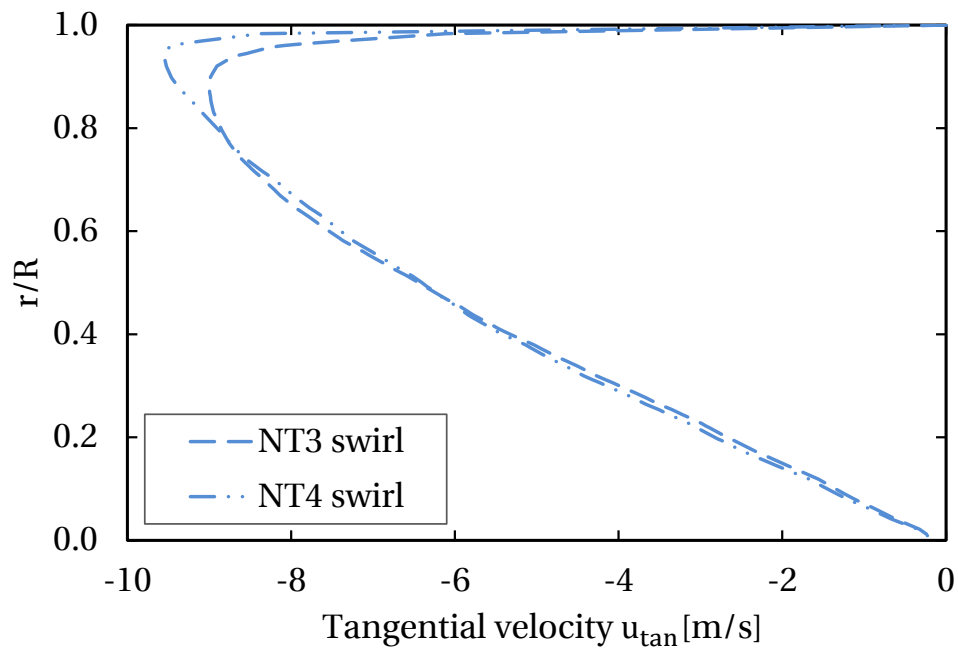


Figure 6.8: Tangential velocity profiles of NT3 swirl and NT4 swirl at CS4.

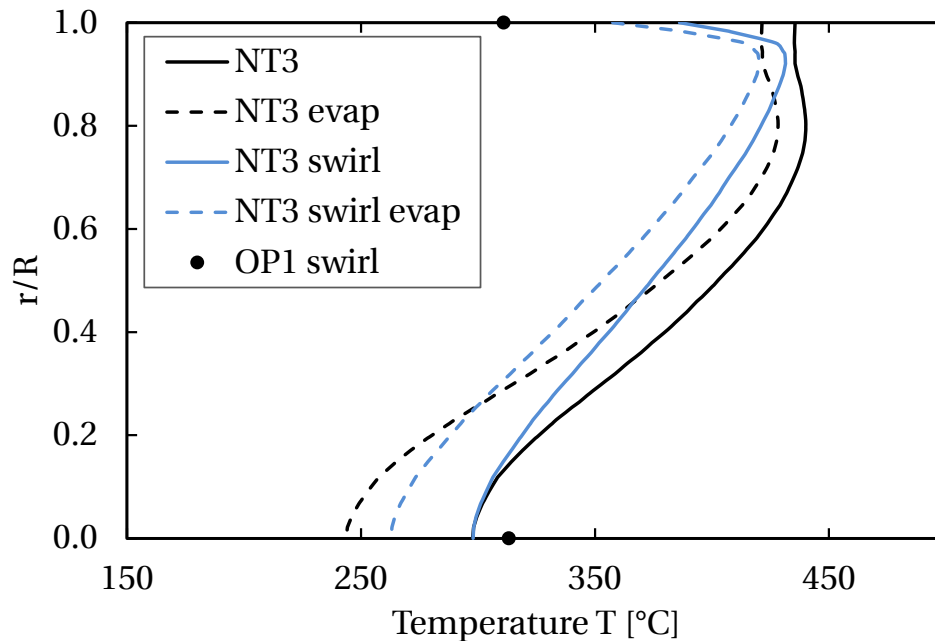


Figure 6.9: Temperatures profiles for NT3 (black line), NT3 swirl (blue line) with remaining liquid mass and NT3 evap (dashed black line), NT3 swirl evap (dashed blue line) incorporating the evaporation of the remaining liquid mass at CS4.

ble 6.3). The temperatures, incorporating the evaporation of the remaining liquid mass, underline this statement. For the optimised cases temperature decreases due to evaporation of the remaining liquid mass are smaller (see figures 6.9 and 6.10: dashed blue lines) than for the baseline reactor (figures 6.9 and 6.10: dashed black lines).

A comparison of the numerical results with the temperature measurements for the engine operating points reveal that the swirl generator has a homogenising effect.

Temperatures measured after the MX structure are nearly equal in the centre and at the wall for OP1 (see figure 6.9). The simulation of OP1 (NT3 swirl evap) reveals a temperature difference of about 150 K between centre and wall. The MX-structure allows a mixing rate of $f_{dis} \approx 0.18$ over the whole length (see section 5.4). Incorporating this for the temperature exchange a homogenisation of

about 30 K could be assumed. Hence, an adaptation of the MX structure influence to temperature exchange “NT3 swirl evap” will not lead to a comparable homogenous temperature profile as the measured one. Here, swirl effects for homogenisation are underestimated.

Looking at “NT4 swirl evap” compared with OP2 (figure 6.10) the temperature differences between centre and wall are nearly equal with approximately 140 K, but the whole profile is shifted towards smaller temperatures. Hence, in this case the homogenising effect of the swirl generator seems a little overestimated.

Another aspect is the backflow developing at the wall of the reactor domain ($0.95 \leq r/R \leq 1$). This is visible for the normalised mass fraction of water vapour (figure 6.11). The mass fraction profiles for the baseline reactor simulations (NT3 / NT4: black lines) are compared with the optimised reactor

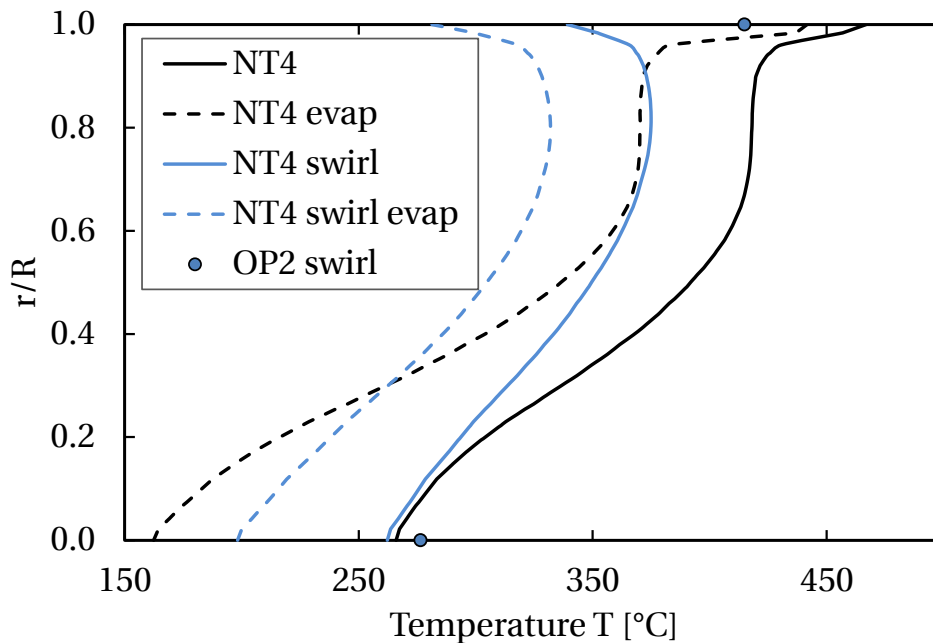


Figure 6.10: Temperatures profiles for NT4 (black line), NT4 swirl (blue line) with remaining liquid mass and NT4 evap (dashed black line), NT4 swirl evap (dashed blue line) incorporating the evaporation of the remaining liquid mass at CS4.

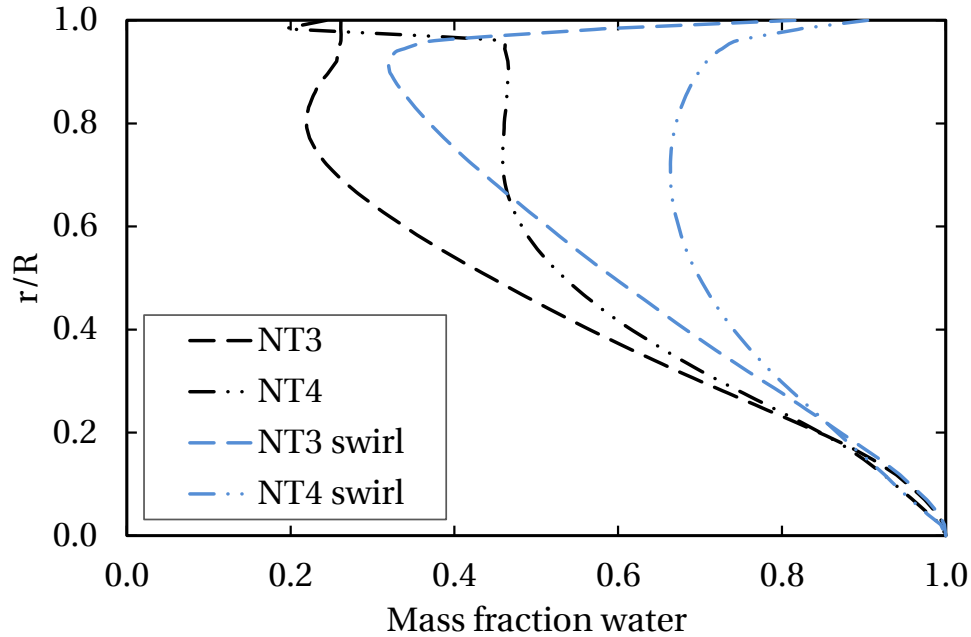


Figure 6.11: Mass fraction of water vapour of NT3 and NT4 for the baseline as well as NT3 swirl and NT4 swirl for the optimised reactor design at CS4.

simulations (NT3 swirl / NT4 swirl: blue lines). At the wall the mass fractions for the optimised cases increase significantly which is the result of the unrealistic backflow. However, the overall distribution away from the wall changes and the homogenisation effects of the swirl generator are reproduced by the numerical simulations.

The higher axial velocity gradient (figure 6.6) results in smaller velocities Δu_m in the centre of CS4 for the optimised reactor setup compared with the baseline reactor setup, leading to a shorter diffusion length (see figure 6.12 compared with figure 5.20). Additionally, the equalised temperatures have a positive effect on diffusion. The results of the diffusion process shown in figure 6.12 are related to the temperature profiles incorporating the evaporation of the remaining liquid mass. These results show that the inlet boundary conditions taken from the outlet profile of the swirl generator domain reproduce the conditions during the experiments.

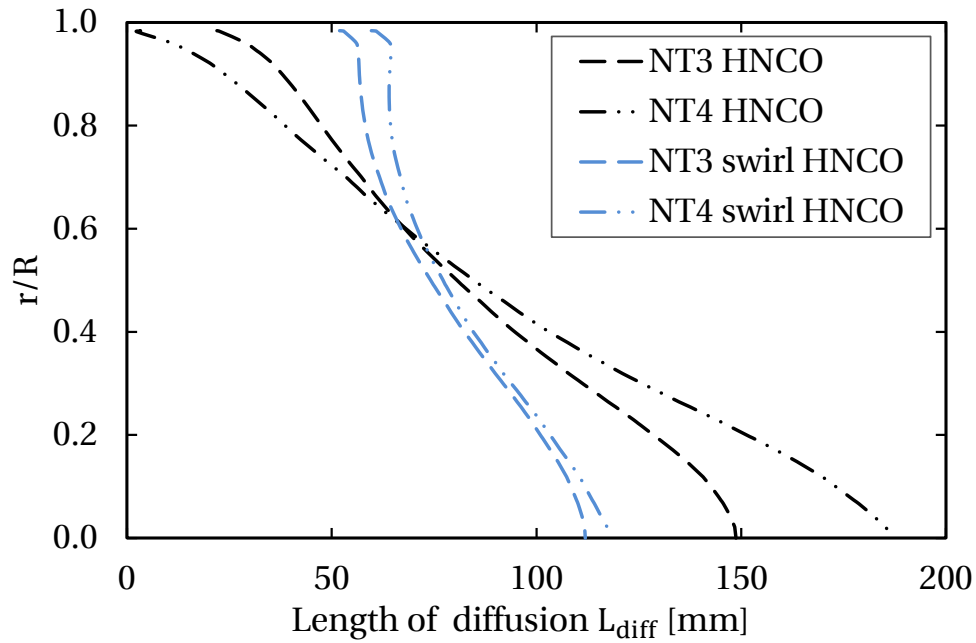


Figure 6.12: Length of diffusion profiles of NT3 HNCO and NT4 HNCO for the baseline and of NT3 swirl HNCO and NT4 swirl HNCO for the optimised reactor design.

To summarise, main aspects of the optimised reactor design are represented well by the numerical simulations. The simulation model is considered applicable as a design method for hydrolysis reactors.

7 Hydrolysis Reactor Design Method

In this chapter the previously discussed analytical and numerical methods are merged to establish a comprehensive method for the design of hydrolysis reactors. The presented procedure provides in a first loop a prediction of performance for an initial design of a reactor, thus it is applicable especially as a pre-design tool. Using this method as an iteration process allows an optimisation of the reactor design (e. g. reduction of overall reactor size). The steps involved in this design method are explained and summarised in a process flow chart (see figure 7.1). For illustration purposes, the design method is applied to a case study.

7.1 Steps of the Design Method

Usually, urea hydrolysis reactors are continuous flow reactors which means that tank reactors are not included in this approach. Furthermore, analytical and numerical models are based on circular cross sections of the reactor and two-phase injectors with a full-cone spray profile, concentrically mounted in the flow reactor upstream of the catalyst. Modifications of analytical or numerical modelling approaches may reduce the restrictions. Figure 7.1 presents an overview of the design method. Steps E1 - E8 are described in the following. Tables 7.1 and 7.2 shows the required and optional input parameters, their origin and function.

7.1 Steps of the Design Method

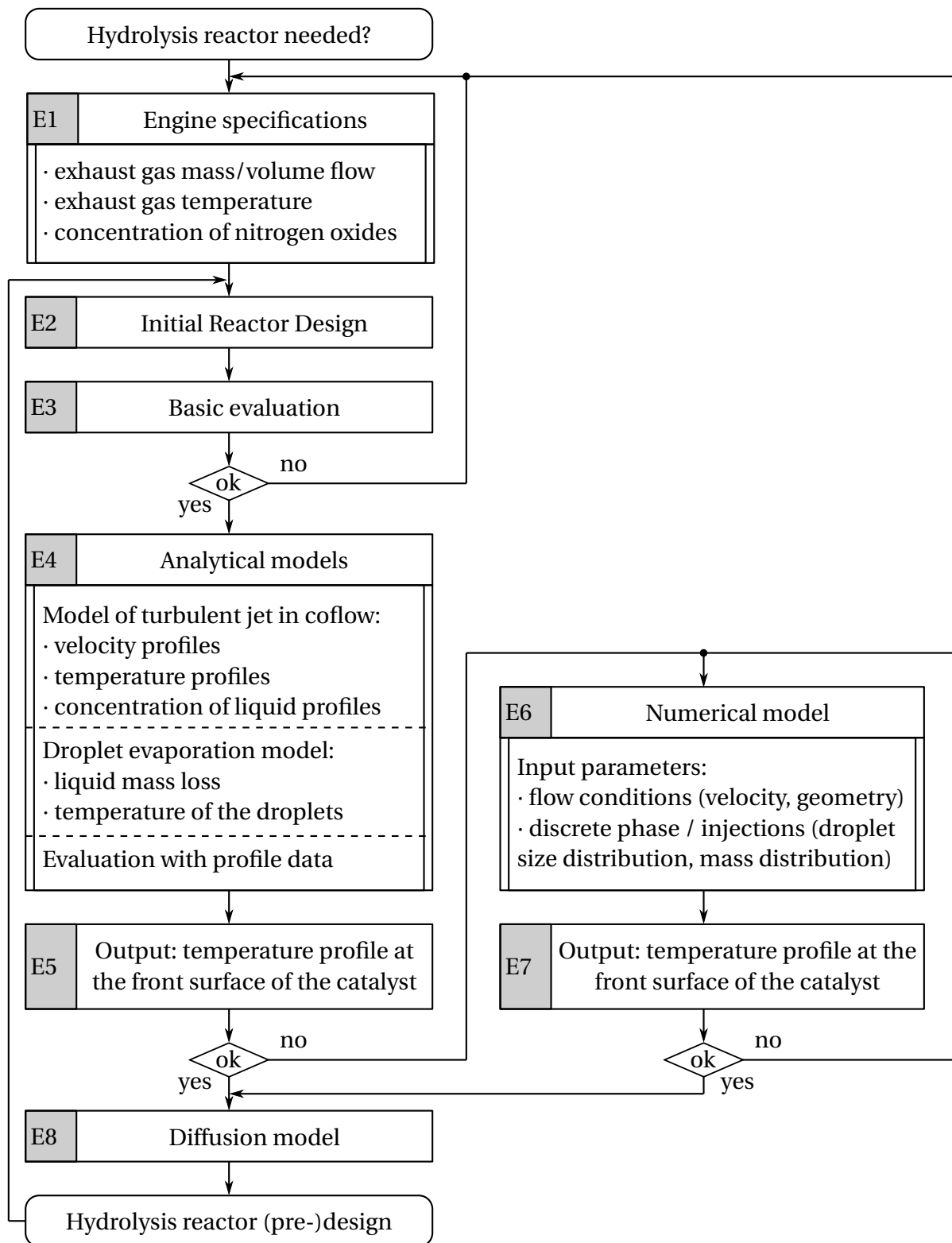


Figure 7.1: Procedure of the hydrolysis reactor design method.

Parameter	Source	Function	Required	Optional
E1 - Engine Specifications				
Exhaust gas mass flow [kg h^{-1}]	Engine specification	fluid dynamic condition	✓	
Exhaust gas temperature [$^{\circ}\text{C}$]	Engine specification	thermal condition	✓	
Content of NO_x [ppm]	Engine specification	amount of urea needed	✓	
E2 - Initial Reactor Design				
Maximum length of reactor [m]	geometric constraints of installation space	thermolysis and hydrolysis of urea	✓	
Maximum length of catalyst [m]	geometric constraints of installation space	hydrolysis of urea		✓
Maximum diameter of catalyst [m]	geometric constraints of installation space	reveal fluid dynamic conditions	✓	
Injector	data sheet	spray properties	✓	

Table 7.1: Required or optional input parameters.

Parameter	Source	Function	Required	Optional
E4 - Analytical Models				
Air-to-liquid ratio injector	individually adjustable (data sheet)	calculation characteristic diameters, needed for two-phase jet modelling	✓	
Droplet size distribution	experiments, injector data sheet, empirical functions	droplet evaporation modelling		✓
Characteristic diameters (e. g. SMD)	experiments, injector data sheet, empirical methods	droplet evaporation modelling	✓	

Table 7.2: Required or optional input parameters.

E1 - Engine Specifications

Engine specifications are assumed to be known, in particular the exhaust gas mass / volume flow, its temperature and content of nitrogen oxides. In general, these parameters vary with the engine operating conditions. It is beneficial to account for the most relevant operating conditions for an initial design. It must be taken into consideration that the most relevant engine operating conditions do not necessarily represent the most critical operating conditions for potential catalyst deactivation due to solid by-product formation. A short explanation to identify potentially critical operating conditions is given after the basic evaluation (see element: E3). From the known engine specifications and the underlying emission standard the required reduction of nitrogen oxide is calculated. The required amount of the reducing agent ammonia or urea is identified accordingly.

E2 - Initial Reactor Design

In the next step of the design method the reactor dimensions have to be defined, especially the diameter and the total length of the reactor, but also the positioning of the two main components (catalyst and injector) in the flow channel. In general, exhaust systems of different applications underlie geometric constraints which are mainly given by the available installation space. Hence, diameter or length of the reactor or both are restricted. The proposed method requires these values as boundary conditions; otherwise, the ideal hydrolysis reactor would be irrationally large, due to the requirement for long residence time and reduction of heat losses (which are not accounted for in the present method). Initial reactor diameter and length should be chosen as large as possible for the pre-design. Beneficial effects of structured catalyst foils are often shown in literature [24, 89], thus structured foils in combination with high GSA values should be chosen. To define an appropriate injector, the liquid mass flow rate to be atomised and the pressurised air mass flow rate available are conditions to fulfill. Suppliers of injectors provide information about characteristic droplet diameters and necessary air-to-liquid ratios. Small droplet sizes at low air-to-liquid ratios are advantageous. Droplets of the spray should only impinge on the catalyst, an impingement on uncoated

wall surfaces upstream of the catalyst should be avoided. The catalyst surface should be used completely, if possible. Hence, three important parameters can be extracted which are dependent on each other in this context: the diameter of the catalyst, the cone angle of the spray and the distance between nozzle and catalyst. If two of these three parameters are known, the remaining one can be calculated. Usually, the catalyst diameter and the spray cone angle are known, thus the distance between the injector and the catalyst is specified:

$$L = \frac{D_{cat}}{2 \cdot \tan(0.5\Phi)}, \quad (7.1)$$

where L is the distance between injector and catalyst, D_{cat} the diameter of the catalyst and Φ the spray cone angle. To summarise, catalyst diameter and type, overall reactor length as well as the injector have to be prescribed to apply the design method. In an iterative loop optimisation is possible.

E3 - Basic Evaluation

In element three (E3) of the process the first iteration loop of the method is shown. On the basis of the engine specifications and the amount of reducing agent needed, a first thermodynamic feasibility analysis (called basic evaluation in the flow chart, see section 2.2.3) is performed:

$$\dot{Q}_{in} = \dot{Q}_{out} + \dot{Q}_{loss} + \dot{Q}_{evap} , \quad (7.2)$$

$$\dot{Q}_{evap} = \dot{m}_l \cdot \Delta h_v . \quad (7.3)$$

This basic evaluation equates heat fluxes within the system (see equation 2.13 and 2.14 for explanation). It is determined whether the heat carried by the exhaust gas stream is sufficient to evaporate the liquid UWS, while the mean flow temperature is still higher than 200–250 °C after evaporation. Additionally, the GHSV, the characterisation value for the chemical decomposition often used in process engineering, can be calculated from the ratio of total volume flow to catalyst volume (see also equation 2.15):

$$\text{GHSV} = \frac{\dot{V}_{\text{evap}}}{V_{\text{cat}}} \quad (7.4)$$

In order to find the most critical operation conditions it is instructive to perform the basic evaluation for different operating points. Results for the average system temperature after evaporation reveal conditions where temperatures are lowest and potentially critically close to temperatures leading to solid by-product formation.

If the feasibility analysis proves that the exhaust gas stream cannot evaporate the entire liquid mass and keep the system temperature higher than 200–250 °C an entirely new setup has to be considered. This aspect indicates the first decision point in the flow chart which leads back to the engine specifications. As engine specifications are in general fixed the return to this point should symbolise that only alternative concepts are realisable in such a case, for example, repositioning the reactor (e. g. in front of the turbocharger) in the exhaust system, where temperatures are higher. An additional heating system for the catalyst may be another possible solution. If the result of the feasibility analysis indicates that the exhaust gas stream can evaporate the liquid mass with system temperature higher than 200–250 °C the next process step can begin.

E4 - Analytical Models

The success of the reactor design is significantly dependent on the decomposition process proceeding without formation of any solid by-products. During the chemical decomposition process, irreversible by-products are primarily formed due to temperatures below the critical reaction temperature. Usually only a part of the liquid mass flow is transferred into gaseous phase by droplet evaporation. The remaining share of liquid phase is evaporated at the catalyst. The impinging droplets are evaporated at the hot surface of the catalyst and remove heat from the catalyst in this region. Further continuous supply of liquid to this surface region leads to a continuous cooling of the surface until the critical temperature is reached, if the regeneration time for heating the sur-

face is too small. Consequently, by-products can be formed globally but also locally at the specific surface region with sub-critical temperature. In general it can be assumed that a major share of droplets impinges on the front surface of the catalyst. As a consequence the risk of irreversible by-products is highest at this location. The design step shown in element four (E4) covers the analytical modelling and is dedicated to the calculation of local temperatures at the front surface of the catalyst. Based on the turbulent jet theory (see chapter 2.5 and 5.3), dimensionless axisymmetric concentration profiles of the liquid distribution are calculated (parameters were introduced in chapter 2.5):

$$\frac{\Delta\chi}{\Delta\chi_m} = \sqrt{\frac{\Delta u}{\Delta u_m}}, \quad (7.5)$$

where

$$\frac{\Delta u}{\Delta u_m} = \left[1 - \left(\frac{y}{b} \right)^{1.5} \right]^2 = (1 - \xi_1^{1.5})^2 \quad (7.6)$$

Incorporating the mass flow rate, a concentration profile is obtained at the front surface of the catalyst.

Droplet evaporation based on the d^2 -model provides the opportunity to calculate the droplet liquid mass loss for specific initial droplet diameters (e. g. Sauter diameter) within the evaporation section:

$$\frac{d(d_{dr})}{dt} = \frac{4 \cdot \lambda_{vap} \ln(1 + B_M)}{\rho_{dr} \cdot c_{p,vap} \cdot d_{dr}} \cdot \frac{Nu}{Nu_0}. \quad (7.7)$$

Hence, the already evaporated liquid mass until the catalyst is reached and the temperature of droplets impinging on the catalyst can be calculated. It can be assumed that evaporated urea has completed the thermolysis process, hence isocyanic acid and ammonia were produced. As isocyanic acid in gaseous state will not condensate at temperatures expected within the reactor (see chapter 2.2 and [30]) only the remaining liquid urea can contribute to

solid by-product formation. This provides an upper bound for the potential rate of solid by-product formation at the catalyst.

E5 - Temperature at the Catalyst

Next, three types of temperature profiles are computed. For the first type, it is assumed that all remaining liquid mass evaporates instantly at the catalyst front surface. In addition, evaporation within the evaporation section is entirely neglected. Assuming complete evaporation at the front surface represents a worst-case for the surface temperature reduction (see chapter 5.4 with equations 5.5 and 5.6):

$$T(r) = T_0 - \frac{\dot{Q}_{evap}(r)}{\dot{m}_A \cdot c_p} , \quad (7.8)$$

where

$$\dot{Q}_{evap}(r) = \frac{\dot{m}_L \cdot \Delta h_v}{\int_0^R \chi(r) dr} \cdot \chi(r) . \quad (7.9)$$

The second one only includes the droplet evaporation (liquid mass reduction) and the effect on the bulk temperature evolution until the catalyst front surface is reached.

The third option integrates the evaporated share of liquid mass within the evaporation section in the concentration distribution. Thereafter, the temperature decrease due to the remaining liquid at the catalyst surface is calculated. Note that this last option, although physically most accurate and complete, shows significant sensitivity of the results on the input values for droplet size. The more precise the droplet size distribution is known and incorporated the more precise the results obtained with this model. Thereby, a comparison of droplet evaporation on the temperature reduction upstream of the catalyst front surface and the temperature reduction resulting from surface evaporation is possible. Additionally, knowing the evaporated liquid mass upstream of the catalyst provides the maximum amount of solid by-products possibly

formed due to surface evaporation (see chapter 2.2).

If the calculated temperatures are higher than the critical one across the whole surface, the design method continues with the last step, the application of the diffusion model. Otherwise, if the calculation reveals regions of low temperature, the second iteration step and decision point in the process is reached. Non-uniform temperature profiles with regions of critically low temperatures are generally the result of an inhomogeneous liquid mass distribution through the injector and / or an inadequate mixing of the droplets with the exhaust gas. To address these potential problems, the first option is to improve the spray (e. g. homogenise the droplet size distribution, generate smaller droplets etc.). The second option is to enhance the mixing of droplets and exhaust gas to achieve a more homogenous mass distribution. A third possibility is the adjustment of the boundary conditions (e. g. engine specifications or a heated catalyst). The present design method offers the second option, an improvement of the mixing process. This is accomplished by the numerical model (see chapter 4, 5.5 and 6.2) in the side branch of the flow chart (element E6).

E6 / E7 - Numerical Model

Numerical simulation provides the opportunity to analyse and optimise the mixing process of spray and exhaust gas. A domain and mesh is generated for the specific reactor considered. Using inlet conditions (mass flow rates, temperature, etc.), injector specifications and reactor dimension of the setup, the numerical model should lead to comparable results between simulation and analytical calculations (and measurements, if existing; see chapters 5.5 and 6.2). In a second step this model is extended by a mixture-improving component, which is a swirl generator in the present work, see chapter 6. Adaptations of the nozzle specifications or of the reactor dimensions could also be studied by the numerical model. The reaction of the system behaviour to changes of specific parameters can be investigated. The iteration process is completed if temperatures above the critical temperature are achieved everywhere at the catalyst front surface (element seven: E7). Following this, the last process step of the method is conducted, the diffusion model in element eight (E8) of the chart flow.

E8 - Diffusion Model

Lastly, the diffusion model is used to calculate the catalyst length required for complete chemical decomposition through the hydrolysis reaction (chapter 2.2.2 and 5.2.2). This process step is related to E5 by the assumption that the entire remaining liquid mass is evaporated at the catalyst front surface and the system temperature is above the critical temperature. The binary diffusion process for gaseous substances in laminar flow inside the catalyst channels is calculated (further equations and explanations are given in chapter 2.2.2). The binary diffusion coefficient is:

$$D_{12} = \frac{0.00143 \cdot T^{1.75} (M_1^{-1} + M_2^{-1})^{0.5}}{p \cdot \sqrt{2} (\sqrt[3]{\sum \Delta v_1} + \sqrt[3]{\sum \Delta v_2})^2}, \quad (7.10)$$

The mass transfer coefficient is defined as:

$$\beta = \frac{D_{12} \cdot \text{Sh}}{d_h}. \quad (7.11)$$

Turbulence promoters of special catalyst structures are not accounted for in this context. As soon as all substances are gaseous the model describes the time a molecule of a specific substance needs to diffuse to the catalytic surface in order to react. The binary diffusion coefficient of molecules of the two reaction partners, HNCO and water, differ because of their difference in the molecular mass. This leads to different diffusion times and paths, where HNCO has higher diffusion times and paths. If a catalyst length is predefined the calculation reveals whether the length is sufficient for complete conversion or whether a part of the decomposition has to be performed at the SCR catalyst. Otherwise, the catalyst length required for complete conversion is determined by the model.

The final result is a hydrolysis reactor pre-design with a substantially higher chance to reach the desired performance, especially with respect avoiding to solid by-product formation. All parameters required to construct a prototype are determined by the design method.

7.2 Application of the Design Method (Case Study)

In the following the model is applied to OP3 as defined in table 3.1. Engine specifications of all operating points are known. OP3 shows a high emission of nitrogen oxides in conjunction with a low exhaust gas temperature and a low exhaust gas mass flow rate compared to other operating points. Hence, this operating point has an unfavourable ratio of required UWS to exhaust gas mass flow and is the one to be identified as a critical operating point for the hydrolysis reactor. Dimensions of the reactor (E2 of the flow chart) were specified by the project partner. The hydrolysis reactor is supposed to be located on a platform between engine and turbocharger in a bypass system to the main exhaust gas system. The platform determined the maximal length of the reactor. The diameter was chosen as DN100 as this is a standard catalyst diameter and because of experience with this size. Standard components were chosen as economic viability had a high priority. Likewise, an in-house developed injector (MAN injector characterised in the present work) was used. The injector design was based on the Schlick 940 nozzle and measurements revealed similar results for both injectors (see 5.1.3). Spray cone angles of both nozzles are known (see figure 5.12, but also data-sheet [84] of Schlick 940) which leads to a calculated distance between injector and catalyst of 0.26 m. Because of the expected jet constriction due to the coflow, the distance was defined a little larger than the calculated one. The length of the catalyst was prescribed with 200 to 250 mm to satisfy the maximum length of the reactor given by the installation space. The basic evaluation in E3 reveals an average temperature of about 335 °C for OP3, the space velocity (GHSV) for OP3 was already calculated in table 5.1. Hence, the iteration loop related to this step of the design method is not necessary and the next step (E4), the calculation of local temperatures at the catalyst front surface, is calculated.

The three temperature profiles calculated from turbulent jet theory equations incorporating droplet evaporation are shown in figure 7.2. Here “OP3 calc surface evap” represents the temperature profile already shown in figure 5.18. “OP3 calc drop evap” represents the droplet evaporation upstream of the catalyst front surface included in the bulk temperature decrease and “OP3 calc

Test		OP1	OP2	OP3	OP4
Temperature front surface ($r/R = 0$) [°C]	calculated (surface evaporation)	328	200	170	216
	measured	250	169	–	–
Temperature front surface ($r/R = 1$) [°C]	calculated (surface evaporation)	458	483	505	545
	measured	426	414	–	–

Table 7.3: Temperatures measured and calculated with turbulent jet theory for all engine operating points.

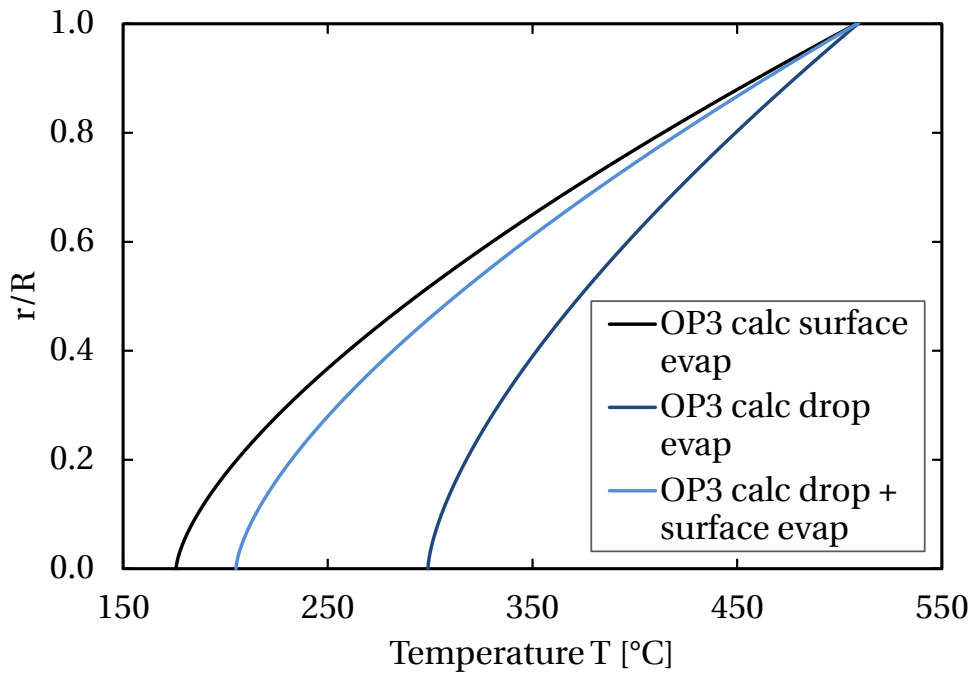


Figure 7.2: Temperature profiles calculated for OP3: surface evaporation of all liquid (OP3 calc surface evap: black line), droplet evaporation and bulk temperature decrease until the catalyst (OP3 calc drop evap: blue line) and incorporating droplet evaporation and surface evaporation of the remaining liquid mass (OP3 calc drop + surface evap: light blue line).

drop + surface evap” the third option described in section 7.1 (element E5), hence the droplet evaporation and surface evaporation of the remaining liq-

	D 1	D 2	D 3	SMD	Total
Diameter [μm]	12	40	110	45	
Volume fraction [%]	7.5	5	7	80.5	100
Evaporated Volume [%]	100	65	1.5	64	
Evaporated liquid mass [%]	7.5	3.3	0.1	51.5	62.4

Table 7.4: Evaporated liquid due to droplet evaporation for OP3.

uid at the catalyst. The droplet evaporation is calculated with the aid of the MATLAB script (see appendix A.4) for 3 characteristic droplet diameters and the Sauter diameter from measurement results for OP3 (see table 7.4). All profiles show a large difference for temperatures near the wall compared to the centre.

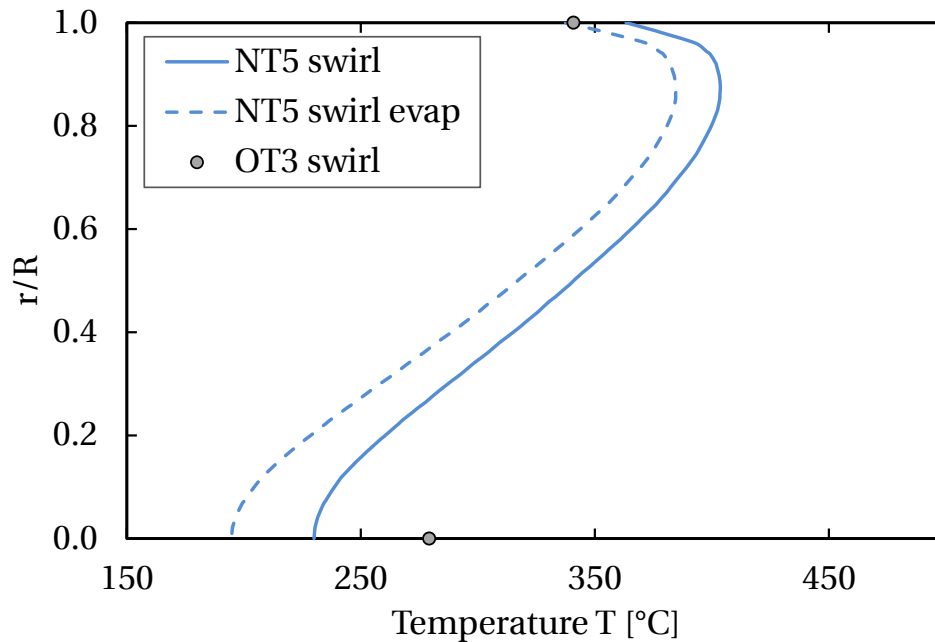


Figure 7.3: Temperature profiles for simulation of OP3 with swirl generator at CS4: with remaining liquid mass (NT5 swirl: blue line) and incorporating the evaporation of the remaining liquid mass (NT5 swirl evap: dashed blue line).

The minimum temperatures calculated for all operating points, except for OP1

and OP4, are lower than the critical temperature of 200–250 °C in the centre of the catalyst, while temperatures at the walls are similar to the inlet temperature of the exhaust gas, (see figure 5.18: 485 °C for OP2 and 502 °C for OP3). The liquid droplet distribution is concentrated in the centre of the spray, thus a significantly higher amount of liquid has to be evaporated in this region. Operating under these conditions will lead to irreversible by-products at the catalyst surface, blocking the channels (see figure 5.1, which shows by-products formed during tests for OP2, but OP3 would be even worse, as the temperature calculated is lower). High concentration of droplets in the centre of the spray can be counter-acted by intensifying the interaction of jet and coflow. This was shown in chapter 6 for OP1 and OP2 or NT3 and NT4. Three-dimensional flow, such as vortex flows provided by a swirl generator, can hardly be described analytically. For this reason a numerical model of the system is set up.

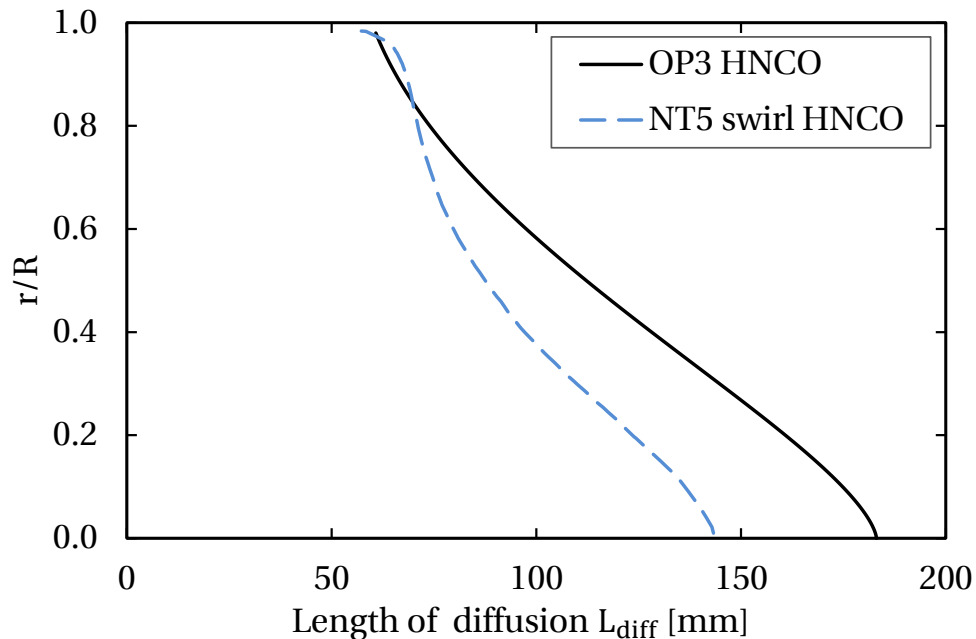


Figure 7.4: Length of diffusion of HNCO: OP3 HNCO for the baseline reactor setup and NT5 swirl HNCO for the optimised reactor design.

The numerical simulation results of OP3 (NT5) for the optimised reactor with swirl generator are displayed in figure 7.3. The interaction of the swirling coflow with the jet is beneficial, and the temperatures at the front surface are

homogenised and higher than 200 °C everywhere. The last step E8 of the design method can be performed, the calculation of the diffusion process (see section 6.2: e. g. figure 6.12). For OP3 the minimum catalyst length is 145 mm to ensure complete conversion, assuming all liquid is gaseous when entering the catalyst. In figure 7.4 the diffusion length is calculated as a function of radius and shown in comparison to the calculated one for the baseline reactor setup in chapter 5.3 figure 5.20.

8 Summary and Conclusion

The introduction of new regulations in MARPOL/Annex VI, including an enforcement of the TIER norm, requires an NO_x reduction of about 70 % in Emission Controlled Areas for the shipping sector. Engine-based measures and combustion optimisation cannot entirely meet these emission targets. Hence, exhaust gas treatment for NO_x is required. Selective catalytic reduction is one of the most efficient conversion techniques for NO_x . It reduces NO_x to H_2O and N_2 with the aid of ammonia, in this case produced from the nontoxic precursor urea, in a catalytic process. The decomposition of urea into ammonia and CO_2 is supported catalytically by a hydrolysis unit. The first objective of the present research was the design of a hydrolysis reactor for large marine diesel engine exhaust gas systems with a significant reduction of the geometrical dimensions. The second objective was the development of a design method for such reactors.

The hydrolysis reactor was placed in a bypass system to reduce the activation energy needed for the decomposition process to gain a wider variability of the boundary conditions. The first hydrolysis reactor design exhibited an insecure performance (solid by-products were formed during operation) for the specified engine operating points. The experiments showed a non-uniform distribution of the liquid urea-water solution which led to critically low temperatures and the formation of solid by-products at the catalyst front surface. An optimised reactor was designed in order to extend the operating limits inherent to the previous design. The radial liquid distribution was homogenised by introducing a swirl generator. Experiments with the optimised reactor design showed a secured process in all operating points and indicated the potential for further mass flow increase. A detailed analysis of the hydrolysis reactor performance was conducted to identify the influence of different parameters on the system performance, such as droplet velocity, gas temperature or wa-

ter content. Ammonia concentration and velocity measurements as well as spray characterisation measurements were conducted. The major findings are as follows:

- Gas and droplet velocity, gas temperature, water content, catalyst structure and length as well as the gas hourly space velocity are identified as relevant parameters influencing system performance. Besides temperature, the flow structure, velocity and water content in the system are identified as the most relevant parameters governing the thermolysis process.
- Investigated parameters have a significantly higher influence on the thermolysis process (thus the evaporation of urea and the first decomposition) than on the hydrolysis which prove to be significant for the system performance.
- Once urea is evaporated the hydrolysis proceeds well.

A modelling approach for hydrolysis reactors in the form of a step-by-step method is presented. As a first step, a feasibility study (basic evaluation) is performed based on geometrical design constraints and engine performance data. Analytical and numerical models are applied in further steps:

- Velocity, temperature and concentration profiles are calculated from the theory of confined jets in coflow. Radial profiles are derived at the front surface of the catalyst. Temperature profiles can reveal low temperatures at the catalyst centre, which can lead to solid by-product formation.
- The d^2 -law is used to estimate the amount of evaporated liquid mass upstream of the catalyst. The reduction of exhaust gas temperature due to droplet evaporation can be determined. For the cases studied in the present work, about one half of liquid mass evaporates upstream of the catalyst surface.
- Binary molecular gaseous diffusion determines the mass transfer coefficient and diffusion length for water and isocyanic acid inside the catalyst channels. The catalyst length required for complete hydrolysis reaction can be computed.

The presented analytical model allows for a comprehensive investigation of flow effects, evaporation, critical surface regions of the catalyst for the formation of irreversible by-products and diffusion processes inside the catalyst.

In addition, numerical simulation allows the validation and optimisation of the design:

- A numerical model including a discrete phase based on specific spray characteristics such as characteristic droplet diameters, spray cone angle and mass distribution is set up. Simulations show encouraging agreement with measurement results. The results underscore the benefits of numerical models in the present context compared to the analytical methods especially for droplet evaporation and swirling flows.
- Variation of parameters governing the system performance leads to an optimised reactor design.

Further loops of the procedure can be used as iterative optimisation tool.

A Appendix

A.1 Droplet Breakup

Droplet formation is separated into so-called primary and secondary breakup. Both can be subdivided further into different breakup mechanisms. One of the most common classifications of primary breakup mechanisms are the modes of disintegration by Reitz (figure A.1). This approach divides the primary breakup in four mechanisms groups.

An increase of the relative velocity between droplet and surrounding gas provokes the secondary breakup. It describes the further breakup of al-

Regime	Description	Predominant drop formation mechanism	Criteria for transition to next regime
1	Rayleigh breakup	Surface tension force	$We_A > 0.4$ $We_A > 1.2 + 3.4Oh^{0.9}$
2	First wind-induced breakup	Surface tension force; dynamic pressure of ambient air	
3	Second wind-induced breakup	Dynamic pressure of ambient air opposed by surface tension force initially	$We_A > 40.3$ $We_A > 13$
4	Atomisation	Unknown	

Table A.1: Classification of jet breakup regimes according to Reitz [64]

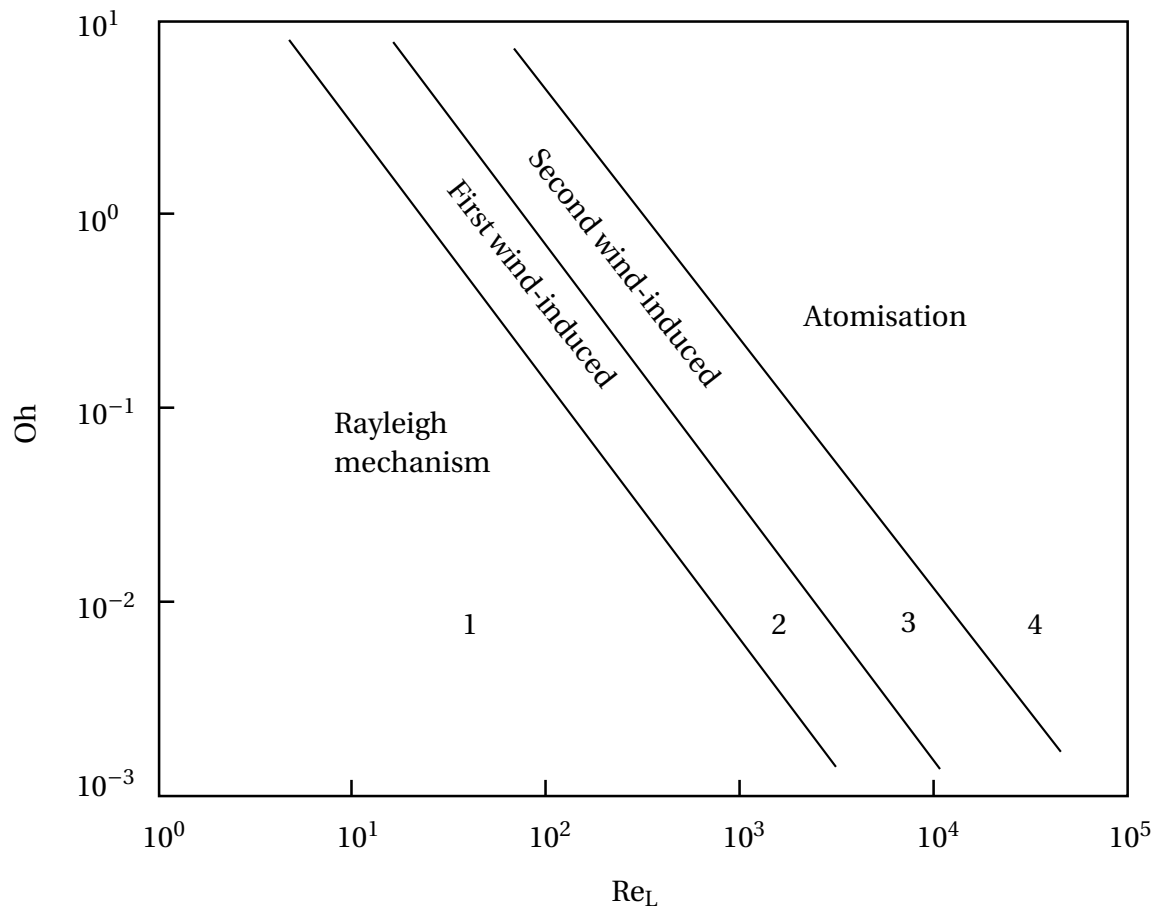


Figure A.1: Modes of disintegration for the primary breakup by Reitz [64].

ready formed droplets from the primary breakup process. The secondary droplet breakup is classified by the critical Weber number in different breakup regimes. Some of these are shown in figure A.2. Detailed description and further information about modelling of secondary breakup mechanisms are given in *Lefebvre and Wozinak* [64, 97].

A.2 Droplet Evaporation






	Vibrational breakup	$We < 12$
	Bag breakup	$12 < We < 50$
	Bag and stamen breakup	$50 < We < 100$
	Sheet stripping	$100 < We < 350$
	Catastrophic breakup	$350 \ll We$

Figure A.2: Secondary droplet breakup mechanisms [63].

A.2 Droplet Evaporation

Heat Transfer

The heat flow given from the hot gas stream to the droplet is calculated by :

$$\dot{Q} = \alpha A_{dr} (T_{\infty} - T_{dr}) \quad (\text{A.1})$$

α is the heat transfer coefficient, A_{dr} the surface of the droplet, T_{∞} the temperature of the hot gas stream and T_{dr} the temperature at the droplet surface. In order to simplify calculations, it is assumed that the temperature at the droplet surface is equivalent to the temperature of the whole droplet, thus no temperature gradient exists inside the droplet. The heat transfer coefficient is defined as:

$$\alpha = \frac{\text{Nu} \cdot \lambda_{vap}}{d_{dr}} \quad (\text{A.2})$$

where λ_{vap} is the thermal conductivity of the gas-vapour mixture surrounding the droplet, d_{dr} the initial diameter of droplet and Nu is the Nusselt number.

Forced convection, characterised by the Nusselt number, accelerates the

droplet evaporation as the velocity differences between gas and droplet lead to a decrease in boundary layer thickness, hydrodynamic as well as thermal. There are two relevant relations given by *Lefebvre* for this key figure [64]:

$$\frac{\text{Nu}}{\text{Nu}_0} = 1 + 0.276 \cdot \text{Re}_{dr}^{0.5} \cdot \text{Pr}^{0.33} , \quad (\text{A.3})$$

and

$$\text{Nu} = 2 + 0.6 \cdot \text{Re}_{dr}^{0.5} \cdot \text{Pr}^{0.33} , \quad (\text{A.4})$$

where $\text{Nu}_0 = 2$ (the Nusselt number of a droplet at rest) and the Prandtl number Pr , describing the relation of viscose to thermal boundary layer, is found as a function of the material properties dynamic viscosity, heat capacity and thermal conductivity:

$$\text{Pr} = \left(\frac{\mu \cdot c_p}{\lambda} \right)_{vap} = \left(\frac{\nu}{a} \right)_{vap} . \quad (\text{A.5})$$

Mass Transfer

As already mentioned in chapter 2.4, mass flow transferred into the gaseous phase is almost linearly dependent on the concentration gradient between liquid and air (for the exact solution refer to [85]). Hence, the vapour composition/concentration surrounding the droplet influences the concentration gradient. This is considered in the derivation of the droplet evaporation process. The mass flow rate transferred for a substance S can be calculated by:

$$\dot{m}_S = \beta_c \cdot A_{sur} \cdot (\rho_{S_{sur}} - \rho_{S_{\infty}}) = \beta_c \cdot \frac{A_{sur}}{R_{spS}} \cdot \left(\frac{p_{S_{sur}}}{T_{sur}} - \frac{p_{S_{\infty}}}{T_{\infty}} \right) , \quad (\text{A.6})$$

where β_c is the mass transfer coefficient, A_{sur} is the surface of the droplet and R_{spS} the specific gas constant for the substance S . The partial pressure at the surface of the droplet ($p_{S_{sur}}$) is equivalent to the vapour pressure:

$$p_0 = k_p \cdot \exp\left(\frac{\Delta h_v}{\bar{R} \cdot T}\right) , \quad (\text{A.7})$$

with the specific evaporation enthalpy Δh_v and the constant k_p . These values can be extracted from two points of the vapour pressure curve. From these equations, the direct connection between heat- and mass transfer is obvious, as the vapour pressure has a dependency on the temperature. The analogy of heat- and mass transfer is commonly known, thus the mass transfer coefficient is calculated similar to the heat transfer coefficient from material properties by:

$$\beta_c = \frac{\text{Sh} \cdot D_{S_{12}}}{d_{dr}} . \quad (\text{A.8})$$

The Sherwood number is a dimensionless number characterising the convective mass transport and $D_{S_{12}}$ is the mass diffusivity of the substance. The Sherwood number has to be considered in the context of forced convection. Once more, the analogy to the heat transfer is visible. The geometric and flow properties are incorporated in the Reynolds number and the Schmidt number describes the ratio of kinematic viscosity to the mass diffusivity. It substitutes the Prandtl number used for heat transfer description (equation A.3 and A.4):

$$\text{Sh} = 1 + 0.724 \cdot \text{Re}_{dr}^{0.48} \cdot \text{Sc}^{1/3} , \quad (\text{A.9})$$

with

$$\text{Sc} = \frac{\nu}{D_{S_{12}}} . \quad (\text{A.10})$$

The mass diffusivity in liquids is a complex value to calculate, as in contrast to the binary mass diffusivity in gases, the concentrations have to be considered besides pressure and temperature [93]. An additional dimensionless number, the Lewis number (Le) can be quantified which is defined as the ratio between the thermal diffusivity and the mass diffusivity. In many cases the Lewis number is estimated to be unity. Hence, one of the two diffusion coefficients has

to be given which is in general the thermal diffusivity (for more detailed information refer to [64]):

$$\text{Le} = \frac{a}{D_{S_{12}}} = \left(\frac{\lambda}{\rho \cdot c_p \cdot D_{S_{12}}} \right)_{vap} \approx 1 . \quad (\text{A.11})$$

Heating Phase and Isothermal Evaporation

To calculate the heating phase the influence of the vapour concentration surrounding the droplet is incorporated. The convective transport is integrated in order to calculate the droplet mass loss over the time. The basis of the following equations is part of the liquid film theory [57] and is used by various authors in this context [16,37].

$$\frac{dT_{sur}}{dt} = \frac{\dot{m}_S \cdot \Delta h_v}{c_{p_{dr}} \cdot m_{dr}} \left(\frac{B_T}{B_M} - 1 \right) , \quad (\text{A.12})$$

represents the differential droplet temperature at the droplet surface. The differential change of droplet diameter during the heating period is given by:

$$\frac{d(d_{dr})}{dt} = \frac{4 \cdot \lambda_{vap} \ln(1 + B_M)}{\rho_{dr} \cdot c_{p_{vap}} \cdot d_{dr}} . \quad (\text{A.13})$$

The assumption made is that the droplet is at rest in relation to the adjoining flow. It is sufficiently exact for small initial droplet sizes as it is expected that they will follow the flow.

For the isotherm evaporation phase the d^2 -law (equation 2.34) was introduced in chapter 2.4.1. The reference temperature in equation 2.35 and the vapour concentration in equation 2.36 are given. Taking the expression for the mass transfer $\ln(1 + B_M)$ from equation A.13 and including the total mass it can be written after further conversion as [37]:

$$\ln(1 + B_M) = \ln\left(\frac{m_t - m_{S_\infty}}{m_t - m_{S_{sur}}}\right) . \quad (\text{A.14})$$

In the end the mass transfer number can be identified as:

$$B_M = \frac{m_{S_{sur}} - m_{S_\infty}}{m_{g_{sur}}} . \quad (\text{A.15})$$

Forced convection is integrated into the previous considerations. The analogy of heat- and mass transfer simplify the integration of the convective terms, as the correlations have to be taken into account only once. The differential diameter change of the droplet is converted to a differential droplet mass change:

$$\frac{dm}{dt} = \frac{d(d_{dr})}{dt} \cdot \frac{\pi}{2} \cdot d_{dr}^2 \cdot \rho_{dr} , \quad (\text{A.16})$$

using this equation, equation A.13 is converted to:

$$\frac{dm \cdot c_{p_{vap}}}{dt} = 2 \cdot \pi \cdot d_{dr}^2 \cdot \lambda_{vap} \cdot \ln(1 + B_M) , \quad (\text{A.17})$$

taking equation A.2 and the assumption of a droplet at rest into account, it leads to:

$$\frac{dm \cdot c_{p_{vap}}}{dt} = 2 \cdot \alpha \cdot \pi \cdot d_{dr}^2 \cdot \ln(1 + B_M) \cdot \frac{1}{\text{Nu}_0} = 2 \cdot \alpha \cdot A_{dr} \cdot \ln(1 + B_M) \cdot \frac{1}{\text{Nu}_0} . \quad (\text{A.18})$$

Hence, the differential droplet diameter change including convection is found to be equivalent to equation A.13, using a correction factor taken from the Nusselt correlation A.3:

$$\frac{d(d_{dr})}{dt} = \frac{4 \cdot \lambda_{vap} \ln(1 + B_M)}{\rho_{dr} \cdot c_{p_{vap}} \cdot d_{dr}} \cdot \frac{\text{Nu}}{\text{Nu}_0} . \quad (\text{A.19})$$

A.2.1 Droplet Evaporation on a Surface

Several factors influence the geometric dimension of the evaporation area. First of all, external requirements such as installation space. Furthermore spray characteristics influence the dimensioning, since urea should not come into contact with uncoated surfaces as this can lead to composition of by-products. Hence, the distance between nozzle and catalyst front surface should be adjusted to the spray cone angle of the atomiser to avoid the contact of urea with the walls of the evaporation area. This leads indirectly to a higher amount of liquid urea to be evaporated at the catalyst surface. Hence, the processes taking place if a droplet impinges coated surfaces in the context of vaporisation and decomposition of urea has to be discussed.

Droplets impinging the catalyst surface evaporate according to the available heat. Thereby, the heat transfer from surface to liquid is dependent on the temperature. The boiling curve of *Nukiyama* categorise four mechanisms (see figure A.3) [72] on heated surfaces. For this theoretical consideration to define the boiling mechanism for droplets impinging the catalyst surface, the cooling of the surface due to evaporation is neglected.

The heat flux (\dot{q}) change is illustrated in dependence to the difference between surface and saturation temperature of water (ΔT). Natural convection boiling (I) occurs for a small difference between wall temperature and saturation temperature, the heat flux is rather small. The nucleate boiling (II) region is characterised by a steady increase of the heat flux until the critical heat flux (CHF) is reached at a temperature difference of 30 K. In this region formed vapour bubbles induce the most effective heat transfer for the evaporation process. A further increase of the temperature difference provokes a decrease of the heat flux as the vapour bubbles merge and develop a vapour film between the hot surface and the liquid. This vapour film is characterised by a small heat transfer coefficient which leads to an decrease of evaporation. The minimum heat flux (MHF) is found at the so-called Leidenfrost-temperature at the intersection from the transition boiling (III) to the film boiling (IV). Region IV entails again an increase of the heat flux. However, the heat transfer coefficient hardly increases, thus an overheating of the surface can occur with a further increase

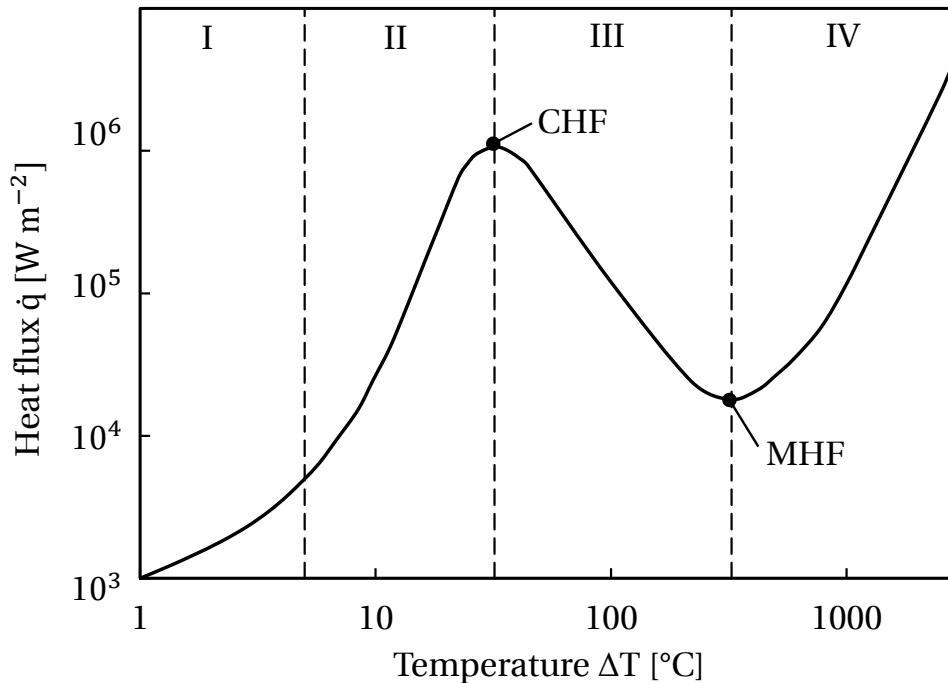


Figure A.3: Boiling curve of *Nukiyama*.

of the temperature difference. In the worst case a destruction of the surface is possible.

Film boiling should be avoided in all technical applications in order to risk surface destruction. Another aspect is the reduced heat transfer respectively heat rate. This provokes longer evaporation times and side reactions by the urea evaporation [15]. *Steinbach* investigates the occurrence of film boiling for urea in consideration of the surface structure and temperature [89]. The results show that for uncoated surfaces film boiling arises at a surface temperature of $\approx 200^{\circ}\text{C}$. Whereas, for coated surfaces nucleate boiling arises at this temperature, an increase of the surface temperature until 500°C reveals no change of the boiling mechanism.

A.3 Turbulent Jets

A.3.1 Jets in Coflow

Initial Region of an Axially Symmetric Jet

A schematic diagram of the boundary layer at the initial region for a jet in coflow is illustrated in figure A.4. Two boundaries are displayed by line one and two and specify the boundary layer thickness. While line one shows the boundary of constant initial jet velocity, line two illustrates the boundary of constant coflow velocity. Line three displays the development of the average velocity of u_0 and u_H . It is visible that the radial distances y_1 and y_2 increase to each other with increasing distance to the orifice.

The changes in the mixing process are investigated in the direction of motion as well as perpendicular to the stream which leads to distribution profiles. The x-axis is aligned with the symmetry axis of the jet. The radial distribution of the axial velocity is given by the velocity profiles at different cross sections.

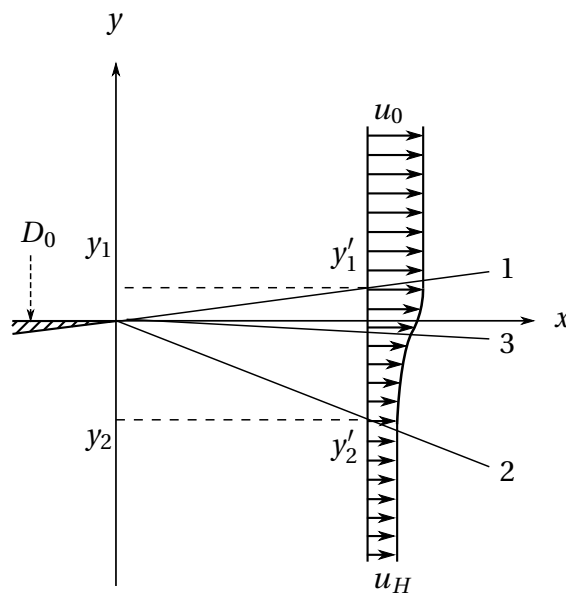


Figure A.4: Schematic illustration of the boundary layer at the initial region of a jet in coflow [1].

By plotting the dimensionless form of the values at different cross sections, all profiles coincide and a curve can be extracted as well as analytically described. The dimensionless form is obtained by relating the values to the initial values. A general formula to describe the velocity profiles at different cross sections is given in the following equation:

$$\frac{u_0 - u}{u_0 - u_H} = f\left(\frac{y - y_2}{b}\right) = f(\eta) \quad , \quad (\text{A.20})$$

where b is the boundary layer thickness and η the dimensionless abscissa:

$$\eta = \frac{y - y_2}{b} \quad . \quad (\text{A.21})$$

Using the theory of Schlichting, the function $f(\eta)$ is:

$$f(\eta) = \left(1 - \eta^{\frac{3}{2}}\right)^2 \quad . \quad (\text{A.22})$$

The derivation of the velocity profiles in the initial region of an axially symmetric jet is based on the boundary layer thickness. It can be seen in equation A.23 that the thickness of the boundary layer b is proportional to the distance of the initial cross section x :

$$b = cx \frac{1 - m}{1 + m} \quad (\text{A.23})$$

Adapting the theory of Schlichting to the jet in coflow, equation A.22 can be written as:

$$\frac{u_0 - u}{u_0 - u_H} = \left(1 - \eta^{\frac{3}{2}}\right)^2 \quad . \quad (\text{A.24})$$

Hence, the dimensionless velocity at the cross section of the jet entry can be obtained:

$$\frac{u}{u_0} = 1 - (1 - m) f(\eta) , \quad (\text{A.25})$$

and taking the velocity of the adjoining medium as the reference for the dimensionless radial velocity profiles, equation A.24 is transformed into:

$$\frac{\Delta u}{\Delta u_0} = \frac{u - u_H}{u_0 - u_H} = 1 - f(\eta) . \quad (\text{A.26})$$

These equations can be used to separate the initial region and the main region mathematically, by calculating the length of the initial region. The beginning of the main region represents the beginning of the turbulent mixing phenomenon as well.

With the conservation of momentum and the assumption of constant density the contours of the boundary layer can be described as:

$$u_0 \pi r_0^2 (u_0 - u_H) = \int_{r_2}^{r_1} u (u - u_H) 2\pi r dr + u_0 (u_0 - u_H) \pi r_1^2 . \quad (\text{A.27})$$

The thickness of the boundary layer is given with the notation:

$$b = r_2 - r_1 , \quad (\text{A.28})$$

where

$$\begin{aligned} r_1 &= r_0 - y_1 , & r_2 &= r_0 - y_2 , & r &= r_0 - y \\ -dr &= dy , & d\eta &= \frac{dy}{b} , \end{aligned} \quad (\text{A.29})$$

for the following equation. Using equations A.24 to A.25 and the notations A.28 and A.29, equation A.27 can be rewritten:

$$1 - \left(1 - \frac{y_1}{r_0}\right)^2 = \left(2 \frac{b}{r_0} - 2 \frac{b^2}{r_0^2} \frac{y_2}{b}\right) f_1 - 2 \frac{b^2}{r_0^2} f_2 \quad (\text{A.30})$$

with

$$\begin{aligned}
 f_1 &= \int_0^1 (1-f) [1 - (1-m)f] d\eta \\
 &= 1 - (2-m) \int_0^1 f d\eta + (1-m) \int_0^1 f^2 d\eta
 \end{aligned}
 \tag{A.31}$$

$$\begin{aligned}
 f_2 &= \int_0^1 (1-f) [1 - (1-m)f] \eta d\eta \\
 &= 0.5 - (2-m) \int_0^1 f\eta d\eta + (1-m) \int_0^1 f^2 \eta d\eta
 \end{aligned}$$

and

$$\begin{aligned}
 \int_0^1 f d\eta &= 0.45, & \int_0^1 f^2 d\eta &= 0.316 \\
 \int_0^1 f\eta d\eta &= 0.127, & \int_0^1 f^2 \eta d\eta &= 0.065
 \end{aligned}$$

the functions f_1 and f_2 are simplified to:

$$\begin{aligned}
 f_1 &= 0.416 + 0.134m \\
 f_2 &= 0.309 + 0.062m
 \end{aligned}
 \tag{A.32}$$

hence integrating equation A.32 into A.30 and under utilisation of equation A.23 the length of the initial region of the jet is:

$$\bar{x}_H = \frac{x_H}{r_0} = \frac{1+m}{c(1-m)\sqrt{0.214+0.144m}}
 \tag{A.33}$$

Main Region of an Axially Symmetric Jet

In the following the velocity distribution along the symmetry axis ($\Delta u_m(x)$) for the main region is discussed. It is derived from the conservation of momentum along the x-axis. Equation A.34 shows the dimensionless velocity profile on the axis in dependence to the transverse section:

$$\Delta \bar{u}_m = \frac{\Delta u_m}{\Delta u_{0m}} = \frac{mA_1}{2A_2(1-m)} \left(\sqrt{1 + p^2 \frac{r_0^2}{r^2}} - 1 \right) \quad (\text{A.34})$$

where

$$p^2 = \frac{8.1(n_{2u} - mn_{1u})}{m^2}, \quad (\text{A.35})$$

$$A_1 = 2 \int_0^1 (1 - \xi^{1.5})^2 \xi d\xi = 0.258$$

$$A_2 = 2 \int_0^1 (1 - \xi^{1.5})^4 \xi d\xi = 0.134, \quad (\text{A.36})$$

$$n_{1u} = \int_0^1 \frac{\rho_0 u_0}{\rho_{0m} u_{0m}} \frac{dF_0}{F_0} = 1$$

$$n_{2u} = \int_0^1 \frac{\rho_0 u_0^2}{\rho_{0m} u_{0m}^2} \frac{dF_0}{F_0} = 1, \quad (\text{A.37})$$

for an axially symmetric jet with uniform velocity and density fields ($u_0 = u_{0m} = \text{const}$, $\rho_0 = \rho_{0m} \approx \text{const}$) at the initial cross section.

To obtain the dimensionless velocity distribution, in reference to a dimensionless ordinate in direction of propagation, a relation of the radius in the transverse cross section to an axial control variable has to be identified. Equation 2.42 is substituted to the increase of boundary layer thickness (equation A.38) which is obtained from the formulation of boundary layer thickness for the initial region (equation A.23).

$$\frac{db}{dx} = c \frac{u_m - u_H}{u_m + u_H} \iff c \frac{db}{dx} = \frac{\Delta u_m + 2u_H}{\Delta u_m} = 1 + 2 \frac{\Delta u_0}{\Delta u_m} \frac{m}{1-m} \quad (\text{A.38})$$

Hence:

$$c \frac{d\bar{x}}{d\bar{r}} = 1 + \frac{4 \frac{A_2}{A_1}}{\sqrt{1 + \frac{p^2}{\bar{r}^2} - 1}} , \quad (\text{A.39})$$

with $\bar{x} = \frac{x}{r_0}$ and $\bar{r} = \frac{r}{r_0}$. The integration of this equation, with the results for A_1 and A_2 , yield to:

$$c(\bar{x} - \bar{x}_0) = \bar{r} + \frac{0.69}{p^2} \left[(\bar{r}^2 + p^2)^{1.5} + \bar{r}^3 - p^3 \right] . \quad (\text{A.40})$$

The results of equation A.40 for different velocity ratios m can be extracted from diagram A.5.

The corresponding temperature and concentration profiles and their relation to the velocity distribution are given with the following formulas (temperature A.41 to A.44, concentration A.45 to A.48).

The dimensionless temperature profile is:

$$\Delta \bar{T}_m = \frac{\Delta T_m}{\Delta T_{0m}} = k_T \Delta \bar{u}_m , \quad (\text{A.41})$$

where

$$k_T = \frac{n_T (1-m)}{n_{2u} - m n_{1u}} \cdot \frac{\Delta \bar{u}_m A_2 (1-m) + A_1 m}{\Delta \bar{u}_m B_2 (1-m) + B_1 m} , \quad (\text{A.42})$$

$$B_1 = \int_0^1 \frac{\rho}{\rho_{0m}} \cdot \frac{c_p}{c_{p0m}} \cdot \frac{\Delta T}{\Delta T_m} \frac{dF}{F} = 2 \int_0^1 (1 - \xi^{1.5}) \xi d\xi = 0.428$$

$$B_2 = \int_0^1 \frac{\rho}{\rho_{0m}} \cdot \frac{c_p}{c_{p0m}} \cdot \frac{\Delta u}{\Delta u_m} \cdot \frac{\Delta T}{\Delta T_m} \frac{dF}{F} = 2 \int_0^1 (1 - \xi^{1.5})^3 \xi d\xi = 0.180 , \quad (\text{A.43})$$

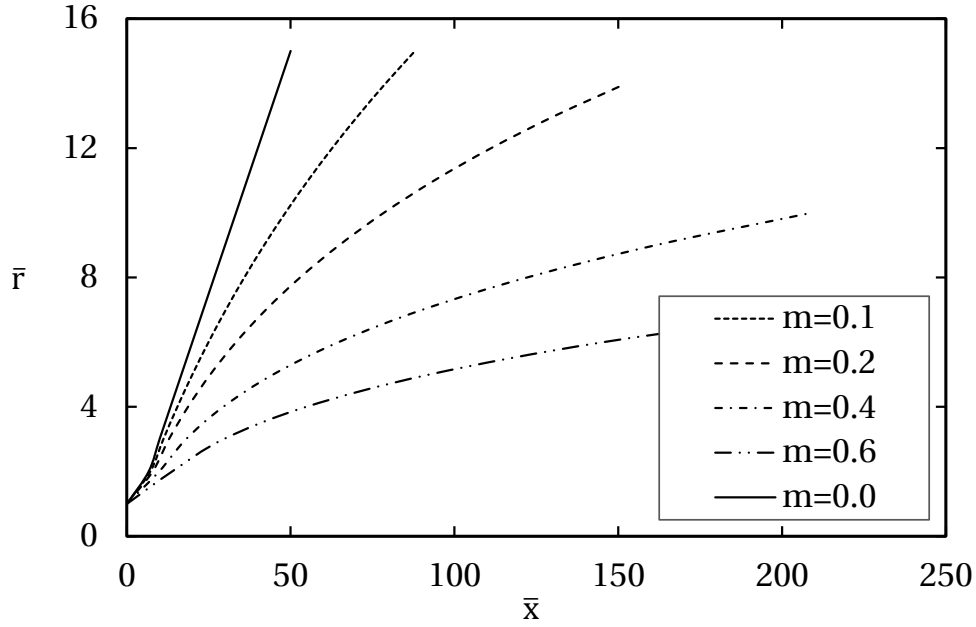


Figure A.5: The results for the boundary relation of \bar{r} to \bar{x} for different initial velocity ratios m .

$$n_T = \int_0^1 \frac{\rho_0}{\rho_{0m}} \cdot \frac{c_{p0}}{c_{p0m}} \cdot \frac{u_0}{u_{0m}} \cdot \frac{\Delta T_0}{\Delta T_{0m}} \frac{dF_0}{F_0} = 1 \quad , \quad (\text{A.44})$$

for jets with uniform velocity, density and temperature fields at the initial cross section.

Equally the dimensionless concentration profile is:

$$\Delta \bar{\chi}_m = \frac{\Delta \chi_m}{\Delta \chi_{0m}} = k_\chi \Delta \bar{u}_m \quad , \quad (\text{A.45})$$

where

$$k_\chi = \frac{n_\chi (1-m)}{n_{2u} - m n_{1u}} \cdot \frac{\Delta \bar{u}_m A_2 (1-m) + A_1 m}{\Delta \bar{u}_m D_2 (1-m) + D_1 m} \quad , \quad (\text{A.46})$$

$$\begin{aligned}
D_1 &= \int_0^1 \frac{\rho}{\rho_{0m}} \cdot \frac{\Delta\chi}{\Delta\chi_m} \frac{dF}{F} = 2 \int_0^1 (1 - \xi^{1.5}) \xi d\xi = 0.428 \\
D_2 &= \int_0^1 \frac{\rho}{\rho_{0m}} \cdot \frac{\Delta u}{\Delta u_m} \cdot \frac{\Delta\chi}{\Delta\chi_m} \frac{dF}{F} = 2 \int_0^1 (1 - \xi^{1.5})^3 \xi d\xi = 0.180 ,
\end{aligned} \tag{A.47}$$

$$n_\chi = \int_0^1 \frac{\rho_0}{\rho_{0m}} \cdot \frac{u_0}{u_{0m}} \cdot \frac{\Delta\chi_0}{\Delta\chi_{0m}} \frac{dF_0}{F_0} = 1 . \tag{A.48}$$

Based on the described equations for the initial and main region of an axially symmetric jet in coflow, it is possible to calculate the velocity, temperature and concentration at specific locations in the jet.

Two-Phase Jets

As mentioned in chapter 2.5.2 basis for the adaptations is the conservation of momentum (equation 2.44) leading to the initial momentum of the two-phase jet (equation 2.45).

Assuming a constant gas density and $F = \pi r^2$, $dF = 2\pi y dy = 2\pi r^2 \zeta d\zeta$ at the initial circular section of the jet, equation 2.44 can be transformed to:

$$\begin{aligned}
\dot{I}_0 &= \rho_B u_m^2 F \cdot 2 \int_0^1 \left(\frac{u}{u_m} \right)^2 (1 + \chi) \zeta d\zeta \\
&= \rho_B u_m^2 F \cdot \left[2 \int_0^1 \left(\frac{u}{u_m} \right)^2 \zeta d\zeta + 2\chi_m \int_0^1 \frac{\chi}{\chi_m} \left(\frac{u}{u_m} \right)^2 \zeta d\zeta \right] .
\end{aligned} \tag{A.49}$$

Incorporating the universal formulas (2.39, 2.41) of the coflow jet, the two integrals can be calculated (the first integral is found to be identical with A_2 from equation A.36):

$$\begin{aligned} A_2 &= 2 \int_0^1 \left(\frac{u}{u_m} \right)^2 \zeta d\zeta = 2 \int_0^1 (1 - \zeta^{1.5})^4 \zeta d\zeta = 0.134 \\ C_2 &= 2 \int_0^1 \frac{\chi}{\chi_m} \left(\frac{u}{u_m} \right)^2 \zeta d\zeta = 2 \int_0^1 (1 - \zeta^{1.5})^3 \zeta d\zeta = 0.108 \end{aligned} \quad (\text{A.50})$$

The velocity decrease on the jet axis is found with equation 2.46.

A.4 MATLAB Code for Droplet Distribution

This code creates the injections from given injection variables which are implemented into Ansys Fluent.

```
function
[]=createInj3d_150518(mpges,T,ymax,velocity,dquer,n,rrln,an,dminrr,dmax
rr,ro,anz,sigma,mu,X90,xshift,rshift,deltax)
%erstellt ein Fluent Injection File aus einer Vielzahl von
%Rosin-Rammler-Verteilungen. Die Verteilungen werden durch eine Vielzahl
von
%Injektionen repräsentiert. Dabei wird ebenfalls die Gewünschte
%Geschwindigkeitsverteilung und die Massenverteilung mit berücksichtigt
mpres=0;
[dsamplearray,mpres]=getsamples(dquer,n,rrln,an,dminrr,dmaxrr,ro,anz);
%mpa=mpges/mpres; wäre für Anzahlverteilungsfit
mpa=mpges/anz;%für Volumenhäufigkeit

fout = fopen('matlabrr3d.inj','wt');
sres='(';
%randwalk=1;
t=T;
x=zeros(3);
v=zeros(3);
%Xres=zeros(anz);
dar=zeros(anz,1);
mpar=zeros(anz,1);
for i=1:anz
    %für stochastik tracking entweder in der folgenden Zeile f->t bei
    %stochastic-on und bei random-eddy-on + bei n-tries die Anzahl der
    %Versuche oder in Fluent für alle Injektionen gemeinsam einstellen
    sres=[sres,'(injection-',int2str(i),' ((type . droplet) (injection-
type . single) (numpts . 2) (dpm-fname . " ") (surfaces . #f) (boundary
-1) (stochastic-on . #f) (random-eddy-on . #f) (ntries . 10) (time-
scale-constant . 0.15) (cloud-on . #f) (cloud-min-dia . 0.) (cloud-max-
dia . 100000.) (material . water-liquid) (scale-by-area . #f) (use-
face-normal . #f) (devolatilizing-species . #f) (evaporating-species .
h2o) (oxidizing-species . #f) (product-species . #f) (rr-distrib . #f)
(rr-uniform-ln-d . #f) (evaporating-liquid-on . #f) (evaporating-
material . #f) (liquid-fraction . 0.) (dpm-domain . none) (collision-
partner . *dem-unknown*) (multiple-surface) (parcel-number . 500)
(parcel-mass . 1e-09) (parcel-diameter . 1e-05) (parcel-model . 0)
(laws (law-1 . "Inert Heating") (law-2 . "Vaporization") (law-3 .
"Boiling") (law-4 . "Inert Heating") (law-5 . "Inactive") (law-6 .
"Inactive") (law-7 . "Inactive") (law-8 . "Inactive") (law-9 .
"Inactive") (law-10 . "Inactive") (switch . "Default")) (udf-inject-
init . "none") (udf-heat-mass . none)'];
```

```

function
[]=createInj3d_150518(mpges,T,ymax,velocity,dquer,n,rrln,an,dminrr,dmax
rr,ro,anz,sigma,mu,X90,xshift,rshift,deltax)
%erstellt ein Fluent Injection File aus einer Vielzahl von
%Rosin-Rammler-Verteilungen. Die Verteilungen werden durch eine Vielzahl
von
%Injectionen repräsentiert. Dabei wird ebenfalls die Gewünschte
%Geschwindigkeitsverteilung und die Massenverteilung mit berücksichtigt
mpres=0;
[dsamplearray,mpres]=getsamples(dquer,n,rrln,an,dminrr,dmaxrr,ro,anz);
%mpa=mpges/mpres; wäre für Anzahlverteilungsfit
mpa=mpges/anz;%für Volumenhäufigkeit

fout = fopen('matlabrr3d.inj','wt');
sres='(';
%randwalk=1;
t=T;
x=zeros(3);
v=zeros(3);
%Xres=zeros(anz);
dar=zeros(anz,1);
mpar=zeros(anz,1);
for i=1:anz
    %für stochastik tracking entweder in der folgenden Zeile f->t bei
    %stochastic-on und bei random-eddy-on + bei n-tries die Anzahl der
    %Versuche oder in Fluent für alle Injectionen gemeinsam einstellen
    sres=[sres,'(injection-',int2str(i),' ((type . droplet) (injection-
type . single) (numpts . 2) (dpm-fname . " ") (surfaces . #f) (boundary
-1) (stochastic-on . #f) (random-eddy-on . #f) (ntries . 10) (time-
scale-constant . 0.15) (cloud-on . #f) (cloud-min-dia . 0.) (cloud-max-
dia . 100000.) (material . water-liquid) (scale-by-area . #f) (use-
face-normal . #f) (devolatilizing-species . #f) (evaporating-species .
h2o) (oxidizing-species . #f) (product-species . #f) (rr-distrib . #f)
(rr-uniform-ln-d . #f) (evaporating-liquid-on . #f) (evaporating-
material . #f) (liquid-fraction . 0.) (dpm-domain . none) (collision-
partner . *dem-unknown*) (multiple-surface) (parcel-number . 500)
(parcel-mass . 1e-09) (parcel-diameter . 1e-05) (parcel-model . 0)
(laws (law-1 . "Inert Heating") (law-2 . "Vaporization") (law-3 .
"Boiling") (law-4 . "Inert Heating") (law-5 . "Inactive") (law-6 .
"Inactive") (law-7 . "Inactive") (law-8 . "Inactive") (law-9 .
"Inactive") (law-10 . "Inactive") (switch . "Default")) (udf-inject-
init . "none") (udf-heat-mass . none)'];

```

The following code ask for injection variables which have to be specified based on experimental data or data sheets provided by the producer of the nozzle. It is needed for the code to create the specific injections (shown before).

A.4 MATLAB Code for Droplet Distribution

```
%Massenstrom:
mpges=(20.3/3600)/6;
%Temperatur in Kelvin
T=300;
%Velocity [m/s] wird derzeit als konstant angenommen
velocity=170;
%RRfits (Anzahl =a)
a=3;
dquer=zeros(a,1);
n=zeros(a,1);
rrln=zeros(a,1);
an=zeros(a,1);
dminrr=zeros(a,1);
dmaxrr=zeros(a,1);
dquer(1)=10e-6;
n(1)=12;
%rrln(1)=0;
an(1)=0.134;
dmin(1)=6e-6;
dmax(1)=3e-4;
dquer(2)=29e-6;
n(2)=2.4;
%rrln(2)=0;
an(2)=0.525;
dmin(2)=6e-6;
dmax(2)=3e-4;
dquer(3)=59e-6;
n(3)=1.6;
%rrln(3)=0;
an(3)=0.341;
dmin(3)=6e-6;
dmax(3)=3e-4;
%Dichte des Sprymediums [kg/m^3]
ro=997;
%Anzahl der Samples
anz=1000;
```

```
%derzeit wird ein Gausfit für die Massenverteilung verwendet (mean =0)
%Var=sigma^2
sigma=130;
mu=0;
%Orientierungswert X90 (in mm) für die maximale Breite der Strahls; die
%Rohrlänge wird im Programm als 300 mm vom Strahl aus berechnet
X90=90;
%xshift verschiebt die xposition [m] der Injektionen
xshift=0;
%rshift entspricht dem minimalen radius in mm ab dem die Injektionen
%starten sollen
rshift=0.2;
%ymax beschreibt die maximale Breite des Auslasses Einheit mm
rmax=1.1;
%deltax ist der Abstand in mm zwischen verschobener Eindüsung und
Patternator, is nur wichtig,
%wenn die Injektionen verschoben zu ihrer physikalsichen Position
iniziert
%werden
deltax=300;
createInj3d_150518 (mpges, T, rmax, velocity, dquer, n, rrln, an, dminrr, dmaxrr,
ro, anz, sigma, mu, X90, xshift, rshift, deltax);
```

A.5 Summary Test Conditions and Additional Results

A.5.1 Summary Test Conditions

Test	Swirl	Length ST [mm]	Length MX [mm]	Cell density [cps]	\dot{m} main air [kg h ⁻¹]	T main air [°C]	\dot{m} UWS [kg h ⁻¹]	UWS [%]	water vapour [%]	UWS/Air $\cdot 10^{-3}$	Re
OP1	no / yes	250 / 200	0 / 50	200	235	460	7.3	40	0	31.1	525
OP2	no / yes	250 / 200	0 / 50	200	195	490	13.4	40	0	68.7	424
OP3	no / yes	250 / 200	0 / 50	200	255	510	20.3	40	0	79.6	545
OP4	no / yes	250 / 200	0 / 50	200	315	550	25.3	40	0	80.3	652
RC	no	100	50	200	290	400	2.4	40	0	8.28	695
TC1	no	100	50	200	290	400	2.4	40	3	8.28	695
TC2	no	100	50	200	290	400	2.6	37	0	8.97	695
TC3	no	100	50	200	290	400	3.2	30	0	11.0	695
TC4	no	100	50	200	385	400	2.4	40	0	6.23	923
TC5	no	200	50	200	290	400	2.4	40	0	8.28	695
TC6	no	150	0	200	290	400	2.4	40	0	8.28	695
TC7	yes	100	50	200	290	400	2.4	40	0	8.28	695
TC8	yes	100	50	200	250	500	14	40	0	56.0	546
TC9	yes	100	50	200	177	500	9.9	40	0	56.0	386
TC10	yes	100	50	400	250	500	14	40	0	56.0	386

Table A.2: Summary of concentration measurement conditions.

Test	\dot{m} / velocity main air [kg h ⁻¹] / [m s ⁻¹]	T main air [°C]	\dot{m} water [kg h ⁻¹]	\dot{V} / velocity air nozzle [L min ⁻¹] / [m s ⁻¹]
Pitot measurements and simulation				
PT1	290 / -	400	0	0 / -
PT2	290 / -	400	0	100 / -
PT1 Sim	- / 16.4	400	0	- / 0
PT2 Sim	- / 16.4	400	0	- / 170
PIV measurements				
OT1	290	300	2.4	100
OT2	290	350	2.4	100
OT3	290	400	2.4	100
OT4	290	300	7.3	100
OT5	290	350	7.3	100
OT6	290	400	7.3	100
Injector Tests				
OP1 S940	0	20	7.3	100
OP2 S940	0	20	13.4	100
OP3 S940	0	20	20.3	100
OP4 S940	0	20	25.3	100 / 190
OP4 MAN	0	20	25.3	100 / 190
Simulations				
NT1	- / 16.4	400	2.4	- / 170
NT2	- / 16.4	400	7.3	- / 170
NT3	- / 14.45	460	7.3	- / 170
NT4	- / 12.65	490	13.4	- / 170
NT5	- / 16.75	510	20.3	- / 170

Table A.3: Summary Pitot, PIV, injector tests and simulation conditions.

A.5.2 Additional Results

A tangential velocity profile for OT3 and OT6 without swirling coflow obtained from PIV measurements is shown in figure A.6.

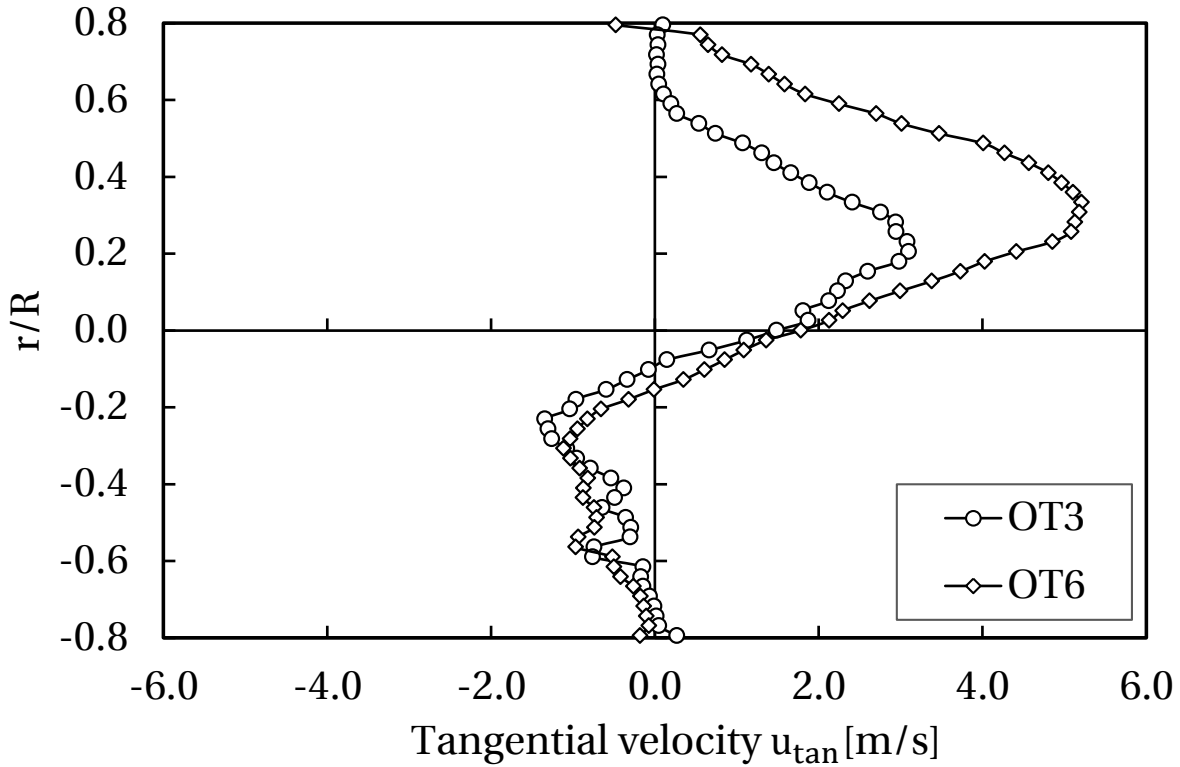


Figure A.6: Tangential droplet velocity to the normalised channel radius in coflow at CS1 (OT3 and OT6).

Supervised Theses

With this Ph.D. thesis a number of student theses are associated (Bachelor-Thesis, Forschungspraktika, Semesterarbeiten, Diplomarbeiten) that were supervised by the author of the present work. These theses were prepared at the Lehrstuhl für Thermodynamik between 2011 and 2014 based on the objectives and close supervision of the present author. Certain aspects and insights of these supervised theses may have been incorporated into this thesis. The author would like to express her sincere gratitude to all supervised students for their dedication to this research project.

Im Rahmen dieser Dissertation entstanden am Lehrstuhl für Thermodynamik in den Jahren 2011 bis 2014 unter wesentlicher wissenschaftlicher, fachlicher und inhaltlicher Anleitung der Autorin die im Folgenden aufgeführten studentischen Arbeiten. Gewisse Aspekte und Erkenntnisse aus diesen Arbeiten können in Teilen in das vorliegende Dokument eingeflossen sein. Die Autorin dankt hiermit nochmals explizit allen betreuten Studenten für ihr Engagement bei der Unterstützung dieser wissenschaftlichen Arbeit.

Supervised Theses

Student	Topic
Henrik Bär	Konstruktion und Aufbau eines Hydrolysekatalysator für SCR-Abgasreinigungsanlagen; Semesterarbeit, submitted in May 2012
Thomas Waim	Düsenentwicklung für die Urea-SCR Technik von Medium Speed Diesel Motoren; Diplomarbeit, submitted in August 2012
Tobias Böttcher	Aufbau und Inbetriebnahme eines Prüfstandes zur Vermessung von Spray-Partikelgrößen-Verteilungen; Bachelor-Thesis, submitted in September 2012
Christoph Kaindl	Experimentelle Untersuchung eines Hydrolysekatalysators für die SCR-Abgasreinigung unter Berücksichtigung motorischer Betriebsparameter; Bachelor-Thesis, submitted in October 2012
Matthias Gigl	Aufbau und Inbetriebnahme eines optischen Messsystems zur Analyse von Spraycharakteristiken; Semesterarbeit, submitted in November 2012
Anna Garcia Teruel	Fluid mechanic and thermodynamic analysis of the flow in the ammonia generator of an SCR process; Semesterarbeit, submitted in March 2014
Viona Müller	Mischvorgänge und Konzentrationsverteilung des Hydrolysereaktors für SCR-Verfahren; Forschungspraktikum, submitted in June 2014
Max Arzberger	Numerische Simulation der Dispersion von Flüssigkeiten für die Anwendung in Hydrolysereaktoren; Bachelor-Thesis, submitted in October 2014
Zita Baumann	Implementierung und experimentelle Untersuchung der Thermolyse sowie der Hydrolyse bei der SCR-Abgasnachbehandlung; Semesterarbeit, submitted in November 2014

Bibliography

- [1] Abramovic, G. N., 1963. *The Theory of Turbulent Jets*. M.I.T. Press.
- [2] Annesini, M. C., Marrelli, L., Piemonte, V., and Turchetti, L., 2017. *Artificial Organ Engineering*, 1 ed. Springer-Verlag London.
- [3] Ansys, I., 2013. *Ansys Fluent 15.0 Theory Guide*.
- [4] Ansys, I., 2013. *Ansys Fluent 15.0 User's Guide*.
- [5] Ashgriz, N., 2011. *Handbook of Atomization and Sprays: Theory and Application*. Springer-Verlag New York.
- [6] Babinsky, E., and Sojka, P. E., 2002. "Modeling drop size distribution". *Progress in Energy and Combustion Science*, **28**(4), pp. 303–329.
- [7] Baerns, M., Behr, A., Brehm, A., Gmehling, J., Hinrichsen, K. O., Hofmann, H., Onken, U., Palkovits, R., and Renken, A., 2013. *Technische Chemie*. Wiley-VCH Verlag.
- [8] Bartholomew, C. H., 2001. "Mechanisms of Catalyst Deactivation". *Applied Catalysis, A: General*, **212**, pp. 17–60.
- [9] Bauerle, G. L., Wu, S. C., and Nobe, K., 1978. "Parametric and Durability Studies of NO_x Reduction with NH₃ and V₂O₅ Catalysts". *Industrial & Engineering Chemistry Product Research and Development*, **17**(2), pp. 117–122.
- [10] Bayvel, L., and Orzechowski, Z., 1993. *Liquid Atomization*. Taylor & Francis Washington, DC.

- [11] Bernhard, A. M., 2012. “Catalytic Urea Decomposition, Side-Reactions and Urea Evaporation in the Selective Catalytic Reduction of NO_x”. PhD thesis, ETH Zürich.
- [12] Bernhard, A. M., Czekaj, I., Elsener, M., Wokaun, A., and Kroecher, O., 2011. “Evaporation of Urea at Atmospheric Pressure”. *Journal of Physical Chemistry A*, **115**(12), pp. 2581–2589.
- [13] Bernhard, A. M., Peitz, D., Elsener, M., Schildhauer, T., and Kroecher, O., 2013. “Catalytic Urea Hydrolysis in the Selective Catalytic Reduction of NO_x: Catalyst Screening and Kinetics on Anatase TiO₂ and ZrO₂”. *Catalysis Science Technology*, **3**(4), pp. 942–951.
- [14] Bernhard, A. M., Peitz, D., Elsener, M., Wokaun, A., and Kroecher, O., 2012. “Hydrolysis and Thermolysis of Urea and its Decomposition Byproducts Biuret, Cyanuric Acid and Melamine over Anatase TiO₂”. *Applied Catalysis B: Environmental*, **115–116**, pp. 129–137.
- [15] Birkhold, F., 2007. “Selektive katalytische Reduktion von Stickoxiden in Kraftfahrzeugen: Untersuchung der Einspritzung von Harnstoffwasserlösung”. PhD thesis, University of Karlsruhe.
- [16] Birkhold, F., Meingast, U., Wassermann, P., and Deutschmann, O., 2006. “Analysis of the Injection of Urea-Water-Solution for Automotive SCR DeNO_x-Systems: Modeling of Two-Phase Flow and Spray/Wall-Interaction”. *SEA Technical Paper*, **2006-01-0643**.
- [17] Birkhold, F., Meingast, U., Wassermann, P., and Deutschmann, O., 2007. “Modeling and Simulation of the Injection of Urea-Water-Solution for Automotive SCR DeNO_x-Systems”. *Applied Catalysis B: Environmental*, **70**, pp. 119–127.
- [18] Bjorklund, R. B., Jaeras, S., Ackleid, U., Odenbrand, C. U. I., Andersson, L. A. H., and Brandin, J. G. . M., 1991. “Effect of Promoters on V₂O₅/SiO₂ Catalysts Active for Selective Reduction of NO”. *Journal of Catalysis*, **128**, pp. 574–580.
- [19] Brandenberger, S., Kroecher, O., Tissler, A., and Althoff, R., 2008. “The State of the Art in Selective Catalytic Reduction of NO_x by Ammonia

- Using Metal-Exchanged Zeolite Catalysts”. *Catalysis Reviews*, **50**(4), pp. 492–531.
- [20] Buzanowski, M. A., and Yang, R., 1990. “Simple Design of Monolith Reactor for Selective Catalytic Reduction of Nitric Oxide for Power Plant Emission Control”. *Industrial & Engineering Chemistry Research*, **29**(10), pp. 2074–2078.
- [21] Casapu, M., Bernhard, A. M., Peitz, D., Mehring, M., Elsener, M., and Kroeher, O., 2011. “A Niobia-Ceria Based Multi-Purpose Catalyst for Selective Catalytic Reduction of NO_x, Urea Hydrolysis and Soot Oxidation in Diesel Exhaust”. *Applied Catalysis B: Environmental*, **103**, pp. 79–84.
- [22] Castellino, F., 2008. “Deactivation of SCR Catalysts by Additives”. PhD thesis, Technical University of Denmark.
- [23] Ciambelli, P., Fortuna, M., Sannino, D., and Baldacci, A., 1996. “The Influence of Sulphate on the Catalytic Properties of V₂O₅-TiO₂ and WO₃-TiO₂ in the Reduction of Nitric Oxide with Ammonia”. *Catalysis Today*, **29**(4), pp. 161–164.
- [24] Cybulski, A., and Moulijn, J. A., 2006. *Structured Catalyst and Reactors*, 2. edition ed. Marcel Drekker Inc.
- [25] Durack, P. J., Wijffels, S. E., and Matear, R. J., 2012. “Ocean Salinities Reveal Strong Global Water Cycle Intensification During 1950 to 2000”. *Science*, **336**(6080), pp. 455–458.
- [26] Ehlers, H., Larjo, J., Antikainen, O., Räikkönen, H., Heinämäki, J., and Yliruusi, J., 2010. “In Situ Droplet Size and Speed Determination in a Fluid-Bed Granulator”. *International Journal of Pharmaceutics*, **391**, pp. 148–154.
- [27] Environmental Protection Agency, 1999. In-Use Marine Diesel Fuel, EPA420-R-99-027. Tech. rep., United States Environmental Protection Agency.

- [28] Eyring, V., Corbett, J. J., Lee, D. S., and Winebrake, J. J., 2007. Brief Summary of the Impact of Ship Emissions on Atmospheric Composition, Climate, and Human Health. Tech. rep., International Maritime Organization.
- [29] Fang, H. L., and DaCosta, H. F., 2003. “Urea Thermolysis and NO_x Reduction with and without SCR Catalysts”. *Applied Catalysis B: Environmental*, **46**(1), pp. 17 – 34.
- [30] Fischer, G., Geith, J., Klapötke, T. M., and Krumm, B., 2002. “Synthesis, Properties and Dimerization Study of Isocyanic Acid”. *Zeitschrift für Naturforschung B*, **57**(1), pp. 19–24.
- [31] Forzatti, P., and Lietti, L., 1999. “Catalyst Deactivation”. *Catalysis Today*, **52**, pp. 165–181.
- [32] Fuchs, N. A., 1959. *Evaporation and Droplet Growth in Gaseous Media*. Pergamon Press London.
- [33] Fuller, E. N., Ensley, K., and Giddings, J. C., 1969. “Diffusion of Halogenated Hydrocarbons in Helium. The Effect of Structure on Collision Cross Sections”. *Journal of Physical Chemistry*, **73**(11), pp. 3679—3685.
- [34] Gel’fand, B. E., Gubin, S. A., and Kogarko, S. M., 1974. “Various Forms of Drop Fractionation in Shock Waves and their Special Characteristics”. *Journal of Engineering Physics*, **27**(1), pp. 877–882.
- [35] Glauert, M. B., 1956. “The Wall Jet”. *Journal of Fluid Mechanics*, **1**, 12, pp. 625 –643.
- [36] Grossale, A., Nova, I., Tronconi, E., Chatterjee, D., and Weibel, M., 2008. “The Chemistry of the NO/NO₂–NH₃ “fast” SCR Reaction over Fe-ZSM5 Investigated by Transient Reaction Analysis”. *Journal of Catalysis*, **256**, pp. 312–322.
- [37] Gruenwald, J., 2007. “Verbesserung der Reduktionsmitteldispersion und-Verdunstung in SCR-Abgasanlagen”. PhD thesis, Technical University Munich.

- [38] Gupta, A. K., Lilley, D. G., and Syred, N., 1984. *Swirl Flows*. Abacus Press.
- [39] Hall, M. G., 1972. “Vortex Breakdown”. *Annual Review of Fluid Mechanics*, **4**, pp. 195–218.
- [40] Hansen, J., Sato, M., and Ruedy, R., 2012. “Perception of Climate Change”. In *Proceedings of the National Academy of Sciences of the United States of America*, Vol. 109.
- [41] Hauck, P., Jentys, A., and Lercher, J. A., 2007. “Surface Chemistry and Kinetics of the Hydrolysis of Isocyanic Acid on Anatase”. *Applied Catalysis B: Environmental*, **70**, pp. 91–99.
- [42] Hauck, P. C. D. P., 2007. “Surface Chemistry and Kinetics of the Hydrolysis of Isocyanic Acid on TiO₂ Anatase”. PhD thesis, Technical University Munich.
- [43] Helden, R. v., Verbeek, R., Willems, F., and Welle, R. v. d., 2004. “Optimization of Urea SCR deNO_x Systems for HD Diesel Engines”. *SAE Technical Paper*, **2004-01-0154**.
- [44] Herr, A., 2004. “Thermische Zersetzung von Festharnstoff für mobile SCR-Katalysatoranwendungen”. PhD thesis, Technical University Kaiserslautern.
- [45] Hsiang, L.-P., and Faeth, M. G., 1992. “Near-Limit Drop Deformation and Secondary Breakup”. *International Journal of Multiphase Flow*, **18**(5), pp. 635–652.
- [46] Hussein, J. H., Capp, S. P., and George, W. K., 1994. “Velocity Measurements in a High-Reynolds-Number, Momentum-Conserving, Axisymmetric, Turbulent Jet”. *Journal of Fluid Mechanics*, **258**, pp. 31–75.
- [47] International Maritime Organization, 2017. Nitrogen Oxides (NO_x) – Regulation 13 .
- [48] Jain, M., Prakash, R. S., Tomar, G., and Ravikrishna, R. V., 2015. “Secondary Breakup of a Drop at Moderate Weber Numbers”. *Proceedings of the Royal Society of London A: Mathematical, Physical and Engineering Sciences*, **471**(2177).

- [49] Juslin, L., Antikainen, O., Merkku, P., and Yliruusi, J., 1995. “Droplet Size Measurement: I. Effect of Three Independent Variables on Droplet Size Distribution and Spray Angle from a Pneumatic Nozzle”. *International Journal of Pharmaceutics*, **123**(2), pp. 247–256.
- [50] Kawahara, K., and Tanford, C., 1966. “Viscosity and Density of Aqueous Solutions of Urea and Guanidine Hydrochloride”. *Journal of Biological Chemistry*, **241**(13), pp. 3228–3232.
- [51] Kim, K. Y., and Marshall, W. R., 1971. “Drop-Size Distributions from Pneumatic Atomizers”. *AIChE Journal*, **17**(3), pp. 575–584.
- [52] Kleemann, M., Elsener, M., Koebel, M., and Wokaun, A., 2000. “Hydrolysis of Isocyanic Acid on SCR Catalysts”. *Industrial & Engineering Chemistry Research*, **39**(11), pp. 4120–4126.
- [53] Koebel, M., and Elsener, M., 1995. “Determination of Urea and its Thermal Decomposition Products by High-Performance Liquid Chromatography”. *Journal of Chromatography*, **A 689**, pp. 164–169.
- [54] Koebel, M., and Elsener, M., 1998. “Selective Catalytic Reduction of NO over Commercial DeNO_x-Catalysts: Experimental Determination of Kinetic and Thermodynamic Parameters”. *Chemical Engineering Science*, **53**(4), pp. 657–669.
- [55] Koebel, M., Elsener, M., and Marti, T., 1996. “NO_x-Reduction in Diesel Exhaust Gas with Urea and Selective Catalytic Reduction”. *Combustion Science and Technology*, **121**, pp. 85–102.
- [56] Koebel, M., and Strutz, E. O., 2003. “Thermal and Hydrolytic Decomposition of Urea for Automotive Selective Catalytic Reduction Systems: Thermochemical and Practical Aspects”. *Industrial & Engineering Chemistry Research*, **42**, pp. 2093–2100.
- [57] Kraume, M., 2012. *Transportvorgänge in der Verfahrenstechnik: Grundlagen und operative Umsetzung*. Springer-Verlag Berlin Heidelberg.
- [58] Kundu, P. K., and Cohen, I. M., 2008. *Fluid Mechanics*, 4th Edition ed. Academic Press.

- [59] Lacroix, A., 2005. “Untersuchung eines Harnstoff-SCR-Systems zur Stickoxidminderung im Diesel-PKW-Praxiseinsatz”. PhD thesis, Technical University Kaiserslautern.
- [60] Lappa, M., 2012. *Rotating Thermal Flows in Natural and Industrial Processes*. John Wiley & Sons.
- [61] Latscha, H. P., Linti, G. W., and Klein, H. A., 2004. *Analytische Chemie – Basiswissen III*. Springer-Verlag Berlin Heidelberg.
- [62] Launder, B. E., and Rodi, W., 1983. “The Turbulent Wall Jet - Measurements and Modeling”. *Annual Review of Fluid Mechanics*, **15**, pp. 429–459.
- [63] Lee, C. S., and Reitz, R. D., 2001. “Effect of Liquid Properties on the Breakup Mechanism of High-Speed Liquid Drops”. *Atomization and Sprays*, **11**(1), pp. 1–19.
- [64] Lefebvre, A. H., 1989. *Atomization and Sprays*. Hemisphere Publishing Corporation.
- [65] Lui, H., 2000. *Science and Engineering of Droplets: Fundamentals and Applications*. Noyes Publications.
- [66] Lynn, K. R., 1965. “Kinetics of Based-Catalyzed Hydrolysis of Urea”. *Journal of Physical Chemistry*, **69**(2), pp. 687–689.
- [67] Marine Environment Protection Committee, 2008. Annex 13, MEPC 58/23/Add.1. Tech. rep., MARPOL.
- [68] Moulijn, J., van Diepen, A., and Kapteijn, F., 2001. “Catalyst Deactivation: is it Predictable? What to do?”. *Applied Catalysis, A: General*, **212**, pp. 3–16.
- [69] Movahednejad, E., Ommi, F., and Hosseinalipour, S. M., 2010. “Prediction of Droplet Size and Velocity Distribution in Droplet Formation Region of Liquid Spray”. *Entropy*, **12**, pp. 1484–1498.
- [70] Nasr, G. G., Yule, A. J., and Bendig, L., 2002. *Industrial Sprays and Atomization - Design, Analysis and Applications*. Springer-Verlag London.

- [71] Nova, I., and Tronconi, E., 2014. *Urea-SCR Technology for deNO_x After Treatment of Diesel Exhausts*. Springer-Verlag Berlin Heidelberg.
- [72] Nukiyama, S., 1966. “The Maximum and Minimum Values of the Heat Q Transmitted from Metal to Boiling Water under Atmospheric Pressure”. *International Journal of Heat and Mass Transfer*, **9**(12), pp. 1419–1433.
- [73] Opfer, L., Weickgennant, C., Roisman, I. V., and Tropea, C., 2012. “Breakup of Complex Liquid Drops and Jets”. In 10th Spray Workshop, Berlin.
- [74] Otic, I., and Class, A. G., 2007. “Numerical Investigation of a Heated Sodium Jet in a Co-Flow”. *ASME/JSME Joint Fluids Engineering Conference*, **2**(FEDSM2007-37566), pp. 225–231.
- [75] Otto, M., 2011. *Analytische Chemie*. Wiley-VCH, Weinheim.
- [76] Pachauri, R. K., and et. al., 2014. Climate Change 2014 Synthesis Report. Tech. rep., IPCC.
- [77] Peitz, D., Bernhard, A., Elsener, M., and Kroeher, O., 2011. “Laboratory Test Reactor for the Investigation of Liquid Reducing Agents in the Selective Catalytic Reduction of NO_x”. *Review of Scientific Instruments*, **82**.
- [78] Pratt, A. S., and Cairns, J. A., 1977. “Noble Metal Catalysts on Metallic Substrates”. *Platinum Metals Review*, **21**(3), pp. 74–83.
- [79] Raffel, M., Willert, C., and Kompenhans, J., 1998. *Particle Image Velocimetry: A Practical Guide*. Springer-Verlag Berlin Heidelberg.
- [80] Reif, K., 2012. *Diesemotor-Management: Systeme, Komponenten, Steuerung und Regelung*. Springer-Verlag Berlin Heidelberg.
- [81] Sazhin, S., 2014. *Droplets and Sprays*. Springer-Verlag London.
- [82] Schaber, P. M., Colson, J., Higgins, S., Thielen, D., Anspach, B., and Brauer, J., 2004. “Thermal Decomposition (Pyrolysis) of Urea in an Open Reaction Vessel”. *Thermochimica Acta*, **424**, pp. 131–142.

- [83] Schlichting, H., and Gersten, K., 2000. *Boundary Layer Theory*, 8th ed. Springer-Verlag Berlin Heidelberg.
- [84] Schlick Atomizing Technologies. *Modulsystemreihe 940*.
- [85] Schönbacher, A., 2002. *Thermische Verfahrenstechnik: Grundlagen und Berechnungsmethoden für Ausrüstungen und Prozesse*. Springer-Verlag Berlin Heidelberg.
- [86] Sigloch, H., 2014. *Technische Fluidmechanik*. Springer-Verlag Berlin Heidelberg.
- [87] Steenbergen, W., 1995. “Turbulent Pipe Flow with Swirl”. PhD thesis, Eindhoven University of Technology.
- [88] Stein, S., 2005. “On-Board-Reduktionsmittelherstellung zur NO_x-Emissionsminderung bei Dieselfahrzeugen”. PhD thesis, RWTH Aachen.
- [89] Steinbach, S., 2007. “Einfluss der Transportvorgänge auf die Effizienz von Harnstoffkatalysatoren in SCR-Abgasanlagen”. PhD thesis, Technical University Munich.
- [90] Steinbach, S., Gruenwald, J., and Sattelmayer, T., 2006. “Urea-SCR-Technology – Performance of Structured Metallic Substrates”. *SAE Technical Paper*, **2006-01-3505**.
- [91] Toshev, P. K., 2015. “NO_x-Reduzierung in motorischem Abgas durch Ammoniakherzeugung im Teilstromverfahren aus Guanidinium Formiat und Harnstoff”. PhD thesis, Technical University Munich.
- [92] van Basshuysen, R., and Schaefer, F., 2015. *Handbuch Verbrennungsmotor: Grundlagen, Komponenten, Systeme, Perspektiven*, 7. ed. Springer-Verlag Berlin Heidelberg.
- [93] VDI-Gesellschaft, 2013. *VDI-Wärmeatlas*, 11. auflage ed. Springer-Verlag Berlin Heidelberg.

- [94] Waim, T., 2012. “Düsenentwicklung für die Urea-SCR Technik von Medium Speed Diesel Motoren”. Master’s thesis, Technical University Munich.
- [95] Wang, W.-N., Purwanto, A., Wuled Lenggoro, I., Okuyama, K., Chang, H., and Jang, H. D., 2008. “Investigation on the Correlations between Droplet and Particle Size Distribution in Ultrasonic Spray Pyrolysis”. *Industrial & Engineering Chemistry Research*, **47**, pp. 1650–1659.
- [96] Williams, J. L., 2001. “Monolith Structures, Materials, Properties and Uses”. *Catalysis Today*, **69**, pp. 3–9.
- [97] Wozniak, G., 2003. *Zerstäubungstechnik: Prinzipien, Verfahren und Geräte*. Springer-Verlag Berlin Heidelberg.
- [98] Yim, S. D., Kim, S. J., Baik, J. H., Nam, I.-S., Mok, Y. S., Lee, J.-H. Cho, B. K., and Oh, S. H., 2004. “Decomposition of Urea into NH₃ for the SCR Process”. *Industrial & Engineering Chemistry Research*, **43**(16), pp. 4856–4863.
- [99] Zhou, G., and Kresta, S. M., 1998. “Correlation of Mean Drop Size and Minimum Drop Size with the Turbulence Energy Dissipation and the Flow in an Agitated Tank”. *Chemical Engineering Science*, **53**(11), pp. 2063–2079.
- [100] Zielke, P. C., 2008. “Experimentelle Untersuchung der Bewegung von Tropfen auf Festkörperoberflächen mit einem Gradienten der Benetzbarkeit”. PhD thesis, University Erlangen-Nürnberg.